JOURNAL OF GEOGRAPHY AND CARTOGRAPHY

Editorial Board

Editor-in-Chief

Dr. Gemma Aiello
National Research Council of Italy (CNR)
Italy

Associate Editor

Dr. Kaveh Ostad-Ali-Askari
Isfahan (Khorasgan) Branch, Islamic Azad University
Islamic Republic of Iran

Editorial Board Member

Journal of Geography and Cartography

Journal of Geography and Cartography

Contents

Review Article

Case Report

Predicting fire hazard areas using vegetation indexes, case study: Forests of Golestan Province, Iran

Akram Karimi¹, Sara Abdollahi², Kaveh Ostad-Ali-Askari³*, Saeid Eslamian⁴, Vijay P. Singh⁵

¹Graduate Degree in Environmental Education, Evaluation and Evaluation Tendency, Karaj Environmental Faculty, Karaj, Iran.

²MSc of Environmental Science, Yazd University, Yazd, Iran.

³Department of Civil Engineering, Isfahan (Khorasgan) Branch, Islamic Azad University, Isfahan, Iran. E-mail: koa.askari@khuisf.ac.ir

⁴Department of Water Engineering, Isfahan University of Technology, Isfahan, Iran.

⁵Department of Biological and Agricultural Engineering & Zachry Department of Civil Engineering, Texas A&M University, College Station, Texas 77843, USA.

ABSTRACT

Every year, hundreds of fires occur in the forests and rangelands across the world and damage thousands hectare of trees, shrubs, and plants which cause environmental and economic damages. This study aims to establish a real time forest fire alert system for better forest management and monitoring in Golestan Province. In this study, in order to prepare fire hazard maps, the required layers were produced based on fire data in Golestan forests and MODIS sensor data. At first, the natural fire data was divided into two categories of training and test samples randomly. Then, the vegetation moisture stresses and greenness were considered using six indexes of NDVI, MSI, WDVI, OSAVI, GVMI and NDWI in natural fire area of training category on the day before fire occurrence and a long period of 15 years, and the risk threshold of the parameters was considered in addition to selecting the best spectral index of vegetation. Finally, the model output was validated for fire occurrences of the test category. The results showed the possibility of prediction of fire site before occurrence of fire with more than 80 percent accuracy.

Keywords: Time Series; MODIS Sensor; Threshold; NDWI

ARTICLE INFO

COPYRIGHT

1. Introduction

Since natural resources are among the most important and valuable national capital of every country, and according to the main role of these resources on economic and social life of human being, their conservation and expansion should be one of the most essential plans in every country. Many factors cause quantitative and qualitative changes on natural ecosystems such as natural extinction, natural disasters such as fire, flood, population density, pests and plant diseases[1]. Among these destructive factors, fire is one of the main causes of natural ecosystem destruction, which leads to significant damages on these areas[2]. Iran has forests and rangelands with different climates and vegetations. According to Forest, Rangelands, and Watershed Management Organization (FRWO) report, natural areas of the country include: forest, rangeland, desert, and shrubbery, which are 83.48 percent of total area of the country[3]. In addition, according to FRWO report, forest and rangelands are 61.82 percent of total area of the country. Investigations show that most of fire occurred in these areas[4]. In Iran, about

160000 hectares of forests have been destroyed by fire during 28 years (1969-1997), After Iranian revolution (from 1979 to 1996), about 87000 hectares of forest destroyed by fire[5].

Determining susceptible areas to fire is one of the first measures for forest and rangeland conservation and protection against fire. Forest fire hazard map can be used as a useful guide for natural fire management and an important prevention strategy. These maps will help the natural resources bureau officers to be aware of fire hazard in natural environment, or do the best thing during fire. Remote sensing can provide useful information about environment, before, during, and after fire, especially monitoring active fire[6,7]. So far, various researches have been carried out on zoning areas with high fire potential[8-11]. Mosavari *et al*. and Shorfi *et al*. categorized fire hazard areas into low to high potential areas using overlaying climate layers and common assessment methodologies, and mentioned that large area of these classes will lead to difficult management efforts[12,13]. In almost all studies related to identification of fire hazard area, quick management will be practically impossible due to zoning and large hazard area. Therefore, in this study, in order to dynamic and long-term consideration of effective factors on fire occurrence to achieve fire hazard threshold and integrate them into a decision tree, a system is trying to be produced for active and dynamic prediction on different times to achieve the least fire potential area for best management of fire occurrence.

2. Materials and methods

2.1 Study area

Golestan Province is located in the southeastern part of Caspian Sea. The area of this province is 20387 square kilometers. This province is located 36° 30' to 38° 08' northern latitude and 53° 51' and 56° 22' eastern longitude. The southern parts of this province are mountainous and northern parts of it are desert area. The area of forests in this province is 451705 hectares that is 22 percent of province total area. Due to lower annual precipitation and proximity to arid regions in the eastern part of the country, Golestan Province forests are more vulnerable to fire[14]. Geographical location of the study area is shown in **Figure 1**.
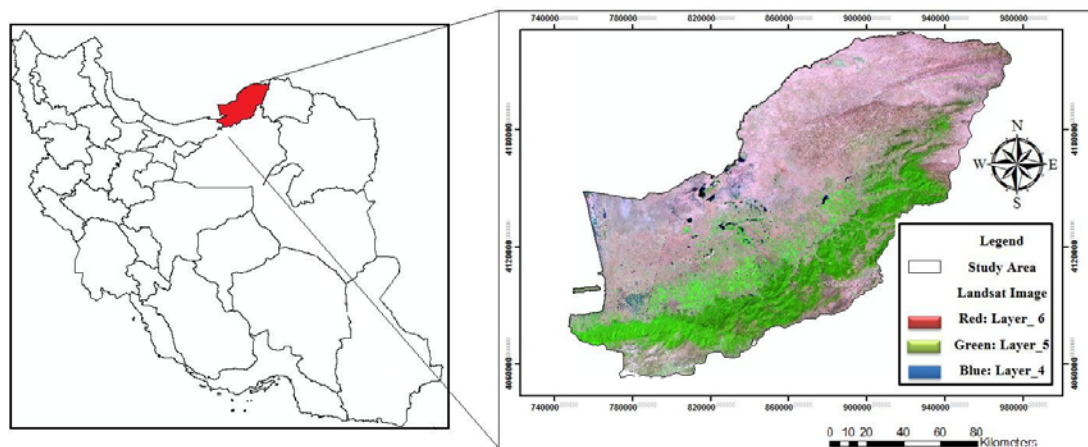
Figure 1. The geographical location of study area within Iran, Golestan Province.

2.2 Methodology

In order to develop a fire alerting system, studying of fire reports showed 75 natural fire occurrences between 2011 and 2015. About 60 percent of these points were used for developing the alerting system and 40 percent of them were used for accuracy assessment. The required data for this study were prepared using satellite imageries. These data were prepared on three steps. At first, natural fire's points were determined and the map of forest type prepared (**Figure 2**). The second step was preparing vegetation's moisture stress map by global vegetation moisture and greenness indexes such as NDVI, MSI, WDVI, OSAVI, GVMI and NDWI, using satellite imageries of MODIS sensor. These factors were considered in a time series of 15 years, a little before fire occurrence. Finally, the best indexes were selected and the threshold was calcu-

2

lated for each of them through comparing factors before fire occurrence and long-term 15 years' normal values. Then accuracy assessment was done to determine the precision of the model predicted areas for 40% of the points. **Figure 3** shows steps 2 and 3 of determining the threshold and producing system.
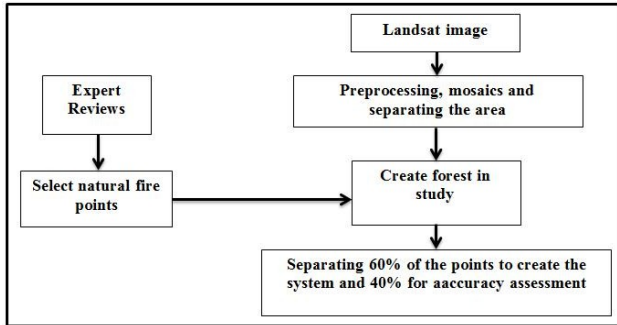
Figure 2. The first step is to provide forest map and fire points.

One of the main functions than we can do by satellite imageries is preparing forest vegetation map[15]. In this study, OLI sensor images on Landsat satellite were used to prepare forest map. These images were suitable as there was no cloud coverage. The steps of pre-processing, geometric corrections and image alignment, radiometric correction, image mosaicing, and finally image clipping were done based on the boundary of the study area on satellite images. Then the natural fire points were put on forest map, which 40% of these points were randomly used to evaluate the accuracy and 60% of them were used to produce the system.

The remote sensing data including satellite imageries of MOD13Q1, MODIS sensor from 2000 to 2015 were used in this study. These images were suitable as there was no cloud coverage. Image clipping was done based on the boundary of the study area on satellite images. Then, according to the previous studies, 4 following indexes were selected from existing indexes (**Table 1**)[16,17]. These indexes were analyzed as before fire occurrence and long-term 15 years in median, mean, minimum and maximum statistics.

Table 1. Remotly sensed Indexes use in study

| Source	Formula	Explanation	Index
Hunt and Rock[18]	MSI = MIR/NIR	Moisture Stress Index	MSI
Rouse *et al.*[19]	NDVI = (NIR - RED)/(NIR + RED)	Normalized Difference Vegetation Index	NDVI
Clevers[20]	WDVI = NIR - αRED	Weighted Difference Vegetation Index	WDVI
Rondeaux *et al.*[21]	OSAVI = 1.16 NIR - RED / NIR + RED + 0.16	Optimized Soil Adjusted Vegetation Index	OSAVI
Gao[22]	NDWI = NIR - SWIR/NIR + SWIR	Normalized Difference Water Index	NDWI
Ceccato *et al.*[23]	$GVMI = \dfrac{(P2 + 0.1) - (p6 + 0.02)}{(P2 + 0.1) + (P6 + 0.02)}$	Global Vegetation Moisture Index	GVMI

2.3 Calculating the threshold and quantify moisture stress indexes

Global indexes of moisture stress and greenness such NDVI, MSI, WDVI, OSAVI, GVMI and NDWI were applied on satellite imageries of MODIS sensor and vegetation moisture stresses map was produced.

By calculating the arithmetic average of factors in each long-term event, the threshold of each factor was calculated. In each factor, the threshold that has the greatest difference with long-term normal values was selected due to early alerting.

2.4 Results

Analyzing time series and number of days before fire occurrence shows the threshold of each index for considering probability of fire occurrence (See **Table 2**).

Table 2. Threshold of indexes for probability of fire occurrence

The threshold is based on the median value	The threshold is based on the minimum value	The threshold is based on the maximum value	The threshold is based on the mean value	Threshold of index
0.82	1.54	1.65	1.55	MSI
0.065	0.11	0.165	0.153	NDVI
0.19	0.245	0.345	0.218	WDVI
0.10	0.18	0.129	0.102	OSAVI
1.175	1.66	1.72	1.58	GVMI
1.42	0.83	1.78	1.593	NDWI

2.5 Selecting the best vegetation index and threshold

For each index, the threshold that describes the fire occurrence better was used, so that the selected

threshold had the highest difference from the normal values obtained from images time series.

Considering these thresholds and comparing remote sensing indexes showed that the NDWI is able to predict fire occurrence better since it has the highest threshold value based on the maximum difference (1.78 is different value from long-term normal value) and then the index GVMI with the threshold of 1.72 is ranked second. In order to continue the study, this index was used to produce fire hazard maps and accuracy assessment.

Therefore, the hazard amount of NDWI and GVMI index was calculated based on the thresholds for accuracy assessment of 40% of fire occurrences (See **Figure 2** and **Figure 3**). And the precision of each index calculated separately. For an example, the hazard map of NDMI is presented for fire occurrence in 2015/1/7.
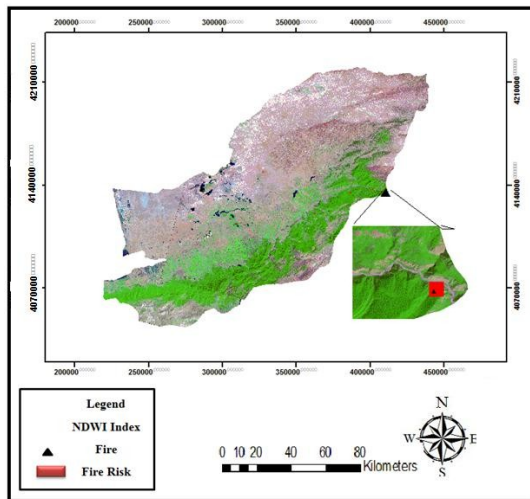
Figure 2. Fire risk is based on the NDWI index.
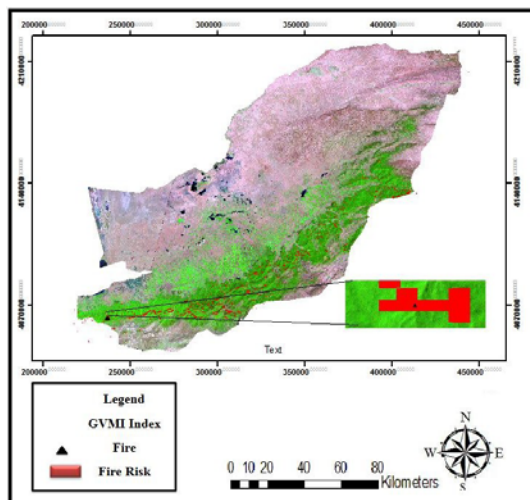
Figure 3. Fire risk is based on the GVMI index.

The Kappa coefficient was calculated for each in-

dex as presented in **Table 3**. Among the studied factors, Normalized Difference Moisture Index (NDWI & GVMI) has the highest accuracy of 85.00%.

Table 3. Evaluation of forest system accuracy

KAPPA	accuracy	Threshold of index
0.4002	50.22%	MSI
0.3508	45.01%	NDVI
0.3684	46.07%	WDVI
0.2197	32.21%	OSAVI
0.8178	85.00%	GVMI
0.9170	94.70%	NDWI

2.6 Discussion

An important tool for estimating high fire hazard areas is predicting fire hazard probability in different areas and preparing special management plans in these areas[24]. Fire prediction is considered as a prerequisite for preparing forest fire management plans. The spatial prediction of fire in different regions can be done in different ways. Using modern prediction methods and spatial modeling of fire hazard, and determining fire probability that is one of the most effective strategies on forest fire management, are much considered. Extensive spatial coverage and use of non-visible wavelengths have made remote sensing a good tool for fire prevention and detection, and preparation fire map. The integration capability of Geographic Information System also has made GIS an essential tool for the preparation of fire hazard maps[25].

Due to lower annual precipitation and proximity to arid regions in the eastern part of the country, Golestan Province forests are more vulnerable to fire. Fire occurrences in recent years, especially in 2011, show that the number and extent of fire has been increased over time. In this study, fire data in 2011 and 2015 were used and fire pixels were detected using vegetation indexes map (NDVI, MSI, WDVI, OSAVI, GVMI and NDWI) by remote sensing and GIS, then the effect of each index was considered and monitored for a period of 15 years, in order to obtain normal values. In addition, the threshold of fire hazard was determined for every occurrence day. Using hazard threshold of each parameters and Boolean logic, the risk maps were combined with each other, and areas with high fire hazard potential in Golestan Province have been identified with combining and overlaying of index-

4

es. The results showed that this method is appropriate for preparing fire hazard map. Contrary to previous researches that often assessed zoning of hazard areas, this method presented areas with fire hazard probability of more than 80 percent dynamically as small manageable patches and can be useful for natural resources management of Golestan Province. Based on the results, it is obvious that this study can be useful in evaluating the sensitivity of forest areas and adopting proper management decisions for fire extinguishing. Based on this map, fire-extinguishing facilities can be established in high-risk areas before the fire season.

Conflict of interest

The authors declare that they have no conflict of interest.

References

1. Hedayati M. Review Forestry Spruce Something North of Iran. Journal of Forest and pasture NO55 2003.
2. Yin H, Kong F, Li X. RS and GIS-based forest fire risk zone mapping in da hinggan mountains. Chinese Geographical Science 2004; 14(3): 251–257.
3. Shariati N. The role and position of forests and pastures and watershed management for the management, development and supply of raw materials of wood and paper industry of the country [Master's thesis] (in Persian). Gorgan: Gorgan University; 2008.
4. Ardakani S, Voldazoj M, Mohamadzade AM. Spectroscopic spectroscopic characterization of fire and field objectives for identification and separation in remote sensing data [PhD thesis]. Tehran: Khaje Naseerdin Toosi University of Technology, Geomechanics faculty; 2010.
5. Jazirei M. Forest conservation (in Persian). Tehran: Tehran Publication and Printing Institute; 2005. p. 230.
6. Merino-de-Miguel S, Huesca M, González-Alonso F. Modis reflectance and active fire data for burn mapping and assessment at regional level. Ecological Modelling 2010; 221(1): 67–74.
7. Portillo-Quintero C, Sanchez-Azofeifa A, Marcos do Espirito-Santo M. Monitoring deforestation with MODIS Active Fires in Neotropical dry forests: An analysis of local-scale assessments in Mexico, Brazil and Bolivia. Journal of Arid Environments 2013; 97: 150–159.
8. Xu D, Dai L, Shao G, *et al.* Forest fire risk zone mapping from satellite images and GIS for Baihe Forestry Bureau, Jilin, China. Journal of Forestry Research 2005; 16(3): 169–174.
9. Sharma MSD, V. Hoa MEPV, Cuong ETV, *et al.* Forest Fire Risk Zonation for Jammu District forest division using Remote Sensing and GIS. 7th FIG Regional Conference, Spatial Data Serving People: Land Governance and the Environment – Building the Capacity. Hanoi, Vietnam; 2009. p. 19–22.
10. Chuvieco E, Congalton RG. Application of remote sensing and geographic information systems to forest fire hazard mapping. Remote Sensing of Environment 1989; 29(2): 147–159.
11. Mohammadi F, Shabani N, Pourhashemi M. Preparation of forest fire hazard map using GIS and AHP in part of Pave forest. Journal of Forest and Poplar Research 2010; 18(4): 569–586.
12. Adhami Mojaddar MH, Mousavir A, Honardoost F. 1390. Fire hazard zonation using GIS, AHP case study-Caspian forests of Northern Iran-Golestan Province (in Persian) 2012.
13. Shorfi S. Investigation and zoning of susceptible forest areas using RS and GIS (in Persian). National Conference on Forests of Central Zagros; 2012 Nov 26-28; Adelaide. Arlington: American Public Power Association; 2012.
14. Nezhad YA, Jafarabadi DM. Comparison of fire damage of two broad-leaved and broad-leaved broadleaf masses mixed with leaf needles in Golestan Province (in Persian). International Conference on Climate Change and Tree Chronology in Caspian Ecosystems; 2009 June 2; Washington D.C. Arlington Heights: The Heartland Institute; 2009.
15. Huete AR. A soil-adjusted vegetation index (SAVI). Remote Sensing of Environment 1988; 25(3): 295–309.
16. Murta Özbayoğlu A, Bozer R. Estimation of the burned area in forest fires using computational intelligence techniques. Procedia Computer Science 2012; 12(1): 282–287.
17. Adab H, Kanniah KD, Solaimani K. GIS-based probability assessment of fire risk in grassland and forested landscapes of Golestan Province, Iran. 2011 International Conference on Environmental and Computer Science（ICECS 2011）; 2011 Sep 16; Singapore. Singapore: IACSIT Press; 2011. p. 66.
18. Hunt ERJr, Rock BN. Detection of changes in leaf water content using near- and middle-infrared reflectances. Remote Sensing of Environment 1989; 30(1): 43–54.
19. Rouse JW, Haas RW, Schell JA, *et al.* Monitoring the vernal advancement and retrogradation (green wave effect) of natural vegetation. Type III, Final Report; 1973 Apr-Sep; Maryland. Greenbelt, MD: NASA/GSFC; 1974. p. 1–69.
20. Clevers JGPW. Application of a weighted infrared vegetation index for estimating leaf. Area Index by Correcting for Soil Moisture Remote Sen- sing of Environment 1989; 29(1): 25–37.
21. Rondeaux G, Steven M, Baret F. Optimization of soil-adjusted vegetation indices. Remote Sensing of Environment 1996; 55(2): 95–107.
22. Gao BC. NDWI—A normalized difference water index for remote sensing of vegetation liquid water from space. Remote Sensing of Environment 1996;

38(3): 257–266.

23. Ceccato P, Gobron N, Flasse S, *et al.* Designing a spectral index to estimate vegetation water content from remote sensing data: Part 1: Theoretical approach. Remote Sensing of Environment 2002; 82(2-3): 188–197.

24. Ghobadi GJ, Gholizadeh B, Dashliburun OM. Forest fire risk zone mapping from geographic information system in Northern Forests of Iran (Case study, Golestan Province). International Journal of Agricultural Crop Science 2012; 4(12): 818–824.

25. Sowmya SV, Somashekar RK. Application of remote sensing and geographical information system in mapping forest fire risk zone at Bhadra wildlife sanctuary, India. Journal of Environmental Biology 2010; 31(6): 969–974.

Case Report

Land use change detection and prediction using Markov-CA and publishing on the web with platform map server, case study: Qom Metropolis, Iran

Mojtaba Pirnazar[1], **Nasrin Haghighi**[2], **Donya Azhand**[3], **Kaveh Ostad-Ali-Askari**[4*], **Saeid Eslamian**[5], **Nicolas R. Dalezios**[6], **Vijay P. Singh**[7]

[1]*Department of Remote Sensing and Geographical Information System, Faculty of Geography and Planning, Tabriz University, Iran.*

[2]*Departement of Urban Design, Faculty of Architecture and Urbanism, Art University of Isfahan, Iran.*

[3]*Department of Remote Sensing and Geographical Information System, Faculty of Geography and Planning, Tabriz University, Iran.*

[4]*Department of Civil Engineering, Isfahan (Khorasgan) Branch, Islamic Azad University, Isfahan, Iran. E-mail: koa.as kari@khuisf.ac.ir*

[5]*Department of Water Engineering, Isfahan University of Technology (IUT), Isfahan, Iran.*

[6]*Department of Civil Engineering, University of Thessaly, Pedion Areos, Volos 38334, Greece.*

[7]*Full Professor, Department of Biological and Agricultural Engineering & Zachry Department of Civil Engineering, Texas A and M University, 321 Scoates Hall, 2117 TAMU, College Station, Texas 77843-2117, U.S.A.*

ABSTRACT

To achieve sustainable development, detailed planning, control and management of land cover changes that occur naturally or by human caused artificial factors, are essential. Urban managers and planners need a tool that represents them the information accurate, fast and in exact time. In this study, land use changes of 3 periods, 1994-2002, 2002-2009, 2009-2015 and predictions of 2009, 2015 and 2023 were assessed. In this paper, Maximum Likelihood method was used to classify the images, so that after evaluation of accuracy, amount of overall accuracy for images of 2013 was 85.55% and its Kappa coefficient was 80.03%. To predict land use changes, Markov-CA model was used after assessing the accuracy, and the amount of overall accuracy for 2009 was 82.57% and for 2015 was 93.865%. Then web GIS application was designed via map server application and evoked shape files through map file and open layers to browser environment and for design of appearance of website CSS, HTML and JavaScript languages were used. HTML is responsible for creating the foundation and overall structure of webpage but beautifying and layout design on CSS.

Keywords: Land Use Change; Urban Growth; Markov-CA; Web Design; Map Server; Web GIS

1. Introduction

1.1 Land use change and prediction

Land use change is one of the world's major studies and especially in developing countries is more important. Land use change is a Complex and dynamic process caused by the action and reaction among environmental, social and economic factors at different spatial and temporal scales[1,2]. Land use change in urban areas usually demonstrates economic development, increased migration to urban areas and population growth accordingly change. Urban growth prediction is for evaluation the development, position, features and conse-

quences of urban development, planning and management decision-making of an urban area[3-7], and also it provides a scientific foundation for decisions about sustainable development and land use[8].

Urbanization and an increase in urban land use is a dynamic process including changes in comprehensive of land cover with the increase of human population[9]. Predictions of changes in land use have a chief role in planning process. Prediction can aid in the appraisal of development factors. It enables urban planners to prepare facilities to keep development[10,11], and suggests directions for future development and this allows landowners to develop a plan[12]. Many studies have been conducted to assess the land cover and land use change (LCLUC) that have implied different methods and software to classify the changes[13-17]. Web-based geographic information system is made to provide GIS services on the web platform and nowadays many of governmental agents, municipal services centers, financial units, location information data base and tourism centers and dozens of agents as such, use these systems to provide their services for the users. Nevertheless, web GIS doesn't only belong with big organizations and agents, with the increasing development of technology and the ease of access to improved software, and providing these services has become important for executives and administration managers for increasing the efficiency and pace of decision making. Many studies have been done about the evaluation of land use change and its prediction through the world, but prediction of urban growth in the field of web, in terms of web GIS, distinguishes the research from the others. This study aimed to evaluate and predict land use changes in framework of web GIS. Coding is done with map server and layout design of the website is done with HTML, CSS and JavaScript. Advantage of web GIS is availability of information layers for all people all over the world.

1.2 Web GIS

Providing information on the Internet is a fast and easy access to information for the public. The geographic information system is capable of processing and analyzing information in a short time with the higher accuracy in this environment. Also graphic and descriptive information with different formats will have different local coordination. If the capabilities and benefits of Internet and geographic information system integrate in an environment as "web GIS" can be a comprehensive information system and efficient tool for management in high levels. Web GIS is a combination of the Internet and GIS (Geographic Information System)[18]. In other definition, web GIS is a kind of technology that is used to illustrate and analyze data and in particular spatial data via Internet. It brings in the advantages of the Internet and GIS. It provides a new ability to access the spatial data for public so that there is no need to buy the expensive GIS software[19].

2. Materials and methods

2.1 Description of study area

Qom, also spelled as Ghom, is the capital of Qom province and eighth largest city in Iran. It lies 125 kilometers or 78 miles by road southwest of Tehran, on a low plain. Its geographic coordination information is 34° 38′ 24″ N, 50° 52′ 35″ E. Its area is about 123,073 km^2. At the 2011 census, its population was 1,074,036, comprising 545,704 men and 528,332 women. It is situated on the banks of the Qom River. The city is located in the boundary of the central desert of Iran (Kavir-e-markazi). **Figure 1** shows the geographic location of the study area.
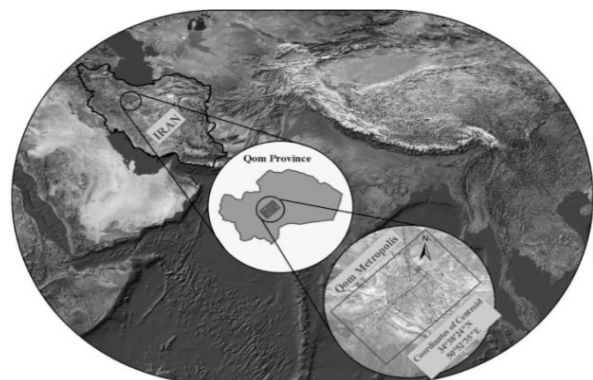

Figure 1. Study area**.**

Qom is counted as one of the focal centers of the Shiʿa both in Iran and around the globe. Since the revolution, the clerical population has risen from around 25,000 to more than 45,000 and the

non-clerical population has more than tripled to about 700,000.

2.2 Article process

Several studies have been conducted about evaluation of land use changes and land use prediction. This study includes 2 stages: (1) Investigation and prediction of changes; (2) Web GIS application design with map server software. The second stage indicates the innovation of the study that hasn't been done in the recent researches.
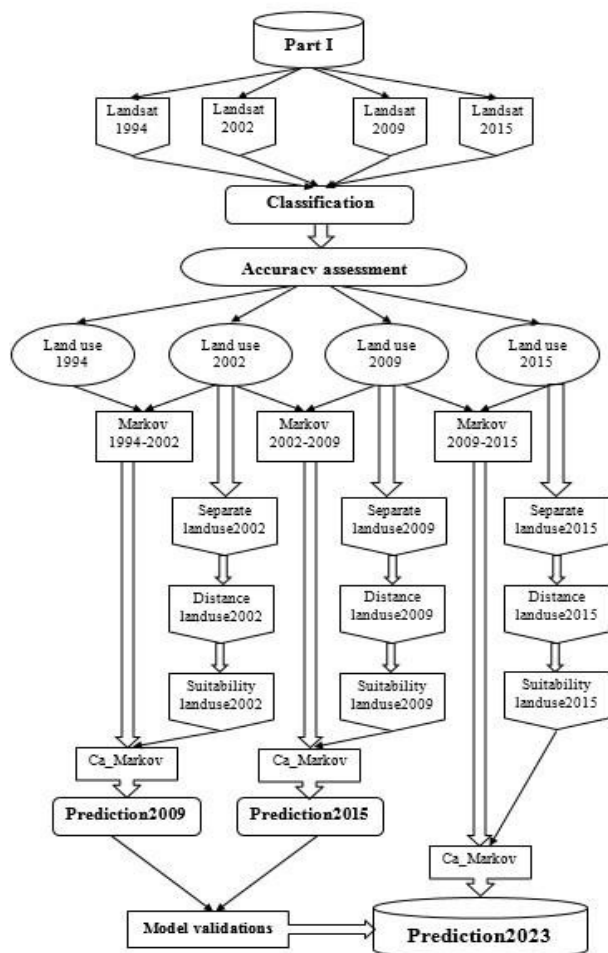
Diagram 1. The steps of the first part of the article**.**
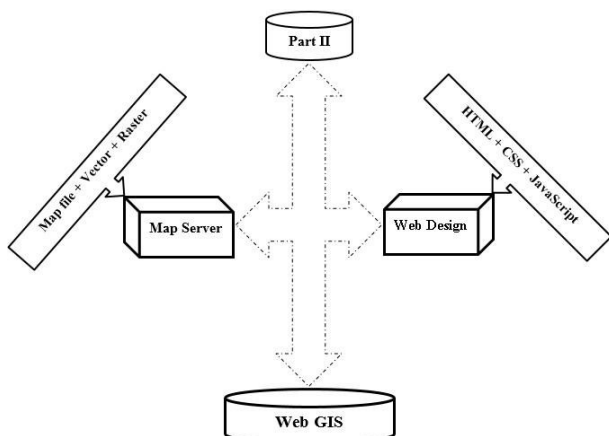
Diagram 2. The steps the second part of the article**.**

Table 1. Features of image of land sat satellite

Satellites	Sensor	Year	Month	Day	Spatial resolution (meters)
LANDSAT_5	TM	1994	August	11	30
LANDSAT_7	ETM+	2002	August	9	30
LANDSAT_5	TM	2009	August	4	30
LANDSAT_8	OLI	2015	August	5	30

In this study, land use changes of 3 periods, 1994-2002, 2002-2009, 2009-2015 and predictions of 2009, 2015 and 2023 is assessed. For this, land use images of 4 mentioned years have been downloaded. The related information is given in **Table 1**. After geometric and radiometric corrections, images were classified and changes and predictions of land use were studied. **Diagram 1** shows the process of first stage of study.

The second stage is to design the web GIS application. To this, coding the map file via Notepad++ is done and raster and vector layers were published on the Web environment via map server and open layer. For designing the layout of web GIS, HTML, CSS and JavaScript have been used. **Diagram 2** indicates the process of second stage of study.

2.3 Land use classification

Classification can be a decision-making process in which image data transmit to the specified class. In fact, the classification is mapping of a multispectral space to complication space. Different bands of image make multispectral space and every pixel in this space defined as a vector, so that every member of this vector represents the amount of pixel in a specific band. Classification methods are of the most common methods for extracting information from satellite images. Diversity of classification methods allows users to produce various information, such as producing of land cover maps, calculating the volume of density of vegetation, uncovering the changes and etc. Flexibility and maximum reliability of classification methods rather than other methods has caused this method to be the most important method to extracting used information. All of the classification methods seek to discover complication (class) that can ascribe the pixel to it with maximum reliability and acceptability. Many classification methods have been introduced to the world of remote sensing, which every method applied a specific

way of classification and extracting accurate information from complications. Each of these methods has taken a general logic and a set of assumptions and based on them, have developed their algorithm. In this paper, Maximum Likelihood classification method is used.

2.3.1 Maximum Likelihood

Maximum Likelihood classification is one of the most popular methods that is a pixel based method. In Maximum Likelihood classification, class is linked to a pixel if most likely that pixel belongs to that class. In the mathematical terms, it can be written in forms of equation 1.

Equation 1 $x \in w_i$ if $P(w_i|x) > P(w_j|x)$ for all $j \neq i$ $x \in w_i$

It means that pixel with the spectral amount vector x belongs to class w_i if the probability of belonging of this pixel to this class meant $P(w_i|x)$ is higher than probability of other classes. For calculating these probabilities, Biz law is used. This law is written as equation 2:

Equation 2 $P(w_i|x) = \frac{P(x|w_i)P(w_i)}{P(x)}$

In this formula, x is the vector of spectral values and w_i is i-th spectral class. $P(w_i|x)$ is the secondary probability (posterior probability) w_i class and it is calculating for all classes. Secondary probabilities will be the basis for decision making in Maximum Likelihood method. $P(x|w_i)$ is the probability of finding a pixel at position X, in the multispectral space. $P(w_i)$ is the initial probability of class of w_i. The initial probability indicates the overall percentage of a class in the image. $P(x)$ is the probability of finding a pixel with definite vector spectral values in the multispectral space. After calculating different parts of Biz law, probability vector of $P(w_i|x)$ can be produced that eventually with which decision will be made. Therefore, algorithm of this classification defines as calculation of these complementation and comparison of different secondary probabilities of various classes with each other.

2.4 CA-Markov model

Markov analysis model is a statistical tool that uses transition probability matrix based on neighborhood effects in a spatial influence algorithm[20]. When applied to land use and many oth-

er applications, Markov chains often specify both time and a finite set of states as discrete values. Transitions between the states of the system are recorded in the form of a transition matrix that records the probability of moving from one state to another[21].

Markov model takes into account past states to predict how a particular variable changes over time. The applicability of Markov model in land-use change modeling is promising because of its ability to quantify not only the states of conversion between land use types but also the rate of conversion among the land use types[22].

One inherent problem with Markov is that it provides no sense of geography. The transition probabilities may be accurate on per category basis, but there is no knowledge of the spatial distribution of occurrences within each land use category. To solve this problem, CA–Markov chain was developed to add a spatial dimension to the model using cellular automata. A cellular automaton is an agent or object that has the ability to change its state based upon the application of a rule that relates the new state to its previous state and its neighbor[23].

Cellular Automaton–Markov (CA–M) model is an interesting approach to model both spatial and temporal changes:

(a) The Markov process controls temporal dynamic among the cover types through the use of transition probabilities. (b) Spatial dynamics are controlled by local rules through a CA mechanism, considering either neighborhood configuration and transition probabilities. (c) GIS and remotely sensed data can be used to define initial conditions, to parameterize CA–M model, to calculate transition probabilities and determine the neighborhood rules[24].

CA-Markov model combines cellular automata, Markov chain, multi-criteria, and multi-objective land allocation to predict land cover change over time[22].

2.5 Map Server

Map Server creates map images from stored spatial digital data format. It can manage both vector and raster data. Map Server can render more than 20 different vector data formats, such

as shape files, Post GIS and Arcs DE geometries, Open DAP, Arc/Info coverages, and Census TIGER files.

It's not necessary all the information represented on a map to be in vector format. For instance, aerial or satellite photos of a region can be showed behind rendered vector data to make a clearer picture of how those vector elements relate to real-world features. Map Server can read two raster formats natively: GeoTIFF and EPPL7, but it can read more than 20 formats (including Windows bitmaps, GIFs, and JPEGs) via the GDAL package. However, although Map Server understands and can render these raster types, it can't tag images with spatial information.

Map Server can operate in two different modes: CGI and Map Script. In CGI mode, Map Server performs as a CGI script in a web server environment. Its setting up is easy and provides a fast, straightforward application. In Map Script mode, the Map Server API is available from Perl, Python, or PHP. The Map Script interface is a flexible, featured application that can still benefit from advantage of Map Server's templating facilities. Map Server is template based. When first conducted in response to a web request, it reads a configuration file (called the map file) that expresses the layers and other elements of the map. It then produces and saves the map. Next, it reads one or more HTML template files that are identified in the map file. Each template contains conventional HTML markup tags and specific Map Server substitution strings. These strings are used, for example, to specify the paths to the map image that Map Server has produced, to clarify which layers are to be rendered, and also to identify zoom level and direction. Map Server substitutes present values for these strings and then send the data stream to the web server, which then forwards it to the browser. When a requester changes any form elements on the page (by changing zoom direction or zoom value, for example) and clicks the submit button, Map Server gets a request from the web server with these new values. Then the cycle starts again. Map Server automatically performs several tasks while produces a map. It labels features and prevents collisions between neighboring labels. It provides for the use of both bitmapped and TrueType fonts. Label sizes can be fixed or can be changed to scale with the scale of the map. The option of not to print labels for specified map scale ranges is also provided.

Map Server generates legends and scale bars (configurable in the map file) and creates reference maps. A reference map indicates the context of the presently showed map. For instance, if the target region is North Dakota, the reference map would display a small map of North Dakota, with the content of the current map outlined within it. Zooming and panning are under user control. Map Server creates maps by stacking layers on top of one another. As each is rendered, it's placed on the top of the stack. Every layer displays features selected from a single data set.

Features that needed to be displayed can be selected by using UNIX regular expressions, string comparisons, and logical expressions. Because of the resemblance of data and the similarity of the styling parameters (like scale, colors, and labels), you can think of a layer as a theme. The display of layers is under interactive control, which lets the user to select layers that are to be rendered. While layers can't be produced on the fly, empty layers can be populated with dynamic data and manipulated via URLs. Map Server has strong and sophisticated query capabilities, but in CGI mode, it lacks the tools that allow the kind of analysis provided by a true GIS. Map Server is not a full-featured GIS: no integrated DBMS (Database Management System) tools, limited analytical abilities, and no tools for georeferencing.

Since Map Server's functions can be accessed via an API from variety of programming languages (such as PHP, Perl, and Python), it can serve as the base of a strong spatially aware application that has many of the analytical and reporting functions of a true GIS. Moreover, as there are not any integrated tools for dealing with spatial data, there are third-party tool sets that perform many (although not all) of these functions. When executing as CGI in a web environment, Map Server can render maps, display feature data, and perform rudimentary spatial queries. When accessed via the API, the application becomes notably more powerful. In this environment, Map Server can execute the same tasks it would as CGI,

but it also has access to external databases via program control, as well as more complex logic and a larger repertoire of possible behaviors.

2.6 Open Layers

Open Layers is an open source, client side JavaScript library for making interactive web Maps, and viewable in nearly any web browser. It is written with JavaScript language that allows maps be easily placed within web pages. Since it is a client side library, it requires no special server side software or settings.

When it is called client side, it refers to the user's computer, specifically their web browser. The only thing you need to do to make Open Layers work is the Open Layers code itself and a web browser. When it is called library, it means that Open Layers is an API (Application Programmer Interface) that provides you with tools to develop your own web maps.

Open Layers supports GeoRSS, KML (Keyhole Markup Language), Geography Markup Language (GML), GeoJSON and map data from any sources using OGC-standards as Web Map Service (WMS) or Web Feature Service (WFS), such as Yahoo maps, Microsoft virtual earth, and Google world wind. This software provides the functions such as zoom and repositioning as well as ability to edit and digitize. Open Layers makes creating powerful web-mapping applications easy and fun. It is very powerful but also easy to use. It's an open source, free, and has a strong community behind it. So if you want to dig into the internal code, or even improve it, you're encouraged to do so.

2.7 Web design

Web design is the skill of making and run of the web pages. Web is part of the Internet. Web is storage of Internet pages that every page has defined address and by which they are routed or found. The user that is logged into the Internet (their computer is connected with the other computers on the Internet) can access to the desired web page through the storage of pages by typing the page address in the address bar.

Web pages contain information, including text, image, video, audio and more. This content displayed to the user by three layers:

1) Content layer (content is created by HTML)

2) Presentation layer (presentation is created by CSS)

3) Behavior layer (behavior is created by JavaScript)

2.7.1 HTML

HTML stands for Hyper Text Markup Language. HTML is the standard language of web design. In fact, HTML language is the first, simplest, most versatile and most important language for web design. Whatever you see when you visit a web page is the results of your browser interpret of HTML. In other words, a browser doesn't know any code or control of server-side, such as the codes of asp and php and understandable code for them is HTML. Generally, all of the web programming languages are somehow related to HTML. For example, php, JavaScript and .NET programming languages, in addition to having the laws and standards, get help from HTML so that written codes in a specific format are places within the HTML codes.

HTML is a markup language which means that different parts are separated by components named tags. Each of which has its own application and related properties. These tags can tell the browser what type of element every section of pages is and what should be displayed.

A HTML document is a text-based file that usually named with suffix of .html or .htm and its content forms from HTML tags. Web browsers are able to understand and interpret the tags of HTML, read every of them from the HTML file and then display (render) its content to the user.

In a HTML page, a variety of elements such as text, headlines, photos, charts, etc. can be used and for each element the related tag of <>….</> should be used.

2.7.2 CSS

HTML is fundamental for web. It is a computer language that is used to develop template and web design. On the other hand, HRML should be used as a language for layout design or adjustment of appearance of web pages. This task is

done with other technologies such as CSS. In fact, nowadays, HTML is used for making foundation and overall structure of the web page and beautifying page layout design is up to CSS.

Cascading Style Sheets (CSS) is a language web that describes the style of an HTML document. CSS explains how HTML elements should be displayed on screen, paper, or in other media. Cascading Style Sheets (CSS) is a mechanism for adding style (e.g., fonts, size, colors, display mode, and spacing) to web documents. CSS can control the layout of multiple web pages all at once. Actually, CSS saves a lot of work. When a browser (e.g., Firefox, Chrome, etc.) reads a style sheet, it will format the HTML document according to the content and information in the style sheet. There are three ways of inserting a style sheet for development: (1) external style sheet; (2) internal style sheet; and (3) inline style. With an external style sheet, it can change the look of an entire website by changing just one file. An internal style sheet may be used, if one single page has a unique style and inline style may be used to apply a unique style for a single element. In this paper, the external style sheet is used.

2.7.3 JavaScript

By means of HTML language, a variety of web pages with all required components such as texts, tables, images, forms etc. can be created. But HTML is merely a design language and is incapable of programming, controlling forms, and responding to the application events and user performance. That is why JavaScript is important to have this capability. JavaScript is just a coding language by which linking the user and the site is possible. JavaScript is a scripting coding language.

Scripting languages recipes are executed by the browser on the user's computer and don't need a certain help to run. These languages are called client side. In contrast, languages such as ASP.NET get run first by the web server and then output in terms of HTML language which is sent to run in the browser. This language is called server side.

JavaScript is a programming language that is placed within the HTML codes and runs on the user's browser. JavaScript has the ability to change the contents of elements displayed on the visitor's browser, so that there is the possibility of dynamic pages.

JavaScript has a variety of abilities and possibilities, such as ability to change the text displayed on the browser, changing the colors, backgrounding color and position of elements used in the web design, changing the specification of elements and their CSS, animating, interacting with user via elements such as Text Box, Radio Button, Text Area etc. reacting to user actions such as changing the pics by moving the mouse over them, displaying a warning message to the user, doing math calculations, making HTML codes dynamically and according to the requirements, interesting menus with animation, collecting users information from the website and surveying them.

2.7.4 Host

Host is so called the server or the computer that can store and save your websites files. These files can be web pages, pictures, CSS files, JavaScript files or any other kind of files. Host space has a unique internet address called IP, a unique domain and a unique name that makes your computer be known in the network. In other words, Hosting of a website is to provide a suitable place as the main base for sending and receiving information via the internet, which technical term is called web Hosting. There are 3 types of Host including: (1) Shared Hosting; (2) Virtual private Server; and (3) Dedicated Server.

2.7.4.1 Shared Hosting

Shared Hosting is the most common, cheapest and most convenient type of hosting. Shared Hosting is a service in which Host space of a server is divided between multiple websites.

Advantages and disadvantages of Shared Hosting:

1) It is the cheapest type of Host. You don't need to pay a large sum of monthly payments.

2) It is easy to use. The server is pre-configured with popular options. Your hosting company takes care of the security and maintenance of changes you make on the website.

3) You have shared your server with other websites. If one of those sites is really "busy"

(number of visits is much), it makes pressure on other websites on this server and makes their speed come down.

4) It is not much flexible and it is incapable of installing software on it.

2.7.4.2 Virtual Private Server—VPS

Virtual private server is basically a service between shared Hosting and dedicated server. In this type of Host, hardware is shared between users of VPS as well, but is partitioning using virtualization technology in which every partition has its own dedicated resources. It can almost fully be configured as a Dedicated Server.

Advantages and disadvantages of virtual server: 1) Full control: customers have full access to the root server and can configure settings in order to meet their needs.

2) It is affordable. The cost of this type of Host is more than Shared Hosting and less than Dedicated Server.

When clients have full access to a server, they can use all of its resources personally. Advantages and disadvantages of Dedicated Server:

1) Flexibility and customization: customers can choose their needed software and hardware from the server to meet their demand.

2) Dedicated resources and guaranteed performance.

3) Full control: customers completely have access to the root and can configure settings in order to meet their needs.

4) Required technical knowledge: in this type of Hosting, the customer is responsible for managing and controlling the server.

5) High cost: the cost of this type of server is not shared with other customers.

3. Results

3.1 Classification and land use change

Remote sensing technology has many applications for mapping land use and land use changes detection. Traditional data collecting method for production of these maps is land mapping which is costly and time consuming. Today, with the help of satellite images and classification methods of images, providing maps is easier. Image classification is done by comparing values and spectral characteristics of each pixel with predetermined characteristics. For this, sample or training points for classification were used. **Figure 2** represents classified images of 1994, 2002, 2009 and 2015.

Due to increasing changes of land use and need of managers and experts to be aware of changes trends in order to policy making and giving solutions to solve the present problems, it seems like that detection methods to determine changes trends over the time are essential (**Figure 3**).
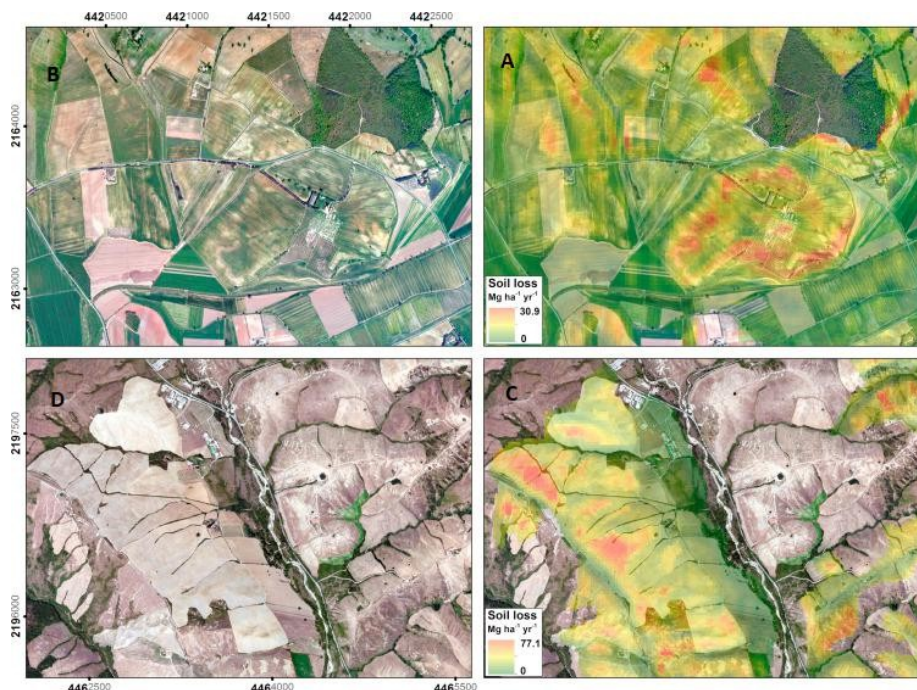

Figure 2. Classified images of Landsat with method Maximum Likelihood. (a): year1994, (b): 2002, (c): 2009, (c): 2015.

14
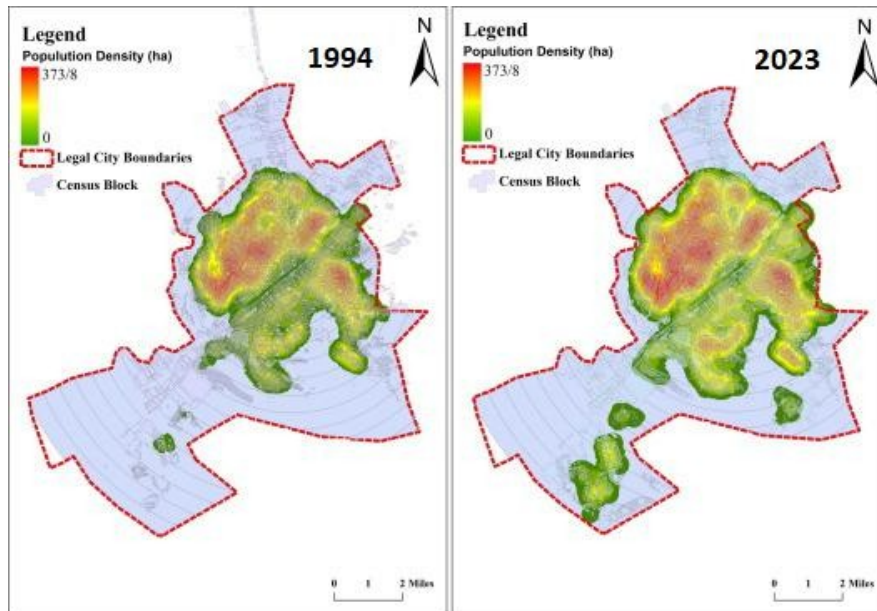
Figure 3. Urban growth between 1994-2023.

3.2 Prediction of land use change

Beside to detection of past changes of a region, forecasting of future changes is of great importance. Forecasting and modeling of spatial phenomenon such as simulation of land use change, growth of urban development and etc. are as tools in the management of natural resources and monitoring of environmental and urban changes. These changes reflect human interaction with the environment and its modeling can be effective in decision making and macro scale planning. In this paper, Markov chain modeling has been used for land use change modeling of Qom city. **Figure 4** indicates predicted land use change map of Qom city for the years 2009, 2015 and 2023.
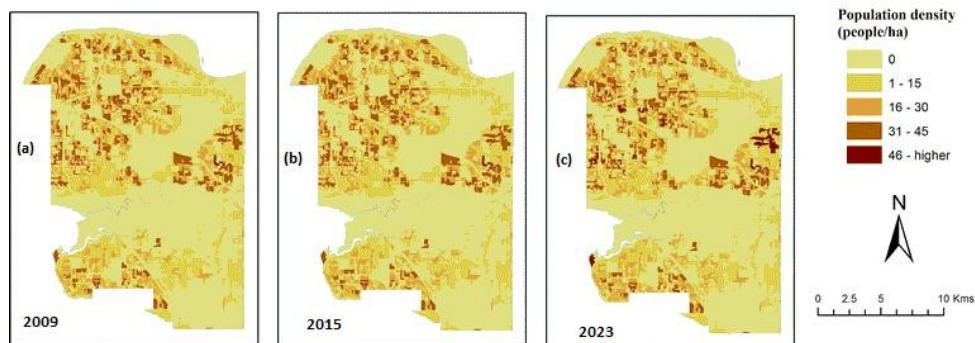
Figure 4. Predicted map with Markov chain method. (a): 2009, (b): 2015, (c): 2023.

Markov chain analysis is a useful tool for modeling of land use change where describing the changes and land process is hard. Markov process is used when modeling of the future of a system completely based on its previous system is possible. Markov chain analysis describes land use change from a period to another and uses it as a basis for mapping the future changes. This act is done via developing of a probability matrix of land use change from time 1 to time 2.

3.3 Accuracy assessment

No classification using remote sensing data is complete without accuracy testing. Analyst and user of classified map want to know with which accuracy amount, the classification on land has been set on the picture. The term precision adapts with accuracy. In digital image processing, the tool for measuring of accuracy is to match the standard information at a given place with the information at the same place on the classified image. In general, accuracy assessment is based on comparing two maps, that one is based on remote sensing data analysis and the second is derived from definite data called Ground Truth or Reference Data. Easiest method of evaluation is

15

the comparison of classified map with defined data with regard to regions placed in each class. This method leads to the production of a report of the spatial content of the class that is in accordance. After all the required parameters were determined, sampling is possible. Sampling can be done via field assessing or via using the previous data like present maps or spatial images.

In this regard, field assessment was adopted. Samples were introduced into the software and required calculations were performed. The results of accuracy assessment represented as error matrix. The variety of parameters and values that indicate the type or accuracy of error in the results are extracted from the error matrix.

3.3.1 Error matrix

Assessing the error and calculating of classification accuracy usually is done according to statistical parameters derived from error matrix. Error matrix is the result of comparison between pi-

xel, defined pixels (on the ground truth) with errors ponding pixels in the classification results. Label of each defined pixel is compared with corresponding pixel. According to matrixes, different parameters are extracted in order to express accuracy and error that the most famous of them are overall accuracy and Kappa coefficient. Overall accuracy is an average of classification precision that shows the ratio of appropriate classified pixels to the sum of the clear pixels and Kappa coefficient calculates the classification accuracy rather than a random classification. It means that Kappa coefficient gives the classification accuracy rather when an image is completely randomly classified. This can be mean that after removing the effect of chance in the classification, the amount of accordance with ground truth will be calculated. **Table 2** shows the classification and prediction accuracy.

Table 2. Classification and prediction accuracy

	Year	Area (Ha)				Accuracy assessment	
		Urban land use	Nonurban	Vegetation	Fallow	Overall accuracy	Kappa
Classification of landsat-8	1994	4443.47	25025.13	2247.13	5803.13	-	-
	2002	5103.64	23274.75	1811.14	7329.32	-	-
	2009	6160.28	19441.43	2298.08	9619.07	-	
	2015	7938.86	19585	1857.13	8136.97	85.55555556	80.03
Prediction	2009	5595.43	22707.5	1759.23	7450.48	82.57	-
	2015	6993.01	19375.5	2536.34	8606.74	93.865	-
	2023	10104.23	18242.74	1627.38	7538.24	-	-

3.4 Application of the web GIS

After coding (Some pieces of written codes are displayed in **Figure 5**), the output will be the application that includes a one level with sub levels (**Figure 6**) that consists of base map (**Figure 7**), and shape file layers of Iran (**Figure 8**), Qom province (**Figure 9**), classified layers (**Figure 10**)

and predicted layers (**Figure 11**) are displayed for different years. For making this application works online, it needs a Host that VPA is the best choice that should be installed map server software on this Host. With this step, the application is publically available on the Internet.

```
28    var map, layer;
29
30    function init(){
31        map = new OpenLayers.Map( 'map' ,{ controls: [] } );
32        layer1 = new OpenLayers.Layer.WMS( "Base Map",
33            "http://localhost/cgi-bin/mapserv.exe", {map: '/ms4w/apps/webgis/htdocs/map1.map',layers: 'raster'}
34            ,{maxResolution: 'auto'} ,  {transitionEffect: 'resize'} ); // more on Resolutions later.
35                // setting maxResolutions to auto is necessary because default is 360 deg / 256 px.
36                layer1.isBaseLayer=true;
37        layer2 = new OpenLayers.Layer.WMS( "Boundaries of Iran",
38            "http://localhost/cgi-bin/mapserv.exe", {map: '/ms4w/apps/webgis/htdocs/map.map',layers: 'Boundaries of Iran'}
39            ,{maxResolution: 'auto'} ,  {transitionEffect: 'resize'} ); // more on Resolutions later.
40                // setting maxResolutions to auto is necessary because default is 360 deg / 256 px.
41                layer2.isBaseLayer=true;
42
43        layer3 = new OpenLayers.Layer.WMS( "Province of Iran country",
44            "http://localhost/cgi-bin/mapserv.exe", {map: '/ms4w/apps/webgis/htdocs/map.map',layers: 'Province of Iran country'}
45            ,{maxResolution: 'auto'} ,  {transitionEffect: 'resize'} ); // more on Resolutions later.
46                // setting maxResolutions to auto is necessary because default is 360 deg / 256 px.
47        layer3.isBaseLayer=true;
48
49
50        layer4 = new OpenLayers.Layer.WMS( "Qom Province",
51            "http://localhost/cgi-bin/mapserv.exe", {map: '/ms4w/apps/webgis/htdocs/map.map',layers: 'Qom Province'}
52            ,{maxResolution: 'auto'} ,  {transitionEffect: 'resize'} ); // more on Resolutions later.
53                // setting maxResolutions to auto is necessary because default is 360 deg / 256 px.
54        layer4.isBaseLayer=true;
```

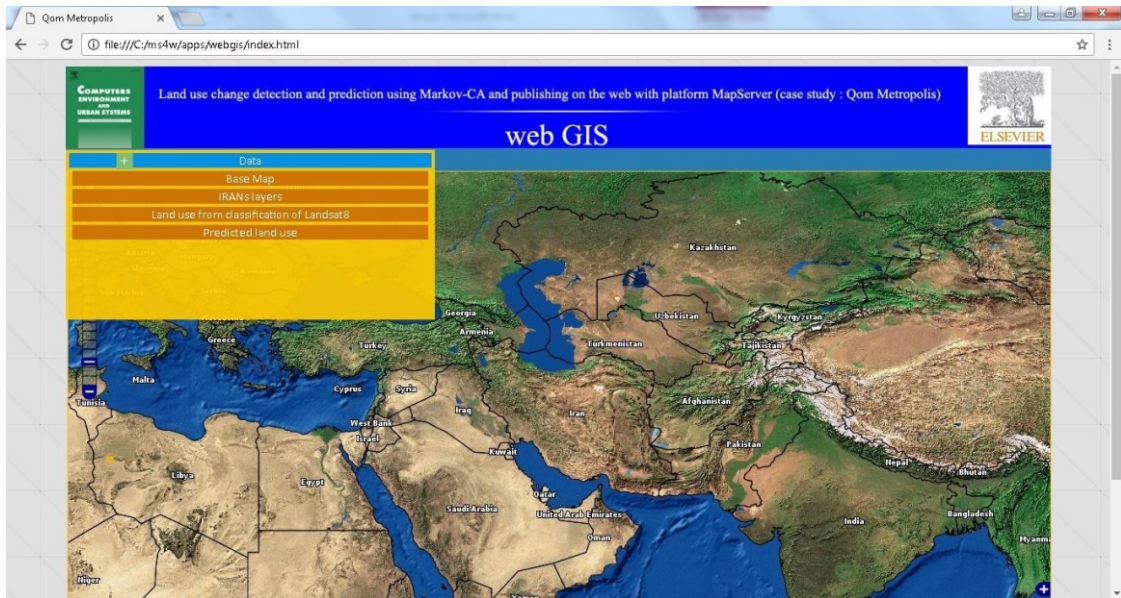**Figure 5.** A view of the Notepad++ software**.**

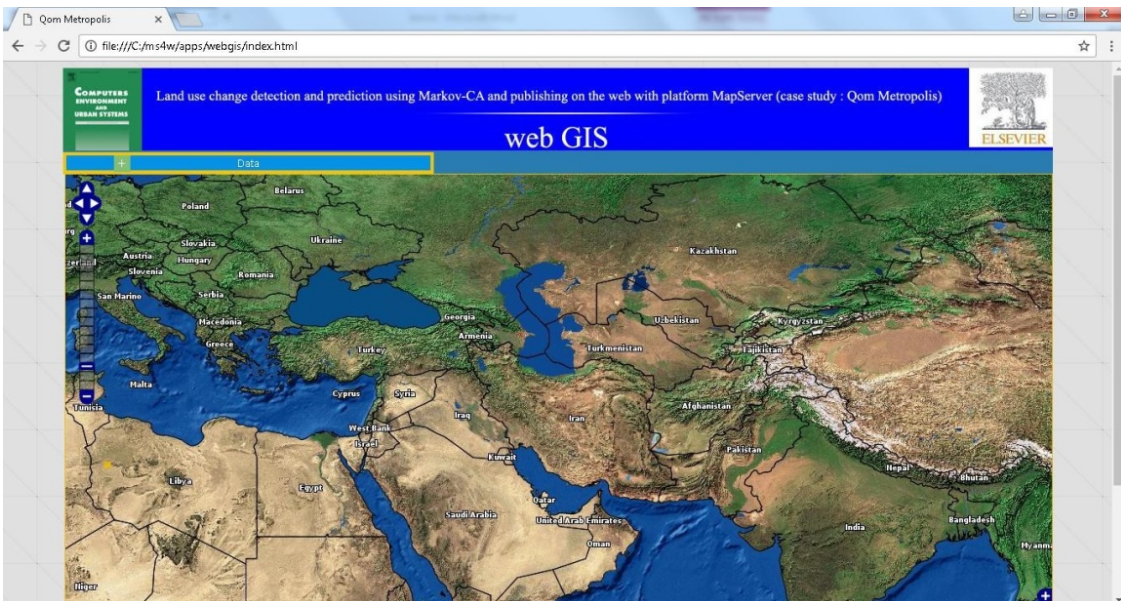**Figure 6.** A view of the designed menue of web GIS**.**

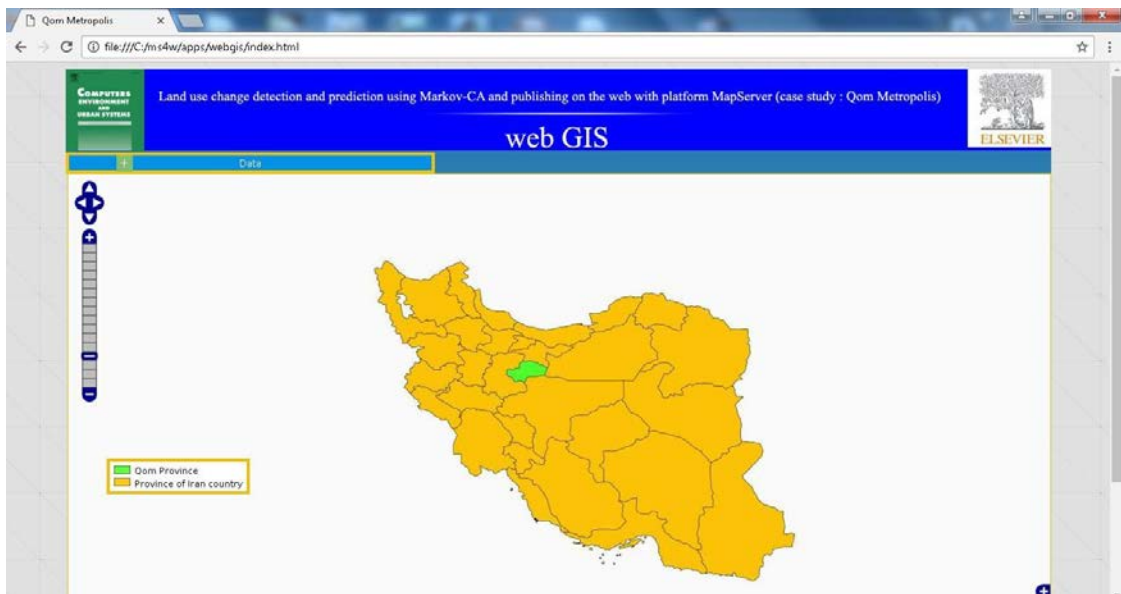**Figure 7.** A view of the designed basemap of web GIS**.**

Figure 8. A view of the shape file layers of Iran**.**
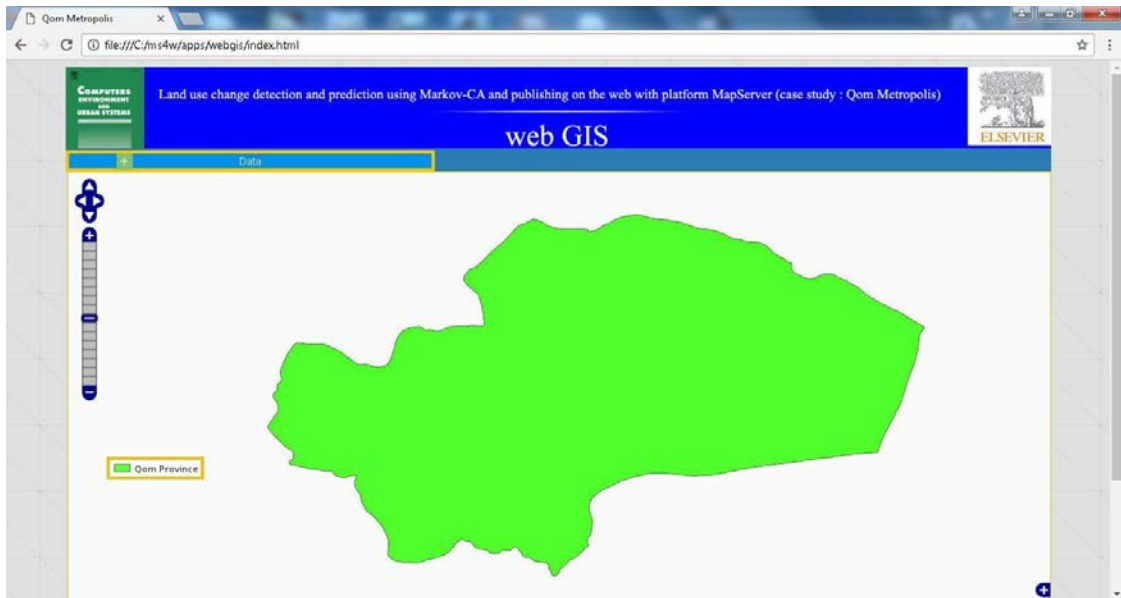
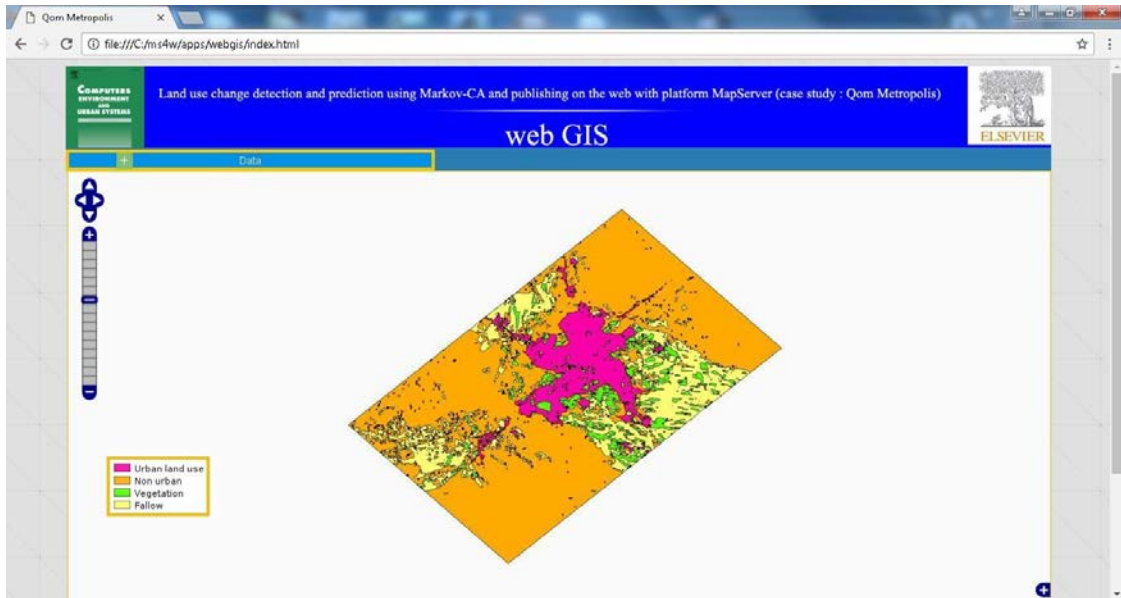**Figure 9.** A view of the Qom province.

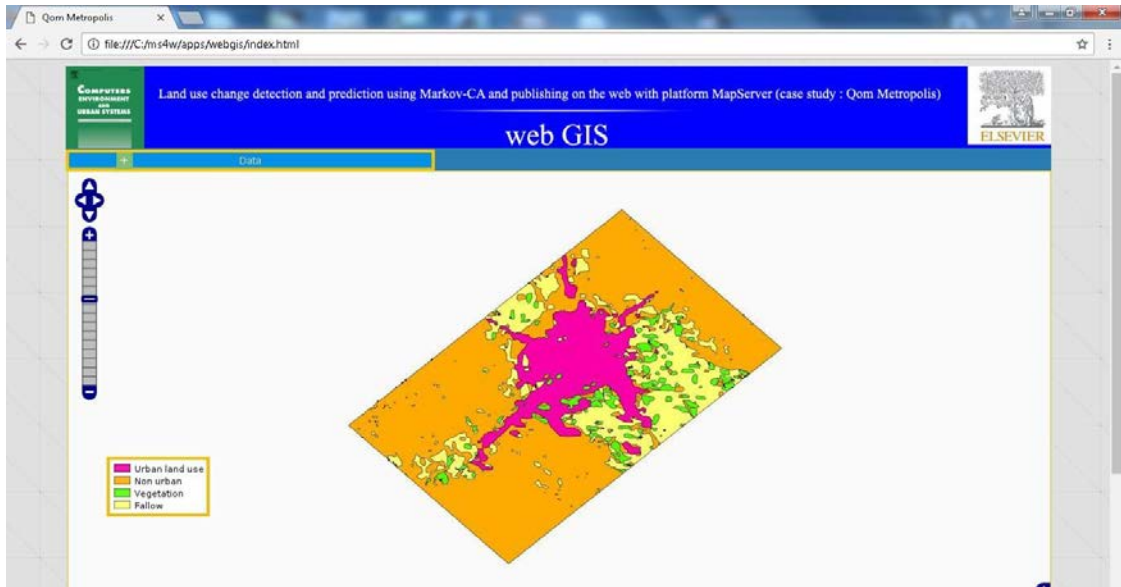**Figure 10.** A view of the classified layers.

Figure 11. A view of the predicted layers.

18

4. Discussion

Due to the fact the great importance of land use and land cover change detection and prediction in management and decision making, the accuracy and availability of the prediction maps is crutial. Many previous researches have been done in this field of study that has concentrated on the producing the detection and prediction maps of land use change but not publishing them to the public. The point that makes present research to be distinguished from previous ones is publishing the results in terms of online and up to date maps on web GIS. In this regard, Markov model helped to predict the urban growth in future to determine the urban growth pattern. CSS, HTML and JavaScript programming languages are open source; therefore they are efficient in design of web GIS and are available for researchers. In this paper, via these programming languages, classification and prediction maps were designed without any problem. Previous studies were just about producing the maps and fast and online availability of these maps for all were neglected. This research demonstrated that it's possible to make all of the researches and studies available, so that leads to the use of map server software through the web GIS map designs.

In addition to the map server open source software, there is other open source software too, such as Geo Server. It is recommended that in future studies, Geo Server software is used beside the map server software.

5. Conclusion

Knowing the direction and pattern of land use changes enables the urban managers and planners to implement the necessary infrastructures and to apply the accurate and precise decisions for the future. This study aimed to predict and detect the land use changes of Qom metropolis. Land use changes of 3 periods containing 1994-2002, 2002-2009, 2009-2015 and predictions of 2009, 2015 and 2023 were studied. In this regard, Maximum Likelihood method was used to classify the images, so that after evaluation of accuracy, amount of overall accuracy for images of 2013 was 85.55 % and its Kappa coefficient was 80.03%. To predict land use changes, CA-Markov model was used. The amount of overall accuracy for 2009 was 82.57% and for 2015 was 93.865%. To make the maps available for the public, web GIS application was designed via map server application and evoked shape files through map file and open layers to browser environment and for design of appearance of website CSS, HTML and JavaScript languages were used.

Results showed that Qom metropolis has changed a lot and land use has dynamically expanded. The direction of urban land use change chiefly is along the routes to outside of the city, however, urban land use has an inside-out growth pattern, and the main changes will occur in south- west.

Conflict of interest

The authors declare that they have no conflict of interest.

References

1. Rindfuss RR, Walsh SJ, Turner BL, *et al.* Developing a science of land change: Challenges and methodological issues. Proceedings of the National Academy of Sciences 2004; 101(39): 13976–13981. doi: 10.1073/pnas.0401545101.
2. Valbuena D, Verburg PH, Bregt AK. A method to define a typology for agent-based analysis in regional land-use research. Agriculture, Ecosystems & Environment 2008; 128(1-2): 27–36. doi: 10.1016/j.agee.2008.04.015.
3. Arsanjani JJ, Helbich M, Kainz W, *et al.* Integration of logistic regression, Markov chain and cellular automata models to simulate urban expansion. International Journal of Applied Earth Observation & Geoinformation 2013; 21: 265–275. doi: 10.1016/j.jag.2011.12.014.
4. Liu H, Zhou Q. Developing urban growth predictions from spatial indicators based on multi-temporal images. Computers Environment & Urban Systems 2005; 29(5): 580–594. doi: 10.1016/j.compenvurbsys.2005.01.004.
5. Pilehforooshha P, Karimi M, Taleai M. A GIS-based agricultural land-use allocation model coupling increase and decrease in land demand. Agricultural Systems 2014; 130: 116–125. doi: 10.1016/j.agsy.2014.07.001.
6. Tan M, Li X, Xie H, *et al.* Urban land expansion and arable land loss in China—A case study of Beijing–Tianjin–Hebei region. Land Use Policy 2005; 22(3): 187–196. doi: 10.1016/j.landusepol.2004.03.003.
7. Weber C, Puissant A. Urbanization pressure and modeling of urban growth: example of the Tunis Metropolitan Area. Remote Sensing of Environment

2003; 86(3): 341–352. doi: 10.1016/s0034-4257(03)00077-4.

8. Gong W, Yuan L, Fan W, *et al.* Analysis and simulation of land use spatial pattern in Harbin prefecture based on trajectories and cellular automata-Markov modelling. International Journal of Applied Earth Observation & Geoinformation 2015; 34: 207–216. doi: 10.1016/j.jag.2014.07.005.

9. Ramachandra TV, Aithal BH, Sanna DD. Insights to urban dynamics through landscape spatial pattern analysis. International Journal of Applied Earth Observations & Geoinformation 2012; 18: 329–343. doi: 10.1016/j.jag.2012.03.005.

10. Li X, Yeh AG. Neural-network-based cellular automata for simulating multiple land use changes using GIS. International Journal of Geographical Information Systems 2002; 16(4): 323–343. doi: 10.1080/13658810210137004.

11. Yang X, Zheng X, Lv L. A spatiotemporal model of land use change based on ant colony optimization, Markov chain and cellular automata. Ecological Modelling 2012; 233(2): 11–19. doi: 10.1016/j.ecolmodel.2012.03.011.

12. Le Q, Park SJ, Vlek P, *et al.* Land-Use Dynamic Simulator (LUDAS): A multi-agent system model for simulating spatio-temporal dynamics of coupled human–landscape system. I. Structure and theoretical specification. Ecological Informatics 2008; 3(2): 135–153. doi: 10.1016/j.ecoinf.2008.04.003.

13. Coulter LL, Stow DA, Tsai YH, *et al.* Classification and assessment of land cover and land use change in southern Ghana using dense stacks of Landsat 7 ETM+ imagery. Remote Sensing of Environment 2016; 184: 396–409. doi: 10.1016/j.rse.2016.07.016.

14. Estoque RC, Murayama Y. Classification and change detection of built-up lands from Landsat-7 ETM+ and Landsat-8 OLI/TIRS imageries: A comparative assessment of various spectral indices. Ecological Indicators 2015; 56: 205–217. doi: 10.1016/j.ecolind.2015.03.037.

15. Jhonnerie R, Siregar VP, Nababan B, *et al.* Random forest classification for mangrove land cover mapping using landsat 5 TM and Alos Palsar Imageries. Procedia Environmental Sciences 2015; 24: 215–221. doi: 10.1016/j.proenv.2015.03.028.

16. Mei A, Manzo C, Fontinovo G, *et al.* Assessment of land cover changes in Lampedusa Island (Italy) using Landsat TM and OLI data. Journal of African Earth Sciences 2016; 122: 15–24. doi: 10.1016/j.jafrearsci.2015.05.014.

17. Vaz EDN, Nijkamp P, Painho M, *et al.* A multiscenario forecast of urban change: A study on urban growth in the Algarve. Landscape and Urban Planning 2012; 104(2): 201–211. doi: 10.1016/j.landurbplan.2011.10.007.

18. Jia Y, Zhao H, Niu C, *et al.* A WebGIS-based system for rainfall-runoff prediction and real-time water resources assessment for Beijing. Computers & Geosciences 2009; 35(7): 1517–1528. doi: 10.1016/j.cageo.2008.10.004.

19. Adam F, Patrick H. Encyclopedia of decision making and decision support technologies. Humphreys, Patrick. New York: Hershey Publication; 2008.

20. Myint SW, Wang L. Multicriteria decision approach for land use land cover change using Markov chain analysis and a cellular automata approach. Canadian Journal of Remote Sensing 2006; 32(6): 390–404. doi: 10.5589/m06-032.

21. Stokey E, Zeckhauser R. A primer for policy analysis: New York: W.W. Norton; 1978.

22. Sang L, Chao Z, Yang J, *et al.* Simulation of land use spatial pattern of towns and villages based on CA–Markov model. Mathematical & Computer Modelling 2011; 54(3-4): 938–943. doi: http://dx.doi.org/10.1016/j.mcm.2010.11.019.

23. Clarke KC, Hoppen S, Gaydos LJ. A self-modifying cellular automaton model of historical urbanization in the San Francisco Bay area. Environment & Planning B Planning & Design 1997; 24(2): 247–261.

24. Araya YH, Cabral P. Analysis and modeling of urban land cover change in Setúbal and Sesimbra, Portugal. Remote Sensing 2010; 2(6): 1549–1563.

Original Research Article

Morris method with improved sampling strategy and Sobol' Variance-based method, as validation tool on Numerical Model of Richard's Equation

Sunny Goh[*]

School of Ocean Engineering, University Malaysia Terengganu, Kuala Terengganu 21030, Terengganu, Malaysia. E-mail: sunny.goh@gmail.com

ABSTRACT

Richard's equation was approximated by finite-difference numerical scheme to model water infiltration profile in variably unsaturated soil[1]. The published data of Philip's semi-analytical solution was used to validate the simulated results from the numerical scheme. A discrepancy was found between the simulated and the published semi-analytical results. Morris method as a global sensitivity tool was used as an alternative to local sensitivity analysis to assess the results discrepancy. Morris method with different sampling strategies were tested, of which Manhattan distance method has resulted a better sensitivity measures and also a better scan of input space than Euclidean method. Moreover, Morris method at $p = 2$, $r = 2$ and Manhattan distance sampling strategy, with only 2 extra simulation runs than local sensitivity analysis, was able to produce reliable sensitivity measures ($\mu*$, σ). The sensitivity analysis results were cross-validated by Sobol' variance-based method with 150,000 simulation runs. The global sensitivity tool has identified three important parameters, of which spatial discretization size was the sole reason of the discrepancy observed. In addition, a high proportion of total output variance contributed by parameters β and θ_s is suggesting a greater significant digits to reduce its input uncertainty range.

Keywords: Richard's Equation; Morris Method; Sobol's Variance-based Method; Euclidean Distance Sampling Strategy; Manhattan Distance Sampling Strategy; Global Sensitivity Analysis

1. Introduction

Generally, there are two ways in testing sensitivity analysis. The commonly used method is to vary parameter value in certain percentage, i.e., 10, 20% or more[2-4], and calculate the sensitivity coefficient. The second method is to calculate sensitivity indices based on uncertainty of parameters, which could be gathered from previous studies, for instance, in Fox *et al*.[5]. While the former provides an overall understanding of each parameter under a defined percentage boundary, the later allows propagation of parameter uncertainty into the corresponding uncertainty in model output.

Morris method provides qualitative sensitivity measures by ranking parameters, and those with the least important parameters could be fixed, without affecting model output[6]. Original Morris method utilizes mean (μ) and standard deviation (σ) of elementary effect as screening procedure, while the improved Morris method by Campolongo *et al*. introduced absolute mean of elementary effect (μ^*) as a complementary to existing[7]. Also, the original Morris method generates a number of random trajectories, while Campolongo *et al*. introcuce a

new sampling strategy using Euclidean distance method to identify a group of trajectories with the greatest spread[7]. They have shown that the new sampling strategy is able to provide a reliable approximation to total effect index (S_{Ti}) at lower simulation runs. However, this sampling method is not widely used. Some researches continue to use original Morris sampling strategy, for instance, Drouet et al. on nitrous oxides emissions at farm level[8], and Chu-Agor et al. on the vulnerability of coastal habitats to sea level rise[9]. Apart from the Euclidean distance method, Campolongo et al. suggested that an alternative method, i.e., Manhattan distance, should be investigated and compared to existing Euclidean distance method[7]. In this study, we compare these methods as one of the objectives.

Morris method is suitable for factor fixing but not for factor prioritization[10], although effort has been made to improve this method into quantitative approach by increasing simulation runs[11]. In this study, we would like to focus on the advantage of improved Morris method by Campolongo et al. as a screening tool. It is commonly accepted in the literature that the 4 levels of input space and/or the 10 random trajectories are sufficient to produce a valuable results[10,11-15]. Some other researchers would prefer different combination of levels and trajectories, such as 5 levels, 120 trajectories in Drouet et al.[8], and 10 levels, 100 trajectories in Moreau et al. [16]. In this study, we would like to determine the extent to which the levels and trajectories could be reduced, while maintaining its screening ability as an objective of our study. The motivation is obvious because the fewer the trajectory is, the fewer simulation runs would be required, which is a direct indication of lesser computational time. This approach is motivated by Saltelli and Annoni [17]:

"[...] non quantitative results can be obtained for screening purposes [...] but already two trajectories can be quite informative as they give a double estimate for the effect of each factor, and by difference of these, an idea of the deviation from linearity acquired."

Quantitative method, for example, variance-based method, can be applied for both factor fixing and factor prioritization, but high in computational cost. Variance-based method is a model free uncertainty analysis tool, and thus, it is used in various applications for sensitivity analysis, such as Kinetic Model for OH-initiated oxidation of DMS[13], HYMOD model[18], flood inundation model (HEC-RAS)[19], dynamic responses of tomato to environment (TOMGRO)[20], to improve process in mineral processing[21], ecological model[22], etc. The usage of variance-based method is to quantify the variance contribution of input parameters to the unconditional variance of model output. This tool is generally applied to determine first order index (S_i) and total effect index (S_{Ti}). In this study, variance-based method is used as a tool to cross-validate the results from improved Morris method.

In general, sensitivity analysis can be used for various reasons[23]. In model development, it can be used for the purposes of model validation or accuracy, simplification, calibration, coping with poor or missing data, and even to identify important parameter for further studies[24]. The aim of this study is to utilize sensitivity analysis method as a validation tool on Richard's equation[25], i.e., to validate simulation results with published Philip semi-analytical solution[26,27]. Also, it is used to study the effect of uncertainty input parameters on variance of simulation output.

According to Namin and Boroomand, Richard's equation numerical solution strategy is still a subject to research[28]. In validating the simulation results to experimental and/or semi-analytical results, sensitivity analysis is one of the important steps that should be carried out, in the least to identify input parameter(s) responsible for discrepancy between simulation and experimental and/or semi-analytical results. There are studies on Richard's equation which would benefit from sensitivity analysis study, e.g., Ma et al.[29] and Caviedes-Voullième et al.[30]. One of the simplest approaches to study sensitivity analysis is to assume ± 20% and ± 40% deviation from base value[8].

2. Sensitivity analysis techniques

The relation of model output (Y) and array of model input parameters (X) can be written in the following form:

$$Y = f(X) = f(X_1, X_2, X_3, ..., X_q) \tag{1}$$

Where, Y could be multiple outputs in terms space and time, or a single model output.

2.1 Improved Morris method

Morris proposed mean (μ) and standard deviation (σ) of elementary effect (EE) that is capable to distinguish input parameters into either: (a) negligible, (b) linear and additive, (c) non-linear, or (d) involved in interactions with other inputs. This method is different from the traditional sensitivity analysis, i.e., varying single input parameter one-at-a-time (OAT). Morris method has improved sensitivity analysis where each OAT of the input parameter of interest is generated at random value of other input parameters. The range of each parameter value is defined between 0 and 1. A technical scheme, Equation (2), to generate random trajectories is as following[6,10,15]:

$$B^* = \left\{ J_{k+1,k}x^* + \left(\tfrac{\Delta}{2}\right)\left[(2B - J_{k+1,k})D^* + J_{k+1,k}\right] \right\}P^* \tag{2}$$

Where: B^* is the randomly generated trajectory in the form of matrix with dimension $(k + 1) \times k$, where k is the number of independent input parameters; Δ is a value in $[1/(p – 1),…,1 – 1/(p – 1)]$ and p is the number of levels, $J_{k+1,k}$ is $(k + 1) \times k$ matrix of 1's; x^* is a randomly chosen base value; B is lower triangular matrix of 1's; D^* is k-dimensional diagonal matrix of which each element is either +1 or -1, by random generation; and P^* is k-by-k random permutation matrix that each row with only one element equal to 1 and no column has more than one element that has 1.

Each trajectory consists of a random step for each input parameter that is either increase or decrease. For instance, Richard's equation has 10 input parameters to be tested, including time-step and spatial discretization size. Thus, there are 10 steps for each trajectory. Total simulation runs is based on $N (k + 1)$, which N refers to random trajectories generated. In this study, various values of N were tested. For example, for $N = 10$, $10(10 + 1) = 110$ simulation, runs would be required.

Campolongo *et al*. have proposed a new sampling strategy to compare geometric distance between pair of trajectories:

$$d_{ml} = \left\{ \sum_{i=1}^{k+1} \sum_{j=1}^{k+1} \sqrt{\sum_{z=1}^{k} \left[X_{z=1}^{(i)}(m) - X_{z=1}^{(j)}(l) \right]^2} \right\}$$
$$m \neq l \tag{3}$$

Where: d_{ml} is distance between a pair of trajectories m and l; $X_{z=1}^{(j)}(l)$ is zth coordinate of the jth point of the lth trajectory; and $X_{z=1}^{(i)}(m)$ is zth coordinate of the ith point of the mth trajectory. They have shown that Equation (3), using Euclidean distance method, can be used to identify a small number of trajectories with the greatest spread. Thus, it reduced the number of trajectories needed to calculate absolute mean of elementary effect and its results shown to be a good approximation to total effect index (S_{Ti}) as original Morris sampling method. Alternatively, they have also suggested Manhattan distance method should be tested, and the equation is shown as following:

$$d_{ml} = \begin{cases} \left\{ \sum_{i=1}^{k+1} \sum_{j=1}^{k+1} \sum_{z=1}^{k} \left| X_{z=1}^{(i)}(m) - X_{z=1}^{(j)}(l) \right| & m \neq l \\ 0 \end{cases} \tag{4}$$

Where all terms are same, except the mathematical operation is simpler than the previous one.

The elementary effect (EE), mean of elementary effect (μ), absolute mean of elementary effect (μ^*) and standard deviation of elementary effect (σ) are as following[7,10,15]:

$$EE_i^j = \frac{y^j(X_1,X_2,...,X_i+\Delta_i,...,X_q) - y^j(X_1,X_2,...,X_i,...,X_q)}{\Delta_i} \tag{5}$$

$$\mu_i = \frac{1}{r}\sum_{j=1}^{r} EE_i^j \tag{6}$$

$$\mu_i^* = \frac{1}{r}\sum_{j=1}^{r} \left| EE_i^j \right| \tag{7}$$

$$\sigma_i^2 = \frac{1}{r-1}\sum_{j=1}^{r} (EE_i^j - \mu_i)^2 \tag{8}$$

Where: $y^j(X_i)$ and $y^j(X_i+\Delta_i)$ are simulation results before and after increment or decrement of Δ value, i.e., Δ_i can either positive or negative value; r is referring to the total number of trajectories; EE_i^j is elementary effect of i input parameter at j trajectory; and σ_i is standard deviation of i input parameter.

2.2 Sobol' method

Sobol' method is based on decomposition of total unconditional variance, $V(Y)$, on Equation (1), into partial variances of increasing dimensionality (Sobol' 1990)[31]:

$$V(Y) = \sum_{i}^{q} V_i + \sum_{i}^{q} \sum_{j>i}^{q} V_{ij} + \cdots + V_{12...q} \tag{9}$$

Where, $V_i = V[E(Y|X_i)]$ is the sum of partial variances that include main effects of each input parameter, $V_{ij} = V[E(Y|X_i, X_j)] - V_i - V_j$, includes all the partial variances of two input parameters interaction, and the main effects. The E indicates expectation operator, and V is the variance operator.

The partial variances of Equation (9) divided by total unconditional variance to give:

$$\sum_i^q S_i + \sum_i^q \sum_{j>i}^q S_{ij} + \cdots + S_{12\ldots q} = 1 \qquad (10)$$

Where, $S_i = V_i/V(Y)$ is first order (or main effect) index; $S_{ij} = V_{ij}/V(Y)$ is the second order index, i.e., also known as interaction effect between parameter i and j, and subsequently for other terms in Equation (10). The equation is exclusive for all input parameters that are independent, i.e., orthogonal from each other.

The ratio of partial variances (e.g. V_i, V_{ij}, etc) to total variance ($V(Y)$) indicates that all the sensitivity indices are scaled between 0 and 1 interval. When the summation of all first order indices gives unity, i.e., $\sum_i^q S_i = 1$, the model is known as additive, i.e. without any interaction effect. Hence, the residual of $1 - \sum_i^q S_i$ indicates interaction effects that could be a combination of second order or higher orders.

The total effect index (S_{T_i}) for each input parameter is given by:

$$S_{T_i} = S_i + \sum_{i \neq j} S_{ij} + \sum_{i \neq j \neq l} S_{ijl} + \cdots \qquad (11)$$

As an example, if, total effect index would be given by:

$$S_{T_1} = S_1 + S_{12} + S_{13} + S_{123} \qquad (12)$$

Where S_1, S_{12}, S_{13} and S_{123} are corresponding to first order index of input parameter 1, second order index of interaction effect between input parameters 1 and 2, second order index of parameters 1 and 3 and third order index of interaction effect between input parameters 1, 2 and 3. The total effect index for S_{T_2} and S_{T_3} can be decomposed with similar approach. Since S_{T_i} includes from first to higher order indices that relating to input parameter i, $S_{T_i} - S_i$ indicates only interaction effect that only account for second and higher order indices. S_i is used to indicate output variance that can be reduced if parameter X_i is fixed, and S_{T_i} represents output variance remains in model output, if X_i cannot be fixed[32].

The first order sensitivity index and total effect index were estimated by quasi-Monte Carlo estimators[33]:

$$S_i = \frac{V(Y) - (1/2N) \sum_{m=1}^N \left(y_B^{(m)} - y_{C_i}^{(m)}\right)^2}{V(Y)} \qquad (13)$$

$$S_{T_i} = \frac{(1/2N) \sum_{m=1}^N \left(y_A^{(m)} - y_{C_i}^{(m)}\right)^2}{V(Y)} \qquad (14)$$

Where, $y_A^{(m)}$, $y_B^{(m)}$ and $y_C^{(m)}$ are model outputs in Equation (13) and (14). Sobol' quasi-random sequences were used to generate two sets of data, i.e., matrix A and B corresponding to model outputs of $y_A^{(m)}$ and $y_B^{(m)}$, and these dataset are confined between 0 and 1. $V(Y)$ is:

$$(1/N) \sum_{m=1}^N (y_A^{(m)})^2 - f_o^2$$

Alternatives are Fourier Amplitude Sensitivity Test (FAST)[34,35] and Extended FAST[36]. In this study, we limit to Sobol quasi-random sequence.

The f_o^2 is given by:

$$(1/N) \sum_{m=1}^N (y_A^{(m)})^2.$$

The $y_{C_i}^{(m)}$ model output was obtained by taking all the dimensions from matrix A, except i column, i.e., dimension is taken from matrix B. Richard's equation has 8 input parameters that must be tested, and thus, 8 dimensions were required for each matrix.

To solve Equations (13) and (14), we need two matrixes (A and B), i.e., $2N$, and k input parameters of N for each input parameter, i.e., kN. In our study, we used $N = 150000$ rows and $k = 8$ columns, i.e., due to 8 input parameters. In total, we have to simulate for $N(k + 2) = 15000(8 + 2) = 150000$ runs. The greater the N value is, the better the estimation of sensitivity indices will be, which stated by Nossent et al.[37], where they have demonstrated that a N value of 12,000 for 26 input parameters is sufficient to obtain reliable estimation.

3. The governing equation of water flow in unsaturated soil, and its numerical solution

The governing equation for transient water flow in unsaturated soil, i.e., Richard's equation[25], based on θ_L-based form, is as following:

$$\frac{\partial \theta_L}{\partial t} = \frac{\partial}{\partial z} \left[\left(K \frac{\partial \psi_m}{\partial \theta_L} \right) \frac{\partial \theta_L}{\partial z} - K \vec{k} \right] \qquad (15)$$

Thus: θ_L is volumetric water content (m³ m⁻³); t is time of simulation (s); z indicates vertical distance of simulation (m); K is hydraulic conductivity of the medium (m s⁻¹); ψ_m is matric pressure head (m); $\vec{k}$ is vector unit with a value of positive one when it is vertically downwards.

Other forms of governing equation, i.e., -based and mixed-based, and their advantages and limitations are stated by Celia *et al.*[38]. We justify the selection of this equation due to its simplicity in relating volumetric water content in the storage term on the left side of the equation to the similar volumetric water content in the flux term on the right side of the equation. The first limitation, calculation degeneration in fully saturated media, was addressed using an approximate value for the θ_L in few decimal points, and the approximate value would give the exact value of θ_L when the value was rounded up. The second limitation, porous material discontinuities produce discontinuous volumetric water content profiles. It could cause problem in simulation, but we have not yet encounter such a difficulty, and the simulation model is thus so far successful in simulating the governing processes.

Equation (15) was approximated numerically and its algebra was implemented in FORTRAN 2008 using Simply FORTRAN Integrated Development Environment. The spatial discretization method used is termed as cell-centered finite difference. The finite difference algebra for Equation (15), i.e., used for sensitivity analysis in the current study is as following:

$$\frac{\theta_{L(k)^{n+1}} - \theta_{L(k)^n}}{\Delta t} =$$
$$\frac{K_{k+\frac{1}{2}}(\frac{\partial \psi_m}{\partial \theta_L})_{k+\frac{1}{2}}}{\Delta Z_k(0.5\Delta Z_{k+1} + 0.5\Delta Z_k)}\left(\theta_{L(k+1)^{n+1}} - \theta_{L(k)^{n+1}}\right) -$$
$$\frac{K_{k-\frac{1}{2}}(\frac{\partial \psi_m}{\partial \theta_L})_{k-\frac{1}{2}}}{\Delta Z_k(0.5\Delta Z_k + 0.5\Delta Z_{k-1})}\left(\theta_{L(k)^{n+1}} - \theta_{L(k-1)^{n+1}}\right) -$$
$$\frac{K_{i,j,k+\frac{1}{2}}\vec{k} - K_{i,j,k-\frac{1}{2}}\vec{k}}{\Delta Z_k} \quad (16)$$

Where: k indicates a cell-centered number in z-direction in Cartesian coordinate system; Δt(s) is time-step size; $\theta_{L(K)^n}$ (m³ m⁻³) and $\theta_{L(K)^{n+1}}$ (m³ m⁻³) are indicating volumetric water content at old time level (n) and new time level ($n+1$), respectively; $K_{k+1/2}$ (m s⁻¹) is hydraulic conductivity at

the interface between cell k and $k + 1$; $K_{k-1/2}$ (m s⁻¹) is hydraulic conductivity at the interface between cell $k - 1$ and k; $(\partial \psi_m / \partial \theta_L)_{k+1/2}$ is partial derivative of ψ_m with respect to θ_L at the interface between the cell k and $k + 1$; $(\partial \psi_m / \partial \theta_L)_{k-1/2}$ is partial derivative of ψ_m with respect to θ_L at the interface between the cell $k - 1$ and k; Δz_{k+1}(m), Δz_k(m) and Δz_{k-1}(m) are corresponding to the spatial sizes of spacing of cell $k + 1$, k and $k - 1$. $\theta_{L(k+1)^{n+1}}$ (m³ m⁻³), $\theta_{L(k)^{n+1}}$ (m³ m⁻³) and $\theta_{L(k-1)^{n+1}}$ (m³ m⁻³) are the volumetric water contents at new time level of cell $k + 1$, k and $k - 1$, respectively.

The numerical solution of Equation (16) was solved by a fully implicit cell-centered finite-difference scheme without any linearization. An iterative method was used to solve the mathematical algebra of Equation (16), i.e., Jacobi iteration[39]. For comparison purpose, modified Newton-Raphson method was also implemented[40]. A convergence factor criterion was used to indicate the condition for iteration termination process, i.e., absolute maximum difference $|\theta_{L(k)^{n+1}} - \theta_{L(k)^n}|$ for every single cell.

4. The constitutive functions of matric pressure head (ψ_m) and hydraulic conductivity (K)

The constitutive functions implemented are from Haverkamp *et al.*[26]:

$$\psi_m = -10^{-2} exp \left[\frac{\alpha(\theta_s - \theta_r)}{\theta_L - \theta_r} - \alpha\right]^{\frac{1}{\beta}} \quad (17)$$

$$K = K_s \frac{A}{A + (-100\psi_m)^B} \quad (18)$$

Where: α, β, A and B are fitting parameters; θ_r (m³ m⁻³) is residual volumetric water content; θ_s (m³ m⁻³) is saturated volumetric water content; and K_s (m s⁻¹) is saturated hydraulic conductivity.

5. Input parameters considered for local and global sensitivity analysis

Referring to Equations (17) and (18), there are basically 8 input parameters from Richard's equations. Out of those input parameters, 3 parameters are relating to hydraulic conductivity of soil medium, i.e., Equation (18), while the other 5 parameters are inputs for matric pressure head,

Equation (17). All the parameters are listed in **Table 1**. The uncertainty range for each parameter was developed based on either input parameter uncertainty or numerical input parameter uncertainty. For time-step size and spatial discretization size, they are termed as numerical input parameters because their influence on simulation output is depending on the implemented numerical solution, e.g. Caviedes-Voullième et al.[30]. Similar as Nossent et al.[37], as we have no prior information on the parameters, the sensitivity analysis was carried out on uniform input parameters distribution. Some other researchers with similar assumption, e.g. Saltelli et al.[15] assumed uniform distribution for 103 parameters; Yang[18] assumed uniform distribution for 5 parameters, and Drouet et al.[8] assumed ±20% and ±40% from base value.

6. Numerical experiment and the default setting of input parameters of the flow problem

Water infiltration into Yolo light clay was used in the numerical experiment. The coefficients of the constitutive functions are tabulated in **Table 1**. Initial condition for the volumetric water content was 0.2376 m³ m⁻³. Lower boundary was set permeable to inflow and outflow of water. Upper boundary was set at 0.495 m³ m⁻³. Total simulation time was set to 600 s, and different time-step sizes were simulated to determine mass balance ratio (MBR) as given by Equation (19). This is required as part of a validation procedure since Celia et al.[38]. The formula of the equation is simply by taking the ratio of storage term over the flux term.

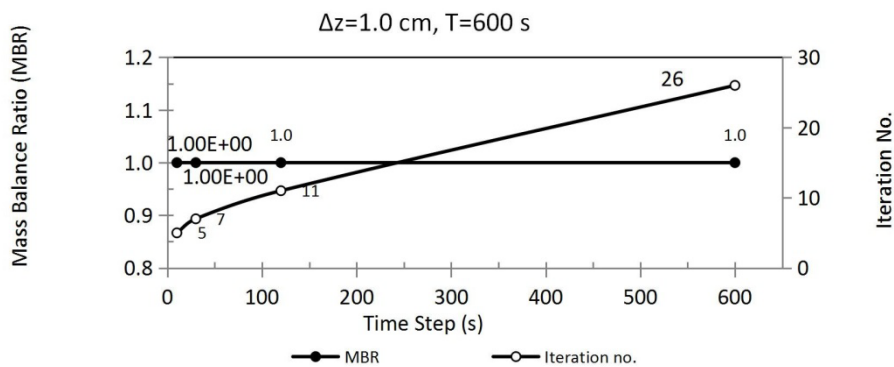**Table 1.** The coefficients value from Haverkamp et al. based on the constitutive Equations (17) and (18). These values were used as base case. Note that θ_r is residual volumetric water content, θ_s is saturated volumetric water content, K_s is saturated hydraulic conductivity, and α, β, A and B are fitting coefficients. $\theta_{L(initial)}$, Δz and Δt are initial spatial discretization size and time-step size, respectively.
ª-Numerical input parameter uncertainty. All other parameters are based on Haverkamp constitutive equations.

Parameter	Base value	Distribution	Uncertainty analysis range
α	739	Uniform	738.5 – 739.499
θ_r	0.124 m³ m⁻³	Uniform	0.1235 – 0.124499
θ_s	0.495 m³ m⁻³	Uniform	0.495 – 0.495499
β	4	Uniform	3.5 – 4.499
A	124.6	Uniform	124.55 – 124.6499
B	1.77	Uniform	1.765 – 1.77499
K_s	4.428x10⁻² cm hr⁻¹	Uniform	4.4275x10⁻² – 4.428499x10⁻²
$\theta_{L(initial)}$	0.2376 m³ m⁻³	Uniform	0.23755–0.2376499
Δz	1 cm	Uniform	0.1 – 1ª
Δt	500 s	Uniform	10 – 500ª

Thus, we generalized the MBR equation in a more explicit form, but in a partial differential form, as following:

$$\text{MBR} = \sum_{k=1}^{N} \frac{(\frac{\partial \theta_L}{\partial t})_k}{\left\{\frac{\partial}{\partial z}\left[\left(K\frac{\partial \psi_m}{\partial \theta_L}\right)\frac{\partial \theta_L}{\partial z} - K\bar{k}\right]\right\}_k} \tag{19}$$

Where, k is the number of cell; and N is the total number of cell. The calculation of MBR was carried out for each time-step. A perfect simulation would give a MBR value of unity, and any increasing or decreasing in the value is indicating unwanted creation or loss of mass, respectively. Also, it should be noted that the MBR equation change according to the governing equation simulated.
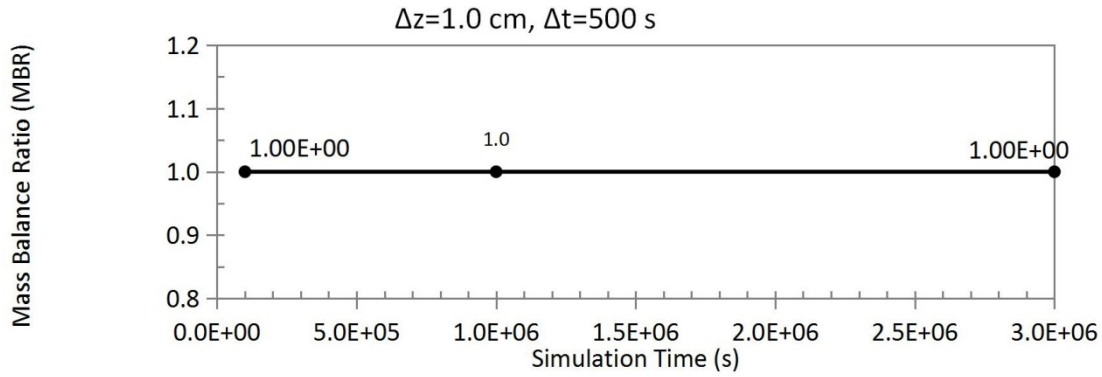

Figure 1. MBR and number of iteration at different time-step sizes, i.e., 10, 30, 120 and 600 s. Note that Δz is spatial spacing size, and T is the total simulation time.

Figure 2. Mass balance ratio at different simulation times, i.e., 10^5, 10^6 and 3×10^6 s, at a time-step size of 500 s. Note that Δz is spatial spacing size, and Δt is time-step size.

Figure 1 shows the MBR of the simulation is unity from 10 to 600 s of time-step size. Hence, in considering the increasing number of iteration due to increasing time-step value, the time-step was taken as 500 s. By using the time-step, the simulation was preceded from 500 to 3×10^6 s, and MBR in **Figure 2** does not show any sign of mass balance problem.
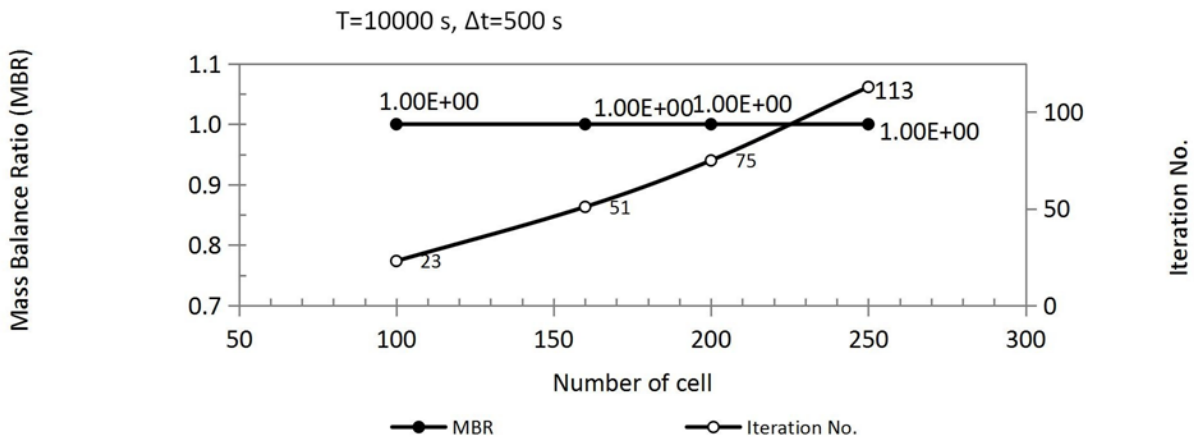

Figure 3. MBR and number of iteration at different cells number, i.e., 100, 160, 200 and 250 cells. The corresponding values of spatial spacing size (Δz) are 2, 1.25, 1 and 0.8 cm. Note that Δt is time-step size, and T is the total simulation time.

The simulation medium was discretized into different spatial spacing sizes to investigate the simulation for any influence of number of cell on MBR and iteration number. The number of cell in the **Figure 3** is corresponding to spatial size of 2, 1.25, 1 and 0.8 cm. The result showed the spatial size does not have any influence on the MBR value, based on the range of simulation. However, the number of iteration increases at a greater rate than the increasing number of cell at high cell number. Thus, without causing excessive heavy load in computer processing time, the current work proceed with the number of cell use in the simulation at 200 cells, which is equivalent to 1 cm per cell, for a total depth of 200 cm.

The effect of convergence value (CV) on MBR and iteration number was investigated (see **Figure 4**). At low convergence value, 10^{-3} m^3 m^{-3}, it produced a MBR of 0.889. Despite it poses a desire property of having a low number of iteration. This is a serious mass problem, as 0.889 is equivalent to a mass loss of 11.1 % resulted by a single time-step before completing 105 s of simulation time. This could be explained by the fact that setting CV at 10^{-3} m^3 m^{-3} is about accepting an error of 0.8 % and 0.2 % of and, respectively, for each cell of the simulation medium. Thus, at lower CV value would only result in unity MBR. Therefore, we stress the limit by setting MBR at 10^{-12} m^3 m^{-3}, i.e., two orders of magnitude lower than 10^{-10} m^3 m^{-3} that there is no significant change observed on the simulated value of volumetric water content, as shown in **Figure 5**. The effects of time-step and spatial spacing size on the

27

volumetric water content were not investigated here because those two parameters would be investigated in the sensitivity analysis as with other parameters.
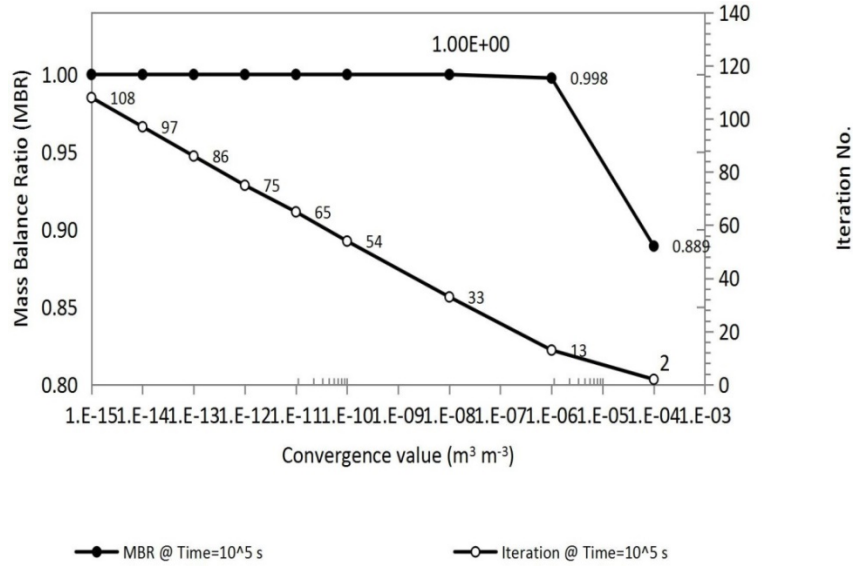

Figure 4. The influence of convergence value on MBR and iteration number.
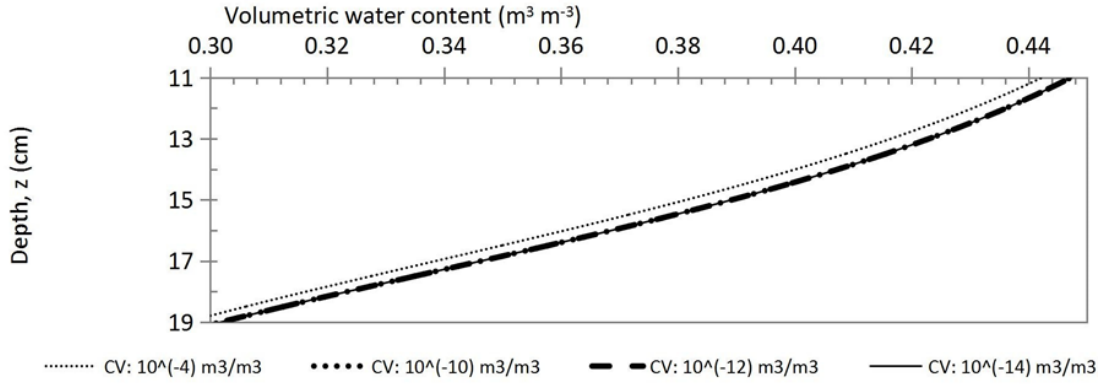
Figure 5. Simulation time of 10^5 s, at different convergence values (CV). Time-step, 500 s, and spatial spacing size, 1 cm.

The iteration methods of Jacobi and modified Newton-Raphson were compared. It was found that the minimum iteration number from the latter was equivalent to the iteration number from the former, when the relaxation factor of the latter was set to unity. Reducing the relaxation factor from unity would result in increasing iteration number. The numerical solution of Equation (15) did not exhibit convergent problem, thus, Jacobi iteration method is sufficient.

7. Statistical measures

In order to determine the goodness of fit between the data and the simulated results, some statistical equations were implemented. The equations are mean of residual error (M) and absolute residual errors (MA), respectively as following[41]:

$$M = \frac{1}{N} \Sigma_{k=1}^{N} (cal_k - obs_k) \qquad (20)$$

$$MA = \frac{1}{N} \Sigma_{k=1}^{N} |cal_k - obs_k| \qquad (21)$$

Where, cal_k is the simulated data at cell k; and obs_k is the analytical solution at cell k.

8. Simulation results and its accuracy

Based on the conditions as stated in previous section, water infiltration into Yolo light clay was simulated up to 3×10^6 s. Data on Philip's semi-analytical solution were collected from Haverkamp et al.[26]. Simulation results were compared with the data to verify the simulation (**Figure 6**). Before referring to any statistical measure, it was evident that the simulation results slightly under-predicted the infiltration flow of water front (**Figure 7**).

28

Figure 6. Simulation results and Philip's semi-analytical solution of water infiltration in Yolo light clay. Data for Philip's solution is from Haverkamp *et al*.

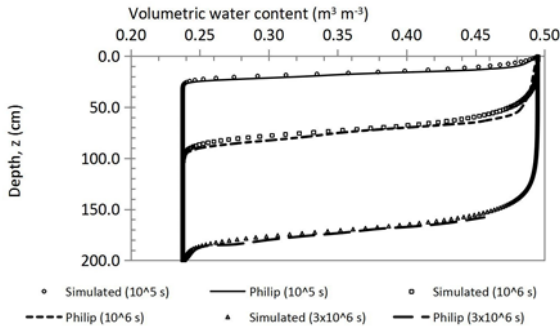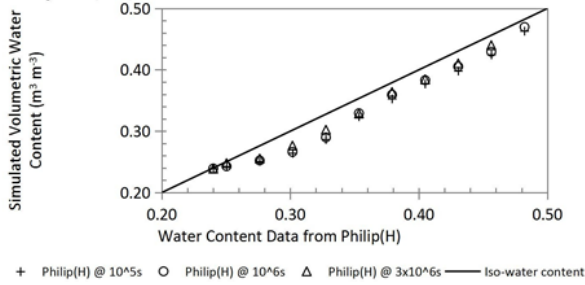**Figure 7.** Overall comparisons of Philip's semi-analytical solution and simulated results. Philip(H) is referring to data from Haverkamp *et al*.

Table 2. Statistical calculations from Equations (20) and (21) at different simulation times. Note that M is mean of residual error, and MA is absolute residual errors

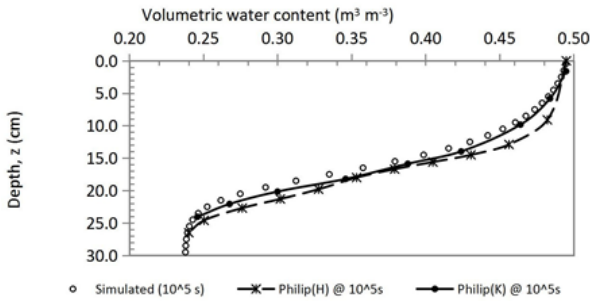| Error	Simulation time (s)		
types	10^5	10^6	3×10^6
M	-2.54×10^{-2}	-2.14×10^{-2}	-1.71×10^{-2}
MA	2.54×10^{-2}	2.14×10^{-2}	1.71×10^{-2}

Figure 8. Comparison of simulated results with Philip's semi-analytical solution, Philip(H) and Philip(K) from Haverkamp *et al*.[26] and Kabala and Milly[27], respectively.

Statistical equations, i.e. Equations (20) and (21), were used to justify goodness of fit between the simulated results and Philip's semi-analytical solution, as indicated by Philip(H) as in **Figure 7**, to further justify the reliability. The result is tabulated in **Table 2**. The mean of residual error (M) and absolute residual errors (MA) are having similar values, but the former value is in negative sign. This indicates that there is no single simulated data greater than the semi-analytical solution. Otherwise, the M value would be lesser

than its current value. These statistical results are agreed with the observation in **Figure 7**. In addition to this, the statistical results, in **Table 2**, also indicates that the developed computer simulation source code was indeed working properly. In order to further reinforce the previous claim, some data was extracted from Kabala and Milly[27], as indicated by Philip(K) as in **Figure 8**, for further comparison. **Figure 8** shows that there is a small discrepancy between Philip(K) and Philip(H), but the former is relatively closer to the simulation results than the latter. At this point of observation, we are not able to determine which of the solutions provided from the literature is accurate. However, results from the figures and table clearly indicate that the simulated result is lesser than the Philip's semi-analytical solution. Therefore, sensitivity analysis was carried out to determine the sensitivity coefficient for all input parameters, and use the sensitivity analysis results to assess the model simulation based on the assumption that possibly the significant digits approximation, as in **Table 1**, could be contributing to the under prediction of the volumetric water content of the simulation.

As mentioned in previous section, we broadly termed the former as numerical input uncertainty and the latter as input parameter uncertainty. We justify the latter selection because the degree of uncertainty in the input parameters was not given, i.e., the published input data could be different from the exact value used by Haverkamp *et al*.[26] in simulating his results. Therefore, sensitivity analysis was carried out to determine the effect of the uncertainties influence on simulation outputs. Moreover, sensitivity analysis is one of the most important steps in evaluating the effect of input parameter on simulation results, and it is also used by other researchers for model validation[42-45].

9. Local sensitivity analysis

Negligible sensitivity response could be resulted by too small perturbation size, and inaccuracy in sensitivity response could be due to too large perturbation size[46]. The input parameter values were subjected to a perturbation size between

-5% and 5% as suggested by Zheng and Bennett[41]. Some other perturbation sizes used by researchers, for example, 90 % in Vereecken *et al.*[2], 20% in De Roo and Offermans[3], and 10% in Davis *et al.*[4]. In considering the simulation time, we limit the sensitivity analysis to a simulation time of 10^5 s. The sensitivity analysis study was based on a single perturbation size of increment or decrement in each simulation.
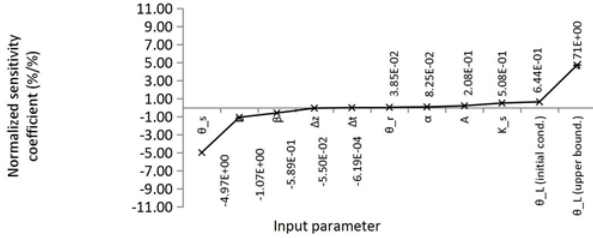

Figure 9. The rank of sensitivity coefficient. Note: θ_s and θ_r are saturated and residual volumetric water content; Δz, spatial spacing size; Δt, time-step size; K_s, saturated hydraulic conductivity; $\theta_{L(initial\ cond.)}$, clay medium initial value of volumetric water content; $\theta_{L(upper\ bound.)}$, upper boundary of volumetric water content; A, B, β and α are fitting parameters from Haverkamp constitutive, as in Equations (17) and (18).

The normalized sensitivity coefficients are shown in **Figure 9**. Some other forms of presentation, for example, RMSE versus model parameters in Jhorar *et al.*[47], relative sensitivity versus percentage change in parameter value in Vereecken *et al.*[2], and TRMSE with parameter and time[48,49]. Generally, there are two groups sensitivity coefficient, i.e., positive and negative relations. In positive relation group, the boundary volumetric water content has the highest sensitivity coefficient. This is followed by initial volumetric water content and saturated hydraulic conductivity. The smallest sensitivity coefficient in the group is the residual volumetric water content. In negative relation group, saturated volumetric water content has the highest sensitivity coefficient, and this group ended with spatial spacing size and time-step size as the smallest sensitivity coefficient. The positive and negative relations were later couple with the range of uncertainty for each parameter to validate model simulation to semi-analytical solution. This procedure has been shown in Goh and Noborio[50]. Similarly, Cohen *et al.*[51] used local sensitivity analysis as part of its validation procedure on Richard's equation. Apart from the advantages of local sensitivity analysis, for example, at researcher convenient, its disad-

vantages have been proven by Saltelli and Annoni[17] through geometric proof, i.e., known as the curse of dimensionality.

10. Global sensitivity analysis

Based on Morris method, only the input parameters separated from the origin of relation σ versus μ^* is considered important. From **Figure 10**, two groups of input parameter could be identified. Those important parameters were β, saturated volumetric water content (θ_s) and spatial discretization size (Δz). The number of significantly important parameters was reduced from 10 to 3. Those parameters considered unimportant that they have limited influence on model output were: α, residual volumetric water content (θ_r), initial volumetric water content of the medium ($\theta_{L(initial)}$), from matric suction relation (Equation (17)); A, B and saturated hydraulic conductivity (K_s) from hydraulic conductivity relation (Equation (18)); time-step size (Δt) as numerical input parameter.

(a)

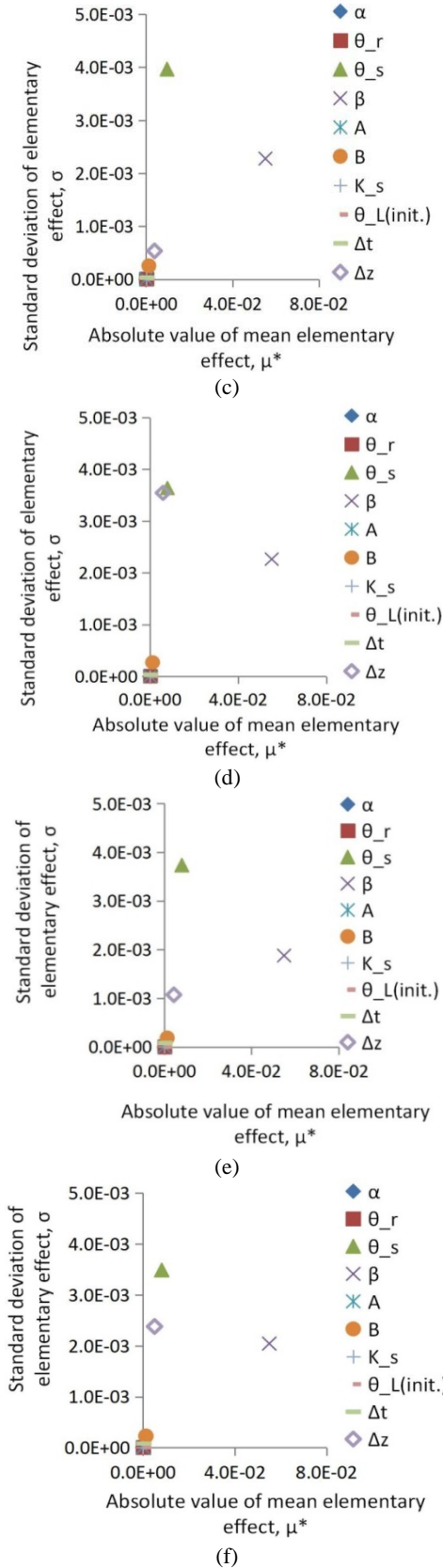(b)

30

(c)

(d)

(e)

(f)
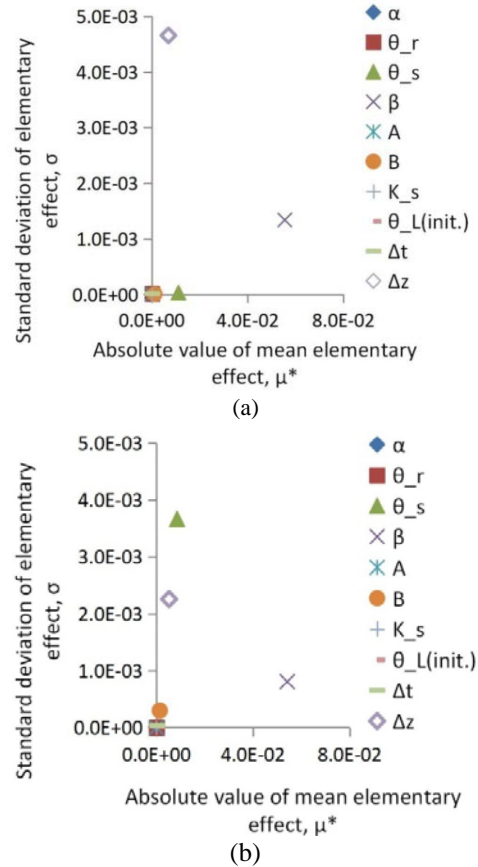
Figure 10. Global sensitivity analysis results from improved Morris method on Richard's equation at different levels (p), trajectories (r) and solved by either Euclidean or Manhattan method: **(a)** $p = 2$, $r = 2$, Euclidean method; **(b)** $p = 2$, $r = 2$, Manhattan method; **(c)** $p = 4$, $r = 4$, Euclidean method; **(d)** $p = 4$, $r = 4$, Manhattan method; **(e)** $p = 4$, $r = 10$, Euclidean method; and **(f)** $p = 4$, $r = 10$, Manhattan method.

The significant influence from parameter Δz was expected as the previous study on local sensitivity analysis has shown similar result[50]. However, the parameters β and θ_s were unexpected. In parameter ranking, based on the values of μ^*, β was indeed the most important parameter, and then, followed by θ_s, Δz, and so on. It is widely accepted that the absolute mean value of elementary effect is to indicate the influence of parameter on model output[10,15]. Hence, a wide input range in **Table 1**, for parameters β and θ_s, was the reason of high μ^*. Goh and Noborio found that parameter with the high percentage of uncertainty and normalized sensitivity coefficient would result in large variation in model output[50].

Parameters β, θ_s and Δz were found to have the highest standard deviation of elementary effect (σ). The high value of the σ is an indication of parameter having non-linearity effect or involved in interactions with other factors[6,10,13]. In a fundamental level, a high value of σ is also suggesting that a large fluctuation of value or sign in the elementary effect (*EE*). The other 7 parameters could be categorized as mainly linear and additive, as indicated by their low σ value.

In original Morris sampling strategy[6], geometric distance between trajectories was not considered. This method is acceptable when a large number of random trajectories are generated, because all the input space of parameters would be fully explored. In search for cost effective sensitivity analysis tool to reduce computational time, the fewer trajectories would translate into lesser computational cost. Euclidean distance method as sampling strategy, as in Equation (3), was first coined by Campolongo *et al.*[7]. They have demonstrated that the improved sampling strategy could significantly reduce the number on **Figure 10(b)**, Δz in **Figures 10(d)** and **(f)**. In addition to this, **Figure 11** has shown Manhattan distance has a better sampling strategy as it exhibits lower variation in input space distribution as indicated by its lower standard deviation values than those of Euclidean distance sampling strategy.

By comparing Morris method between different levels ($p = 2 - 4$), trajectories ($r = 2 - 10$) and sampling strategies (Manhattan or Euclidean), we have found $p = 2$, $r = 2$ and Manhattan

distance sampling strategy was sufficient to provide reliable distinction between important and unimportant parameters. The computational experiment was carried out on an upper limit of $p = 4$, $r = 10$, because it is greatly accepted that this limit would be sufficient to produce valuable results[12-14]. Moreover, these results would be cross-validated by Sobol' variance-based method.

f trajectories are needed, while maintaining a good approximation to total effect index. In addition to Euclidean distance method, there is also Manhattan distance method as stated in Campolongo et al.[7], but not tested. In general, **Figures 10(a)**, **(c)** and **(e)** have shown that at different levels (p) and trajectories (r), Euclidean distance has a comparable results as the Manhattan distance sampling strategy in **Figures 10(b)**, **(d)** and **(f)**. However, a better estimation of σ was shown by Manhattan distance method on parameter θ_s.
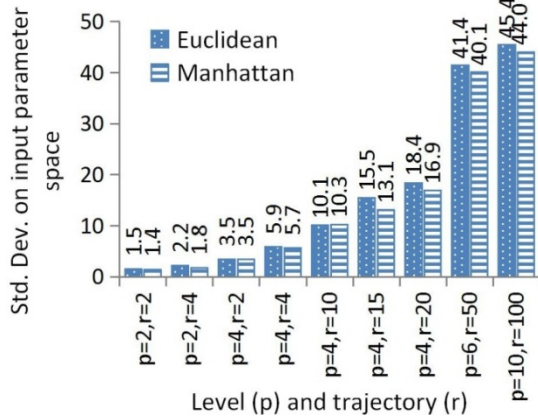

Figure 11. Standard deviation on input parameter space versus level (p) and trajectory (r).

An added advantage of $p = 2$, $r = 2$, and Manhattan distance sampling strategy is that it only requires 2 *trajectories* × (10 *parameters* + 1) = 22 simulation runs, while local sensitivity analysis with 10 parameters would require at least 2 × (10 *parameters*) = 20 runs, i.e., one run for each value of lower and upper range for each parameter. Irrespective of the number of parameters, the former is always only 2 runs greater than the latter. In addition, the parameter sensitivity measures of the former were estimated randomly at various input spaces of other parameters, while the latter was estimated by varying input space of parameter of interest and keeping other parameters constant. It is also important to note that the former is based on statistical theory, whereas the latter is

not. Therefore, it is compelling to practice Morris method of $p = 2$, $r = 2$, and Manhattan distance sampling strategy with only 2 runs extra from Sobol' variance-based method was carried out to cross-validate the results from Morris method. All parameters were subjected to variance-based analysis, except spatial discretization size and time-step size, because their computational time would be too long to be executed efficiently. Nevertheless, the 8 parameters' μ^* values from Morris method at $p = 2$, $r = 2$ (Manhattan distance sampling strategy) were compared to total effect index (S_{T_i}) of Sobol' variance-based method, i.e., the results of 150,000 runs using quasi-Monte Carlo estimator (Equation (14)), referring to **Figure 12** local sensitivity analysis.
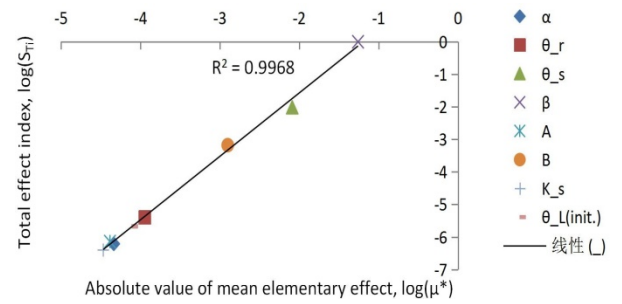
Figure 12. Total effect index (S_{T_i}) versus absolute value of mean elementary effect (μ^*).

There were good agreements between those two for all 8 parameters. Similar effort in justifying the validity of results from Morris method by comparing μ^* with S_{T_i} was showed by Campolongo et al.[7]. Thus, it indicates the absolute mean of elementary effect from Morris method of $p = 2$, $r = 2$ (Manhattan distance sampling strategy) was indeed correctly determined. In addition, the results of S_i, in **Table 3**, has shown similar trend as the S_{T_i}.

Table 3. First order sensitivity index (S_i) and total effect index (S_{T_i}) on input parameters. Note that θ_r is residual volumetric water content, θ_s is saturated volumetric water content, K_s is saturated hydraulic conductivity, and α, β, A and B are fitting coefficients. $\theta_{L(initial)}$, Δz and Δt are initial spatial discretization size and time-step size, respectively

Input parameters	Model outputs (÷100)		
	0.0000	0.0001	0.0001
	0.0000	0.0004	0.0004
	0.9038	0.9631	0.0593
	98.9704	99.0293	0.0589
Total	0.0000	0.0001	0.0001
	0.0136	0.0663	0.0527
	0.0000	0.0000	0.0000
	0.0000	0.0002	0.0002
	99.887	100.0596	

The total sum of first order sensitivity index ($\sum_i^q S_i$) was slightly less than one, which indicates the presence of interaction effect, i.e., second order and higher orders. The $S_{T_i} - S_i$ indicates the presence of interaction effects between parameters, but it was found that each parameter has negligible contribution on model output variance, for instance, 0.06 % of output variance was contributed by θ_s interactions with other parameters, which was among the highest.

Figure 13. Water infiltration profile by numerical solution and semi-analytical solution. The validation was carried out with β 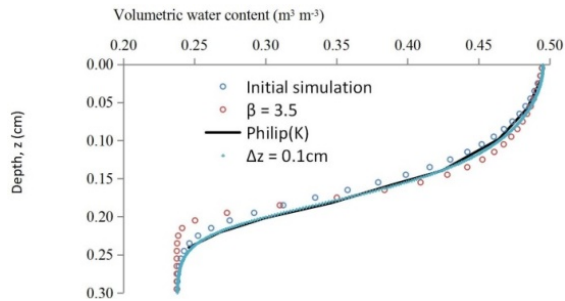at 3.5 and spatial discretization size at 0.1 cm. The initially simulated water profile is also included in the graph for comparison purpose. The total simulation time was 10^5 s.

In previous section, water infiltration was simulated using Richard's equation and was found to under predict the semi-analytical solution, referring to **Figures 6-8**. An overall summary of global sensitivity analysis has indicated that three important parameters, i.e., Δz, β and θ_s, out of 10 parameters. This suggests the parameters have significant influence on model outputs. Based on the sensitivity analysis results, to increase the advancement of water infiltration profile is either to reduce single or a combination parameters among Δz, β and θ_s. The θ_s value cannot be less than 0.495 m^3 m^{-3}, because it would cause simulation failure, and hence, it was excluded. Single adjustment of Δz value was sufficient to result in good approximation of numerical solution to semi-analytical solution than the β. The validation results are showed in **Figure 13**. Therefore, Δz was the sole reason of the discrepancy between simulation result and semi-analytical solution.

11. Conclusions

Global sensitivity analysis tool of Morris method with extended sampling strategy, i.e., Euclidean distance method, by Campolongo *et al.*

was implemented and compared with Man-hattan distance sampling strategy. They were tested on Richard's equation, which is commonly used to govern water flow in variably unsaturated soils. The absolute mean of elementary effect (μ^*) estimated by Morris method with Manhattan sampling strategy has comparable results to those with Euclidean distance method. However, the standard deviation of elementary effect (σ) estimated through Manhattan method has proven better results than Euclidean method. Moreover, Manhattan method has a better scan of input space as indicated by lower standard deviation on input parameter space distribution than Euclidean method. Even at $p = 2$, $r = 2$ which only has 2 extra runs than the local sensitivity analysis, it was able to provide reliable estimation of sensitivity measures. The simulated results were cross-validated by sensitivity index of Sobol' variance-based method, of which μ^* has shown consistent relation with total effect index (S_{T_i}). The global sensitivity analysis also managed to identify three important parameters, of which the spatial discretization size (Δz) was later found responsible for the discrepancy observed. This analysis suggests a better spatial numerical scheme should be implemented, or the numerical scheme would have to use a smaller Δz for accurate simulation. In addition, a great proportion of total output variance was contributed by β and θ_s, which suggests a higher parameter significant digits published with lower input value uncertainty would reduce their variance contribution on the total output.

Conflict of interest

No conflict of interest was reported by the author.

References

1. Caviedes-Voullième D, Garcı´a-Navarro P, Murillo J. Verification, conservation, stability and efficiency of a finite volume method for the 1D Richards equation. Journal of Hydrology 2013; 480: 69–84.
2. Vereecken H, Maes J, Feyen J. Estimating unsaturated hdraulic conductivity from easily measured soil properties. Soil Science 1990; 149(1): 1–12.
3. De Roo APJ, Offermans RJE. LISEM: a physically-based hydrological and soil erosion model for basin-scale water and sediment management. In:

Simonovic SP, Kundzewicz ZW, Rosbjerg D, *et al.* (editors). Modelling and Management of Sustainable Basin-scale Water Resource Systems (Proceedings of a Boulder Symposium). Oxfordshire: IAHS Publication; 1995. p. 399–407.

4. Davis A, Kamp S, Fennemore G, *et al.* Environmental policy analysis, peer reviewed: A risk-based approach to soil remediation modeling. Environmental Science & Technology 1997; 31(11): 520A–525A. doi: 10.1021/es9725662.

5. Fox GA, Muñoz-Carpena R, Sabbagh GJ. Influence of flow concentration on parameter importance and prediction uncertainty of pesticide trapping by vegetative filter strips. Journal of Hydrology 2010; 384(1-2): 164–173. doi: 10.1016/j.jhydrol.2010.01.020.

6. Morris MD. Factorial sampling plans for preliminary computational experiments. Technometrics 1991; 33(2): 161–174. doi: 10.2307/1269043.

7. Campolongo F, Cariboni J, Saltelli A. An effective screening design for sensitivity analysis of large models. Environmental Modelling & Software 2007; 22(10): 1509–1518. doi: 10.1016/j.envsoft.2006.10.004.

8. Drouet JL, Capian N, Fiorelli JL, *et al.* Sensitivity analysis for models of greenhouse gas emissions at farm level. Case study of N_2O emissions simulated by the CERES-EGC model. Environmental Pollution 2011; 159(11): 3156–3161). doi: 10.1016/j.envpol.2011.01.019.

9. Chu-Agor ML, Muñoz-Carpena R, Kiker G, *et al.* Exploring vulnerability of coastal habitats to sea level rise through global sensitivity and uncertainty analyses. Environmental Modelling & Software 2011; 26(5): 593–604. doi: 10.1016/j.envsoft.2010.12.003.

10. Saltelli A, Ratto M, Andres T, *et al.* Elementary effects method. In: Global Sensitivity Analysis. The Primer. New York: John Wiley & Sons, Inc.; 2008. p. 109–154.

11. Campolongo F, Saltelli A, Cariboni J. From screening to quantitative sensitivity analysis. A unified approach. Computer Physics Communications 2011; 182(4): 978–988. doi: 10.1016/j.cpc.2010.12.039.

12. Campolongo F, Saltelli A. Sensitivity analysis of an environmental model: An application of different analysis methods. Reliability Engineering & System Safety 1997; 57(1): 49–69. doi: http://dx.doi.org/10.1016/S0951-8320(97)00021-5.

13. Campolongo F, Tarantola S, Saltelli A. Tackling quantitatively large dimensionality problems. Computer Physics Communications 1999; 117(1-2): 75–85. doi: 10.1016/S0010-4655(98)00165-9.

14. Saltelli A, Chan K, Scott EM (editors). Sensitivity analysis. Wiley series in probability and statistics. New York: John Wiley & Sons, Inc.; 2000. p. 494.

15. Saltelli A, Tarantola S, Campolongo F, *et al.* The Screening Exercise. In: McCulloch A (editor). Sensitivity Analysis in Practice: A Guide to Assessing Scientific Models. New York: John Wiley & Sons, Inc.; 2004. p. 91–108.

16. Moreau P, Viaud V, Parnaudeau V, *et al.* An approach for global sensitivity analysis of a complex environmental model to spatial inputs and parameters: A case study of an agro-hydrological model. Environmental Modelling & Software 2013; 47: 74–87. doi: http://dx.doi.org/10.1016/j.envsoft.2013.04.006.

17. Saltelli A, Annoni P. How to avoid a perfunctory sensitivity analysis. Environmental Modelling & Software 2010; 25(12): 1508–1517. doi: 10.1016/j.envsoft.2010.04.012.

18. Yang J. Convergence and uncertainty analyses in Monte-Carlo based sensitivity analysis. Environmental Modelling & Software 2011; 26(4): 444–457. doi: http://dx.doi.org/10.1016/j.envsoft.2010.10.007.

19. Pappenberger F, Beven KJ, Ratto M, *et al.* Multi-method global sensitivity analysis of flood inundation models. Advances in Water Resources 2008; 31(1): 1–14. doi: http://dx.doi.org/10.1016/j.advwatres.2007.04.009.

20. Vazquez-Cruz MA, Guzman-Cruz R, Lopez-Cruz IL, *et al.* Global sensitivity analysis by means of EFAST and Sobol' methods and calibration of reduced state-variable TOMGRO model using genetic algorithms. Computers and Electronics in Agriculture 2014; 100), 1–12. doi: 10.1016/j.compag.2013.10.006.

21. Sepúlveda FD, Cisternas LA, Gálvez ED. The use of global sensitivity analysis for improving processes: Applications to mineral processing. Computers & Chemical Engineering 2014; 66: 221–232. doi: 10.1016/j.compchemeng.2014.01.008.

22. Lagerwall G, Kiker G, Muñoz-Carpena R, *et al.* Global uncertainty and sensitivity analysis of a spatially distributed ecological model. Ecological Modelling 2014; 275: 22–30. doi: http://dx.doi.org/10.1016/j.ecolmodel.2013.12.010.

23. Saltelli A, Ratto M, Andres T, *et al.* Variance-Based Methods. In: Global Sensitivity Analysis. The Primer. New York: John Wiley & Sons, Inc.; 2008. p. 155–182.

24. Pannell DJ. Sensitivity analysis of normative economic models: theoretical framework and practical strategies. Agricultural Economics 1997; 16(2): 139–152. doi: 10.1016/S0169-5150(96)01217-0.

25. Richards LA. Capillary Conduction of Liquids through Porous Mediums. Journal of Applied Physics 1931; 1(5): 318–333. doi: 10.1063/1.1745010.

26. Haverkamp R, Vauclin M, Touma J, *et al.* A comparison of numerical simulation models for one-dimensional infiltration. Soil Science Society of America Journal 1977; 41(2): 285–294. doi: 10.2136/sssaj1977.03615995004100020024x.

27. Kabala ZJ, Milly PCD. Sensitivity analysis of flow in unsaturated heterogeneous porous media: Theory, numerical model, and its verification. Water Resources Research 1990; 26(4): 593–610. doi: 10.1029/WR026i004p00593.

28. Namin MM, Boroomand MR. A time splitting algorithm for numerical solution of Richard's equation. Journal of Hydrology 2012; 444-445: 10–21.

doi: http://dx.doi.org/10.1016/j.jhydrol.2012.03.029.

29. Ma Y, Feng S, Su D, et al. Modeling water infiltration in a large layered soil column with a modified Green–Ampt model and HYDRUS-1D. Computers and Electronics in Agriculture 2010; 71, Supplement 1: S40–S47. doi: http://dx.doi.org/10.1016/j.compag.2009.07.006.

30. Caviedes-Voullième D, Garcı́a-Navarro P, Murillo J. Verification, conservation, stability and efficiency of a finite volume method for the 1D Richards equation. Journal of Hydrology 2013; 480: 69–84.

31. Sobol IM. Sensitivity estimates for nonlinear mathematical models. Matematicheskoe Modelirovanie 1990; 2(1): 112–118.

32. Tarantola S, Giglioli N, Jesinghaus J, et al. Can global sensitivity analysis steer the implementation of models for environmental assessments and decision-making? Stochastic Environmental Research and Risk Assessment 2002; 16(1): 63–76. doi: 10.1007/s00477-001-0085-x.

33. Saltelli A, Annoni P, Azzini I, et al. Variance based sensitivity analysis of model output. Design and estimator for the total sensitivity index. Computer Physics Communications 2010; 181(2): 259–270. doi: http://dx.doi.org/10.1016/j.cpc. 2009.09. 018.

34. Cukier RI, Fortuin CM, Shuler KE, et al. Study of the sensitivity of coupled reaction systems to uncertainties in rate coefficients. I Theory. The Journal of Chemical Physics 1973; 59(8): 3873–3878. doi: http://dx.doi.org/10.1063/1.1680571.

35. Schaibly JH, Shuler KE. Study of the sensitivity of coupled reaction systems to uncertainties in rate coefficients. II Applications. The Journal of Chemical Physics 1973; 59(8): 3879–3888. doi: http://dx.doi.org/10.1063/1.1680572.

36. Saltelli A, Tarantola S, Chan KPS. Technometrics, 1999, 41(1):39-56. A quantitative model-independent method for global sensitivity analysis of model output. Technometrics 1999; 41(1): 39–56. doi: 10.1080/00401706.1999.10485594.

37. Nossent J, Elsen P, Bauwens W. Sobol' sensitivity analysis of a complex environmental model. Environmental Modelling & Software 2011; 26(12): 1515–1525. doi: http://dx.doi.org/10.1016/j.envsoft.2011.08.010.

38. Celia MA, Bouloutas ET, Zarba RL. A general mass-conservative numerical solution for the unsaturated flow equation. Water Resources Research 1990; 26(7): 1483–1496. doi:10.1029/WR026i007p01483.

39. Tu J, Yeoh GH, Liu C. Computational fluid dynamics: A practical approach. 2nd ed. Oxford, Waltham: Butterworth-Heinemann; 2007.

40. Istok J. Step 4: Solve System of Equations. In: Groundwater Modeling by the Finite Element Method. Washington, DC: American Geophysical Union; 2013. p. 171–225.

41. Zheng C, Bennett GD. Applied contaminant transport modeling. 2nd ed. New York: John Wiley & Sons, Inc.; 2002.

42. Stange F, Butterbach-Bahl K, Papen H, et al. A process-oriented model of N_2O and NO emissions from forest soils: 2. Sensitivity analysis and validation. Journal of Geophysical Research: Atmospheres 2000; 105(D4): 4385–4398. doi: 10.1029/1999jd900948.

43. Nathan R, Safriel UN, Noy-Meir I. Field validation and sensitivity analysis of a mechanistic model for tree seed dispersal by wind. Ecology 2001; 82(2): 374–388. doi: 10.1890/0012-9658(2001)082[0374:fvasao]2.0.co;2.

44. Min CH, He YL, Liu XL, et al. Parameter sensitivity examination and discussion of PEM fuel cell simulation model validation: Part II: Results of sensitivity analysis and validation of the model. Journal of Power Sources 2006; 160(1): 374–385. doi: 10.1016/j.jpowsour.2006.01.080.

45. Gosling SN, Arnell NW. Simulating current global river runoff with a global hydrological model: model revisions, validation, and sensitivity analysis. Hydrological Processes 2011; 25(7): 1129–1145. doi: 10.1002/hyp.7727.

46. Poeter EP, Hill MC. Documentation of UCODE: A computer code for universal inverse modeling. Denver: DIANE Publishing; 1998.

47. Jhorar RK, Bastiaanssen WGM, Feddes RA, et al. Inversely estimating soil hydraulic functions using evapotranspiration fluxes. Journal of Hydrology 2002; 258(1-4): 198–213. doi: http://dx.doi.org/10.1016/S0022-1694(01)00564-9.

48. Tang Y, Reed P, Wagener T, et al. Comparing sensitivity analysis methods to advance lumped watershed model identification and evaluation. Hydrology and Earth System Sciences 2007; 3(6): 793–817. doi: 10.5194/hess-11-793-2007.

49. Wagener T, Werkhoven KV, Reed P, et al. Multi-objective sensitivity analysis to understand the information content in streamflow observations for distributed watershed modeling. Water Resources Research 2009; 45(2). doi: 10.1029/2008WR007347.

50. Goh EG, Noborio K. Sensitivity analysis on the infiltration of water into unsaturated soil. Proceedings of Soil Moisture Workshop, Hiroshima University Tokyo Office in Campus Innovation Center; 2013. p. 66–68.

51. Cohen D, Person M, Daannen R, et al. Groundwater-supported evapotranspiration within glaciated watersheds under conditions of climate change. Journal of Hydrology 2006; 320(3-4): 484–500. doi: http://dx.doi.org/10.1016/j.jhydrol.2005.07.051.

ORIGINAL RESEARCH ARTICLE

Earthquake response control of ground soft storey

Sakshi A Manchalwar[*]

Priyadarshini College of Engineering, Department of Civil Engineering, Nagpur 440019, India. E-mail: manchalwarsakshi@gmail.com

ABSTRACT

In the present study, friction damper, an energy dissipating passive device is explored to reduce the response of open ground storey building under lateral loading due to earthquake. This damper is installed in the selected bays of open ground storey so that the response is reduced. The masonry infill wall is macro-modeled in the form of compression only diagonal members. Three different types of bracing system were installed along with Pall friction damper – single diagonal tension – compression brace with friction damper, tension only cross brace with friction damper and chevron brace with friction damper were modeled using Wen's plastic link element in SAP2000. G+4 storey buildings were analyzed using nonlinear time history analysis. The storey displacement and inter-storey drift for all the cases were compared in the study.

Keywords: Ground Storey; Friction Dampers; Infill Masonry Wall; Floor Displacement Response

1. Introduction

Buildings resting on ground experience motion at base due to earthquake. According to Newton's law of inertia, even though the base of the building moves with the ground, the roof has a tendency to retain its original position. But the flexible columns will drag the roof along with them. Due to this flexibility of columns, the motion of roof is different from that of the ground. As the ground moves, the building is thrown backwards and the roof experiences inertia force. Internal forces are developed in the columns as they are forced to bend due to the relative movement between their ends as shown in **Figure 1**.
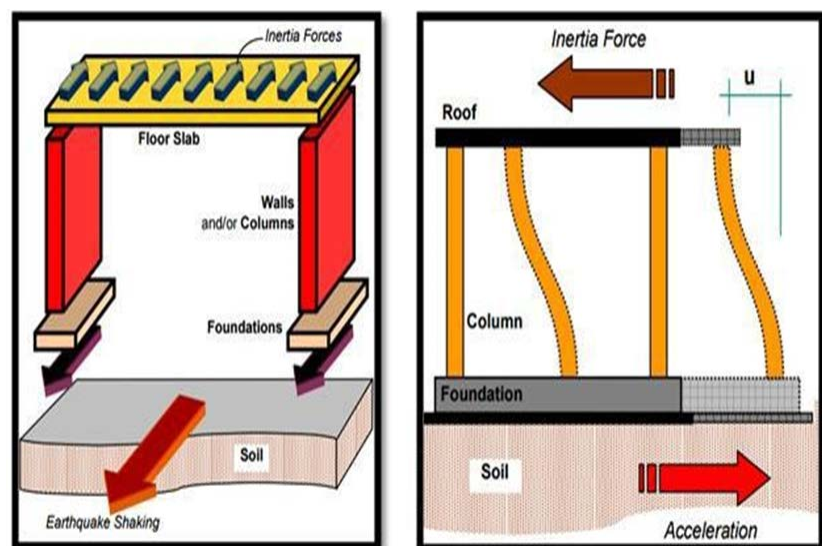

Figure 1. Effect of Inertia in a building when shaken at its base**.**

Earthquakes are thus a severe structural hazard for structures designed for gravity loads as they may not sustain the horizontal shaking. Structures like buildings, elevated surface reservoir, bridges, towers, etc. may experience extreme vibrations during earthquake.

Reinforced concrete (RC) is the most commonly used construction material used these days, primarily owning to its low cost, easy availability of materials, simpler execution without requirements of any special machineries or labour. Generally, the RC buildings are analyzed and designed such that, the moment resisting frame actions are developed in each member. The masonry infill walls are normally considered as non-structural elements used to create partitions or to protect the inside of the building and thus are ignored in analysis and design. Such construction practices are followed by many countries, including India. However, under the action of lateral forces like the once due to earthquake and wind, these infill wall panel's stiffness, strength and mass affect the behavior of RC frame building.

At times, due to uneven distribution of mass, strength and stiffness in either plan or in elevation, irregularities are introduced in RC frame buildings. If the masonry walls are not symmetrically placed, then in that case, the eccentricity between centre of mass and centre of rigidity may induce torsional effects causing additional stresses. In recent times, it has been a common practice to construct RC buildings with open ground storey, i.e., the columns in the ground storey do not have any infill walls between them. This provision generally kept for the purpose of parking, garages, and various recreational purposes introduce a vertical irregularity in the structure.

An open ground storey building, having only columns in the ground storey and both partition walls and columns in the upper storey have two distinct characteristics, namely:

1) It is relatively flexible in the ground storey, i.e., the relative horizontal displacement it undergoes in the ground storey is much larger than what each of the storey above it does.

2) It is relatively weak in ground storey, i.e., the total horizontal earthquake force it can carry in the ground storey is significantly smaller than

what each of the storey above it can carry. Thus, there is a requirement of seismic strengthening of such open ground storey RC frame buildings. Various types of energy dissipating devices based on wide range of concepts have been explored in the recent past.

1.1 Requirement of retrofitting of open ground storey structures

In many densely populated urban cities of the world, including many cities in India, it has been a common practice since last two-three decades to provide an open ground storey in the multistorey reinforced concrete buildings for parking, garages, or various recreational purposes.

To avoid this huge forecasted hazard, it is very essential to strengthen the open-ground storey buildings, which are having a very poor performance history during earthquake. **Figure 2** shows the collapse of an open ground storey building of 5 storeys in Kathmandu, Nepal.

Figure 2. Open ground storey failure of 5 storeys building in Kathmandu during the 2015 Nepal Earthquake**.**

The five-general passive energy dissipation approaches can be mentioned as:

1) Controlled by structural design;

2) Controlled by conventional localized additions – by using shear walls, braced frames;

3) Controlled by additional damping – by using dampers;

4) Controlled by base isolation – using base isolators;

5) Combinations of the above mentioned.

Arlekar *et al.*[1] analyzed the seismic response of four storeys RC frame building with open ground storeys, using equivalent static anal-

ysis and response spectrum analysis to find the resultant forces and displacements. Negro and Verzeletti[2] studied the effects of the infills on the global behavior of the structure by performing series of pseudo-dynamic tests on the full-scaled four-storey reinforced concrete frame. In an attempt to determine the seismic vulnerability of masonry-infilled non-ductile reinforced concrete frames, Al-Chaar[3] carried out an experiment to evaluate the behavior of five half scale, single-storey laboratory models with different number of bays. Davis et al.[4] illustrated the influence of masonry infill on the response of multi-storeyed building under seismic loading by considering two existing buildings in which one building has soft storey while the other is symmetric.

While Pall[5] was describing the merits of Pall Friction Dampers, its various practical applications and its design criteria, mentioned that, the slippage of friction damper in an elastic brace consists of non-linearity. For the MUCTC Building used friction dampers in steel bracing, as upgrade with conventional methods of seismic rehabilitation, would have required expensive and time consuming foundation work besides interfering with the heritage character of the structure[6]. Lee et al.[7] dealt with the numerical model of a bracing-friction damper system and its operation used the optimal slip load distribution for the seismic retrofitting of a building. Singh and Moreschi[8] focused on the optimal design of friction dampers for multi-story buildings exposed to seismic motions. The procedure defined the optimal locations, slip loads for the dampers and the stiffness of the bracings that must be used. Kitajima et al.[9] outlined the response control retrofit method, using external damping braces equipped with friction dampers. They highlighted the advantage of the retrofit method without interrupting the use of building.

2. Modeling of friction dampers

The slippage of friction damper in an elastic brace consists of non-linearity. The amount of energy dissipation or equivalent structural damping is proportional to the displacement. Therefore, the design of friction-damped buildings requires the use of nonlinear time-history dynamic analysis to accurately understand the response of the structure during and after an earthquake. The "NEHRP Guidelines for the Seismic Rehabilitation of Buildings, FEMA 356, issued in 2000"[10] can be used for the analysis and design of friction dampers. Since different earthquake records, even of the same intensity, give widely varying structural responses, results obtained using a single record may not be conclusive. Therefore, at least three time-history records which are suitable for the region should be used, one of which should be preferably site specific. The average response for design should be used. NEHRP guidelines require that friction dampers are designed for 130% MCE displacements and all bracing and connections are designed for 130% of damper slip load[11].

2.1 Modeling of chevron pall friction dampers

The Chevron Friction Damper as shown in **Figure 3** can be modeled, using the following link properties:

Type = Plastic (Wen)

W = Weight of damper = 2.22 (units: kN-m)

Rotational inertia 1 = Rotational inertia 2 = Rotational inertia 3 = 0

Direction = U1

Ke = Effective Stiffness = 1000 x damper slip load (units: kN-m)

Yield Strength = Slip load of friction damper

Post Yield Stiffness Ratio = 0.0001
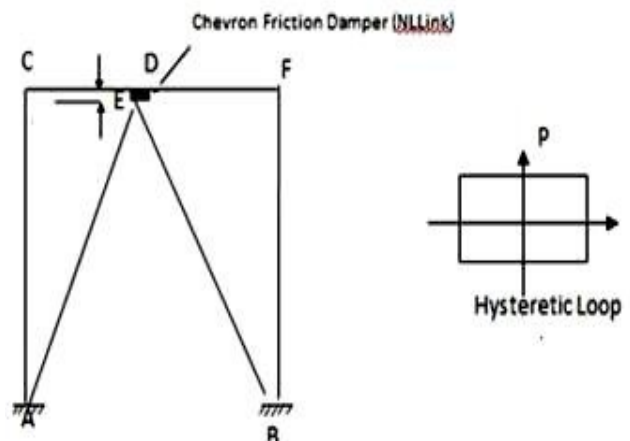
Yielding exponent = 10

Figure 3. Chevron brace with pall friction damper.

The brace is modelled as frame element. Braces are from joints A and E and joints B and E.

The beams at top are from joints C and D and joints D and F. The friction damper is modeled as a nonlinear axial link element between joints D and E. Joint E is lower and away from joint D as in **Figure 3**.

3. Description of building

Typical five-bay five-storey, eight-storey and twelve-storey RC building with open-ground storey as shown in **Figure 4** and **Figure 5** are considered as the prototype structures in this study. Overall size of the building in plan is 30.0 m × 24.0 m with bay width of 6.0 m in each orthogonal direction.
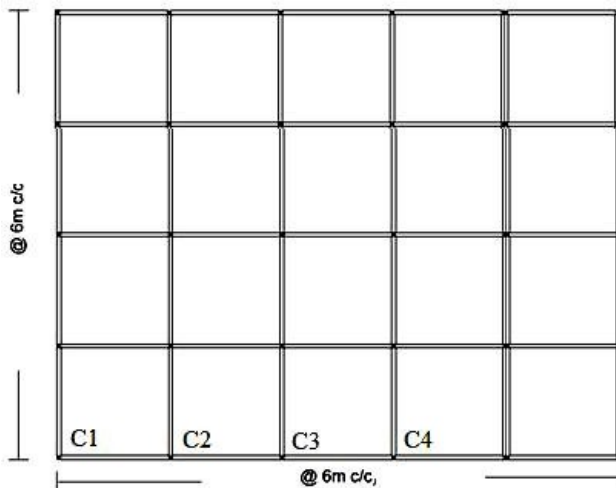

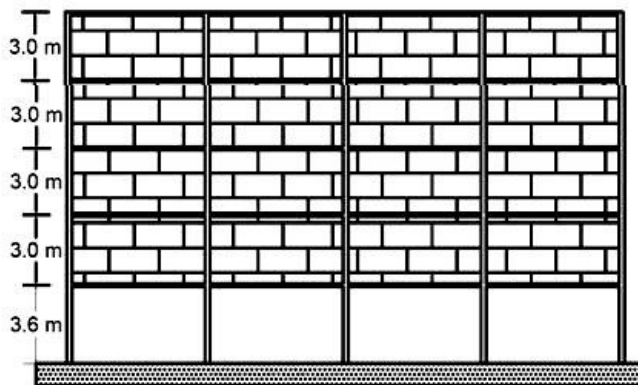**Figure 4.** Plan of the prototype building.

Figure 5. Elevation of the prototype building. G+4 storey.

The height of ground storey is considered as 3.6 m, whereas the storey height of upper storeys is assumed as 3.0 m. The upper storeys of building are fully in filled with unreinforced brick masonry of 250 mm thickness. The thickness of roof and floor slab is taken as 180 mm. The building is founded on a rock site in seismic zone-V, the region of highest seismicity as per IS: 1893 (Part 1):

2002. Since the buildings are symmetric in both orthogonal directions in plan, torsional response under pure lateral forces is avoided, and hence, the present study is focused only on the weak and soft storey problem due to open-ground-storey. Unit weights of concrete and masonry infill are considered as 25 kN/m^3 and 20 kN/m^3, respectively. Dead load on the beams consisted of self-weight of beam, slab and masonry infill, including floor finish of 1.0 kPa. Live loads on the floors and roof are assumed as 3.0 kN/m^2 and 1.5 kN/m^2, respectively.

3.1 Modeling of infill masonry wall

The properties of the masonry infill wall considered for analysis are as summarized in **Table 1**. The masonry is assumed to satisfy the requirements of good condition masonry as specified by FEMA 356 (2000). These properties can be used to macro-model. The infill panels in the form of two compression only strut joining the diagonally opposite corners of the infill panel.

Table 1. Properties of infill masonry wall

Properties	Values
Weight density (kN/m^3)	20
Poisson's ratio	0.2
Thickness of infill (mm)	250
Prism compressive strength	4.5
Elastic modulus in compression Eme (MPa)	3412
Flexural tensile strength, ftm (MPa)	0.1
Shear strength fvm (MPa)	0.14

The width "a" of equivalent diagonal compression strut can be calculated as below:

$$a = 0.175(\lambda_l h_{col})^{-0.4} r_{inf}$$

Where,

$$\lambda_1 = \left[\frac{E_{me} t_{inf} \sin 2\theta}{4 E_{fe} I_{col} h_{inf}}\right]^{\frac{1}{4}}$$

A reduction factor for existing infill panel damage can takes values from 0.7 to 0.4, and from moderate to severe damage. Thus, the infill masonry wall can be macro-modeled as an equivalent compression strut of depth 250 mm and thickness "a" mm.

3.2 Selection of ground motions

Four different ground motions recorded in different parts of the world were selected as direct integration time-history analysis in present study. The ground motions are so selected that, their re-

corded peak ground acceleration (PGA) value is nearly about 0.36g which represents the highest seismic zone-V in India as per IS: 1893 (Part 1): 2002. The recorded ground motions represent common site conditions with hypo-central distance from the source lie within 20 km to the site depicting near source-site effect. **Table 2** summarizes the earthquake data and site characteristics of selected ground motions.

Table 2. Selected ground motions

Sr. No	Name of Earthquake	Richter Magnitude	PGA (g)
1	El Centro (1940)	6.9	0.35
2	Chi – Chi (1999)	7.6	0.31
3	Whittier (1987)	6.6	0.43
4	Superstition Hills (1987)	6.6	0.38

4. Evaluation of strengthened RC frame building

The seismic evaluation of typical non-ductile designed five-storey RC building with open ground storey by time history analysis uses a computer package SAP2000. A strengthening scheme involving friction damper is adopted to enhance the performance of the non-ductile prototype buildings considered. All columns of the study frame were chosen to be rectangular sections of size 450mm × 550mm, whereas the size of beam sections was considered as 300mm × 450 mm. As stated earlier, the unreinforced masonry infill in the upper storey of study frame was not designed for any forces to which it may be subjected to as followed in normal practice.

Seismic performance of the building was evaluated by linear modal analysis and nonlinear time history analysis using SAP2000. The properties of frame members, infill masonry, and friction dampers were used as discussed earlier. **Figure 6** shows the elevation of G + 4 open ground storey RC frame building with different types of friction dampers modeled in SAP2000 and installed in the selected bays of ground storey.

(a) Single diagonal tension/compression friction damped bracing

(b) Tension only cross braced friction dampers

(c) Chevron braced friction damper
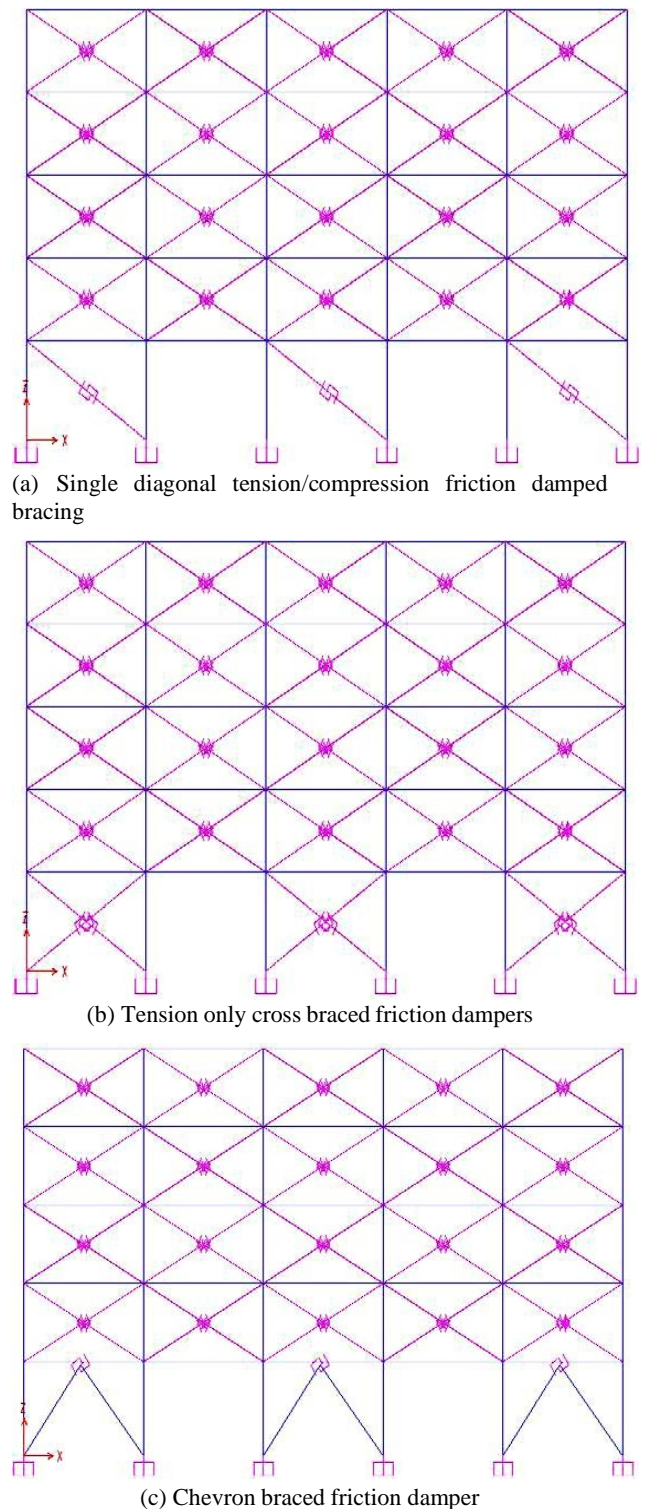
Figure 6. Elevation of G + G open ground storey buildings strengthened with different types of friction dampers as modeled in SAP2000.

4.1 Floor displacement response

Figure 7 shows the variation of peak values of floor displacements for both non-ductile and strengthened RC frames in various ground motions.
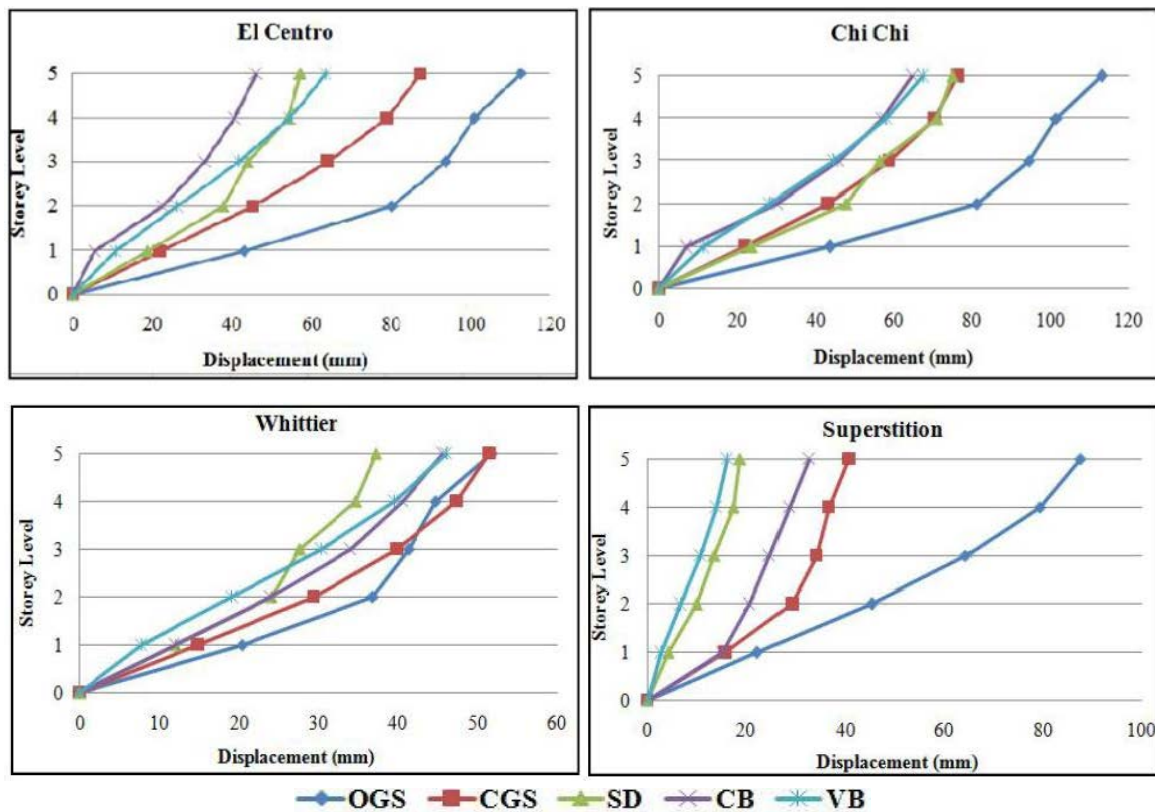
Figure 7. Store Displacement of building with and without dampers for the considered ground Motions.

With the installation of dampers, there can be seen a significant reduction in the storey displacement predominantly at the ground level as well as at the upper storey levels. **Figure 8** shows inter-storey displacement response. Inter-storey displacements at various storey levels of RC frames were computed from the difference between their peak values of absolute displacements and adjacent storey. As expected, significant intersto-

rey displacement was observed only at the ground storey and a very negligible difference was noted in the upper floors of each frame as shown in **Figure 8**. The frame without dampers exhibited maximum inter-storey displacement at the ground storey in all ground motions. In contrast, significant reduction in inter-storey displacement was observed in the strengthened frame.

Figure 8. Inter storey drift of building with and without dampers for the considered ground motions.

41

Thus, strengthening of non-ductile RC frames with friction damper significantly reduces inter-storey displacement between floors.

5. Conclusion
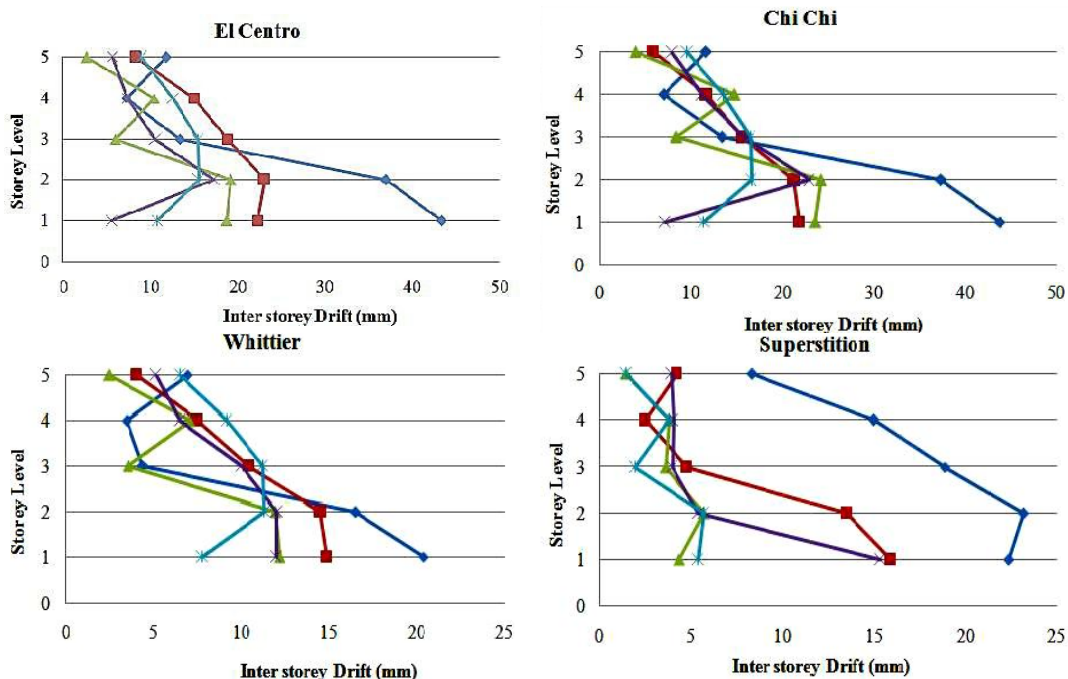
The results obtained from the analytical study using software package SAP2000 are mentioned in this chapter. The various observations incorporated from the results are described in this chapter. With the installation of friction dampers, a considerable reduction was observed in the displacement of ground storey and inter-storey drift of the building. With the installation of dampers, the lateral-load transfer mechanism of the structure changes from predominant frame action to predominant truss action.

Following conclusions can be drawn based on the work performed in this project.

1) Use of friction dampers is an effective tool in seismically strengthening the buildings with open ground storey.

2) Use of passive energy dissipating devices is more predominant than others, owing to their reliable performance during earthquake.

3) The time period of the structure decreases with the installation of friction dampers, indicating the increase in the stiffness of the structure owing to strengthened ground storey.

4) The ground storey displacement and inter- storey drift are found to reduce with installation of dampers at the ground storey.

There is response reduction not just on the ground storey but also for the upper storey.

Conflict of interest

No conflict of interest was reported by the author.

References

1. Arlekar JN, Jain SK, Murty CVR (editors). Seismic response of RC frame buildings with soft first storeys. New Delhi: Proceedings of CBRI Golden Jubilee Conference on Natural Hazards in Urban Habitat; 1997 Jan; Berlin: ResearchGate; 1997. p. 10–11.

2. Negro P, Verzeletti G. Effect of infills on the global behaviour of R/C frames: Energy considerations from pseudodynamic tests. Earthquake Engineering & Structural Dynamics 1996; 25(8): 753–773.

3. Al-Chaar G, Issa MA, Sweeney S. Behavior of masonry-infilled nonductile reinforced concrete frames. Journal of Structural Engineering 2002; 128 (8): 1055–63.

4. Davis R, Krishnan P, Menon D, *et al.* Effect of infill stiffness on seismic performance of multi-storey RC framed buildings in India. 13th World Conference on Earthquake Engineering; 2004 Aug 1-6; Vancouver, B.C. Amsterdam: Mendeley, Elsevier; 2004. p. 1–9.

5. Pall A, Pall RT Performance-based design using pall friction dampers — An economical design solution. 13th World Conference on Earthquake Engineering; 2004 Aug 1-6; Vancouver, B.C. Montreal: Pall Dynamics Limited; 2004. p. 576–571.

6. Vezina S, Pall RT. Seismic retrofit of MUCTC building using friction dampers, Palais Des Congres, Montreal. 13th World Conference on Earthquake Engineering; 2004 Aug 1-6; Vancouver, B.C. Montreal: Pall Dynamics Limited; 2004. p. 1–6.

7. Lee SK, Park JH, Moon BW, *et al.* Design of a bracing-friction damper system for seismic retrofitting. Smart Structures and Systems 2008; 4(5): 685–696.

8. Singh MP, Moreschi LM. Optimal seismic design of building structures with friction dampers. 1st ed. In: Spencer BF, Hu Y (editors). Earthquake Engineering Frontiers in the New Millennium. London: Taylor & Francis Group; 2001. p. 482.

9. Kitajima K, Chikui H, Ageta H, *et al.* Application to response control retrofit method by means of external damping braces using friction dampers. Proceedings of the 13th World Conference on Earthquake Engineering; 2004 Aug 1-6; Vancouver. Vancouver (BC): International Association for Energy Economics (IAEE); 2004.

10. American Society of Civil Engineers (ASCE). Prestandard and commentary for the seismic rehabilitation of buildings. Report FEMA-356 2000.

11. Council AT, Rojahn C, Shapiro D, *et al.* NEHRP guidelines for the seismic rehabilitation of buildings. Report FEMA-273 1997.

12. Pall A. Design – Slip load of friction dampers. Pall Dynamics – Pioneers of friction dampers for seismic control of buildings [Internet]. Montreal: Pall Dynamics Limited; 1984 [cited 2020]. Available from: http://www.palldynamics.com/DesignWithFrictionDampers.htm.

13. Crime Scene Investigation (CSI). CSI analysis reference manual for SAP2000, ETABS and SAFE. Berkeley, CA.: Computers and Structures Inc.; 2007.

14. Crime Scene Investigation (CSI). SAP2000 Advanced. Berkeley, CA.: Computer and Structures Inc.; 2007.

ORIGINAL RESEARCH ARTICLE

Rinnenkarren systems and the development of their main channels

Márton Veress[*], **Zoltán Mitre**

Department of Medieval and Early Modern History, Faculty of Humaities, Eötvös Loránd University, Budapest 1011-1239, Hungary. E-mail: veress.marton@sek.elte.hu

ABSTRACT

In this study, the development of rinnenkarren systems is analyzed. During the field studies, 36 rinnenkarren systems were investigated. The width and depth were measured at every 10 cm on the main channels and then shape was calculated to these places (the quotient of channel width and depth). Water flow was performed on artificial rinnenkarren system. A relation was looked for between the density of tributary channels and the average shape of the main channel, between the distance of tributary channels from each other and the shape of a given place of the main channel. The density and total length of the tributary channels on the lower and upper sections of the main channels being narrow at their lower end (11 pieces) and being wide at their lower end (10 pieces) of the rinnenkarren systems were calculated as well as their average proportional distance from the lower end of the main channel. The number of channel hollows was determined on the lower and upper sections of these main channels. It can be stated that the average shape of the main channel calculated to its total length depends on the density of the tributary channels and on the distance of tributary channels from each other. The main channel shape is smaller if less water flows on the floor for a long time because of the small density of the tributary channels and the great distance between the tributary channels. In this case, the channel deepens, but it does not widen. The width of the main channel depends on the number and location of the rivulets developing on channel-free relief. The main channel becomes narrow towards its lower end if the tributary rivulets are denser and longer on the upper part of the main rivulet developing on the channel-free, plain terrain and their distance is larger compared to the lower end. The channel hollows develop mainly at those places where the later developing tributary channels are hanging above the floor of the main channel. Thus, the former ones are younger than the latter ones. It can be stated that the morphology of the main channels (shape, channel hollows, and width changes of the main channel) is determined by the tributary channels (their number, location and age).

Keywords: A Rinnenkarren System; Channel; Tributary Channel; Channel Shape; Discharge; Transit Time; Channel Hollow

1. Introduction

In this study, the shape (the shape is given by the quotient of the channel width and depth) of the main channels of the rinnenkarren systems and change of width (separating the main channels being wide and narrow on their lower end) and channel hollows were investigated in order to interpret the characteristics of growth of the main channels and the morphology of rinnenkarren systems and to familiarize ourselves with the way of their development.

Karren is widespread on karst, but it is the main characteristic of the bare surfaces of the glacier valleys of glaciokarst (e.g. the Alps, the Pyrenees, the Dinarides, and the Caucasus). The most common karren features of bare surfaces are rillenkarren, rinnenkarren, wallkarren, meander karren, grikes, kamenitzas and trittkarren. Karren is main small

features of karst areas that developed by dissolution. They can develop by flowing water and seeping water[1-3]. Features developing by flowing water are hydraulic forms (White, 1988) or hydrodynamically controlled[2], while features developing by seeping water are etched forms[1] or fracture controlled forms[2]. Karren of flowing origin such as rillenkarren, rinnenkarren (channel, runnel), wall karren and meander karren develop on bare surfaces, however, according to some authors[4,5] Song (1986) and Slabe and Liu (2009), rinnenkarren can develop beneath soil as well. Karren of seeping origin (for instance grikes) can form on both bare and soil (sediment) covered rocks.

On the bare surfaces of glaciokarst, karren often occur[6], mainly rinnenkarren. Thus, in the eastern Alps, in the zone of Pinus mugo, the specific width (being the width of karren features over a 1 m distance) represented by them is 67%[3]. However, they can also occur on bare surfaces of other karsts such as mediterranean and tropical karst[7-9]. Because of their widespread occurrence and large density (sometimes they determine the landscape of the karst area), several researchers have studied their occurrence, morphology and development[1,7,10-17].

Rinnenkarren are channels with downslope direction. Their lower end is connected to karst wells (pipes) and grikes. Thus, the water flowing in them is conducted beneath the surface. Their cross-section can be U-shaped, V-shaped and widening downwards[10-12]. Their width and depth are a few decimeters, while their length may be some 10s of meters.

Channels or rinnenkarren develop under rivulets[18-20]. The rivulets are fed by rainwater, the water of snow patch or that of kamenitza. The rivulets only occur in the channels during rainy season (active period). During most part of the year, the floor of rinnenkarren (channel) is completely waterless (non-active period).

Channels are complex features. On their floor, kamenitzas, pipes, small basins, hollows, karren sinkholes, karren terraces and steps may occur, while on their side walls, scallops and rillenkarren may occur[3,15,17,21,22]. Several varieties

can be distinguished, such as rundkarren, Hortonian type channels, decantation runnels, simple and complex channels and type A and type B channels[2,3,15,23]. The crests between the channels of rundkarren are rounded[15,18]. The rounded crests developed by dissolution under soil[18]. The Hortonian type channels can consist of several runnels[20]. The decantation runnels can develop at point-like water supply places[20], thus, at kamenitzas[24] too. The width and depth of decantation runnels decreases downslope[2,20]. Veress (2009, 2010) distinguished simple and complex channels. The simple channel can be of Type I, II and III. The depth and width of channel Type I are some decimeters. These values are some centimetres in the case of channel Type III, while the size of channel Type II lies between the size of types I and III. In case of complex channels, Type II channels may develop in Type I channels, while Type III channels may develop in Type II channels. Karren meanders are channels with asymmetric cross-section. It is common that the lower end of the symmetric channel turns into asymmetric, thus, the lower part of the rinnenkarren transforms into meander karren[3]. Type III meander karren can occur on the floor of Type I channels[25]. Karren meanders may be looping, remnant, perishing and developing meanders[25].

According to previous investigations[3,23,26], two types of rinnenkarren can be distinguished according to their size and shape. These are the type A and type B channels. Type B channels have a greater size. Their sides are steep (U-shaped). They have a great catchment area and a great specific catchment area. Type A channels are smaller size. Their sides are more gentle (V-shaped). They have a small catchment area and a small specific catchment area. Type B channels can consist of only one channel or can create rinnenkarren systems[23]. A relation can be presented between the density of type A and B channels and the angle of the bearing slope. The density of type A channels increases by the growth of the slope angle, while that of type B channels decreases[23].

The channels often constitute rinnenkarren systems (**Figure1**). The rinnenkarren systems are

made up of main channels (the length of which can be often 30-50 m) and of type A and type B tributary channels are connected to them. Type B tributary channels can also be complex. In this case, the tributary channels may have smaller type B and type A tributary channels. Both type A and type B tributary channels can be hanging and non-hanging ones. The floor of the hanging tributary channel terminates at the conjunction site, some centimetres or some tens of centimetres above the floor of the main channel. By this, a step develops at the conjunction site. The floor of the non-hanging tributary channels is located at the level of the floor of the main channels.
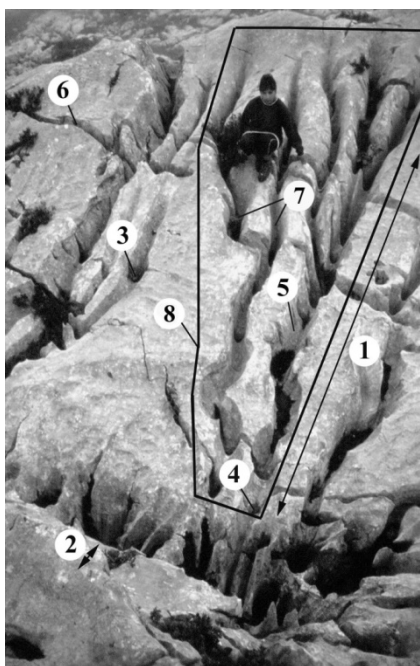

Figure 1. The main channel of the rinnenkarren system which becomes narrower on its lower part (Totes Gebirge). Legend: 1. Surface with bedding planes; 2. Step front; 3. Pipe on the floor; 4. Pipe at the end of the channel; 5. Main channel; 6. Grike; 7. Tributary channel; 8. Rinnenkarren system**.**

The channel shape of the main channels, which expresses what depth belongs to a given channel width, is rarely the same on its different parts. On some parts of the main channel, the width increases locally and channel hollows develop. The channel hollows develop because the water flowing from the tributary channel triggers vorticity which causes the local increase of dissolution[22]. Apart from channel hollows, it often occurs that the channels widen from their upper end towards their lower end (**Figure 1**). This can occur if the widening is of greater extent than the

deepening, but in a reverse situation too. It is possible that their width decreases on their lower part, not only relatively (compared to their depth) but actually too. The decrease always happens in case of decantation runnels, but it also occurs on the lower parts of the main channels of the rinnenkarren systems (**Figures 1, 2**).

Figure 2. Channels which become narrower have a smaller cross-section downwards (Totes Gebirge). Legend: 1. dip direction of the slope**.**
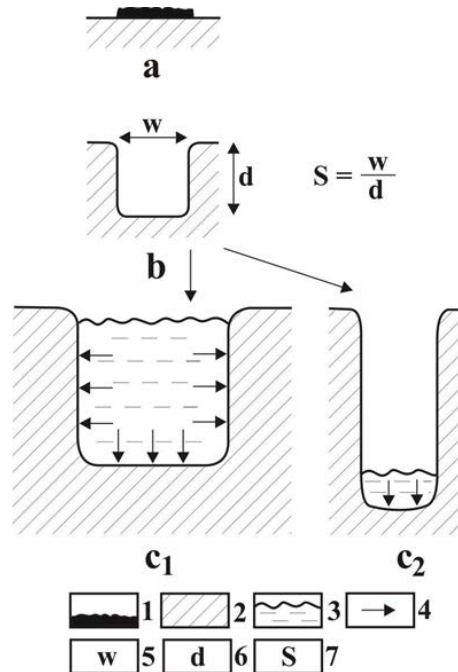
Figure 3. Model of the channel shape and its development. Legend: 1. Rivulet on the surface; 2. Rock; 3. Rivulet in the channel; 4. Place of dissolution; 5. Width of the channel; 6. The depth of the channel; 7. Shape of the channel: a. rivulet; b. development of the channel; c_1. Large channel shape (there is dissolution on the channel walls too); c_2. Small channel shape (there is dissolution on the channel floor only)**.**

Apart from local effects of biogenic origin, the channel shape is formed by the water flowing with solution capacity (the water of the rivulet) in the channel. If a large amount of water flows (the channel is filled with water which is called large

discharges later) in the channel for a longer time and it has solution capacity, both the channel wall and channel floor are solved. Thus, the channel widens and deepens too (**Figure 3c$_1$**). The cross-section of the channel grows in a way that the proportion of width and depth does not change. If a little amount of water flows in the channel for a longer time (the water just covers the floor of the channel, it is called small discharge later), solution happens on the floor only. The channel does not widen, but it deepens only (**Figure 3c$_2$**).

In a main channel, the durations of the large and small discharges changes. The proportion of the durations of the two different discharges determines the shape of the channel, that is, the proportion of width and depth. The longer the duration of the large discharge as compared to the small discharge at a given place is, the larger width and the larger cross-section the channel has. The shorter the duration of the large discharge is, the smaller width and the less large cross-section the channel has (however, because of deepening, the cross-section also increases).

In the former case, the channel shape is large or of increasing tendency, while in the latter case, it is small or of decreasing tendency during the channel development. Since transitional discharges also occur between large and small discharges, the channel sides do not necessarily dissolve uniformly[21]. It can be observed that there are channels widening towards their margins (V-shaped) and channels widening towards their floor. This study does not include the interpretation of the development of these cross-sections.

The potential change of the channel shape also depends on the size of the cross-section. In case of a larger cross-section, only a larger decrease (change) of discharge can cause dissolution on the floor, that is, change of shape. This is caused by the fact that in case of a larger cross section, the same amount of water covers the floor only. While in case of a smaller cross-section, a smaller change of discharge can also cause dissolution on the floor only, that is, change of shape.

If the width of the main rivulet increases towards its lower end on the terrain being exempt from channels, also the width of the main channel increases towards its lower end. If the width of the

main rivulet decreases towards its lower end on the terrain exempt from channels, also the width of the main channel decreases towards its lower end.

The development of the channel hollows of the main channels is caused by the tributary channels. The rivulet of the tributary channel conjoining the rivulet of the main channel causes turbulence which increases dissolution locally[22]. Vortexes are larger, and turbulence is more intensive and thus, dissolution is larger where the tributary channels are hanging over the floor of the main channel. Hanging tributary channels develop if the rivulets of the tributary channels develop later than the rivulet of the main channel (it means that the development of the tributary channels began later than that of the main channel).

2. Method

On our sample site in Totes Gebirge, 36 rinnenkarren systems were mapped in the glacier valley under the Tragl peak near Tauplitz Alm. A various number (about 25-30) of rinnenkarren systems were included in our different processings. In some cases, the tributary channel of some rinnenkarren systems creating a more complex system (as a rinnenkarren system) was also investigated separately (thus, the number of measurements exceeded 30 during the given processings). The width and depth of the channels were measured at every 10 cm too.

The shape (S) of the channels was calculated at every 10 cm in the following way (**Figure 3b**):

$$S = \frac{w}{d}$$

Where w is the width, and d is the depth.

The cross-section area (A) of the channels was calculated at every 10 cm in case of a U cross-section in the following way:

A = wxd

While in case of a V cross-section in the following way:

A = ½ x w x d

The density (D) of the tributary channels of the rinnenkarren system was calculated in the following way (**Figure 4**):

$$D = \frac{N}{l_m}$$

Where, N is the number of tributary channels, and l_m is the length of the main channel.
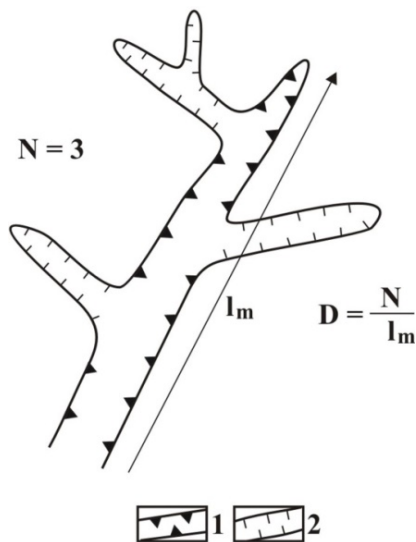

Figure 4. The calculation of the density of tributary channels. Legend: 1. Main channel; 2. Tributary channel: N is the number of tributary channels, and l_m is the length of the main channel.

A functional relation was looked for between the average shape of the main channel (S_0), (which was calculated from the average of the shapes calculated to the total length at every 10 cm) and the density of tributary channels.

A functional relation was looked for between the distance (l_t) of the two tributary channels from each other and the shape (S) of the place [$S(l_t)$] of the main channel which is directly above the conjunction site of the tributary channel with a lower position (**Figure 5**).
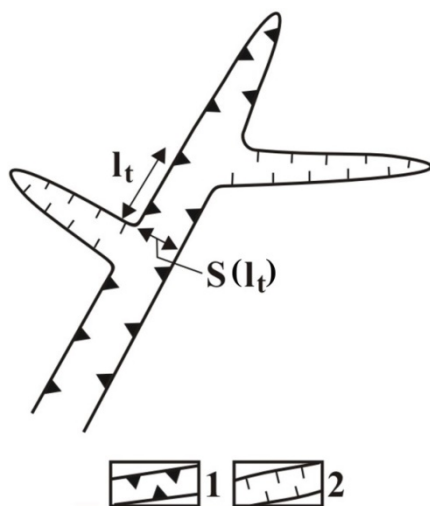

Figure 5. The distance of tributary channels from each other and the place where the data of the shape of the main channel was taken into consideration. Legend: 1. Main channel; 2. Tributary channel. l_t is the distance between two tributary channels. $S(lt)$ is the place where the shape of the main channel was taken into account.

In laboratory, a rinnenkarren system was created on a slope with an inclination of 15° made of Plasticine (**Figure 6 and 7**). The depth of the main channels was 0.7 cm, and their width was between 0.5 and 1 cm, while the depth of the tributary channels was 0.5 cm and their width was 1 cm. The length of the main channel was 200 cm that of the tributary channels was 30 cm. The number of tributary channels was 4, the distance between them was 40 cm, and the junction angle into the main channel was 45°. We let 1.7 cm^3 water into the channels separately from a pipette with free fall and we measured the transit time (actual transit time) of the incoming water at the lower end of the main channel by calculating the difference between the beginning and the end of the transit time. First, we only got water into one channel (first experiment series). In the followings, we got 1.7 cm^3 - 1.7 cm^3 water into 2 channels (second experiment series), then into 3 channels (third experiment series) and into 4 channels (fourth experiment series) simultaneously. Finally, we got water into 5 channels simultaneously (fifth experiment series). Water supply was always carried out at the upper end of the channels. As it can be seen in **Table 1**, 5 experiments belong to the first experiment series, 10 experiments belong to the second and third experiment series, 5 experiments belong to the fourth experiment series and 1 experiment belongs to the fifth experiment series.
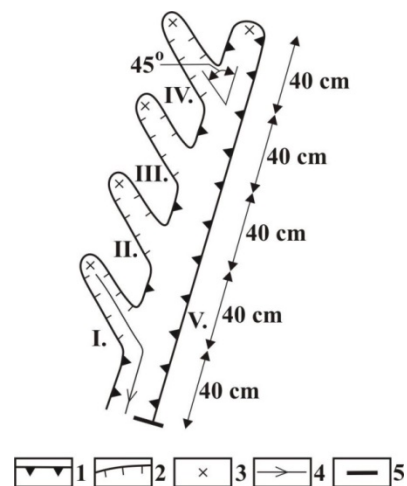

Figure 6. The theoretical figure of the rinnenkarren system of the laboratory experiment. Legend: 1. Main channel; 2. Tributary channel; 3. Place of water supply; 4. Water flow; 5. Place of measurement of the transit time, I-IV. tributary channels, V. main channel.
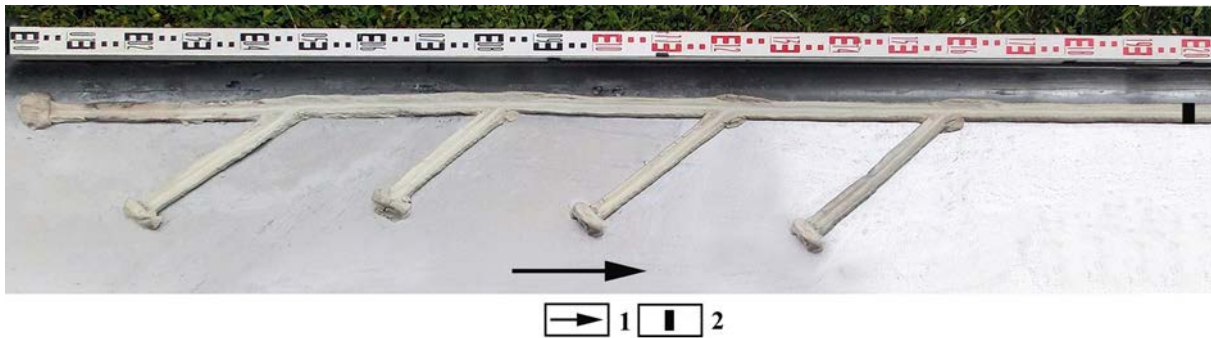
Figure 7. Rinnenkarren system created in laboratory. Legend: 1. Dip direction of the tray; 2. Place of measurement.

Table 1. Transit times measured on the experimental rinnenkarren system

Experiment series	The number of experiment series	Places of water supply	The number of places of water intake	Total waterflow length compared to the measurement place [cm]	Beginning of waterflow	End of water flow	Actual transit time [sec]	Total transit time[sec]
1	1	I	1	70	1.33	4.113	2.783	2.783
	2	II	1	110	1.916	5.903	3.987	3.987
	3	III	1	150	2.6	6.94	4.34	4.34
	4	IV	1	190	3.2	8.21	5.01	5.01
	5	V	1	200	3.297	8.61	5.313	5.313
2	1	I,II	2	100	1.356	3.452	2.096	6.77
	2	I,III	2	140	1.404	4.512	3.108	7.123
	3	I,IV	2	180	1.406	3.974	2.568	7.793
	4	I,V	2	190	1.34	4.012	2.672	8.096
	5	II,III	2	140	2.084	4.168	2.084	8.327
	6	II,IV	2	180	1.846	4.084	2.238	8.997
	7	II,V	2	190	1.862	3.922	2.06	9.3
	8	III,IV	2	180	2.51	4.226	1.716	9.35
	9	III,V	2	190	2.566	4.298	1.732	9.653
	10	IV,V	2	190	2.926	5.816	2.89	10.323
3	1	I,II,III	3	170	1.424	6.846	5.422	11.11
	2	I,II,IV	3	210	1.332	8.172	6.84	11.78
	3	I,II,V	3	220	1.368	8.034	6.666	12.083
	4	I,III,IV	3	210	1.396	8.564	7.168	12.133
	5	I,III,V	3	220	1.41	8.178	6.768	12.436
	6	I,IV,V	3	220	1.378	8.786	7.408	13.106
	7	II,III,IV	3	210	1.924	8.828	6.904	13.337
	8	II,III,V	3	220	1.928	8.952	7.024	13.64
	9	II,IV,V	3	220	1.904	9.008	7.104	14.31
	10	III,IV,V	3	220	2.466	8.992	6.526	14.663
4	1	I, II, III,IV	4	240	1.362	8.212	6.85	16.12
	2	I,II,III,V	4	250	1.352	8.742	7.39	16.423
	3	I,II,IV,V	4	250	1.458	8.474	7.016	17.093
	4	I,III,IV,V	4	250	1.308	9.114	7.806	17.446
	5	II,III,IV,V	4	250	1.886	8.714	6.828	18.65
5	1	I,II,III,IV,V	5	320	1.392	9.032	7.64	21.433

In case of the laboratory experiment (first experiment series), a functional relation was looked for between the transit time and the distance between the place of water supply and the place of measurement.

We investigated how the duration of the actual transit time and the total transit time compared to each other changed when we increased the density and distance of water supply places (second, third, fourth and fifth experiment series).

The actual transit time is calculated, as it was already mentioned by the difference of the beginning and end of the water flow at the place of measurement. The total transit time is calculated by adding the different actual transit times measured at certain channels (thus, those involved in experiment series 2, 3, 4, 5) during the first experiment series.

The relation between discharge (and thus, the extent to which the channel is filled with water) and the actual transit time was analyzed. If the amount of water supply increases, but the actual transit time is smaller at the measurement site as compared to a smaller amount of water supply, the rate of flow and thus, the discharge increases too. If the amount of water supply increases or it is of the same degree, but the actual transit time increases or is the same at the measurement site as compared to a smaller amount of water supply, the velocity of flow and thus, the discharge decreases too. The extent to which the channel is filled with water is larger in the former case, while it is smaller in the latter.

Parallel laboratory and field studies are simultaneously necessary, since we can only measure transit time in case of the laboratory experiment. We do not get data for channel shape and its change in lack of dissolution. However, in case of the field investigation, we draw a conclusion to dissolution from the shape only, since we do not know the transit time (this could not be measured because of the intermittent nature of the rivulet).

From the area of the above mentioned glacier valley, further main channels were investigated. 11 channels were being narrow towards their lower end and 10 channels were being wide towards their lower end. (These latter ones were chosen from the above mentioned 30 rinnenkarren systems.) In the case of the first ones, the rate of the length being narrow at the lower end as compared to the total length was determined and its average was calculated. With the help of this rate, the length of the lower part was marked on the main channels being wide at their lower end.

In case of both varieties (main channel being narrow and being wide at the lower end), the density, the total length of tributary channels were calculated regarding the lower and upper sections as well as the proportional distance of the non-hanging tributary channels from the lower end of the main channel (the average of the distance of each non-hanging tributary channel was calculated). Proportional distance means at what proportion (as compared to the lower end of the main channel), the non-hanging tributary channel is located on the main channel regarded as one unit.

Average proportional distance means the average of the proportional distance of tributary channels occurring at main channels being wide and being narrow on their lower end.

The number of non-hanging and hanging tributary channels having a channel hollow was determined. The length and width of the channel hollows were measured. The average width and length of the channel hollows occurring at the hanging and non-hanging tributary channel were calculated separately.

3. Results

According to the result of the laboratory measurement, if the distance of water supply increases (first experiment series), the actual transit time (**Table 1**) increases at the measurement place which can be explained by the "stretching" of the water of the rivulet. Because of the growth of the actual transit time, the duration of cove redness with water increased on the channel floor (**Figure 8**). As apart from the place of intake, the amount of water intake was the same in all cases at the measurement place. The discharge decreased by the increase of the actual transit time.
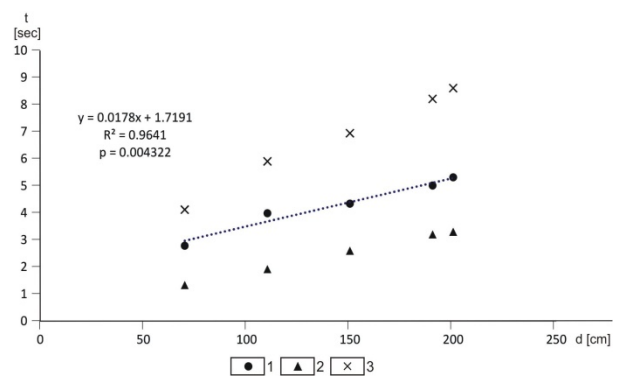
Figure 8. The functional relation between the place of water supply and the actual transit time at the model experiment when there was a water supply simultaneously at one place only (first experiment series)**.** Legend: 1. Actual transit time; 2. The beginning of the arrival of the intake water at the place of measurement; 3. The end of the flow of the intake water at the place of measurement; t. duration of measurement; d. distance between the place of measurement and the place of water supply**.**

It can be stated that by the increase of the distance of the place of water intake, the actual transit time increases and thus the discharge decreases. Under natural circumstances, it means that in case of increasing distances between the tributary channels as compared to the given place

49

of the main channel and in case of the same water inflow (water intake), the actual transit time increases on the lower part of the main channel and thus discharge decreases. Therefore, dissolution is more and more concentrated to the channel floor.

This statement is in harmony with the data of the field measurements. The larger the distance between two tributary channels is, the smaller the shape of the main channel above the tributary channel in a lower position is (**Figure 9**). This can be explained by the fact that with the growth of the distance between the tributary channels, the water coming from the upper tributary channel flows for a longer time (thus, the discharge will be smaller and smaller) through that part of the main channel which is above the junction site of the lower tributary channel. This results in the two things: the dissolution time will become longer and the dissolution will be focused to the channel floor. Since the shape decreases logarithmically in the function of distance, the dissolution time on the channel floor increases to a growing extent with the increase of the distance. From **Figure 9**, we can read that in case of a distance smaller than 100 cm, the average shape of the main channel changes from value 1 to almost 1.8 with the increase of the distance. However, in case of distances between 2 and 5 meters, even though the shape is smaller, its value shows a slight change. At 2 m, shapes between 0.6-0.8 occur, while at 5 m, a value close to 0.4 can be seen. From the above mentioned things, it can be concluded that in case of small water supply distance, a larger change of shape belongs to the same section change as compared to the same change of section in case of a larger water supply distance. This can be attributed to the fact that at a smaller water supply distance, the discharge decreases to a larger degree even in case of a larger water supply than in case of a larger water supply distance. By this, with the increase of distance, the duration of the small discharge increases at the expense of the duration of large discharge. Because of the increase of the duration of the small discharge, the dissolution is more and more concentrated to the floor of the main channel farther and farther from the place of water supply.
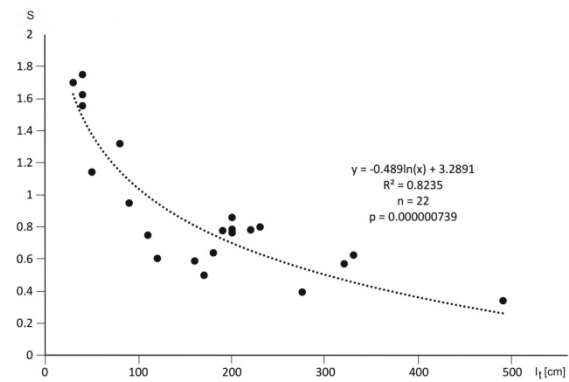

Figure 9. The functional relation between the distance of two tributary channels of the main channel from each other (l_t) and the shape (S) calculated at the place of the lower tributary channel of the main channel $S(l_t)$.

During studying the relation between the density of the tributary channels of the rinnenkarren systems and the shape of the main channel, it turned out that the average channel shape increases with the increase of the density (**Figure 10**).
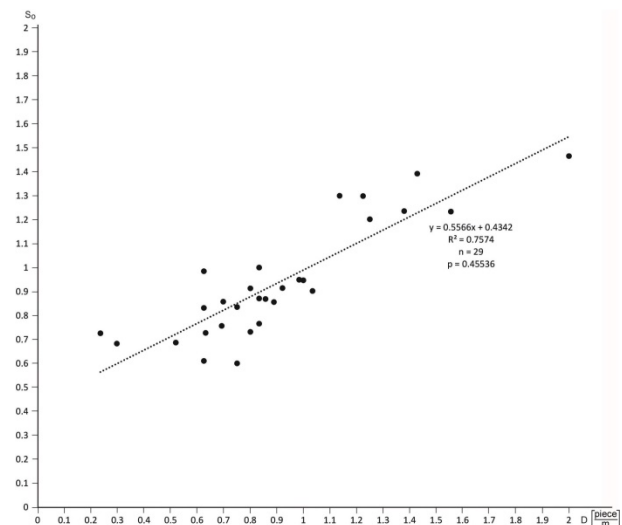
Figure 10. The functional relation between the average density of tributary channels (D) and the average shape of the main channel (S_0).

This is possible if the more densely tributary channels occur, the better the water of the rivulets flowing from them confluence and it causes a growth of discharge in the main channel. The same can be seen in case of channels developed under superficial deposit or soil. According to Song (1986), the channels widen at those places where the water seeping through the cover is led to the water flowing between the bedrock and the cover. If the density of tributary channels is small or becoming smaller and smaller, the discharge will be smaller and smaller too, because the water flowing from the tributary channels is not added up. This results in the fact that in the main channel,

50

in case of an increasingly smaller density of tributary channels, a smaller and smaller amount of water flows for an increasingly longer period. In other words, the dissolution on the floor will be more dominant and thus the channel will become more and more deep while, but its width will be the same.

The confluence of tributary rivulets is also proved by our laboratory measurements. In the experimental rinnenkarren system, the actual transit time is smaller than the total transit time in case of a larger amount of water supply (**Table 1**). With the increase of the number of place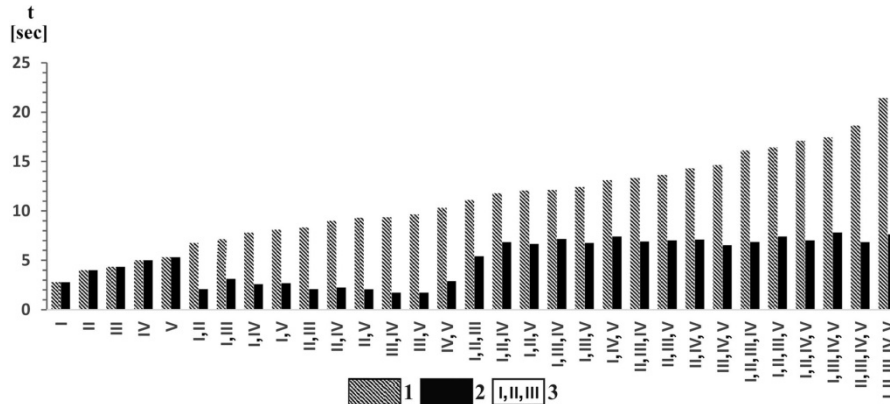s of water supply, the difference of the two is increasingly larger (**Figure 11**). In the followings, there are some examples for this.

Figure 11. Transit times measured in the artificial rinnenkarren system. Legend: 1. Total transit time; 2. Actual transit time; 3. The number of the Roman numerals shows the number of places from where water supply occurred.

In case of a separate water supply of tributary channels I, II, and III, the actual transit time is 2.78 sec., 3.99 sec, and 4.34 sec. (first experiment series). When a simultaneous water supply was carried out from these three tributary channels into the main channel, the amount of water intake was added up and 5.1 cm^3 water was flowing during an actual transit time of 5.42 sec (during the first experiment of the third experiment series, **Table 1**, **Figure 11**). If we look at the total transit time, its value is 11.11 sec. In other words, the total transit time will be larger than the actual transit time. In case of a water supply at four tributary channels (at the first experiment of the fourth experiment series), the total transit time (16.12 sec.) will be even larger than the actual transit time (6.85 sec.). The difference of the two will be larger, because in case of an increasingly larger number of water supply places, the confluence of the rivulets will be of larger extent.

However, the tributary rivulets can not only have a role hindering drainage, but also a role accelerating drainage. In the experiment, the accelerating role can mainly be experienced in case of water supply at two places (**Figure 11**). In this case, the transit time also decreases actually (thus, discharge increases in the main channel) as compared to the transit time of water supply from one tributary channel. It is likely that if the distance between the tributary channels and their distance from the observation place increase simultaneously, it decreases the actual transit time. Experiments III and V of the second experiment series can be good examples for this (**Figure 11**). However, in case of water supply at four or five places, the actual transit times did not increase either as compared to the transit times of water supply at three places as it would have been expected. In spite of the fact, the amount of water supply increases. All of these draw attention to the fact that the water of the tributary channel entering the main channel can not only accelerate but also hinder the water flow in the main channel. Various actual transit times and various discharges may occur in the main channel depending on the fact in how many tributary channels water flows and in those channels where it does what the distribution and position of the tributary channels is. Thus, if we take into consideration the experimental rinnenkarren system, if water flows in tributary channels I and III, the discharge of the main channel will be smaller (since the actual transit time is larger) as compared to the situation when water flows in channels III and V only.

51

During drainage, discharge can be divided into large and small discharges. A small discharge can occur both at the beginning and at the end of water flow. Thus, if the value of the large discharge can change, its transit time changes too. The value and thus, the time of the small discharge can change too. Because of this, the duration of the transit times of the two discharges as compared to each other is modified too. The proportion of the two discharges also depends on the size of the cross-section. In case of a larger cross-section, the duration of the small discharge also increases at the same water input. Therefore, the pattern of the rivulet of the tributary channels (by this, we mean in which of the existing tributary channels, there is a water flow) and the growth of the cross-section affect the proportion of the duration of the large and small discharges. Therefore, during the growth of the main channel, the duration of the small discharge can be different at the same density of the tributary channels too. Because of this, in case of the same densities of tributary channels, very diverse channel shapes may also occur. Thus, for example, shapes of 0.6 or even 1.0 also belong to a density of tributary channels between 0.6 and 0.7 (**Figure 10**).

On the wide part of the studied main channels being narrow towards their lower end (n = 11), the density of the non-hanging tributary channels is 0.001477 piece/cm (piece number is 8), and their total length is 3813 cm. On the narrow lower end of the main channels, the density of the non-hanging tributary channels is 0.0008577 piece/cm (piece number is 3), and their total length is 550 cm. It can be stated that both the density and the length of the non-hanging tributary channels are smaller on the lower, narrow part of the main channel than on its upper, wide part. However, the average proportional distance of the tributary channels (0.629) is larger than in the case of the main channels being wide at their lower end (0.5485). Thus, both the density and the length of the tributary rivulets were also smaller here when neither a main channel nor a tributary channel existed on the bearing terrain. A smaller amount of water arrived at the lower end of the main rivulet (because of the smaller number of the tributary rivulets, but also because their catchment

area was smaller because of their smaller length). Thus, its width did not increase as compared to the upper part of the rivulet. Towards the lower end of the main rivulet, the decrease of the density and length of the tributary rivulets does not mean the decrease of the width of the main rivulet. But it means that the width of the rivulet does not increase towards the lower end of the main rivulet. However, since the tributary rivulets are farther from the lower end of the main rivulet (main channel), which is presented by the relative large average proportional distance of tributary channels, the transit time increases because of the larger distance of water supply. Thus, the width of the main rivulet can decrease actually too.

On the upper part of the main channels being wide at their lower part (n = 10), the density of the non-hanging tributary channels is 0.001595 piece/cm (piece number is 7), and their total length is 650 cm, while the density of the non-hanging tributary channels on their lower part is 0.003974 piece/cm (piece number is 17), and their total length is 4381 cm. On the lower part of the main channels, the large density and the great total length of the tributary channels refer to the fact that before the development of the channels, both the density and the length of the tributary rivulets were larger on the lower part of the main rivulet than on the upper part of the main rivulet. Although the confluence of the rivulets could occur in this case too, the channel wall, since it does not exist, could not limit the widening of the rivulet. This resulted in the fact that the lower part of the main rivulet got more water than the upper part and thus, it became wide because the developing main channel became wider on it lower part than on its upper part.

On the lower part of the main channels being narrow at their lower end, there are no channel hollows either at the conjunction sites of the hanging (n = 18), or that of the non-hanging tributary channels (n = 3). However, on their wide, upper part, where there are altogether 40 hanging channels, 26 have channel hollows, while 2 out of 8 non-hanging tributary channels have them.

The distribution of the channel hollows presented above refers to the fact that they develop mainly in case of steps of hanging tributary chan-

nels, but they can also develop at non-hanging tributary channels. At the steps, the effect of the gradient of the rivulet is reflected in the different size of the channel hollows. Thus, in case of the hanging tributary channels, the average width of the channel hollows (n = 53) is 54,07 cm, and their length is 70,07 cm, while in case of the non-hanging ones (n = 13) average width is 39,3 cm, and the average length is 51,46 cm (the size of the channel hollows of the main channels becoming narrow towards their lower end was not taken into account since the number of measurements of the channel hollows related to the non-hanging tributary channels is only 2). Thus, vorticity and the local hollow on the main channel is mainly caused by the increase of the gradient of the rivulet at the steps, but it can also develop with a smaller possibility though, during the joining of rivulets without gradient. Since on the narrow part of the main channels being narrow at their lower end, they do not develop either at hanging, nor at non-hanging tributary channels, the condition of their development can be the fact that the main channel is wide enough.

4. Conclusion

The tributary rivulets of the channel-free surface control the width relations of the later developing main channel. (These former rivulets are represented by the present non-hanging tributary channels.) The developed tributary channels have an effect on the shape of the developing main channel and on the rate of growth of the width and depth of a main channel with a given width. Mainly, the later developing tributary channels (these are the hanging tributary channels) are responsible for the development of channel hollows.

The discharge of the channels is affected by the stretching of the rivulet, the confluence of the rivulets and the impeding and accelerating effect of the tributary rivulet to the flow of the main rivulet. The more the rivulet stretches, the lesser the different rivulets confluence and the lesser a rivulet impedes another in its flow, the smaller the discharge of the rivulet is. These conditions exist if the rivulet is in channel.

The shape of the main channels of the rin-nenkarren systems depends on the duration of their large discharges and that of their small discharges. However, the duration of the small and large discharges depends on the density of the tributary channels and on the place of the tributary channels on the main channel (the distance of a tributary channel measured from a given place of the main channel). Therefore, the rarely tributary channels occur, the longer their distance from a given section of the main channels is, the more the dissolution to the channel floor focuses since the small discharge is of an increasingly longer duration. Because of the dissolution on the floor, a small channel shape is created. The longer the duration of the larger discharge is, the greater the chance for the development of a large channel shape in the main channel is because dissolution takes place not only on the channel floor, but in the sides of the channel too. This occurs if the density of the tributary channels is high or the distance of the tributary channel from the given place of the main channel is small.

The type of the width change of the main channels depends on the development age of the tributary channels compared to that of the main channels. A width change in its total length is only characteristic of the main channel if the tributary channel and the main channel developed simultaneously. The main channel widens from its upper end to its lower end if the density of the tributary channels increases downwards and on the lower part of the main channel, the total length of these tributary channels is larger than on the part above this section. Because of these characteristics, the discharge of the rivulet of the main channel increases on the still channel-free terrain, towards its lower end, which results in the increase of the width of the main channel from its upper end towards its lower end. The width of the main channel decreases towards its lower end if the density and total length of the tributary channels being the same age as the main channel are smaller on the lower section than on the part being above this section and if the proportional distance of the tributary channels is large as compared to the lower end of the main channel. In this case, the discharge of the rivulet being responsible for the development of the main channel does not in-

crease on the lower, narrowing part of the main channel, or the still channel-free terrain, but it decreases because of the relatively large transit time. This results in the actual narrowing of the main rivulet and thus, the development of a narrower channel section.

Channel hollows develop with a larger number and size on the main channel, mainly if the development of the tributary channels is younger than that of the main channel or if their deepening is slower. In this case, at the steps of the tributary channel, the larger gradient of the tributary rivulet enhances the vorticity originating from the confluence of the rivulets and thus, the increase of channel hollows too.

Conflict of interest

The authors declare that they have no conflict of interest.

References

1. White WB. Geomorphology and hydrology of karst terrains. New York: Oxford University Press; 1988. p. 464.
2. Ford D, Williams P. Karst hydrogeology and geomorphology. Chichester: John Wiley & Sons, Ltd; 2007. p. 562.
3. Veress M. Karst environments: Karren formation in high mountains. Berlin: Springer Science & Business Media; 2010. p. 230.
4. Song L. Origination of stone forest in China. International Journal of Speleology 1986; 15(1-4): 3–13.
5. Slabe T, Liu H. Significant subsoil rock forms. In: Ginés Á, Knez M, Slabe T, *et al.* (editors). Karst Rock Features. Karren Sculpturing. Postojna: Založba ZRC, ZRC SAZU; 2009. p.123–138.
6. Smart C. Glacierized and glaciated karst. In: John Gunn (editor). Encyclopedia of Caves and Karst Science. London: Taylor & Francis; 2004. p. 388–390.
7. Hutchinson DW. Runnels, rinnenkarren and mäanderkarren: Form, classification and relationships. In: Fornos Asto JJ, Gines Gracia A (editors). Karren Landforms: Proceedings of the International Symposium on Karren Landforms: Sóller on 19-24th of September 1995. Palma de Mallorca: Universitat de les Illes Balears; 1996. p. 209–224.
8. Ginés J, Ginés A. Mid-mountain Karrenfields at Serra de Tramuntana in Mallorca Island. In: Gines A, Knez M, Slabe T, *et al.* (editors). Karst Rock Features. Karren Sculpturing. Postojna: Založba ZRC, ZRC SAZU; 2009. p. 375–390.

9. Veress M, Lóczy D, Zentai Z, *et al.* The origin of the Bemaraha tsingy (Madagascar). International Journal of Speleology 2008; 37(2): 131–142.
10. Eckert M. Die Karren oder Schratten. Peterm. Mitteilangen 1898; 69–71.
11. Wagner G. Around Hochifen and Gottesacker area. An introduction to the growth and decay of an alpine landscape (in German). Öhringen: Verlag der Hohenloheschen Buchhandlung Rau, Öhringen; 1950. p. 161.
12. Sweeting MM. The landforms of north-west Country Clare, Ireland. Transactions and papers (Institute of British Geographers) 1955; 21: 33–49.
13. Haserodt K. Investigations into the height and age structure of the karst forms in the Northern Limestone Alps (in German). Regensburg: Michale Lassleben Verlag; 1965. p. 169.
14. Louis H. General geomorphology (in German). 3rd ed. Berlin: Walter de Gruyter & Co.; 1968. p. 109.
15. Bögli A. Die Wichtigsten Karrenformen der Kalkalpen. In: Karst Processes and Relevants Landforms. Berlin: International Speleological Union, Symposium on karst denudation; 1976. p. 141–149.
16. Jennings JN. Karst Geomorphology. 2nd ed. Oxford, UK; New York: Basil Blackwell; 1985. p. 293.
17. Gladysz K. Karren on the Quatsino Limestone [Bachelor's thesis]. Hamilton: McMaster University; 1987.
18. Bögli A. Kalklösung und Karrenbildung. Zeitschrift für Geomorphologie. Suppl 1960; 2: 4–21.
19. Trudgill S. Limestone geomorphology. Geomorphology texts. London: Longman; 1985. p. 196.
20. Ford DC, Williams PW. Karst geomorphology and hydrology. London: Chapman & Hall; 1989. p. 601.
21. Veress M. Rinnenkarren. In: Gines A, Knez M, Slabe T, *et al.* (editors). Karst Rock Features, Karren Sculpturing. Postojna: Založba ZRC, ZRC SAZU; 2009. p. 211–222.
22. Veress M, Zentai Z, Péntek K, *et al.* Flow dynamics and shape of rinnenkarren systems. Geomorphology 2013; 198: 115–127.
23. Veress M, Unger Z. Baradla-domica: Large cave system on the Hungarian-Slovak border.In: Dénes L (editor). Landscapes and Landforms of Hungary. Switzerland: Springer International Publishing; 2015. p. 167–175.
24. Sauro U. The geomorphological mapping of "Karrenfelder" using very large scales: An example. Karst Processes and Relevant Landforms 1976; 189–199.
25. Veress M, Tóth G. Types of meandering karren. Zeitschrift Für Geomorphologie 2004; 48(1): 53–77.
26. Kozma K, Mitre Z. Variations of type A channels in Totes Gebirge. Zeitschrift Für Geomorphologie 2012; 56(2): 37–46.

ORIGINAL RESEARCH ARTICLE

Marine geological maps of the Campania region (Southern Tyrrhenian Sea, Italy): Considerations and contributions to a different scale of geological survey

Gemma Aiello[*]

National Research Council of Italy (CNR). E-mail: gemma.aiello@iamc.cnr.it

ABSTRACT

Marine geological maps of the Campania region have been constructed both to a 1:25.000 and to a 1:10.000 scale in the frame of the research projects financed by the Italian National Geological Survey, focusing, in particular, on the Gulf of Naples (Southern Tyrrhenian Sea), a complex volcanic area where volcanic and sedimentary processes strongly interacted during the Late Quaternary and on the Cilento Promontory offshore. In this paper, the examples of the geological sheets n. 464 "Isola di Ischia" and n. 502 "Agropoli" have been studied. The integration of the geological maps with the seismo-stratigraphic setting of the study areas has also been performed based on the realization of interpreted seismic profiles, providing interesting data on the geological setting of the subsurface. The coastal geological sedimentation in the Ischia and Agropoli offshore has been studied in detail. The mapped geological units are represented by: i) the rocky units of the acoustic basement (volcanic and/or sedimentary); ii) the deposits of the littoral environment, including the deposits of submerged beach and the deposits of toe of coastal cliff; iii) the deposits of the inner shelf environment, including the inner shelf deposits and the bioclastic deposits; iv) the deposits of the outer shelf environment, including the clastic deposits and the bioclastic deposits; v) the lowstand system tract; vi) the Pleistocene relict marine units; vii) different volcanic units in Pleistocene age. The seismo-stratigraphic data, coupled with the sedimentological and environmental data provided by the geological maps, provided us with new insights on the geologic evolution of this area during the Late Quaternary.

Keywords: Marine Geological Maps; Geological Survey; Coastal and Marine Environments; Seismo-stratigraphic Units; Campania Offshore; Southern Tyrrhenian Sea

1. Introduction

One main aim of this paper is to discuss selected examples of marine geological maps of the Campania offshore (Southern Tyrrhenian Sea, Italy) both to a 1:25.000 and to a 1:10.000 scale, focusing on selected examples in the geological sheets n. 464 "Isola di Ischia" and n. 502 "Agropoli". These geological maps have been produced during two research projects aimed at the geological mapping of the Campania region, which carried out at the Geomare Sud CNR research institute of Naples, Italy, now Institute of Marine and Coastal Environment (IAMC) of Naples (National Research Council of Italy). Firstly, a research program on Naples and Salerno Gulfs has been carried out, aiming at constructing, from 1998 to 2000, geological and thematic maps of selected coastal and marine areas at a 1:25.000 scale. In this context, marine geological maps pertaining to the geological sheets n. 465 "Isola di Procida", n. 466 "Sorrento" and n. 467 "Salerno" have been constructed and are published in the Institute

for Environmental Protection and Research (ISPRA) (Department of National Geological Survey of Italy) website. The survey activities have included the use of cartographic software (Global Mapper) aimed at carrying out the geologic interpretation and the geologic mapping of morpho-structural lineaments and faults, the definition of cartographic areas representative of the distribution of the sediments cropping out at the sea bottom and of the Late Quaternary depositional sequence. The interpretation and the informatics graphic realization of stratigraphic sketches and interpreted seismic sections, representing integrant elements of the geological maps have been realized.

The second research project on the marine geological survey of the Campania region to a 1:10.000 scale was promoted and financed by the Campania region. The sea bottoms surrounding the coast may be considered as the natural geologic and morphologic prosecution of the emerged coastal belt. In this framework, they show morpho-structural and lithologic analogies with the surrounding coastal sectors. The geological reconstruction of the evolution of the submerged sectors represents an important ring of junction with the geological history of the sectors of the coastal belt now emerged and an adjoining element with the deeper marine sectors.

The flooding of significant parts of the Italian coasts gave rise during the Post-Glacial, perhaps only in some areas, for instance in the Campania region, with repeated phases of subaerial exposure, which have been controlled by tectonic and volcanic processes. A comparative reading of these three sectors (emerged coastal belt, submerged coastal belt and marine coastal belt) has shown the more recent stages relative to the sea level rises, the more significant role of the Quaternary tectonics involving the Southern Apennines[1-7].

The geological survey of the Campania offshore at a 1:10.000 scale is not a cartographic product derived from the national cartography (the first research project), but the basic geologic map, where the whole geologic and geomorphological data recorded at both a 1:10.000 and a 1:5000 scale have been reported. These data, opportunely generalized,

have been plotted in the national geological maps at a 1:50.000 scale.

In the geological maps, this change in scale has imposed a revision of the methods of data acquisition and cartographic criteria to use for the geological survey to a detailed scale of cartographic representation of the geological structures and Quaternary deposits. It has also created an opportunity of both an interchange of the obtained information and active participation to the construction and phases of elaboration of the national cartography.

Some scientific results have been previously obtained, mainly regarding the morpho-bathymetry, the geology and the sedimentology of the coastal and marine environments in the Phlegrean island of Ischia, Procida and Vivara[8-19]. Many other geological studies have been produced on the marine geology of the Naples and Pozzuoli Bays, including the Ischia Island. As a general rule, the Naples Bay is composed of three main volcanic and physiographic domains: the Somma-Vesuvius volcano and its offshore, the Phlegrean Fields and the Gulf of Pozzuoli and the Island of Ischia and Procida[20]. The Somma-Vesuvius volcano has been deeply studied regarding the eruptive events, the recent seismicity, the geochemistry, the ground movements of the volcano and the volcanic hazard[21-26]. The Phlegrean Fields and the Gulf of Pozzuoli, i.e., the submerged border of the Phlegrean caldera, have also been studied by many authors and are continuously monitored by the National Institute of Geophysics and Volcanology (INGV).

2. Materials and methods

The geological maps of the Campania region with a scale of 1:10.000 have been realized through detailed bathymetric bases. Regarding the coastline, the coastline of the Campania region has been digitized based on the most recent aerial photographs. The acquisition surveys of the bathymetric data have been realized using the GPS differential system. The maps have been geo-referenced using the datum WGS84, while the used projection was the Universal Transverse Mercator. While the distance between the isobaths is of 1 m, their representation in the maps is every 5 m.

The criteria for the realization of the geology-ical maps are quite different for the submerged coastal belt from 0 to 30 m of water depth and for the continental shelf/upper slope from 30 m to 200 m of water depth. These criteria are herein descri-bed in two bathymetric and morpho-depositional domains.

2.1 Submerged coastal belt from 0 to 30 m of water depth

For the sea bottoms having depths lower than 5 m, the interpretation of the geophysical data has been carried out using high resolution bathymetric data recorded through the Multibeam Reson Sea Bat 8125, 455 kHz, elaborated in a morpho-bathy-metric key and in a backscattering photomosaic (side option). The geological mapping of wide areas has been supported by ecographic data to a lateral scanning Sidescan Sonar Edgetech DF 1000 and Klein 2000 (100-500 kHz). The interpretative hypotheses on the morpho-structural setting have been supported by high resolution single-channel Sparker data.

During a next working phase, the dives have been planned based on the preliminary observation of the geophysical data following three main objectives, the first one consisting of the calibration of the interpretative keys, the second one represent-ed by the acquisition of direct data (structural, stratigraphic and sedimentologic) and the third one composed of the sampling of the loose sediments and the rocky sea bottom.

The criteria for the construction of the keys for the 1:10.000 geological maps have included the lithostratigraphic units, the Quaternary deposits, the symbols, the archeological structures and the main biological associations. One of the most important lithostratigraphic units was represented by the Cretaceous limestones with Radiolitids, cropping out in the Sorrento Peninsula. The peri-coastal sea bottoms may be considered as the natural geologic and geomorphologic prosecution of the emerged coastal belt.

2.2 Continental shelf/upper slope from 30 m to 200 m of water depth

The acquisition of the geophysical and geological data has been carried out with enough detail to ensure the accuracy compatible with the adopted survey scale. These data are morpho-acoustic, morpho-bathymetric and geologic (box-corers, cores and dredges). The elaboration of the data has allowed, during the first work phase, the cartographic restitution of the bathymetric data collected by the Multibeam echosounder as bathymetric maps with isobaths and shaded relief maps for the geologic interpretation of the main morpho-structural lineaments. During a next work phase, grain-size analyses have been carried out on previously sampled sediments at the sea bottom, and classified according to Folk[27].

The geologic interpretation is based on the recognition of the acoustic facies, which is carried out through the integrated interpretation of Multi-beam and Sidescan Sonar data calibrated in terms of their lithology through the results obtained from the grain-size analyses of the samples at the sea bottom.

The interpretation of the high resolution seismic profiles has been a valid support for the reconstruction of the stratigraphic and structural setting of the continental shelf and slope success-ions. The seismo-stratigraphic analysis has allowed distinguishing the volcanic and sedimentary seismic units separated by regional unconformities and controlled by both the tectonics and the eustasy. In the Naples Bay, the Dohrn Canyon represents an important morpho-structural lineament, which sepa-rates the sedimentary units occurring on the eastern slope of the Gulf from the volcanic units occurring on the western shelf and in correspondence to the Ischia and Procida Islands. Then, the seismic units have been interpreted in terms of the occurrence of Type 1 or Type 2 sequence boundaries or classified in terms of local unconformities, mainly at the top of relict volcanic edifices or at the top of volcanic seismic units.

The geological map realized in this way shows the distribution of the different lithostratigraphic units cropping out at the sea bottom and the different morphological lineaments, according to the CARG guidelines to a1:50.000 and 1:25.000 scale[28]. The main stratigraphic units, so individua-

ted through the analysis of the sediments at the sea bottom, belong to the Late Quaternary depositional sequence. The different criteria of subdivision of the Holocene deposits occurring at the sea bottom at the passage from the geological maps at a 1:50. 000 scale to the geological maps at a 1:10.000 scale have been outlined. In particular, the Holocene deposits cropping out at the sea bottom in the continental shelf areas have been framed in the depositional elements and represent the final phases (High stand System Tract) of the Late Quaternary depositional sequence (Late Pleistocene-Holocene). The space and time geologic evolution and the lateral and vertical migration of the depositional environments from marine and coastal environments, continental shelf and slope during the Late Pleistocene-Holocene time interval have been recognized in this sequence.

The stratigraphic succession investigated through the marine geological survey has recorded the variations of the accommodation space of the Late Quaternary deposits during the last 4th order cycle, ranging between 128 ky B.P. (Tyrrhenian stage) and actual times (isotopic stage 5e)[28]. One of the main aims was the cartographic representation of the lithofacies associations, which have been grouped in depositional elements (representing portions of system tracts), in relationships to the morpho-structural elements recognized through the geologic interpretation of the geophysical data and the geologic evolution of the sedimentary environments. An integrated approach of the classical stratigraphic approach, the sequence stratigraphic approach and the characterization of the depositional systems and elements has been realized. The prevalent volcanic activity which has controlled the stratigraphic architecture of the Naples Bay[20,29-37] has disallowed for a classical stratigraphic approach in the geological mapping, which has been realized taking into account for the associations of depositional systems and the interlayered volcanic and volcaniclastic bodies.

Being bounded below and above by temporal surfaces, the system tracts of the Late Quaternary depositional sequence may be considered as the equivalent to the unconformity bounded stratigraph-

ic units (UBSU)[38-47]. Perhaps, they can be considered as the basic units in the cartographic representation. The so-defined stratigraphic units are groups of strata bounded by mainly synchronous surfaces or by related stratigraphic intervals, whose inner part may be characterized by cores or sea bottom samples. The textural classes have been determined from the interpretation of the geophysical data coupled with direct sampling at the sea bottom, in such a way, to carry out a further differentiation of the mapped depositional elements.

As it has been stated in the guidelines to the geological survey of the Italian seas[48], the purposed stratigraphic subdivision derives from the types of data used in marine geology (mainly the reflection seismic data calibrated through cores) and from the methods of geologic interpretation (high resolution sequence stratigraphy). The geological bodies which have been represented are the system tracts of the Late Quaternary depositional sequence, which refer respectively to: 1) the phase of sea-level fall (Falling Sea Level System Tract)[49]; 2) the phase of sea level lowstand (Lowstand System Tract) and the related internal subdivisions, as it is possible[50]; 3) the phase of sea level rise (Transgressive System Tract)[51-52]; 4) the phase of sea level highstand (Highstand System Tract)[53]. These system tracts, so defined, have been indicated as FST, LST, TST and HST (**Figure 1**).
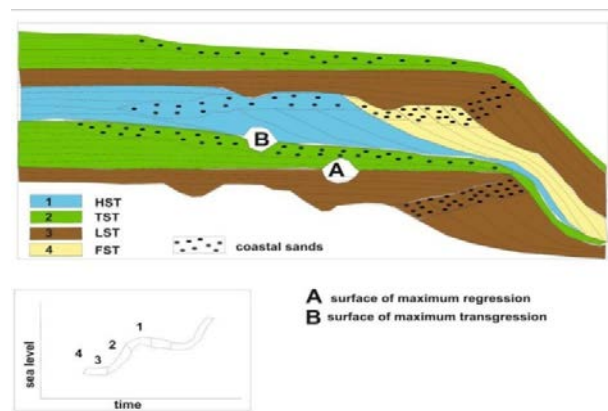

Figure 1. Sketch diagram showing the stacking patterns of system tracts in two ideal depositional sequences.

The choice to represent the system tracts of the Late Quaternary depositional sequence, in particular the HST and the TST, in the geological map of the sea bottom, constitutes a logic starting point and

satisfies the following points: 1) to individuate and map the depositional bodies as three-dimensional objects, referring to their relative stratigraphic location; 2) to give information on the nature of the surface sediments through a high-resolution physical stratigraphic setting tied with samplings and absolute datings of marker horizons. This allows for an indirect characterization of the surface sediments and gives complementary stratigraphic information about the nature of the individuated depositional bodies and about the processes which have controlled their deposition and preservation. The reconstructed depositional systems may be put in relationships with the Late Quaternary sea level fluctuations; 3) to obtain comparable information on all the Italian continental margins without being excessively influenced by local or particular aspects.

The last Late Quaternary sea level rise, having an excursion of about 120 m and a maximum rate in the order of 10 m/1000 y[48] has left evidence on the morphologic and stratigraphic setting of all the continental margins of the world. The deposits related to this process are strongly different from area to area as a function of several variables, including the sedimentary supply, the morphologic setting and the oceanographic regime. The mapping of these deposits allows for the correlation of the most significant stratigraphic surfaces (erosional and non-depositional) and the comparison of the facies, inner geometry and the deposits, which have recorded the sea level rise in a different way along the continental margins.

3. Results

The characterization of the sea bottom sediments in relationships to the sedimentary structures and the grain-size of the deposits have allowed to map different lithologic associations occurring in the sedimentary environments from the littoral to the inner shelf, which have been resumed in **Table 1**.

Table 1. Lithologic associations occurring in submerged beach, toe of coastal cliff and inner shelf deposits.

Depositional environment	Deposits	Facies associations
Littoral environment	Submerged beach deposits Toe of coastal cliff deposits	Blocks Gravels Sands
Inner shelf environment	Proximal inner shelf deposits Lithoclastic deposits Bioclastic deposits	Silts and shales

3.1 Geological map n. 464 Isola d'Ischia

The example of the geological map of the Ischia Island is herein discussed[15]. Submerged beach, inner and outer shelf and slope environments have been distinguished, coupled with debris avalanches and debris flows and undifferentiated volcanic deposits. The depositional environments and the corresponding deposits are resumed in **Table 2**. The geological map n.464 section 030 (scale 1:10.000) is shown as an example of geological map in the western Ischia offshore (**Figure 2**).

Table 2. Depositional environments and corresponding deposits on Ischia Island

Depositional environment	Deposits	Facies associations
Littoral environment	Submerged beach deposits	Well sorted sands and gravels composed of lithic elements having a volcanic nature, from rounded to sub-rounded, with a pelitic matrix and scattered bioclasts. The pelitic matrix increases in the sectors protected from the wave motion and towards the outer boundary of the submerged beach.
Inner shelf environment	Inner shelf deposits Bioclastic deposits	Coarse-to-middle-grained sands and fine-grained pelitic sands. Sandy belts aligned along the lines of the sea bottom occur. The western sectors of inner continental shelf are characterized by wide fields of ripples and mega ripples. Sands and gravelly sands, mainly bioclastic in scarce pelitic matrix. Subordinately,

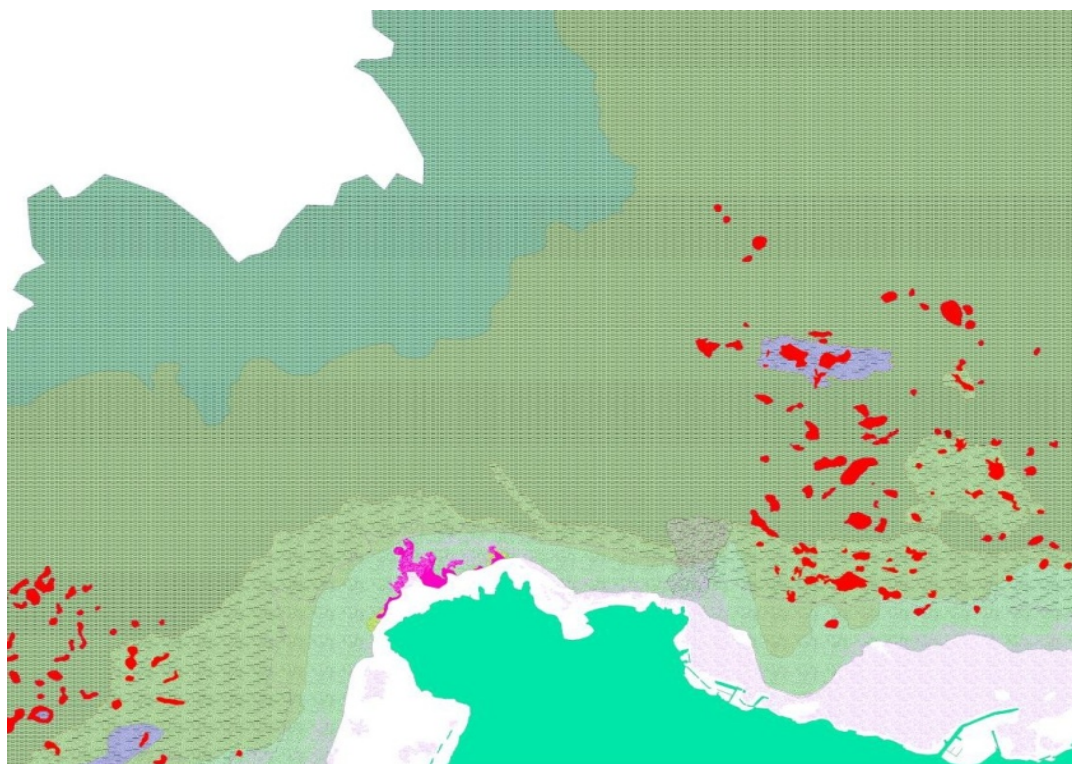|		detrital facies derived from the reworking of organogenic materials on consolidated and lithoid sea bottoms. Middle-grained bioclastic sands in a scarce pelitic matrix located on the morphological highs (Ischia Channel) or to the top of volcanic banks (Forio bank).
Outer shelf environment	Outer shelf deposits Bioclastic deposits	Pelites with variable fractions of middle-fine-grained sands with volcaniclastics and bioclastics and subordinately marine phanerogams. In the northern and south-eastern sectors of the outer shelf some lineaments linked to the occurrence of sea bottom currents occur and are sub-parallel to the isobaths. Detrital bioclastic sands in abundant pelitic matrix characterized by the occurrence of calcareous algae (coastal detritics) whose elements are composed of fragments of bryozoans, echinids and algae. The detrital cover is thick up to several decimeters and overlies mainly pelitic sea bottoms.
Slope environment	Slope deposits	Pelites and sandy pelites. The sandy component, more abundant in correspondence to the canyons and the tributary channels are composed of lithoclasts and bioclasts.
Shelf and slope environment	Debris avalanches and debris flows	Heterometric blocks and accumulations of blocks of tuffs and lavas having dimensions from several hm to dam, interstratified in a detrital matrix, from coarse-to-fine-grained (northern Ischia sector from Lacco Ameno to Casamicciola) and western Ischia sector from Punta del Soccorso and Punta Imperatore).
Shelf and slope environment	Undifferentiated volcanic deposits	Volcanic deposits

Figure 2. Example of geologic map of north-western Ischia Island offshore (scale 1:10. 000)**.**
Note: The red circles indicate the debris avalanche deposits occurring in the northern and western Ischia offshore.

The Ischia Island lies on a volcanic ridge showing a mainly E-W trend. In the western offshore of the island, a strong field of magnetic anomalies has suggested the occurrence of a magmatic system, now inactive. Two main structural trends exist in the E-W trending volcanic ridge of the Ischia Island: one is E-W trending and the other is ENE-WSW trending, recognized especially in the western offshore of the Island of Ischia. To a regional scale, the comparison between the distribution of magnetic sources and the morpho-structures indicates a poor correlation for the E-W trending

60

morpho-structures and a high correlation for the ENE-WSW[16-18, 34,35,37,54,55].

The seismo-stratigraphic setting of Ischia Island has been shown by the geological interpretation of seismic sections located in the northern and western offshore of the island (**Figure 3**)[15,19]. Three categories of seismic units have been distinguished, including sedimentary seismic units (Sm1, Sm2; Sm3 and Sm4), volcanic seismic units (X1, X2, X3, X4 and Svi) and submarine slide units (da,da1, da2, da3, da4), as is shown in **Figure 3**. The sedimentary seismic units are represented by thick relict prograding wedges, probably in Late Pleistocene age, which have been crossed both parallelly (seismic line L32 in the lower part of **Figure 3**) and perpendicularly (seismic lines L27 and L34 in the upper and intermediate part of **Figure 3**) to the direction of progradation. On the other side, the volcanic seismic units are represented by thick volcanic deposits, constituting the acoustic substratum (X1 and X2 in the seismic profiles L27 and L32, located in the upper and lower part of **Figure 3**), sometimes revealing the occurrence of volcanic intrusions (X2 in the seismic profile L32 and Svi in the seismic profile L34). Submarine slide deposits appear to be emplaced during different phases, as evidenced by their complex stratigraphic architecture, suggesting at least four phases of emplacement in the western Ischia offshore, evidenced by the corresponding deposits (da1, da2, da3 and da4 in **Figure 3**).
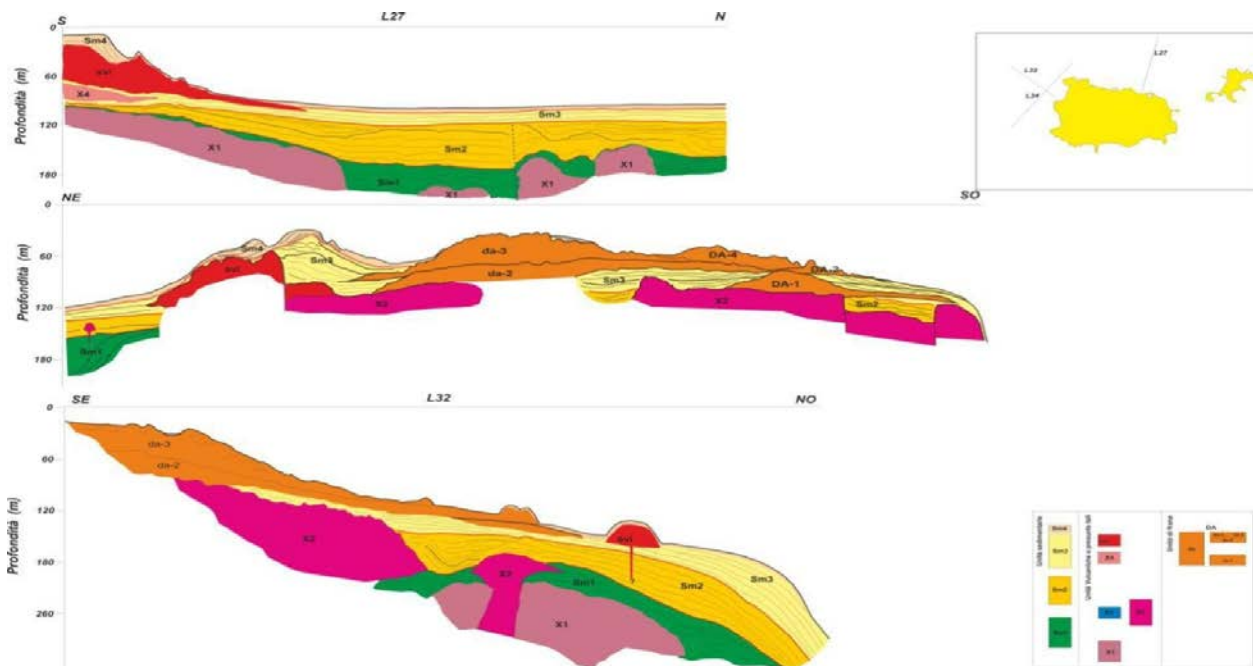

Figure 3. Stratigraphic sketch diagram showing the interpreted seismic sections in the Ischia offshore.

3.2 Geological map n. 502 Agropoli

Significant results have been obtained regarding the geological mapping of the Agropoli continental shelf located in the Northern Cilento Promontory (geological map n. 502 Agropoli). Its morpho-bathymetric setting has been outlined through the construction of four geological maps. One of them is herein shown in **Figure 4**. The map has represented a continental shelf deep up to 95 m with low gradients. In the north-eastern corner of the map, the Paestum Plain has been represented as well as the corresponding offshore sectors, which are characterized by low water depths, up to 35m. Proceeding southwards, the next physiographic unit is represented by the Agropoli promontory. In the corresponding offshore, the isobaths are convex and conditioned from the trending of the rocky shoreline, where the siliciclastic units pertaining to the Cilento Flysch crop out[56]. Another rocky promontory is distinguished between the Tresino Cape and the Pagliarolo Cape. It strongly controls the physiography of the submerged area. This area is characte-

61

rized by high coastlines and convex isobaths.

The geological units identified through the Agropoli geological map are represented by the rocky units of the substratum and the Quaternary marine deposits (**Figure 4**). And these deposits and corresponding acoustic substratum have been resumed in the **Table 3**.
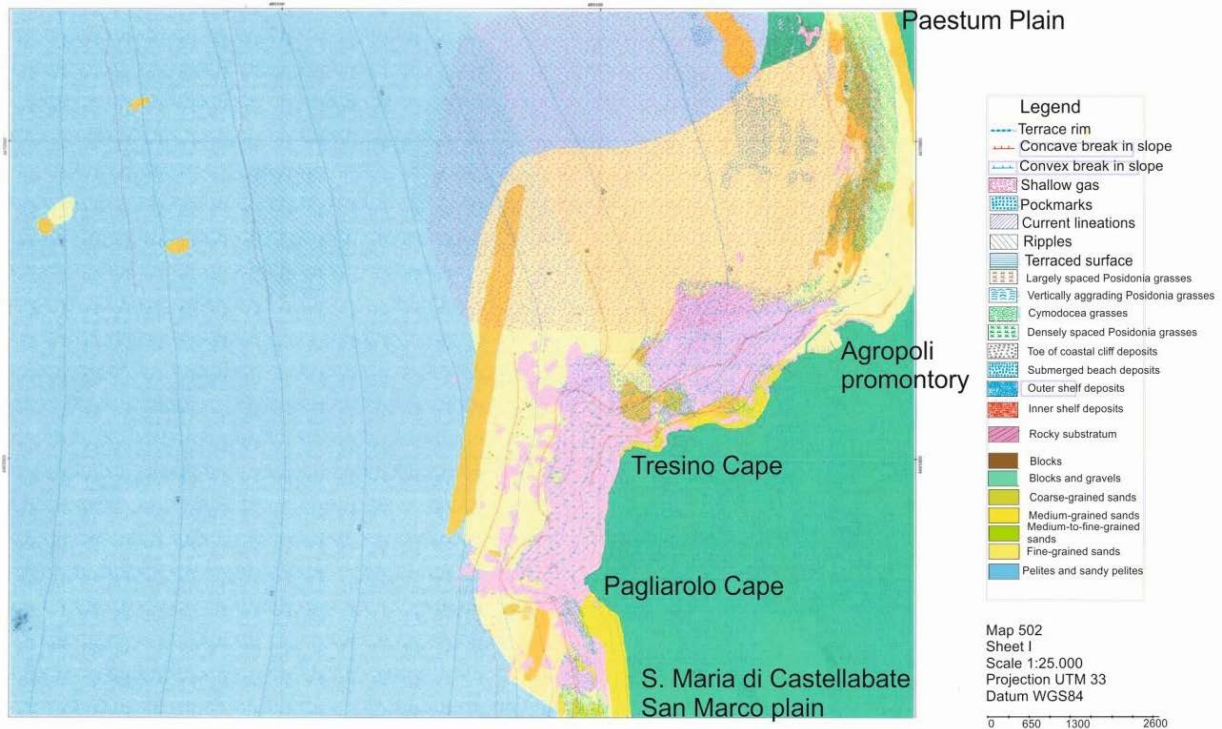

Figure 4. Example of geological map in the Agropoli offshore (southern Campania) to a 1:10, 000 scale.

Table 3. Depositional environments and corresponding deposits in the Agropoli offshore (Cilento Promontory, Campania).

Depositional environments	Deposits	Facies associations
Rocky units of the substratum	Cenozoic substratum	Siliciclastic deposits of the Cilento Flysch, cropping out at the sea bottom in correspondence with the morpho-structural high of the Licosa Cape. Marine terraces at the top of this unit corresponding with polycyclic erosional surfaces. Wide grasses of marine Phanerogams up to water depth of 30 m.
Littoral environment	Submerged beach deposits Toe of coastal cliff deposits	Gravels, sandy gravels and coarse-grained sands, with rounded to sub-rounded pebbles in a middle-to-fine-grained sandy matrix. Coarse-to-middle-grained sands, from rounded to sub-rounded, with gravels, pebbles and blocks. Siliciclastic heterometric blocks, from metric to decametric and siliciclastic heterometric gravels, from centimetric to metric.
Inner shelf environment	Inner shelf deposits Bioclastic deposits	Litho-bioclastic, coarse-grained sands, from well-sorted to poorly-sorted, medium-to-fine-grained litho-bioclastic sands and fine-grained pelitic sands. The sandy fraction is composed of bioclastic fragments. Occurrence of sandy ridges and current lineaments parallel to the isobaths. Heterometric gravels, gravelly sands and bioclastic sands, sometimes in a pelitic matrix, often located at the top of the outcrops of acoustic basement.

		Medium-to-fine-grained sands with lithoclasts and bioclasts and abundant rhyzoms of marine phanerogams, pelites and sandy pelites rich in small gastropods, vermetids and small mollusks. Occurrence of current lineaments.
Outer shelf environment	Outer shelf deposits Bioclastic deposits	Calcareous sands in an abundant pelitic matrix, overlying on the top of outcrops of acoustic basement.
Lowstand system tract	Lowstand deposits	Coarse-grained organogenic sands including abundant shell fragments and fragments of mollusks, echinid sand bryozoans, grading upwards into medium-grained sands and pelitic covers. These deposits form coastal wedges overlying the shelf margin progradations and represent portions of submerged beach linked to the last sea level lowstand.
Remnants Pleistocene of beach systems	Coarse-to-fine-grained marine deposits of well-sorted sands and gravels with bioclastic fragments and medium-to-fine-grained sands with a pelitic coverage	Pleistocene marine units representing relics of beach and continental shelf environments.

The Cenozoic substratum is composed of Cenozoic siliciclastic rocks, genetically related to the Cilento Flysch. This unit mainly crops out in the inner continental shelf, particularly offshore the Licosa Cape morpho-structural high and is terraced at its top by polycyclic erosional surfaces and covered by wide beds of marine phanerogams.

The littoral environment is characterized by the submerged beach deposits, including gravels, sandy gravels and coarse-grained sands, with rounded to sub-rounded pebbles in a middle-to-fine-grained sandy matrix, coarse to middle-grained sands, from rounded to sub-rounded, with gravels, pebbles and blocks. Moreover, the toe of coastal cliff deposits composed of siliciclastic heterometric blocks occur. The coastal cliffs are incised in the arenaceous successions of the Cilento Flysch[56].

The inner shelf environment is distinguished from inner shelf deposits and bioclastic deposits. The first ones are composed of coarse-grained litho-bioclastic sands, middle-to-fine-grained litho-bioclastic sands and fine-grained pelitic sands. The second ones are composed of heterometric gravels, gravel sands and bioclastic sands in a pelitic matrix.

The outer shelf environment is characterized by clastic deposits and bioclastic deposits. The first ones are composed of middle-fine-grained sands located at the top of wide outcrops of Cenozoic substratum, pelites and sandy pelites. The second ones are composed of bioclastic calcareous sands in a pelitic matrix organized as sedimentary drapes located at the top of outcrops of Cenozoic acoustic basement.

The lowstand system tract (LST) is characterized by coarse-grained organogenic sands, grading upwards into the middle-grained sands and the pelitic drapes. It is represented by the relict littoral deposits organized as coastal wedges overlying the shelf margin progradations. Moreover, they represent parts of submerged beaches related to the sea level low stand and related to the isotopic stage 2.

In conclusion, the Pleistocene relict marine units are represented by coarse-to-fine-grained marine deposits, probably composed of well-sorted sands and gravels with bioclastic sands and by medium-fine-grained sands, with a pelitic cover with a different thickness, but less than 2 m. These units have been mapped in the north-western and south-eastern sectors of the continental shelf and have been interpreted as the remnants of older beach systems, which are genetically related to the isotopic stages 4 and 3.

3.3 Description of the seismic units in the Agropoli offshore

Six seismo-stratigraphic units have been recognized on seismic profiles and are herein described in **Figure 5** (Units 3, 4, 5 and 6). They are separated by significant seismic reflectors, corresponding to regional unconformities and/or

correlative conformities in **Figure 5** (C; D; E). These seismo-stratigraphic units are underlain by an acoustically-transparent seismic unit, representing the acoustic basement in **Figure 5** (S unit).

The B50 seismic profile is composed of two successive acquisitions B50 and B50_1 in NNW-SSE trending and has been recorded at water depths ranging between 18.75 m (beginning acquisition) and 16.5 m (ending acquisition). The vertical penetration is about 100 msec (about 62 m). The sea bottom is covered by grasses with marine phanerogams widely occurring in this bathymetric belt. A terrace rim has been recognized at the top of the acoustic basement at water depths of 17 m (**Figure 5**). The seismo-stratigraphic units are herein described.

Unit 3: This unit is characterized by an acoustically-transparent seismic facies and by an irregular outer morphology. In particular, on the seismic line B50, it designs a palaeo-structural high (**Figure 5**). The base of this unit can not be recognized due to the occurrence of the sea bottom multiple (**Figure 5**). The top of this unit is represented by an irregular unconformity (namely the C unconformity), with landwards and onlaps on the S unit, corresponding with the acoustic basement (**Figure 5**).
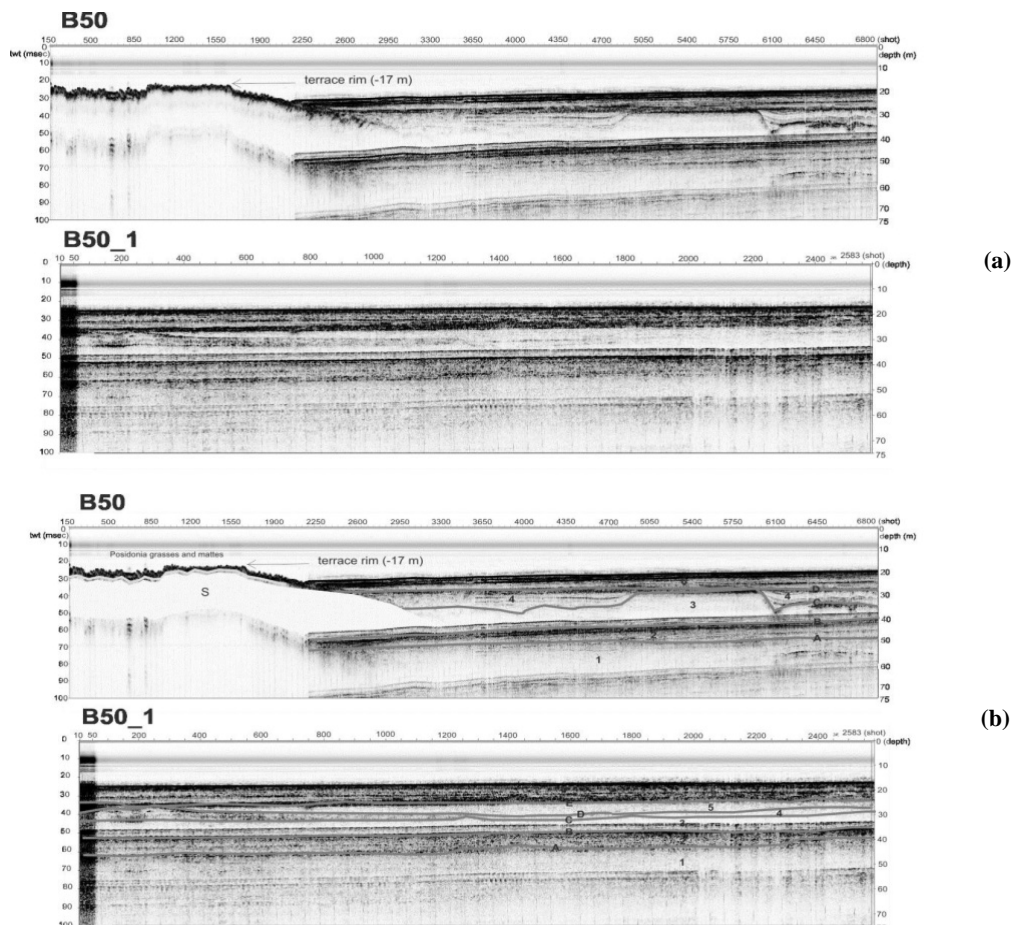

Figure 5. Subbottom chirp profiles B50 and B50_1 located in the Agropoli offshore and corresponding geologic interpretation.

Unit 4: This unit forms the filling of wide palaeo-channels located at the top of the underlying seismic unit and is characterized by discontinuous and sub-parallel seismic reflectors. Its top is marked by an erosional unconformity (D unconformity).

Unit 5: It has been recognized only on the chirp line B50_1 and is characterized by an acousti-cally-transparent seismic facies. Its top is characterized by a highly continuous seismic reflector (E unconformity). The outer geometry of the seismic unit suggests that it represents a wedge.

Unit 6: It is characterized by parallel and continuous seismic reflectors. It crops out at the sea bottom, being the most recent seismic unit. Its base

is represented by the D unconformity (seismic line B50) or alternatively, by the E unconformity (seismic line B50_1).

S acoustic basement is characterized by an acoustically-transparent seismic facies. It crops out at the sea bottom near shore (**Figure 5**). The strong scattering of the seismic signal in correspondence to the top of the S unit has been observed. A terrace rim should be suggested at water depths of 17 m.

The seismic profile B51 (**Figure 5**) extend as long as 6.1 kilometers in NNE-SSW trending and has been recorded in water depths ranging between –19.5 m (beginning of the acquisition) and –12 m (end of the acquisition). The vertical penetration of the studied section is of about 100 msec (64.5 m). A terrace rim has been recognized at water depths of 18 m, genetically related with the terrace rim recognized at 17 m of water depth on the seismic profile B50 (**Figure 5**). The following seismo-stratigraphic units have been recognized, separated by significant seismic reflectors corresponding with regional unconformities and/or paraconformities:

Unit 3 is characterized by an irregular outer morphology, delineating two palaeo-structural highs, bounded by three palaeo-channels, whose infill is represented by the seismic unit 4. The top of the seismic unit is represented by an irregular unconformity with different depths, deeper in correspondence to the palaeo-channels and shallower in correspondence to the palaeo-structural highs. Its base cannot be identified due to the occurrence of the sea bottom multiple. Shallow gas widely affects this seismic unit, making the seismic facies locally acoustically-transparent.

Unit 4 is characterized by parallel and discontinuous seismic reflectors, representing the infill of wide palaeo-channels. Geometric configurations of bidirectional onlaps may be seen. The top of the seismic unit corresponds with the D regional unconformity.

Unit 6 is characterized by parallel and continuous seismic reflectors, having a wedge-shaped external geometry.

S acoustic basement is distinguished from an acoustically-transparent seismic facies. A strong scattering of the acoustic signal has evidenced the occurrence of posidonia grasses and locally, posidonia mattes.

4. Discussion and conclusion

4.1 Ischia geological map

The geological evolution of the Ischia volcanic complex has been reconstructed based on recently acquired submarine seismic reflection data coupled with geological maps. The Ischia offshore is characterized by alkali-potassic volcanic rocks (trachytes, latites and alkali-basalts) erupted from a volcanic complex, whose activity lasted the last 55ky B.P. and was realized during four main phases. The first phase, older than 150 ky B.P., included the eruption of pyroclastic products and interstratified lava flows. The second phase (150-75 ky B.P.) controlled the rising of lava domes along extensional faults controlled by a strong tectonic activity and the eruption of pyroclastites. The third phase (55-20 ky B.P.) was dominated by the eruption of the Epomeo Green Tuffs, covering the coastal relief of the island and filling the Ischia graben. The fourth phase (10 ky B.P.-1302 A.D.) acted mainly in the Ischia graben, except the Zarolava flow.

The main seismic sequences of the Ischia offshore have been reconstructed. Interpreted seismic sections crossing submarine slide deposits and submarine canyon systems have been constructed based on seismic interpretation to improve the understanding of submarine features of the island offshore. The up-to-dated volcanology and stratigraphy of the onshore sectors have allowed to reconstructed a detailed geologic evolution of Punta Imperatore, Capo Negro, Maronti, Barano, Punta San Pancrazio and Ischia bank sectors[57-60]. New insights on the detailed seismo-stratigraphic setting and the geological transects located at Succhivo, Punta dello Schiavo, Spiaggia degli Inglesi and Cava dell'Isola) have recently been suggested through the geological interpretation of seismic profiles[35].

4.2 Agropoli geological map

Four seismo-stratigraphic units have been interpreted and correlated with Quaternary marine deposits which characterize the stratigraphic archi-

tecture of the continental shelf offshore the Cilento Promontory. The geological interpretation of these units is herein described. One of the most complete stratigraphic records of the Quaternary sequence and underlying acoustic basement, probably in Upper Miocene age, is offered from the seismic sections B50 and B50_1, crossing the inner Cilento continental shelf (**Figure 5**).

A tentative interpretation of the seismic units is herein proposed based on the acoustic facies detected on seismic profiles. Unfortunately, no core data or well lithostratigraphic data are available in the area to perform a quantitative interpretation in terms of lithology. Nonetheless, marine geological maps have been constructed in the same area. The data available for geological mapping included sea bottom samples which have been used for the calibration of the Sidescan Sonar acoustic facies, representing the base for the marine geological maps.

A sketch table has been constructed in order to show the seismic facies and the corresponding geologic interpretation studied in this paper (**Figure 6**).
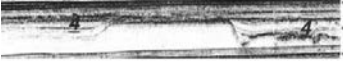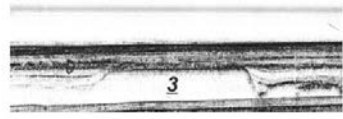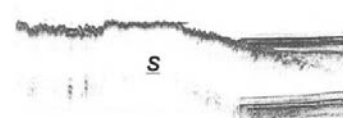

Seismic facies

6 Parallel and continuous seismic reflectors. Its base is represented by the D unconformity (seismic line B50) or alternatively, by the E unconformity (seismic line B50_1).

5 Acoustically-transparent seismic facies. The top is characterized by a highly continuous seismic reflector (E unconformity). Wedge-shaped external geometry.

4 Discontinuous and sub-parallel seismic reflectors. Geometric configurations of bidirectional onlaps.

3 Acoustically-transparent seismic facies. Irregular external morphology. The base of the seismic unit is marked by the B unconformity. The top of the seismic unit is represented by an irregular erosional unconformity (C unconformity).

2 Discontinuous and parallel seismic reflectors. The base of the unit is marked by the A unconformity. The top of the unit is represented by a highly continuous seismic reflector (B unconformity).
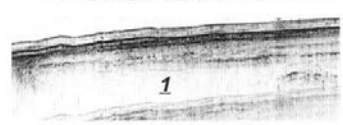
1 Low penetration of the seismic signal. The base of the seismic unit cannot be identified due to the penetration of the seismic profiles. The top of the seismic unit is represented by a highly continuous seismic reflector (A unconformity). Occurrence of fossil convex palaeo-morphologies.

S Acoustically deaf body characterized by a strong echo in correspondence to the surface of separation. Inclined reflectors laterally occur.

Geologic interpretation

Sixth seismo-stratigraphic unit of the Cilento continental shelf. Holocene marine deposits, probably representing the highstand system tract of the Late Quaternary depositional sequence.

Fifth seismo-stratigraphic unit of the Cilento continental shelf. It should be composed by sands, whose facies has been strongly influenced by the occurrence of gas. This unit occurs only locally. Due to its stratigraphic location it should represent the upper part of the transgressive system tract of the Late Quaternary depositional sequence (TST).

Fourth seismo-stratigraphic unit of the Cilento continental shelf. It has been interpreted as the filling of wide palaeo-channels, which have been created by the erosion in correspondence with the underlying unconformity. Due to its stratigraphic location it should represent the lower part of the transgressive system tract of the Late Quaternary depositional sequence (TST).

Third seismo-stratigraphic unit of the Cilento continental shelf. It should be represented by conglomerates derived from the erosion of the underlying Cilento Flysch. Its geological structure is represented by palaeo-structural highs. Occurrence of shallow gas pockets. These conglomerates are interstratified within the Late Quaternary depositional sequence.

Second seismo-stratigraphic unit of the Cilento continental shelf. It is probably represented by interlayered sands and shales of a coastal environment. Due to its stratigraphic location it should represent the upper part of the lowstand system tract of the Late Quaternary depositional sequence (LST).

First seismo-stratigraphic unit of the Cilento continental shelf. It is probably represented by sands with interstratified channel lobes. Due to its stratigraphic location it should represent the lower part of the lowstand system tract of the Late Quaternary depositional sequence (LST).

Rocky acoustic basement cropping out at the sea bottom or directly in the subsurface genetically related with the Cilento Flysch deposits.

Figure 6. Sketch table showing the seismic facies and the corresponding geologic interpretation in the Agropoli offshore (southern Campania)**.**

The unit 6 has been interpreted as the sixth seismo-stratigraphic unit of the Cilento continental shelf represented by Holocene deposits, i.e., the highstand system tract (HST) of the Late Quarternary depositional sequence (**Figure 6**).

The unit 5 has been interpreted as the fifth seismo-stratigraphic unit of the Cilento continental shelf, probably composed of sands, whose seismic facies have been strongly influenced by the occurrence of gas. A local occurrence of this seismic unit has been detected. Due to its stratigraphic location, the unit should represent the upper part of the transgressive system tract (TST) of the Late Quaternary depositional sequence (**Figure 6**).

The unit 4 has been interpreted as the filling of wide palaeo-channels occurring in correspondence to the underlying unconformity. Its stratigraphic

66

location suggests that it represents the basal part of the transgressive system tract (TST) of the Late Quaternary depositional sequence (**Figure 6**).

The unit 3 occurs as palaeo-structural highs, which was highly affected by shallow gas (**Figure 6**). It represents the third seismo-stratigraphic unit of the Cilento continental shelf, probably represented by conglomerates derived from the erosion of the underlying Cilento Flysch(S unit).

The S acoustic basement is depicted from an acoustically deaf body, characterized by a strong echo in correspondence to the surface of separation (**Figure 6**). Inclined reflectors laterally occur.

The acoustic basement underlying the Quarternary seismo-stratigraphic unit has been interpreted as genetically related with the Cilento Flysch. It widely crops out at the sea bottom and at the sub-bottom in areas surrounding the Cilento Promontory. The results of outcrops in the acoustic basement were wider than those previously mentioned in the Cilento area[61,62].

Ethics Statement

The author states that this manuscript complies with the ethical norm required.

Conflict of interest

No conflict of interest was reported by the author.

Acknowledgements

References

1. Cello G, Mazzoli S. Apennine tectonics in southern Italy: A review. Journal of Geodynamics 1998; 27(2): 191–211.

2. Critelli S. The interplay of lithospheric flexure and thrust accommodation in forming stratigraphic sequences in the southern Apennines foreland basin system, Italy. Rendiconti Lincei. Scienze Fisiche e Naturali 1999; 10(4): 257–326. doi: https://doi.org/10.1007/BF02904390.

3. Schiattarella M, Di Leo P, Beneduce P, *et al*. Quaternary uplift vs. tectonic loading: A case study from the Lucanian Apennine, southern Italy. Quaternary International 2003; 01-102: 239–251.

4. Catalano S, Monaco C, Tortorici L, *et al*. Neogene-Quaternary tectonic evolution of the southern Apennines. Tectonics 2004; 23(2): 1–19. doi: https://doi.org/10.1029/2003TC001512.

5. Rosenbaum G, Lister GS. Neogene and Quaternary rollback evolution of the Tyrrhenian Sea, the Apennines, and the Sicilian Maghrebides.Tectonics 2004; 23(1): 1–17. doi:10.1029/2003TC001518.

6. Ferranti L, Oldow JS. Latest Miocene to Quaternary horizontal and vertical displacement rates during simultaneous contraction and extension in the Southern Apennines orogen, Italy. Terra Nova 2005; 17(3): 209–214. doi:10.1111/j.1365-3121.2005.00593.x.

7. Caiazzo C, Ascione A, Cinque A. Late Tertiary-Quaternary tectonics of the Southern Apennines (Italy): New evidences from the Tyrrhenian slope. Tectonophysics 2006; 421 (1-2): 23–51.

8. De Alteriis G, Toscano F. Introduzione alla geologia dei mari circostanti le isole Flegree di Ischia, Procida e Vivara. In: Gambi MC, De Lauro M, Iannuzzi F (editors). Ambiente marino costiero e territorio delle isole flegree (Ischia Procida Vivara — Golfo di Napoli). Risultati di uno studio multidisciplinare; 2003. p. 3–26.

9. Budillon F, Violante C, De Lauro M. I fondali delle isole flegree: Geologia e morfologia. In: Gambi M, De Lauro M, Iannuzzi F (editors). Ambiente marino costiero e territorio delle isole flegree (Ischia Procida Vivara — Golfo di Napoli). Risultati di uno studio multidisciplinare; 2003. p. 45–66.

10. Budillon F, de Alteriis G, Ferraro L, *et al*. I fondali dell' Isolad' Ischia: Morfo-batimetria e geologiatra Punta del Chiarito e Punta San Pancrazio. In: Gambi MC, De Lauro M, Iannuzzi F (editors). Ambiente marino costiero e territorio delle isole flegree (Ischia ProcidaVivara — Golfo di Napoli). Risultati di uno studio multidisciplinare; 2003. p. 83–102.

11. Ferraro L, Molisso F. Sedimenti e associazioni a foraminiferi bentonici di settori selezionati della piattaforma continentale dell' isolad' Ischia. In: Gambi MC, De Lauro M, Iannuzzi F (editors). Ambiente marino costiero e territorio delle isole flegree (Ischia ProcidaVivara — Golfo di Napoli) Risultati di uno studio multidisciplinare; 2003. p. 67–82.

12. Aiello G, Marsella E, Passaro S. Submarine instability processes on the continental slopes off the Campania region (Southern Tyrrhenian sea, Italy):

The case history of the Ischia Island (Naples Bay). Bollettino di GeofisicaTeoricaApplicata 2009; 50: 193–207.

13. Putignano ML, Schiattarella M. Geomorfologia strutturale e domini di frattura dei fondali marini pericostieri dell' Isola di Procida (Campi Flegrei insulari, Italia meridionale). Il Quaternario 2010; 23(2): 229–242.

14. Biagio G, Cubellis E, Faccenna C, *et al*. Carta Geologica della Regione Campania, scala 1:10000, Foglio 464 Isola di Ischia, Note Illustrative. LAC Firenze: Regione Campania, Assessorato Difesa del Suolo; 2011.

15. Sbrana A, Toccaceli RM, Faccenna C, *et al*. Geologico 464 Isola d'Ischia della Carta 1:25.000 dell' I.G.M. ISPRA (Servizio Geologico d'Italia). Regione Campania, Settore Difesa del Suolo, Geotermia e Geotecnica; 2011.

16. Aiello G, Marsella E, Passaro S. Stratigraphic and structural setting of the Ischia volcanic complex (Naples Bay, Southern Italy) revealed by submarine seismic reflection data. Rendiconti Lincei 2012; 23: 387–408.

17. Aiello G, Marsella E. Interactions between Late Quaternary volcanic and sedimentary processes in the Naples Bay, southern Tyrrhenian Sea. Italian Journal of Geosciences 2015; 134 (2): 367–382. doi: 10.3301/IJG.2014.56.

18. Aiello G, Marsella E. Geological evolution of the Ischia volcanic complex (Naples Bay, Tyrrhenian Sea) based on submarine seismic reflection profiles. In: Rotonda T, Cecconi M, Silvestri F, *et al*. (editors). Proceedings Volcanic Rocks and Soils; London: Taylor and Francis Group; 2015. p. 305–312.

19. Aiello G. The geophysical and geological setting of Northern Ischia Island (Naples Bay, Southern Tyrrhenian Sea, Italy) based on high resolution seismic reflection profiles. In: Reimer A (editor). Horizons in world physics. New York: Nova Science Publishers; 2017. p. 53–85.

20. Aiello G, Marsella E. Marine geophysics of the Naples Bay (Southern Tyrrhenian Sea, Italy): Principles, applications and emerging technologies. In: Aiello G (editor). Geophysics: Principles, applications and emerging technologies. New York: Nova Publishers; 2016. p. 61–121.

21. Cassano E, La Torre P. Geophysics. In: Santacroce R (editor). Somma-Vesuvius. Roma: Quaderni De la Ricerca Scientifica; 1987.

22. Santacroce R (editor). Somma-Vesuvius. Roma: Quaderni De La Ricerca Scientifica; 1987.

23. Castellano M, Buonocunto C, Capello M, *et al*. Seismic surveillance of active volcanoes: The Osservatorio Vesuviano seismic network (OVSN, Southern Italy). Seismology Research Letters 2002; 73(2): 177–184.

24. Ongaro ET, Neri A, Todesco M, *et al*. Pyroclastic flow hazard assessment at Vesuvius (Italy) by using numerical modelling II: Analysis of local flow variables. Bulletin of Volcanology 2002; 64: 178–191.

25. Saccorotti G, Guido V, Vilardo G. Seismic swarms related to diffusive processes: The case of Somma-Vesuvius volcano, Italy. Geophysics 2002; 67(1): 199–203.

26. Scarpa R, Tronca F, Bianco F, *et al*. High-resolution velocity structure beneath Mount Vesuvius from seismic array data. Geophysical Research Letters 2002; 29(21): 1–4. doi 10.1029/2002GL015576.

27. Folk, RL. The distinction between grain size and mineral composition in sedimentary rock nomenclature. The Journal of Geology 1954; 62(4): 344–359.

28. Catalano R, Bartolini C, Fabbri A, *et al*. Norme generali delle line guida di rilevamento geologico nelle aree marine da sottoporre al Servizio Geologico Italiano - Rapporto finale. Commissione di studio per la cartografiag eologica marina; 1996.

29. Aiello G, Budillon F, Cristofalo G, *et al*. Marine geology and morpho-bathymetry in the Bay of Naples (South-Eastern Tyrrhenian Sea, Italy). In: Faranda FM, Guglielmo L Spezie G (editors). Mediterranean ecosystems: Structures and processes. Napoli: Springer-Verlag Italia; 2001. p. 1–8.

30. D'Argenio B, Aiello G, De Alteriis G, *et al*. Digital elevation model of the Naples Bay and surrounding areas (Eastern Tyrrhenian Sea). In: Mapping Geology in Italy. Atlante di Cartografia Geologica, Convegno Internazionale "Firenze 2004".

31. Aiello G, Marsella E, Passaro S. Stratigraphic and structural setting of the Ischia volcanic complex (Naples Bay, southern Italy) revealed by submarine seismic reflection data. Rendiconti Lincei.2012; 23: 387–408.

32. Aiello G, Marsella E, Di Fiore V. New seismo-stratigraphic and marine magnetic data of the Gulf of Pozzuoli (Naples Bay, Tyrrhenian Sea, Italy): Inferences for the tectonic and magmatic events of the Phlegrean Fields volcanic complex (Campania). Marine Geophysical Research 2012; 33: 97–125.

33. Aiello G, Angelino A, D'Argenio B, *et al*. Buried volcanic structures in the Gulf of Naples (Southern Tyrrhenian Sea, Italy) resulting from high resolution magnetic survey and seismic profiling. Annals of Geophysics 2005; 48(6): 883–897.

34. Passaro S, de Alteriis G, Sacchi M. Bathymetry of Ischia Island and its offshore (Italy), scale 1:50.000. Journal of Maps 2016; 12 (1): 152–159. doi:10.108 0/17445647.2014.998302.

35. Aiello G. New insights on the Late Quaternary geologic evolution of the Ischia Island coastal belt based on high resolution seismic profiles. Italian Journal of Geosciences 2017; 137(1): 87–106. doi: 10.3301/IJG.2017.19.

36. Aiello G, Insinga DD, Iorio M, *et al*. On the occurrence of the Neapolitan Yellow Tuff tephra as a stratigraphic marker in the Southern Gaeta Bay (Eastern Tyrrhenian Margin, Italy). Italian Journal of Geosciences 2017; 136(2): 263–274.

37. Passaro S, Sacchi M, Tamburrino S, *et al*. Fluid

vents, flank instability and seafloor processes along the submarine slopes of the Somma-Vesuvius Volcano, Eastern Tyrrhenian Margin. Geosciences 2018; 8(2): 60. doi:10.3390/geosciences8020060.

38. Chang KH. Unconformity-bounded stratigraphic units. GSA Bulletin. 1975; 86(11): 1544–1552.

39. Mitchum RM, Vail PR, Sangree JB. Stratigraphic interpretation of seismic reflection patterns in depositional sequences. In: Payton CE (editor). Seismic Stratigraphy — Applications to Hydrocarbon Exploration 1977; 26: 117–133.

40. Nummendal D, Swift DJP. Transgressive stratigraphy at sequence-bounding unconformities: Some principles derived from Holocene and Cretaceous examples. In: Nummedal D, Pilkey OH, Howard JD (editors). Sea level fluctuation and coastal evolution. SEPM Special Publication; 1987. p. 241–260.

41. Galloway WB. Genetic stratigraphic sequences in basin analysis I: Architecture and genesis of flooding surface bounded depositional units. AAPG Bulletin. 1989; 73(2): 125–142.

42. Sacchi M, Horvath F, Magyari O. Role of unconformity-bounded units in the stratigraphy of the continental record: A case study from the Late Miocene of the western Pannonian Basin, Hungary. Geological Society of London Special Publications 1999; 156(1): 357–390.

43. Catuneanu O. Principles of sequence stratigraphy. 1st ed. Elsevier Science Ltd.; 2006. p. 1–386.

44. Rossi M, Mosca P, Polino R, et al. New outcrop and subsurface data in the Tertiary piedmont basin (NW Italy): Unconformity-bounded stratigraphic units and their relationships with basin-modification phases. Rivista Italiana di Paleontologia e Stratigrafia 2009; 115(3): 305–335.

45. Tibaldi A. A new geological map of Stromboli volcano (Tyrrhenian Sea, Italy) based on application of lithostratigraphic and UBS units. Geological Society of America Bulletin 2010; 464: 33–49.

46. Catuneanu O, Bhattacharya JP, Blum MD, et al. Sequence stratigraphy: Common ground after three decades of development. Stratigraphy 2010; 28: 21–34.

47. Zecchin M, Catuneanu O. High-resolution sequence stratigraphy of clastic shelves I: Units and bounding surfaces. Marine and Petroleum Geology 2013; 39: 1–25.

48. Fabbri A, Argnani A, Bortoluzzi G, et al. Carta geologica dei mari italiani alla scala 1:250.000 — Guida al rilevamento. Quaderni serie III. Servizio Geologico Italiano; 2002. p. 8.

49. Helland-Hansen W, Gjelberg JG. Conceptual basis and variability in sequence stratigraphy: A different perspective. Sedimentary Geology 1994; 92: 31–52.

50. Posamentier HW, Erskine RD, Mitchum RM. Models for submarine-fan deposition within a sequence — Stratigraphic framework. In: Seismic facies and sedimentary processes of submarine fans and turbidite systems; New York: Springer; 1991. p. 127–136.

51. Posamentier HW, Allen GP. Variability of the sequence stratigraphic model: Effects of local basin factors. Sedimentary Geology 1993; 86: 91–109.

52. Trincardi F, Correggiari A, Roveri M. Late Quarternary trasgressive erosion and deposition in a modern epicontinental shelf: The Adriatic semienclosed basin. Geomarine Letters 1994; 4: 41–51.

53. Posamentier HW, Vail PR. Eustatic controls on clastic deposition II — Sequence and systems tract models. In: Wilgus CK, Hastings BS, Kendall CG (editors). Sea level change — An integrated approach. Tulsa: SEPM Special Publication; 1988. p. 125–154.

54. Bruno PPG, De Alteriis G, Florio G. The western undersea section of the Ischia volcanic complex (Italy, Tyrrhenian Sea) inferred from marine geophysical data. Geophysical Research Letters 2002; 29 (9): 1343. doi:10.1029/2001GL013904.

55. Passaro S. Integrazione di datimagnetici e morfobatimetrici in aree marine vulcaniche e non Vulcaniche. Tesi di Dottorato di Ricerca in Scienze ed Ingegneria del Mare, Università degli Studi di Napoli "Federico II"; 2005.

56. Bonardi G, Amore FO, Ciampo G, et al. Il Complesso Liguride Auct: Stato delle conoscenze e problem aperti sull'evoluzione pre-appenninica ed i suoi rapporti con l'Arco Calabro. Memorie della Società Geologica Italiana 1992; 41: 17–35.

57. Vezzoli. Island of Ischia. Quaderni de La Ricerca Scientifica 1988; 114 (10): 230.

58. Orsi G, De Vita S, Di Vito MA, et al. The Neapolitan active volcanoes (Vesuvio, Campi Flegrei, Ischia): Science and impact on human life. 32nd International Congress "Firenze 2004", Field Trip Guidebook B 28; 2004.

59. Brown RJ, Orsi G, De Vita S. New insights into Late Pleistocene explosive volcanic activity and caldera formation on Ischia (Southern Italy). Bulletin of Volcanology 2008; 70: 583–603.

60. Aiello G, Marsella E. The Southern Ischia canyon system: Examples of deep sea depositional systems on the continental slope off Campania (Italy). Rendiconti Online della Società Geologica Italiana 2014; 32: 28–36.

61. Coppa MG, Madonna M, Pescatore TS, et al. Elementi geomorfologici e faunistici del margine continentale tirrenicotra Punta Campanella e Punta degli Infreschi (Golfo di Salerno). Memorie della Società Geologica Italiana 1988; 41: 541–546.

62. Ferraro L, Pescatore T, Russo B, et al. Studi di geologia marina sul margine tirrenico: la piattaforma continentale tra Punta Licosa e Capo Palinuro (Tirreno meridionale). Bollettino della Società Geologica Italiana 1997; 116: 473–48.

ORIGINAL RESEARCH ARTICLE

The effects of mobile thermal power plants on air quality in Turkey

Andaç Akdemir[*], Osman Nuri Ergun

Department of Environmental Engineering, Ondokuz Mayis University, Samsun 55200, Turkey; Tel: +903623121919 (1324); E-mail: aakdemir@omu.edu.tr

ABSTRACT

In this study, daily averages of air quality parameters were measured in two stations (S1 and S2) of the organized industrial district in Samsun. The meteorological variables were measured at only one station (S1), such as temperature, relative humidity, wind speed, solar radiation, and ambient pressure in 2007, and the daily promised limit for nitrogen dioxide has been especially exceeded at 206 times for 1st station. However, exceeds of the limit value in 2006 for 1st station was reduced by approximately 3.5 times. The daily nitrogen dioxide concentration did not exceed the daily limit of WHO[1] as for 2nd station. The results obtained showed that under the influence of dominant wind direction, the second station measurement results are higher than that of the first station. To determine all of the possible environmental effects, the measurements should be analyzed from a multi-point perspective.

Keywords: Mobile; Power Plant; Ambient Air Quality; Samsun

1. Introduction

Fossil-fuelled power plants have been supplying electricity for industrial use since the late 1880s[2]. In thermal power plant, the heat used for boiling the water is obtained by burning a fossil fuel, where the heat is delivered by the exhaust of a gas turbine[3]. Conventional fossil-fuel power plants are the major source of industrial air pollution and major gaseous pollutants emitted are carbon monoxide (CO), sulphur dioxide (SO_2), nitrogen dioxides (NO_x), and certain hydrocarbons and volatile organic compounds (VOC_s)[4]. The main fuel types used in industries are fuel oil, lignite, liquefied petroleum gas, natural gas, and others (wood, biomass, petroleum coke, biogas) in the developing countries[5,6].

No. 6 fuel oil (also called Bunker C oil or residual fuel oil) widely used in Thermal Power Plant in developing countries is the residuum from crude oil after naphtha-gasoline, whereas No. 1 fuel oil and No. 2 fuel oil have been removed. No. 6 fuel oil can be blended directly to heavy fuel oil or made into asphalt. Residual fuel oil is more complex in composition and impurities than distillate fuels. Polycyclic aromatic hydrocarbons (including the alkylated derivatives) and metal-containing constituents are components of No. 6 fuel oil[7]. **Table 1** lists the details of the illustrative analysis of typical residual oil (No.6). The sulphur in heavy fuel oil (No.6) contributes significantly to the particulate emissions by virtue of its oxidation and combination with water to generate sulphates, which bind together with the soot to increase the emissions[8].

Table 1. Typical properties of residual oil

Parameters	Fuel oil (No.6)
ASTM maximum kinematic viscosity, cs	50 (212º F)
ASTM water and sediment, max. vol.%	2.0
Specific gravity, 60/60º F (15.5º C)	0.986
Carbon residue, %	12.0
Ash, wt%	0.10
Netheating value, Btu/lb (kcal/kg)	17.677 (9.821)
Sulfur, wt%	2.7
Oxygen, wt%	0.62
Nitrogen, wt%	0.32
Hydrogen, wt%	10.5

The annual installed capacities of Turkey are composed of 66.8% thermal, 32.8% hydroelectric and 0.4% geothermal and wind energy, respectively. Turkey's primary energy sources include hard coal, lignite, fuel oil, natural gas, hydro, geothermal, wood, animal and plant wastes, solar, as well as secondary energy sources like coke briquettes[9]. The distribution of installed capacity by primary energy resources are 5.3% for hard coal and asphaltite, 18.3% for lignite, 3.7% for fuel oil, 0.1% for diesel oil, and 26.4% for natural gas in Turkey[10]. Thermal power plants (with a total installed power capacity of 12808.9 MW) in Turkey are generally used to meet the electricity demand as seen in **Table 2**.

Table 2. Thermal power plants in Turkey[10]

Name of power plant	Location	Fuel type	Total capacity (MW)	Type of unit
Çatalağzı	Zonguldak	Hard coal	3,000	Steam
Afşin-Elbistan A	K. Maraş	Lignite	13,550	Steam
Afşin-Elbistan B	K. Maraş	Lignite	14,400	Steam
Çan	Çanakkkale	Lignite	3,200	Steam
Kangal	Sivas	Lignite	4,570	Steam
Orhaneli	Bursa	Lignite	2,100	Steam
Seyitömer	Kütahya	Lignite	6,000	Steam
Tunçbilek A	Kütahya	Lignite	650	Steam
Tunçbilek B	Kütahya	Lignite	3,000	Steam
Ambarlı	İstanbul	Fuel oil No.5/No.6	6,300	Steam
Hopa	Artvin	Fuel oil No.4	500	Steam
Çukurca	Hakkari	Diesel oil	10	Internal combustion
Ambarlı KÇ	İstanbul	Natural gas	13,509	Combined cycle
Bursa KÇ	Bursa	Natural gas	14,320	Combined cycle
Aliağa GT+KÇ	İzmir	Natural gas	1,800	Combined cycle
Hamitabat KÇ	Kırkale	Natural gas	1,1200	Combined cycle
Soma A	Manisa	Lignite	440	Combined cycle
Soma B	Manisa	Lignite	9,900	Steam
Kemerköy 1,2,3	Muğla	Lignite	6,300	Steam
Yatağan	Muğla	Lignite	6,300	Steam
Yeniköy	Muğla	Lignite	4,200	Steam
Samsun 1	Samsun	Natural gas	2,400	Combined cycle

2. Experimental protocols

2.1 Site description

The organized industrial district (OID) in the present study located (41º14′51″ N-41º13′21″ N; 36º25′57″ E-36º28′57″ E) at Tekkekoy in Samsun as seen in **Figure 1**. OID is situated at a distance of 12 km in the east from city center of Samsun. There are small and medium scale units of industries and big scale units of several industries in this area.

Figure 1. Location of the monitoring site and air pollutant of sources in the map of Orion-ME (from Google Earth)**.**
Note: MS1:1st Measurement Station; MS2: 2nd Measurement Station; TP1: Thermal Power Plant 1; TP2: Thermal Power Plant 2**.**
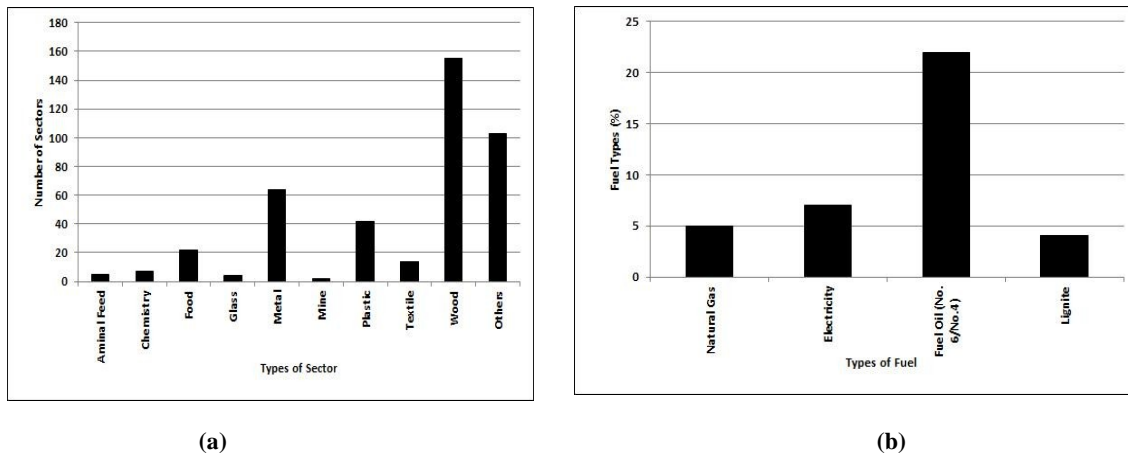

(a)

(b)

Figure 2. The percent of industries according to type sectors **(a)** and using fuel **(b)** OID in Samsun**.**

The types of fuel used for the plants in the industrial regions are as follows: natural gas (33%), electricity (59%), fuel oil of No.4 and No.6 (5%) and lignite (3%) as seen in **Figure 2b**. Natural gas and electricity are the primary fuel type in the organized industrial region.

The mobile power plants are situated about 14 Km North East of Samsun. The power plant selected for the study was 262 MW fuel oil (No.6) fired-power plant with totally two units (131 and 131 MW). The fuel oil type used in mobile power plants located in Samsun is fuel oil No. 6 in residue fuel oil obtained from İzmir Refinery of Tupras Turkey Petroleum Co. The total sulfur content of residue fuel oil was % 2.8 by weighing[11,12].

Petroleum fuels, named fuel oil NO. 6, which

are residual fuels, are used in the mobile power plants. The total fuel oil-feed consumption in the mobile power plants are approximately 1168.49 ton/day (610.60 and 557.89 ton/day)[12]. The average properties of the fuel-oil in the mobile power plant in Samsun are given in **Table 3**[12,13]. The mobile power plants were operated from 1 August 2007 to 16 February 2008. In this study, the air quality data were collected from observational station St-1 from April 2006 to April 2008 and from observational station St-2 from August 2007 to April 2008.

Table 3. Properties of fuel oil in the mobile power plant in Samsun[12]

Parameters	MPP-1 (Samsun-1)	MPP-1 (Samsun-2)
	Fuel oil (No.6)	Fuel oil (No.6)
Sulfur (%)	2.74	2.74
Ash (%)	-	0.042
Lower heating value (Kcal/kg)	9850	9,850
Fuel Consumption (ton/day)	610,60	55,789

2.2 Meteorological data

All meteorological data for 1st station was measured by using meteorological sensors produced by Lastem Company. Fifteen minutes surface meteorological data recorded at the 1st station at fifteen minute intervals include wind speed and direction, air temperature, relative humidity, barometric pressure, and solar radiation. Meteorological data were collection started on 1 April 2006 and ended on 15 November 2007 as seen in **Figure 3a**. Meteorological sensors were placed on the top of air quality measurement vehicle and 4.5 m on the surface of the ground for 1st measurement station. All data were recorded at fifteen minutes intervals.

2.3 Pollutant data for station-1 (S1)

The sensor of air quality parameters were placed on the top of air quality measurement vehicle and 4.5 m on the surface of the ground (**Figure 3a**). Measurements were made continuously during every 15 minutes and ninety-six data values were collected daily. The instruments were calibrated at least eight times in a year by using calibration gases. Calibration of the ozone analyzer was done regularly with the help of a built-in ozone generator. A sulfur dioxide is measured using an analyzer AF 22 M of Environment S.A. (France) based on absorption of UV Fluorescence Method. The minimum detection limit of the analyzer is about 1 ppb and its response is about 10 s. The linearity is reported as ±1 % of F.S (Environment S.A. France). Nitrogen Oxides (NO, NO_X, NO_2) are measured using an analyzer AC 32M of Environment S.A. based on Chemiluminescence Method. The minimum detection limits of the analyzer are reported to be about 0.2 ppb (response time 30 s.). A Carbon monoxide is measured using an analyzer CO 12M of Environment S.A. (France) based on absorption of infrared light. The minimum detection limits of the analyzer are reported to be about 50 ppb (response time 30 s). A particulate matter was measured by using an analyzer PM 101M of Environment S.A. (France) based on the absorption of beta radiation by matter. The minimum detection limits of the analyzer are reported to be about 0.5 $\mu g.m^{-3}$.

2.4 Pollutant data for station-2 (S2)

The sensor of air quality parameters were placed approximate 2.5 m on the surface of the ground (**Figure 3b**). A sulfur dioxide is measured using an analyzer 100 EH of Teledyne API (USA) based on absorption of UV Fluorescence Method. The minimum detection limit of the analyzer is about 1 ppb and its response is about 30 s. The linearity is reported as ± 1% of F.S. Nitrogen Oxides (NO, NO_X, NO_2) are measured using an analyzer 200E of Teledyne API based on Chemiluminescence Method. The minimum detection limits of the analyzer are reported to be about 0.4 ppb. A carbon monoxide is measured using an analyzer 300E of Teledyne API based on absorption of infrared light. The minimum detection limits of the analyzer are reported to be about 40 ppb. A

particulate matter is measured by using an analyzer PM 101 M of Teledyne API based on the absorption of beta radiation by matter. The minimum detection limits of the analyzer are reported to be about 0.5 $\mu g.m^{-3}$.

Figure 3. The 1st and 2ed ambient air quality measurement stations, S1 **(a)** and S2 **(b).**

3. Results and discussion

The average yearly temperature, relative humidity, and solar radiation are 15.3 ± 6.6 $^{\circ}$C, 77.3 ± 17.8 %, and 154.19 ± 253.7 $W.m^{-2}$ respectively. The average annual of wind speed is 1.11 ± 0.78 $m.s^{-1}$. At a height of 4.5 m, wind speed recorded was always less than 8.9 $m.s^{-1}$. The wind speeds well around 1-2 $m.s^{-1}$ during the day and almost 0.1-1.2 $m.s^{-1}$ during the night. North (N) and Northwest (NW) were found out to be dominating wind direction as seen in **Figure 4**.

The removal rate of the pollutants by the wind is supposed to be proportional to the sum of the projection of the effective wind direction, and on the pollutant concentration[14].

The wind speed has reached the highest values between July and August according to the daily average total 518 values in 2006 and 2007 (**Figure 4**). An average monthly of the wind speed increased for July and August of about 2-2.5 $m.s^{-1}$.

The wind speed was also decreased for an increase in NO_2, higher decrease of carbon monoxide (CO), particulate matter (PM), and sulfur dioxide (SO_2) during July and August 2006. A Nitrogen dioxide (NO_2) increased during July and August 2006, while carbon monoxide (CO), particulate matter (PM), and sulfur dioxide (SO_2) were also decreased, with higher wind speed during July and August 2006[14].

In this period, the prevailing wind direction is northwest and northeast of the measurement points covering the region thought to be caused by the increase of large-scale industrial facilities. In 2007, the wind speed is higher in July and August signifies east tending the prevailing wind direction is south. During this period, the increase in the amount of CO and SO_2 was observed.
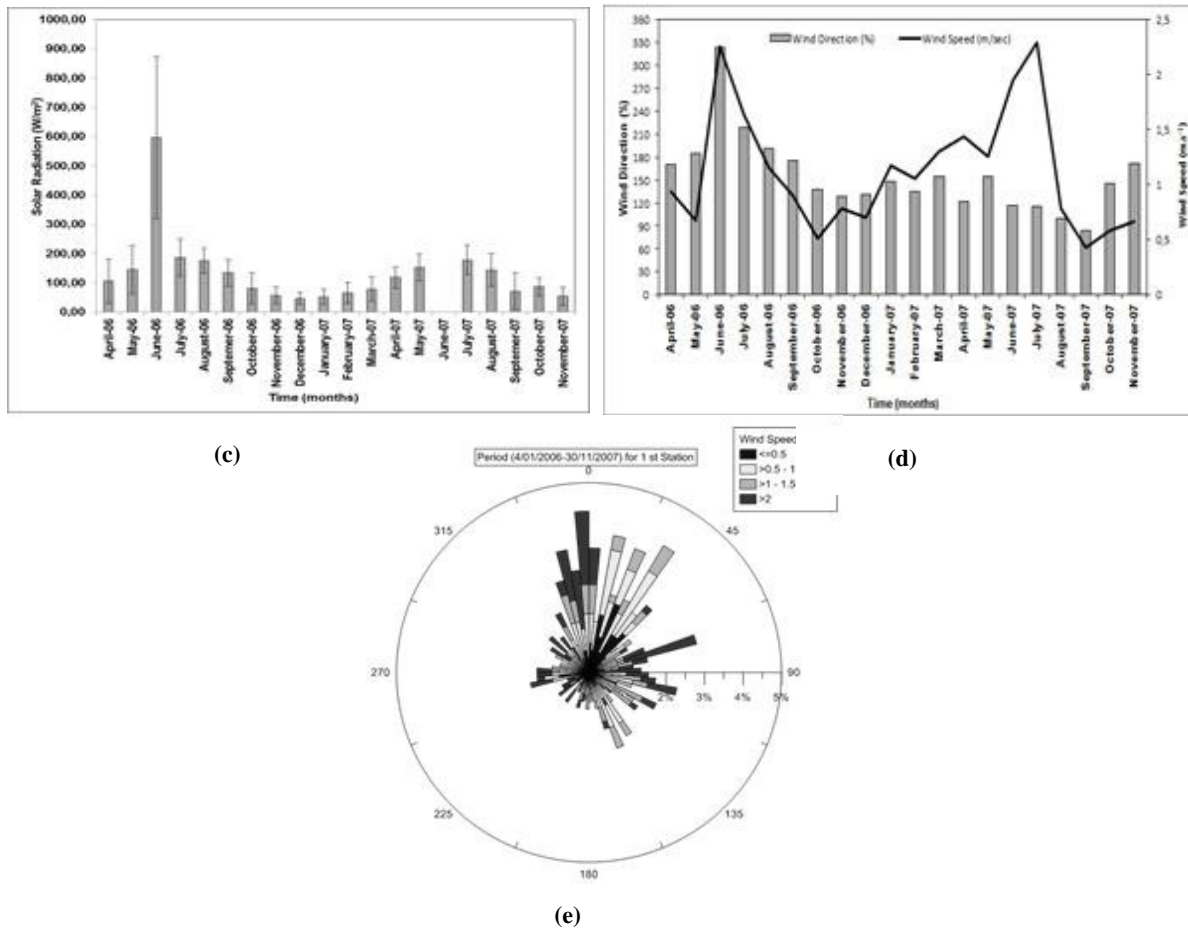

(a)

(b)

(c)

(d)

(e)
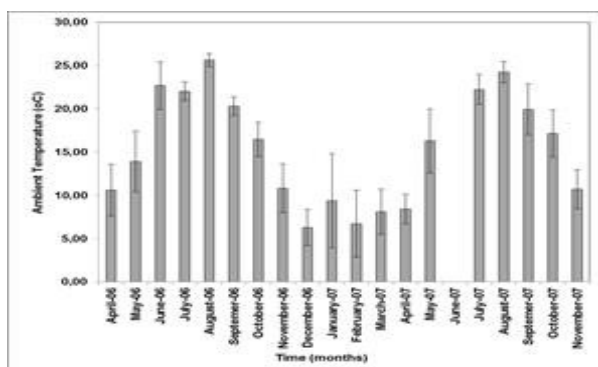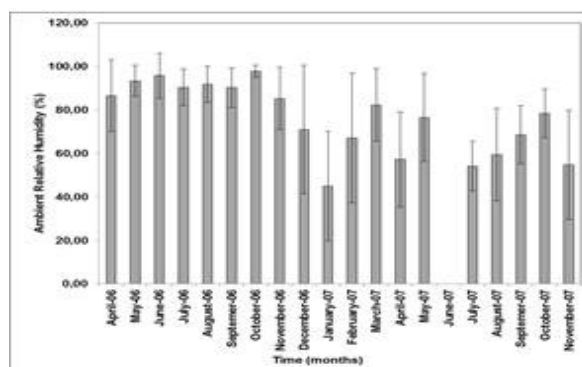
Figure 4. The ambient air temperature (**a**), ambient relative humidity (**b**), solar radiation (**c**), dominant wind direction (**d**), and wind speed (**e**) for in the 1st station.

3.1 Carbon monoxide

The carbon monoxide measurements were only carried out July to December mounts as seen in **Figure 5**. When between these mounts measured, carbon monoxide values are examined, and carbon monoxide values in second situation was higher than that in first situation, but it was seen that European Union limit values did not exceeded in both the situations as seen in **Table 4**. Carbon monoxide at the 1st station was measured lower when thermal power plant was operated. During the same period, Carbon monoxide at the 2nd station was measured lower than 1st station. The reason is that the predominant wind direction was southwest from August to December.

3.2 Particulate matter

The measurements of particulate matter at the 1st station were higher than 2nd station between July and December and the limit values have exceeded

(**Figure 5**). This situation shows that the increases in particulate matter in the area are higher than sulfur dioxide, and while the mobile station has operated, the measured values have exceeded the limits (**Table 4**).

Daily average values of PM between the months of April to July in 2007 showed a decrease from the previous year, and this is thought to result from the prevailing wind direction. In addition, in the two measuring stations, PM value of the second measurement station was higher from August to November 2007. That is because the second measurement station lies in the vicinity of industrial coal screening, crushing plants or the Samsun high-way vehicles from the Army.

3.3 Nitrogen oxides

In terms of nitrogen oxides, the limit values were not exceeded during all the year, but results of measurement in the 2nd station are higher than first situation when July to December is compared

75

(**Figure 5**). Although the annual limit is not exceed in the first station, the hourly limit values of European Union were exceed especially for nitrogen dioxide 733 times in 2006 and 206 times in 2007 as seen in **Table 4**.

Nitrogen dioxide — NO_2 time series analysis shows that NO_2 concentrations measured during spring are higher than those observed during autumn for station-1 in 2006. While the mobile power plant was operating, an increase of approximately 136 % in NO_2 concentrations was observed in relation to previous year in the autumn of 2007 and an increase approximately 370 % in total NO_x concentration was observed according to previous year in the autumn of 2007.

Thermal power plants are operating in NO_2 values between August and December in 2007 according to the same period in 2006 increased by first station. However, considering the wind direction, the prevailing wind direction is south, while it turns to be east tending for the period of August to December. Thus, in 2007, an increase of NO_2 is fully rooted in thermal power plants because the southeast wind pollutant is provided transport to the Black Sea. According to research done throughout the year in 2007, there was a reduction of NO_2.
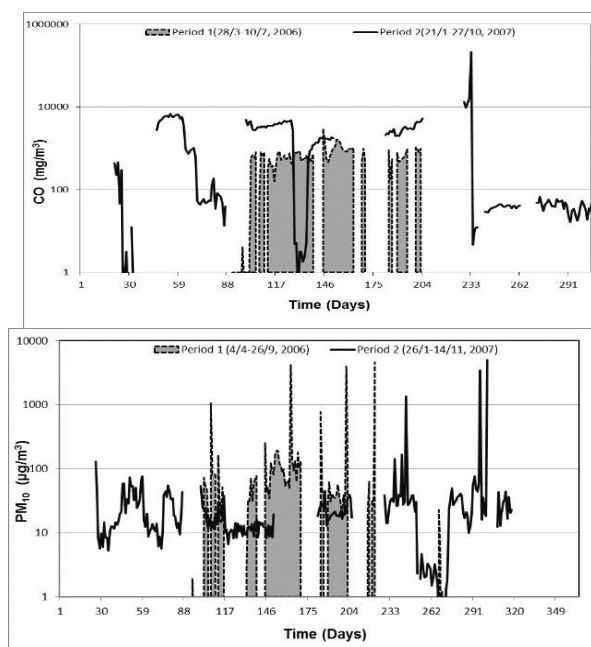
3.4 Sulfur dioxide

The measurements at the 1st station were continued from April 2006 to November 2007 as seen in **Figure 6a**. The measurements at the 2nd station had continued until July 2007 to December 2007. After the mobile power plant operated again in July 2007, the sulfur dioxide at the 1st station was increasing in proportion to the previous year. But the sulfur dioxide at the 1st and 2nd station did not overcome upon 70 $\mu g/m^3$ between July and December and the measurements at the 1st station for 2006 and 2007 between July and December was higher than 2nd station. The reason for this was that the wind direction at the 1st station was northeasterly (NE) despite the wind direction was southern west (SW) at 2nd station. The sulfur dioxide measurement at the 2nd station was not received any day over European Union limit values (**Table 4**). The limit values were exceeded only one day at the 1st station in 2007.

Measurements of SO_2 thermal power station is operating in 1st August to December, 2007, with period increased slightly from the previous year. Comparison could not be made due to technical problems and measurements of SO_2 level. Compared with the daily SO_2 levels between 09/25/2007 and 10/16/2007, 1st station 2nd station data and the prevailing wind direction are higher than that measured in the southeast.
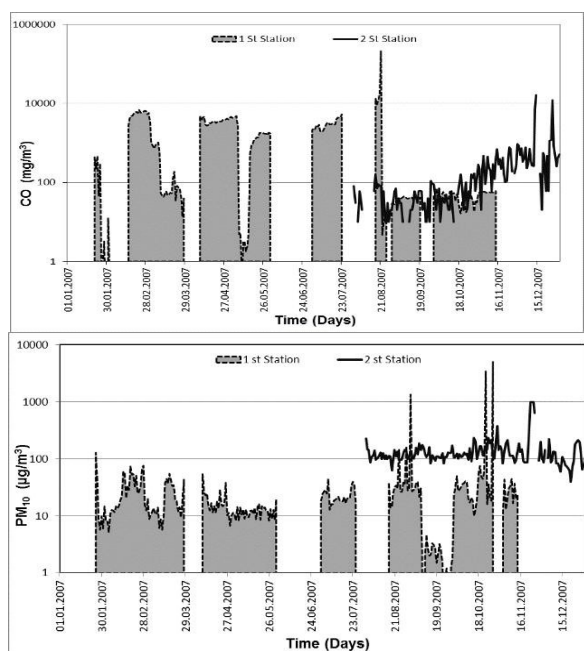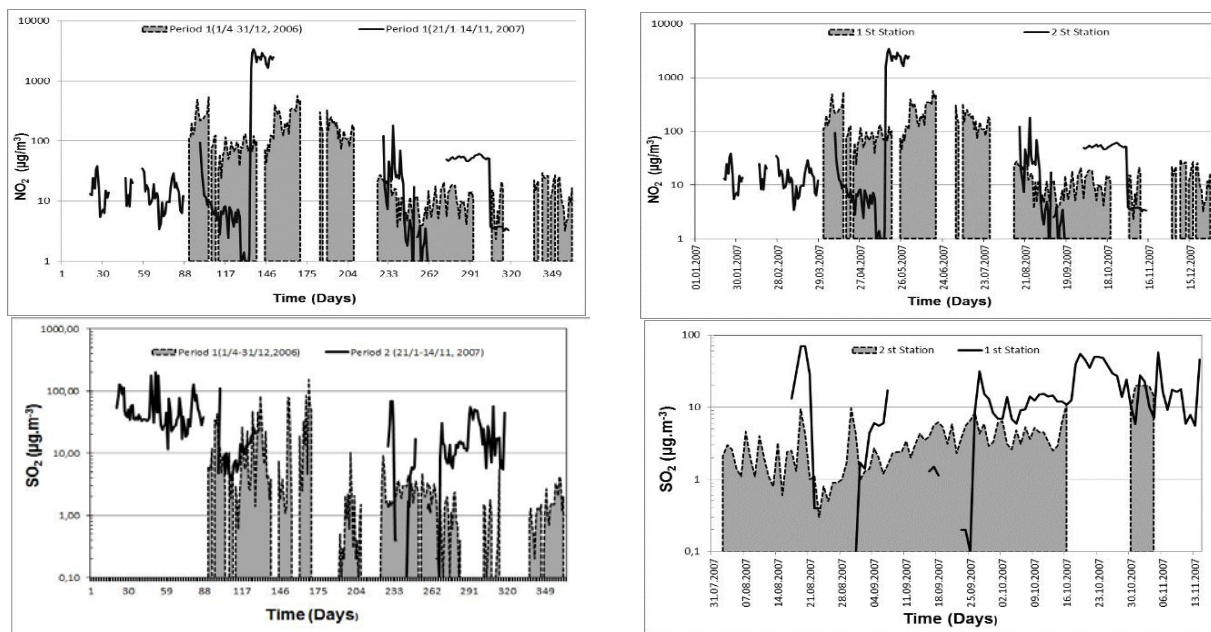
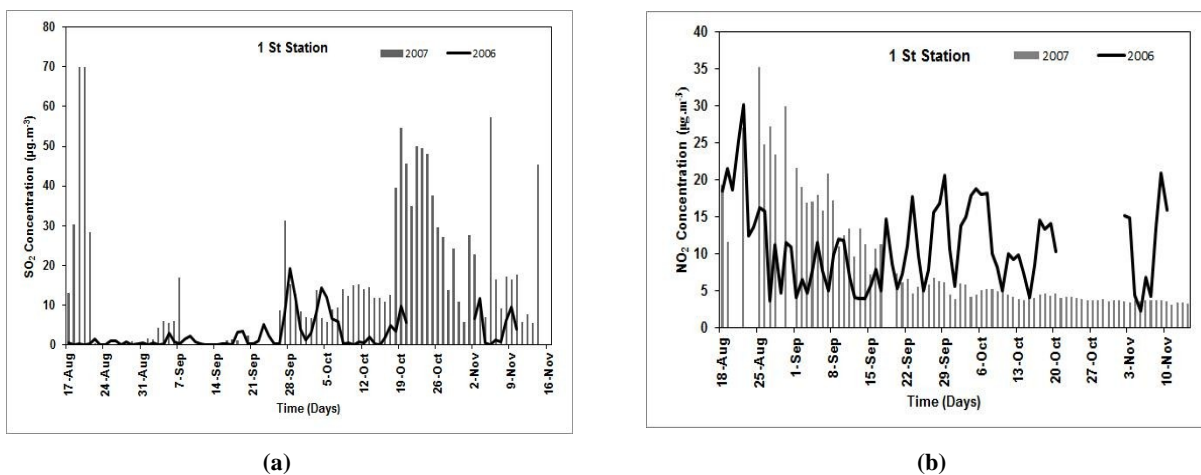**Figure 5**. Time series of pollutants observed at 1st station for 2006 to 2007 and 2nd station for 2007.

(a) (b)

Figure 6. Time series of pollutants observed at 1st station (a) and 2nd station (b) for 2006 to 2007.

In **Figure 6**, According to the previous year, the amount of thermal power plants operated has increased with a higher SO_2 emission level. However, the value of low SO_2 in the months of August to September of 2007 was caused by the south-southwest prevailing wind direction. However, the thermal power plants are operating in the summer and autumn of 2007 during the previous year, according to an exponential reduction in NO_2 concentrations.

Table 4. The amount of pollutants exceeded limit values for 1st station

Air pollutants	Stations	Period	Limit (as $\mu g/m^3$)	Limit exceeded (2006)	Limit exceeded (2007)	References
PM$_{10}$	1	Daily	50	44 times	12 times	1999/30/EC (EU Directive)[15]
	2	Daily	50	-	50 times*	1999/30/EC (EU Directive)
SO$_2$	1	Daily	125	Once	5 times	1999/30/EC (EU Directive)
	2	Daily	125	-	-	1999/30/EC (EU Directive)
NO$_2$	1	Hourly	200	733 times	206 times	1999/30/EC (EU Directive)
	2	Daily	150	-	-	1999/30/EC (EU Directive)
CO	1	Hourly	10000	-	-	2000/69/EC (EU Directive)[16]
	2	Hourly	10000	-	-	2000/69/EC (EU Directive)

Note: * Only five months (August, September, October, November, and December)

77

4. Conclusions

In this study, the effects of mobile thermal power plants were investigated. When measurements of 1st and 2nd stations were compared at the same time period, finding that the 2nd station measurement results was higher than that of 1st station.

In 2007, the daily limit for nitrogen dioxide has been especially exceeded at 206 times for 1st station. However, the total time exceeds of the limit value in 2006 for 1st station was reduced by approximately 3.5 times.

The region's main sources of nitrogen dioxide pollution from mobile plants have not been concluded in 2007. In the region, between the years 2006 and 2007, increasing use of natural gas has led to reduction of pollutant concentrations. The daily nitrogen dioxide concentration did not exceed the daily limit of WHO as for 2nd station. In general, the maximum pollution results from nitrogen dioxide in both the two stations. But, in this case, the entire region in terms of nitrogen dioxide pollution could be the result that does not reveal. However, the entire region in terms of nitrogen dioxide pollution can not be revealed in this case. The results can be obtained that the dominant wind direction is considered dominant wind direction in the entire region.

For the first station, a decrease in the concentration of particulate matter has been observed compared with the previous year in 2007. However, for the second station, an increase in the concentration of particulate matter has been observed. The sources of the particulate matter pollution in the second station are estimated as mobile power plants, Samsun-Ordu of highway and other plants in OID.

The carbon monoxide and sulfur dioxide measurements for each in the two stations are under the limit values.

The second station measurement results were higher than that of the first station. This is because the prevailing wind direction is north and northeast. In terms of carbon monoxide and sulfur dioxide, pollution in the two stations has not been determined. The use of natural gas to reduce the pollutant concentration is affected by OID. The hourly nitrogen dioxide concentration did exceed the daily limit of EU Directive in the first station. This is not only caused by mobile power plants but also industrial plants in this region. For a full assessment of the impact of mobile power plants, there shall made multi-point measurements in these two stations.

Conflict of interest

The authors declare that they have no conflict of interest.

Acknowledgments

References

1. WHO regional office for Europe. Air quality guidelines. 2nd ed. Copenhagen; 2000.
2. Cregan M, Flynn D. Advances in power plant technology. In: Flynn D (editor). Thermal power plant simulation and control. London: The Institution of Electrical Engineers; 2003. p. 1.
3. Lindsley D. Power plant control and instrumentation. London: The Institution of Electrical Engineers; 2005. p. 25.
4. Arya SP. Air pollution meteorology and dispersion. New York: Oxford University Press; 1999. p. 3.
5. Elbir T, Müezzinoğlu A. Estimation of emission strengths of primary air pollutants in the city of Izmir, Turkey. Atmospheric Environment 2004; 38(13): 1851–1857.
6. Karademir A. Evaluation of the potential air pollution from fuel combustion in industrial boilers in Kocaeli, Turkey. Fuel 2006; 85(12-13): 1894–1903.
7. Speight JG. Synthetic fuels handbook: Properties, process, and performance. USA: The McGraw-Hill Companies, Inc.; 2008. p. 99.
8. Sher E (editor). Handbook of air pollution from internal combustion engines. USA: Academic Press; 1998. p. 540.
9. Ogulata RT. Sectoral energy consumption in Turkey. Renewable and Sustainable Energy Reviews 2002; 6(5): 471–480.
10 Turkey Electricity Transmission Company (TEIAS). Electricity generation & transmission statistics of Turkey; 2009. Available from: http://www.teias.gov.tr/istatistik2009/index.htm.
11. Karaca H, Yildiz Z. Desulphurization kinetics of Number 6 fuel oil via a chemical method. Petroleum Science and Technology 2005; 23(1): 17–28.

12. PRCR. Parliament research commission report No: 10/29,31. Chair of the grand national assembly of Turkey. Ankara; 2003.

13. Akdemir A. An investigation of the relationships with meteorological parameters and monitoring of air quality parameters in organized industrial region of Samsun (PhD thesis). Ondokuz Mayis University; 2007.

14. Yildirim Y, Demircioglu N, Kopya M, *et al.* A mathematical modeling of sulphur dioxide pollution in Erzurum City. Environmental Pollution 2002; 118(3): 411–417.

15. European Union (EU). Council Directive 1999/30/EC of 22 April 1999 relating to limit values for sulphur dioxide, nitrogen dioxide and oxides of nitrogen, particulate matter and lead in ambient air. Official Journal of the European Communities; Annex I-II-III, 22 April 1999.

16. European Union (EU). EU Directive 2000/69/EC of the European Parliament and of the Council of 16 November 2000 relating to limit values for benzene and carbon monoxide in ambient air. Official Journal of the European Communities; Annex II, 16 November 2000.

Original research Article

A modified range migration algorithm for FMCW SAR processing

Yake Li[1*], Siu O'Young[2]

[1] *Faculty of Engineering and Applied Science, Memorial University of Newfoundland, St. John's, Canada. E-mail: yl1323@mun.ca1*

[2] *Faculty of Engineering and Applied Science, Memorial University of Newfoundland, St. John's, Canada.*

ABSTRACT

The range migration algorithm (RMA) is an accurate imaging method for processing synthetic aperture radar (SAR) signals. However, this algorithm requires a big amount of computation when performing Stolt mapping. In high squint and wide beamwidth imaging, this operation also requires big memory size to store the result spectrum after Stolt mapping because the spectrum will be significantly expanded. A modified Stolt mapping that does not expand the signal spectrum while still maintains the processing accuracy is proposed in this paper to improve the efficiency of the RMA when processing frequency modulated continuous wave (FMCW) SAR signals. The modified RMA has roughly the same computational load and required the same memory size as the range Doppler algorithm (RDA) when processing FMCW SAR data. In extreme cases when the original spectrum is significantly modified by the Stolt mapping, the modified RMA achieves better focusing quality than the traditional RMA. Simulation and real data is used to verify the performance of the proposed RMA.

Keywords: FMCW SAR; Range Migration Algorithm

ARTICLE INFO

COPYRIGHT

1. Introduction

Frequency modulated continuous wave (FMCW) synthetic aperture radar (SAR) has been developed and experimented extensively in recent years[1–7]. A common technique employed in these systems is the dechirp-on-receive demodulation that can reduce the requirements for radar receivers. The intermediate frequency (IF) signal after dechirp-on-receive does not relate to the transmitted signal bandwidth, which allows FMCW SAR to achieve high resolution without a complex analog to digital convertor (ADC) system. Another difference of FMCW SAR from pulsed SAR is the longer pulse length, which allows the Doppler shift inside the pulse to be measurable and compensable. The major pulsed SAR processing algorithms have been modified and applied in FMCW SAR signal processing[8–11].

The RMA[12,13] is an accurate algorithm that is especially effective for processing large squint and wide beamwidth SAR signals. Motion compensation[14] and autofocus[15,16] has been integrated into RMA to image quality improvement. The extensions of RMA combine this algorithm with motion compensation[14] or autofocus[15,16]. However, the computational load of RMA is considerably high[10], especially when the Stolt mapping has to extensively expand the target spectrum in wide beamwidth or high squint imagery. In addition, the expansion of

the spectrum size requires more memory capability, which limits the application of RMA in real-time processing.

Dechirp-on-receive compresses the range modulation before ADC. According to the time-frequency relationship of a chirp signal, this operation has equivalently transformed the IF data to its range frequency domain[17].

This makes it convenient for the application of RMA because only one azimuth Fourier Transform (FT) is needed to obtain the two dimensional spectrum. Also, the in-pulse Doppler shift[8] induced by the continuous moving of the aircraft corresponds to an azimuth-frequency dependent phase term in the two dimensional frequency domain, which could be easily removed by the reference function multiplication (RFM) in RMA.

Except for the convenience in application, dechirp-on-receive can also improve the efficiency of the Stolt mapping by exploring the character of the IF signal, which is the content of this paper. The modified Stolt mapping has two differences from the traditional one. The first difference is that the mapping equation is changed to eliminate the parallel shifting of the spectrum. The second difference is that the range of the new variable after Stolt mapping can be limited without losing accuracy. The modified RMA has roughly the same computational load and the same memory requirements as the range-Doppler algorithm (RDA) but can handle more general SAR imaging configurations. This makes the proposed RMA an efficient and practical algorithm to process FMCW SAR signals in either real-time or post-processing.

This paper organizes as follows. Section 2 discusses the range resolution of the FMCW radar. The result is crucial to demonstrate the range resolution of the modified Stolt mapping. Section 3 derives the spectral model for the FMCW SAR signal and introduced the modified RMA. Section 4 shows the flow diagram of the RMA, which compares with the RDA flow chart. Simulation and actual data are used in Section 5 to verify proposed algorithm.

2. Range resolution of the IF signal

in FMCW SAR

A sawtooth linear frequency modulated (LFM) signal (shown in Figure 1) can be expressed as

$$s_T(t) = rect\left(\frac{t}{T}\right) \exp\left(j\pi k t^2 + j2\pi f_0 t\right) \tag{1}$$

where

$$rect(\frac{t}{T}) = \begin{cases} 1 & |t| \leq T/2 \\ 0 & others \end{cases} \tag{2}$$

is the gate function. T is the period of the signal, f_0 is the centre frequency, Bw is bandwidth and $k = Bw/T$ is the frequency modulation (FM) rate. The returned signal can be expressed as
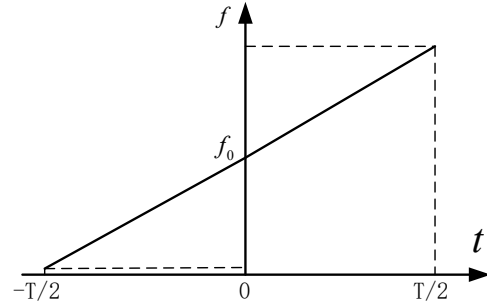

Figure 1. Sawtooth LFM signal.

$$s_R(t) = rect\left(\frac{t}{T}\right) \exp\left[j\pi k(t-\tau)^2 + j2\pi f_0(t-\tau)\right] \tag{3}$$

where $\tau = 2R_0/c$ is the two-way time delay, R_0 is the distance between the radar and the target, c is the speed of light. The amplitude of the returned signal is assumed to be one without loss of generality. In real case, R_0 is normally no more than several kilometers for FMCW SAR, hence the time delay τ is in the order of tens of microseconds. This delay will slightly decrease the frequency beating length between the reference signal and the received signal, which will reduce the resolution. Since the delay is very small compared with T (usually in the order of milliseconds), its effect on the resolution could be neglected. Therefore, it is neglected in the rectangular function in (3). However, τ cannot be neglected in the phase because its coefficient in the phase is sufficiently large to make the two-way time delay a significant contribution to the change of the phase.

81

By measuring the changes in phase, the linear frequency modulated (LFM) signal could measure the distance of the target.

The IF signal is the result of multiplying the received signal (3) with the transmitted signal (1), which is

$$s_{IF}(t) = rect\left(\frac{t}{T}\right)\exp\left(j2\pi k\tau t - j\pi k\tau^2 + j2\pi f_0\tau\right) \quad (4)$$

This is the so-called dechirp-on-receive demodulation. The FT of (4) is used to measure the range of the target, which is

$$S_{IF}(f) = T\mathrm{sinc}\left[T(f - k\tau)\right]e^{j2\pi f_0\tau}e^{-j\pi k\tau^2} \quad (5)$$

$$\mathrm{sinc(x)} = \frac{\sin(\pi x)}{\pi x}$$

Equation (5) shows that the FT result of the IF signal is a sinc signal at $f = k\tau$ Hz.

After ADC sampling, the 3dB width of the sinc function shown in (5) in the digital frequency domain is[14]

$$\frac{1}{T}(Hz) = 1(\text{sample}) \quad (6)$$

The center of the sinc function is at

$$\frac{k\tau}{\Delta f} = \frac{(Bw/T)\cdot(2R_0/c)}{(1/T)} = \frac{R_0}{(c/(2\cdot Bw))} = \frac{R_0}{\rho_s} \quad (\text{samples}) \quad (7)$$

where $\rho_s = C/(2\cdot Bw)$ is the range resolution of the transmitted signal.

In a pulsed radar system, orthogonal demodulation is normally used to demodulate the received signal instead of the dechirp-on-receive technique. Then the absolute value of the pulse compression results in an orthogonal demodulation radar system when transmitting the signal shown by (1) will be[18]

$$s_1(t) = T\sin c\left[kT\left(t - \frac{2R_0}{c}\right)\right] \quad (8)$$

whose 3 dB width is $1/kT$. Compare (8) with (5), it can be seen that the expression of the resolution for the IF signal is different in FMCW SAR from that in pulse SAR. This is not surprising because the resolution is realized in the frequency domain in dechirp-on-receive radar while in orthogonal demodulation system, the resolution is expressed in the time domain. Therefore, the implementation of the traditional Stolt mapping in pulse SAR signal processing

can be made more efficient in FMCW SAR signal processing.

3. The modified range migration algorithm

3.1 The equivalent two-dimensional spectrum of FMCW SAR

Assuming the transmitted signal is

$$s_T(t,\eta) = rect_r\left(\frac{t}{T}\right)rect_a\left(\frac{\eta - \eta_c}{T_a}\right)e^{j\pi kt^2}e^{j2\pi f_0 t} \quad (9)$$

where t is range time (fast time) and η is azimuth time (slow time), η_c is the zero azimuth Doppler time. The azimuth envelop is assumed to have a rectangular shape, though its precise form is similar to the main lobe of a sinc function[18]. T_a is the synthetic aperture time. The amplitude is assumed to be 1 without loss of generality. k is the FM rate and f_0 is the carrier frequency. Assuming the SAR operates in broadside strip map mode, the received signal is

$$s_R(t,\eta) = \sigma(R_0,\eta_c)rect_r\left(\frac{t}{T}\right)rect_a\left(\frac{\eta - \eta_c}{T_a}\right)e^{j\pi k(t-\tau)^2}e^{j2\pi f_0(t-\tau)} \quad (10)$$

where

$$\tau = \frac{2R(\eta)}{c} = \frac{2}{c}\sqrt{R_0^2 + v^2(\eta + t - \eta_c)^2} \quad (11)$$

$\sigma(R_0,\eta_c)$ is the reflection coefficient for the target at (R_0,η_c). A more accurate expression for the two-way delay time can be found in[11]. The expression of (11) is accurate enough in normal airborne situations[10].

The IF signal is the multiplication of (10) with the conjugate of (9), which is

$$s_{IF}(t,\eta) = \sigma(R_0,\eta_c)rect_r\left(\frac{t}{T}\right)rect_a\left(\frac{\eta - \eta_c}{T_a}\right)e^{j2\pi f_0\tau}e^{j2\pi ktt}e^{-j\pi k\tau^2} \quad (12)$$

The last exponential term $e^{-j\pi k\tau^2}$ in (12) is the residual video phase (RVP) and can be compensated before the start of image formation. Literature[17] gives a method to remove the RVP term. In the following derivation, this term is neglected.

Because the dechirp-on-receive has readily transformed the signal to its equivalent range frequency domain, only one azimuth FT is needed to generate the equivalent two-dimensional frequency

expression, which is

$$S(t,f_\eta) = \sigma(R_0,\eta_c)\,rect\left(\frac{t}{T}\right)\int rect_a\left(\frac{\eta-\eta_c}{T_a}\right)e^{j2\pi f_0\tau}e^{j2\pi kt\tau}e^{-j2\pi f_\eta\eta}d\eta \quad (13)$$

As can be seen, the signal is actually in the range-time azimuth-frequency domain. The reason it is called equivalent two-dimensional frequency domain is that the expression in (13) actually has the characteristic of the two-dimensional frequency domain due to dechirp-on-receive[17]. After using POSP (principle of stationary phase)[17], the equivalent two-dimensional spectrum of the IF signal can be expressed by

$$S(t,f_\eta) = \sigma(R_0,\eta_c)\,rect\left(\frac{t}{T}\right)rect_a\left(\frac{f_\eta}{Bw_a}\right)\exp\left(j\Phi(t,f_\eta)\right) \quad (14)$$

where

$$\Phi(t,f_\eta) = \frac{4\pi R_0}{c}\sqrt{(f_0+kt)^2 - \frac{c^2 f_\eta^2}{4v^2}} + 2\pi f_\eta t - 2\pi f_\eta \eta_c \quad (15)$$

and Bw_a is the azimuth bandwidth. It is an equivalent 'two-dimensional' spectrum because the range direction is actually the range time but not frequency. However, as the signal in range-time of FMCW SAR has the same form and properties as that in range-frequency of the pulsed radar, (15) is named equivalent two-dimensional spectrum in this paper.

Taylor expansion can be used to approximate the square root in (15) for better understanding the modified Stolt mapping. By using Taylor expansion, we have

$$\Phi(t,f_\eta) = \frac{4\pi R_0}{c}\left[f_0 D(f_\eta,v) + \frac{k}{D(f_\eta,v)}t - \frac{k^2 c^2 f_\eta^2}{8v^2 f_0^2 D^3(f_\eta,v)}t^2 + o(t^2)\right] - 2\pi f_\eta t - 2\pi f_\eta \eta_c \quad (16)$$

where

$$D(f_\eta,v) = \sqrt{1 - \frac{c^2 f_\eta^2}{4v^2 f_0^2}} \quad (17)$$

is the cosine of the instantaneous incidence angle of the radar. $o(t^2)$ of (16) is the higher-order term in Taylor expansion. The terms in the square bracket represent the Taylor expansion of the square root. The traditional Stolt mapping tries to correct all the terms in the square brackets to finish azimuth compression, range cell migration correction (RCMC), SRC (second range compression), and higher-order terms correction.

3.2 The modified RMA

3.2.1 Reference function multiplication

The first step of the modified RMA is to multiply the reference function multiplication (RFM),

$$\exp\left(j\Phi_1(t,f_\eta)\right) = \exp\left(-j\frac{4\pi R_{ref}}{c}\sqrt{(f_0+kt)^2 - \frac{c^2 f_\eta^2}{4v^2}} + j2\pi f_\eta t\right) \quad (18)$$

This operation focuses on the points in the reference range. The last term of (18) is to remove the in-pulse Doppler effect. The expression after RFM is

$$S_1(t,f_\eta) = \sigma(R_0,\eta_c)\,rect\left(\frac{t}{T}\right)rect_a\left(\frac{f_\eta}{Bw_a}\right)\exp\left(j\frac{4\pi\Delta R}{c}\sqrt{(f_0+kt)^2 - \frac{c^2 f_\eta^2}{4v_{ref}^2}} - j2\pi f_\eta\eta_c\right) \quad (19)$$

where $\Delta R = R_0 - R_{ref}$.

3.2.2 Modified stolt mapping

The second step of the modified RMA is the modified Stolt mapping, which is applied to the square root of the phase-in (19). Before introducing the modified Stolt mapping, the traditional Stolt mapping is analyzed and the problems of its application in FMCW SAR processing are addressed. The traditional Stolt mapping is

$$\sqrt{(f_0+kt)^2 - \frac{c^2 f_\eta^2}{4v_{ref}^2}} = f_0 + kt_1 \quad (20)$$

where t_1 is the new time variable. This step is actually a change of variables, which corresponds to a mapping of the original time variable. For simplicity, we only use the first two terms in the square bracket of (16) to represent the square root of (20). The higher-order terms will also be corrected by the Stolt mapping. However, as they have no effect in the following derivation, they are neglected in the equations. Then we obtain the form of the variable change,

$$t_1 = \frac{f_0}{k}\left(D(f_\eta,v)-1\right) + \frac{t}{D(f_\eta,v)} \quad (21)$$

The first term on the right side of (21) is a time shift (parallel shift) that is dependent on azimuth-frequency, and the second term performs scaling of time. Since $D(f_\eta,v)$ is always no more than one, the change of variable is always an expansion of the data size in the range time direction, and the change

83

caused by the first term in (21) is normally much larger than the change caused by the second term.

Two problems could happen when applying the traditional Stolt mapping of (20) in FMCW SAR signal processing. First, in wide beamwidth or high squint imagery, the term $D(f_\eta, v)$ can be considerably smaller than 1. This will greatly expand the resulting spectrum after Stolt mapping and hence will significantly increase the burden of calculation and the requirements for the memory size to store the resulting spectrum. Furthermore, the degeneration in focus quality is also reported as the increase in the value of variable change[19]. Second, the scaling in the original time variable is different for different values of f_η, which means the signal length of the range dimension after Stolt mapping is different for different azimuth positions. Therefore, the whole spectrum has to be zero-padded in range to make the length of range dimension the same for all f_η values. However, as can be seen in (6), the original range resolution is one sample after range FFT, hence it is not necessary to conduct zero paddings, which will smear the peak energy of the sinc function in (5) to adjacent range bins (will be explained later) if some modifications can be made. The modified RMA takes two steps of modification to solve the problems.

The first step modifies the Stolt mapping expression. Instead of the traditional Stolt mapping used in (20), the following variable change is used

$$\sqrt{(f_0 + kt)^2 - \frac{c^2 f_\eta^2}{4v^2}} = D(f_\eta, v) f_0 + kt_1 \quad (22)$$

By using (22) as the Stolt mapping formula, the first term on the right side of (21) disappears, and the mapping now only corresponds to an expansion of the original time variable, which is

$$t_1 = \frac{t}{D(f_\eta, v)} \quad (23)$$

This mapping removes the parallel shift of the spectrum along the range dimension, which can be huge when the azimuth frequency is high. Meantime, this modified mapping still completes all the critical operations of the traditional Stolt mapping except

the azimuth compression. After the modified Stolt mapping and range FFT, the azimuth signal needs to be compressed in the equivalent 'range-Doppler domain' (range-frequency azimuth-frequency).

The second step of modifying RMA is to limit the range of the new time variable. As indicated by (5) and (6) in Section 2, the range resolution of the original signal is 1 sample independent of the range sampling frequency f_s. In Stolt mapping, because the signal in zero azimuth-frequency bin does not change ($D(0, v) = 1$), the time interval between two adjacent samples after Stolt mapping in other azimuth bins should be the same as the interval in zero azimuth-frequency bin, which is $1/f_s$. Therefore, the total samples in range after Stolt mapping would be

$$N_t = T_t f_s = \left(\frac{f_0}{k} \left(D(f_{\eta max}, v) - 1 \right) - \frac{T}{2} \frac{D(f_{\eta max}, v) + 1}{D(f_{\eta max}, v)} \right) f_s \quad (24)$$

in traditional Stolt mapping or

$$N_c = T_c f_s = \frac{T}{D(f_{\eta max}, v)} f_s \quad (25)$$

in the case of using (25), where T is defined by Figure 1.

First, the situation when using (22) to perform the Stolt mapping is considered. Substitute (22) into (19) and use the approximation (23) in the range envelope, we have

$$S_{11}(t_1, f_\eta) = \sigma(R_0, \eta_c) rect\left(\frac{t_1}{T/D_m} \right) rect_a\left(\frac{f_\eta}{Bw_a} \right)$$
$$\exp\left(j \frac{4\pi \Delta R}{c} kt_1 + j \frac{4\pi \Delta R}{c} Df_0 - j2\pi f_\eta \eta_c \right) \quad (26)$$

where $D(f_\eta, v)$ is replaced by D and $D(f_{\eta max}, v)$ is replaced by D_m for simplicity. The length of the range envelop is T/D_m because the signal is zero-padded to length T/D_m at all azimuth frequency bins. After range FFT, we have

$$S_{12}(f_1, f_\eta) = A(R_0, \eta_c) sinc\left(\frac{T}{D_m} \left(f_1 - \frac{2\Delta R}{c} k \right) \right)$$
$$rect_a\left(\frac{f_\eta}{Bw_a} \right) \exp\left(j \frac{4\pi \Delta R}{c} Df_0 - j2\pi f_\eta \eta_c \right) \quad (27)$$

where all the coefficient is absorbed by $A(R_0, \eta_c)$. Following the steps from (5) to (6), the 3dB width of the peak of (27) is

$$P_1 = D_m \frac{T_c}{T} > 1 \quad \text{samples} \tag{28}$$

As expected, the width of the peak of the sinc function is wider than 1 sample because of the zero paddings (corresponds to an interpolation) before range FFT. However, the zero paddings are not necessary because the original range resolution is only 1 sample. Therefore, there is no need to widen the peak. In the case of wide beamwidth, T_c can be many times bigger than T, and hence the peak of (27) will occupy many samples in range frequency after range FFT. The negative effect of widening the peak in the range is that the energy of the peak is smeared along with the range.

Using the same analysis steps for the traditional Stolt mapping shows the same result as in (28). Therefore, it is not necessary to imply the complete Stolt mapping even in (23) for expanding the range variable to $\left[-T/2D(f_\eta, v), T/2D(f_\eta, v) \right]$. The range of the new variable can be the same as that of the old-time variable for all $D(f_\eta, v)$, which is

$$-\frac{T}{2} \le t_1 \le \frac{T}{2} \tag{29}$$

For the azimuth bin in which $D = 0.9$, the length of the Stolt mapped signal by using both (23) and (29) will be 10% shorter than that mapped by only using (23). At the same time, the result still keeps the original range resolution and the energy is more concentrated after range FFT.

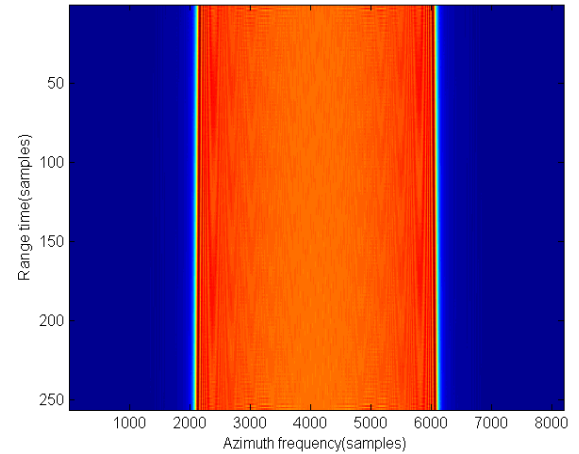An example of the spectrums after different Stolt mapping methods are shown in **Figure 2**. The SAR parameters are shown in **Table 1**.
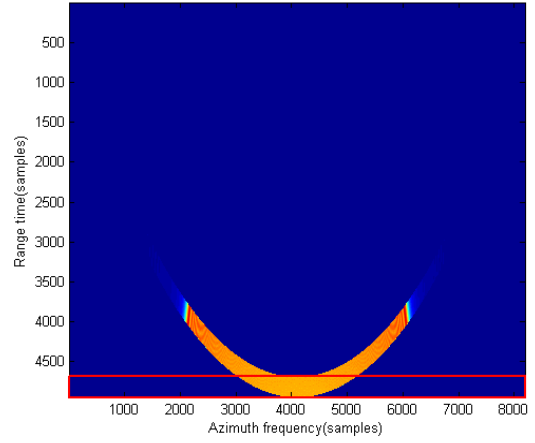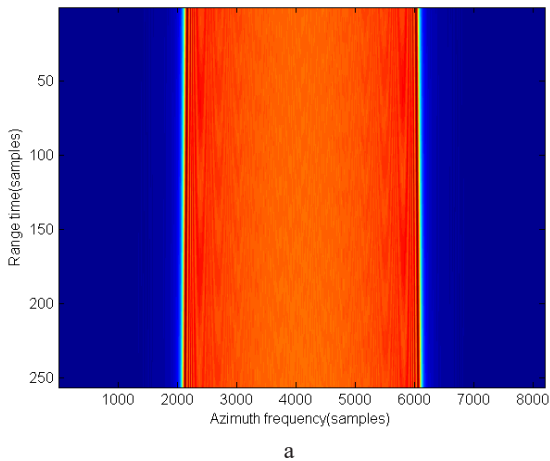
b
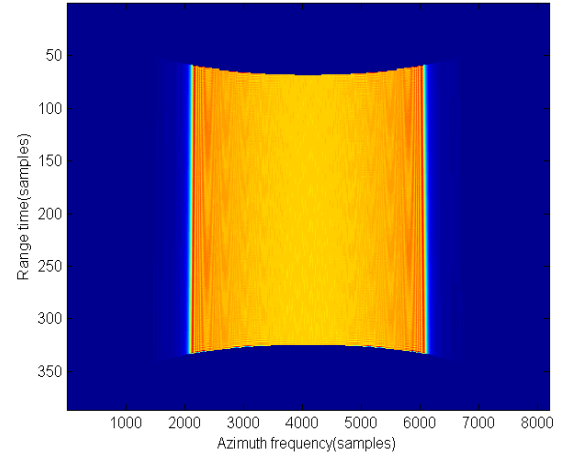
c

d

Figure 2. Flow diagrams for RMA and RDA. a) Original spectrum; b) Spectrum after traditional Stolt mapping; c) Spectrum using only the first step of the modified Stolt mapping (eq. (23)); d) Spectrum using the full modified Stolt mapping (eq.(23) and (29)).

a

85

Figure 2a shows the original 'two-dimensional spectrum' before Stolt mapping, which is 256 samples (range) by 8,192 samples (azimuth). **Figure 2b** shows the spectrum after the traditional Stolt mapping, which expands the spectrum to 5000 samples (range) by 8,192 samples (azimuth). **Figure 2c** is the spectrum using only the first step of the modified Stolt mapping. As can be seen, after removing the parallel shift of the time variable, the Stolt mapping only corresponds to a scaling of the variable, and the size of the resulting spectrum has reduced to approximately 400 samples (range) by 8,192 samples (azimuth). **Figure 2d** is the resulting spectrum of the modified Stolt mapping. It has the same size as the original spectrum. Therefore, after applying the two changes to the traditional Stolt mapping, the resulted spectrum size will be minimal after Stolt mapping without losing the range resolution. Moreover, the peak energy will still concentrate in one sample after range FFT.

3.2.3 Azimuth compression

After modified Stolt mapping, the expression for the resulting signal is

$$S_2(t_1, f_\eta) = \sigma(R_0, \eta_c) rect\left(\frac{t_1}{T}\right) rect_a\left(\frac{f_\eta}{k_a T_a}\right)$$
$$\cdot \exp\left(j\frac{4\pi(R_0 - R_{ref})}{c}\left(D(f_\eta, v)f_0 + kt_1\right) - j2\pi f_\eta \eta_c\right) \quad (30)$$

in which the range-azimuth coupling has been removed. The range FT is then applied and we have

$$S_3(f_1, f_\eta) = \int S_1(t_1, f_\eta)\exp(-j2\pi f_1 t_1)dt_1$$
$$= T\sigma(R_0, \eta_c)\mathrm{sinc}\left[T\left(f_1 - \frac{2k(R_0 - R_{ref})}{c}\right)\right] \cdot rect_a\left(\frac{f_\eta}{k_a T_a}\right)$$
$$\cdot \exp\left(j\frac{4\pi(R_0 - R_{ref})}{c}D(f_\eta, v)f_0\right)\exp(-j2\pi f_\eta \eta_c)$$
$$\quad (31)$$

where f_1 is the new range frequency variable. As implied by the sinc function in (31), the range signal has been focused and the RCM has been removed. The next step is to multiply the azimuth matched filter to perform the azimuth compression, which is

$$\exp\left(j\Phi_2(f_1, f_\eta)\right) = \exp\left(-j\frac{4\pi(R_0 - R_{ref})}{c}D(f_\eta, v)f_0\right)$$

$$\quad (32)$$

Then we have

$$S_4(f_1, f_\eta) = T\sigma(R_0, \eta_c)\mathrm{sinc}\left[T\left(f_1 - \frac{2k(R_0 - R_{ref})}{c}\right)\right] \quad (33)$$
$$\cdot rect_a\left(\frac{f_\eta}{k_a T_a}\right)\exp(-j2\pi f_\eta \eta_c)$$

3.2.4 Azimuth inverse Fourier transform

An azimuth IFT (inverse Fourier transform) then generates the focused image, which is

$$s(f_1, \eta) = \frac{1}{2\pi}\int S_4(f_1, f_\eta)\exp(j2\pi f_\eta \eta)d\eta$$
$$= A\sigma(R_0, \eta_c)\mathrm{sinc}\left[T\left(f_1 - \frac{2k(R_0 - R_{ref})}{c}\right)\right]\mathrm{sinc}\left[k_a T_a(\eta - \eta_c)\right] \quad (34)$$

where A is a constant amplitude. The amplitude of the target point is now a two-dimensional sinc function and the resolutions are determined by signal fast time duration T in range and azimuth bandwidth $k_a T_a$ in azimuth.

4. Comparison with the RDA

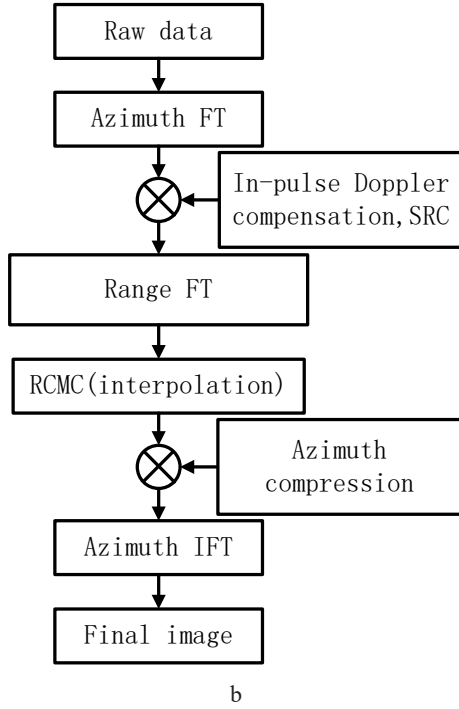The flow diagrams for RMA and RDA when processing FMCW SAR signals are shown in **Figure 2**.

a

b
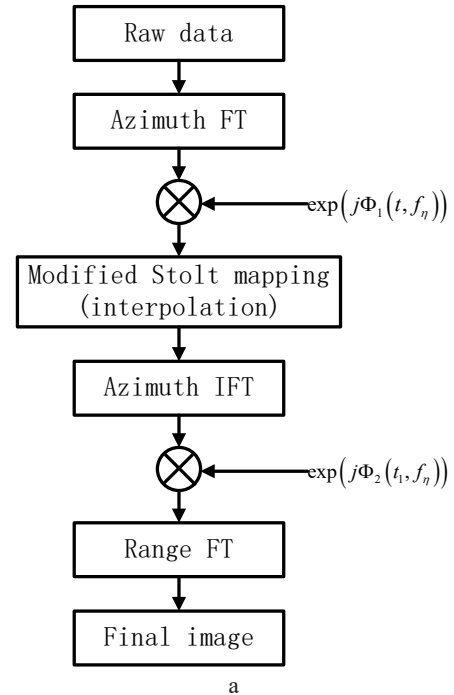
Figure 3. Flow diagrams for RMA and RDA. a) modified RMA; b) RDA**.**

Figure 3a shows the flow chart of the RMA. The first phase multiplication finishes the in-pulse Doppler effect removal and the RFM. The Second phase multiplication completes the azimuth compression. One range FT, one azimuth FT, one azimuth IFT and one interpolation operation for Stolt mapping are needed for the signal processing.

Figure 3b shows the flow diagram of the RDA. The first phase multiplication finishes the in-pulse Doppler effect removal and the approximated SRC. The other options of applying the SRC can be found in[18]. The Second phase multiplication completes the azimuth compression. One range FT, one azimuth FT, one azimuth IFT and one interpolation operation for RCMC need the processing.

As can be seen from **Figure 3**, the modified RMA has roughly the same computational load and the same memory requirements as the RDA if the same orders of interpolation are used. This is because the modified RMA does not expand the spectrum in range direction when performing the Stolt mapping. The RMA will generate a better image than RDA because it does not make any approximations during the image processing, while the RDA only approximately compensates the SRC and neglects the high-

er-order terms of range-azimuth coupling.

5. Results

This section first uses simulation and then uses real data to verify modified RMA.

5.1 Simulation

The parameters for simulation are shown in **Table 1**.

Figure 4 shows the parallel shift ($f_0\left(D\left(f_\eta,v\right)-1\right)/k$) of the variable in the traditional Stolt mapping, which corresponds to the first term of (21).

Table 1. Simulation parameters

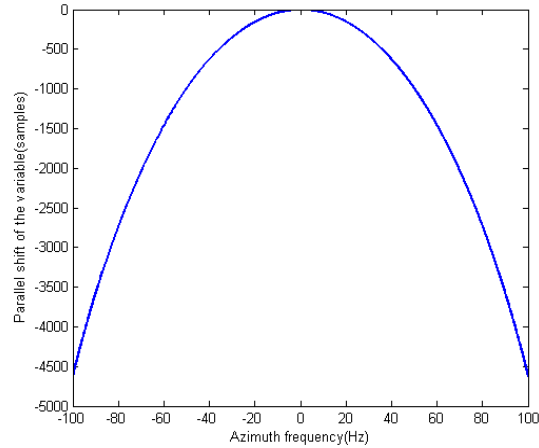| Parameter	Value	Units
SAR speed	50	m/s
PRF (Pulse repetition frequency)	200	Hz
Squint angle	0	rad
Centre frequency	400	MHz
Signal bandwidth	7.5	MHz
Target distance	2000	m
Scene centre	2560	m
Antenna beamwidth	42.97	degree
Data azimuth length	8192	samples
Data range length	256	samples

Figure 4. Parallel shift of the variable in Stolt mapping**.**

As shown by **Figure 4**, at both edges of the azimuth aperture, the parallel shift caused by the first term of (21) is more than 4500 samples, which means the length of the range spectrum should expand to store the whole result of Stolt mapping. This corresponds to a significant expansion in the size of the signal spectrum (see **Figure 2b**) because the length of the original spectrum before Stolt mapping is only 256 samples in range. The modified vari-

87

able substitution avoids this parallel shifting, which greatly reduces the computational load and required memory size for performing the Stolt mapping (see **Figure 2c**).

Figure 5 shows the $D(f_\eta, v)$ defined in (17). At the edge of the azimuth aperture, $D(0, v)$ is 0.66 in this simulation. This means the variable change in (22) will still expand the time variable to 1/0.66 times of its original length. This expansion is not necessary and can avoid if we define the new variable in the range shown by (29). As a result, this modified Stolt mapping does not expand the original spectrum length while still maintaining the same range resolution as the original signal (see **Figure 2d**).

The range FFT of the Stolt mapped spectrum (equivalent range-Doppler domain) shows in **Figure 6**. **Figure 6a** is the range FFT result of the traditional Stolt mapped spectrum. As expected, the RCM has been removed. However, the range width of the azimuth trajectory is wide because of the zero padding (due to Stolt mapping) before FFT. As can be seen, the energy smears in range. **Figure 6b** is the range FFT after the modified Stolt mapping. The RCM has been corrected and the energy concentrates in one range bin. The range resolution is the same as the original signal.
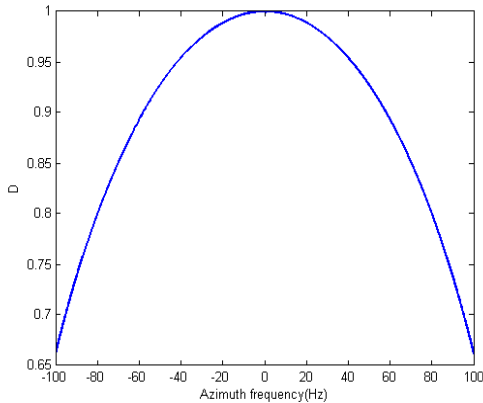
a

b

Figure 6. Range FFT of the Stolt mapped spectrum.

Figure 5. $D(f_\eta, v)$ defined by (17). a) Using traditional Stolt mapping; b) Using modified Stolt mapping.
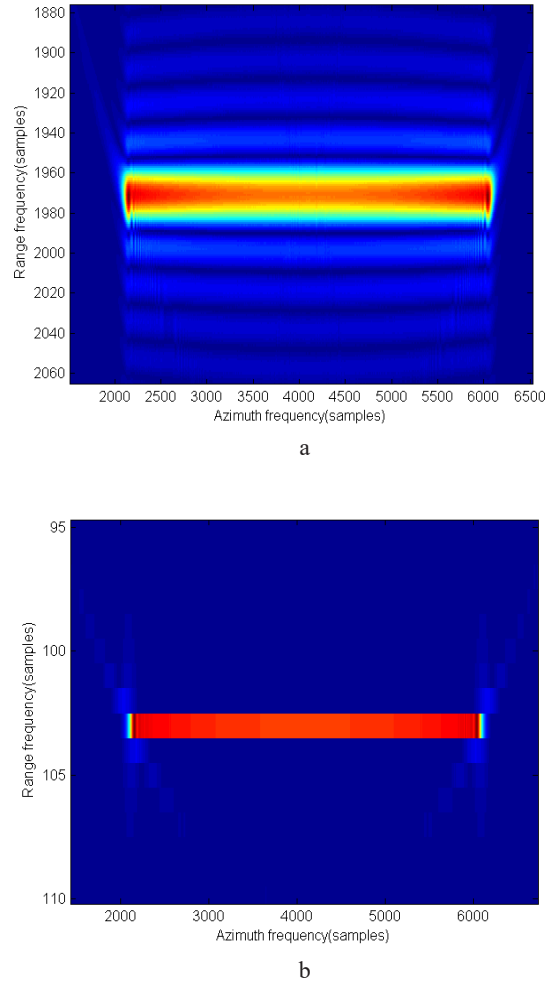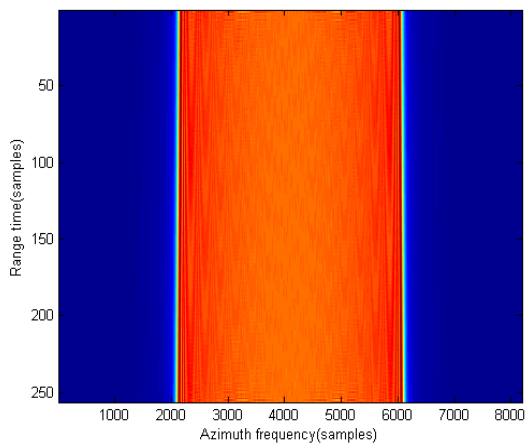
One method of using the spectrum (**Figure 2b**) after the traditional Stolt mapping shows in[17]. This method cuts a rectangular area in the resulting spectrum for imaging. However, when the Stolt mapping significantly skews the original spectrum due to large beamwidth or high squint angle, the rectangular area for imaging is very small. In this case, the range resolution will be decreased.

A way of keeping the range resolution is to maintain the range length of the spectrum after traditional Stolt mapping the same as the original spectrum, which corresponds to truncate the first 256 range samples (original spectrum is 256 samples in range). The truncated spectrum after traditional Stolt mapping and the spectrum after modified Stolt mapping is shown in **Figure 7**.
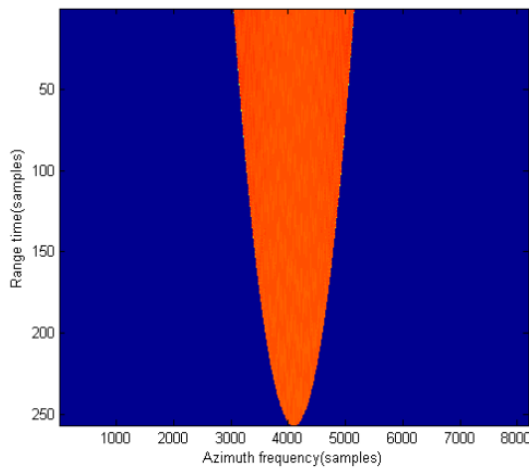
Figure 7a is the result of the modified Stotl mapping, which is the same as the results shown in **Figure 2d**. **Figure 7b** is the resulting spectrum (256

samples by 8,192 samples) cut from the bottom of Figure 2b (the part in the red rectangular in Figure 2b).

Figure 8 shows the compression results of the traditional RMA and the modified RMA by using the spectrums in **Figure 7a** and **Figure 7b**. Interpolation is used to reveal the sidelobes more clearly. In **Figure 8a**, the point target is well focused by using the proposed RMA. In **Figure 8b**, the target is defocused, and the azimuth main lobe is wider than the range main lobe because the azimuth bandwidth is significantly reduced as shown by **Figure 7b**.

a

a

b

Figure 8. Compression results by using the modified RMA and the traditional RMA by using the same size of spectrum. a) Proposed RMA;b) Traditional RMA**.**
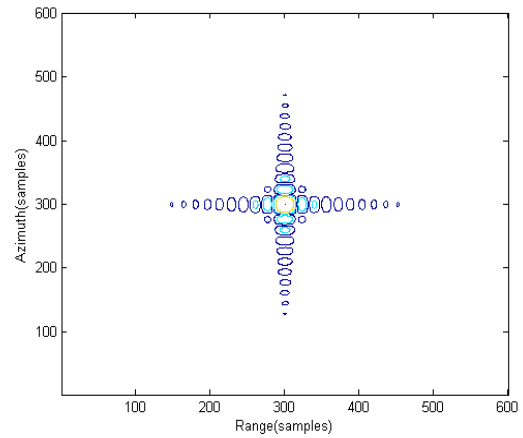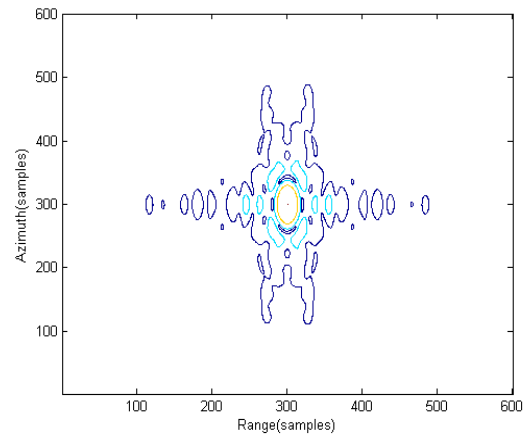

b

Figure 7. Original spectrum and the result spectrums after Stolt mapping. a) Result of the modified Stolt mapping; b) Truncated spectrum of the traditional Stolt mapping result**.**
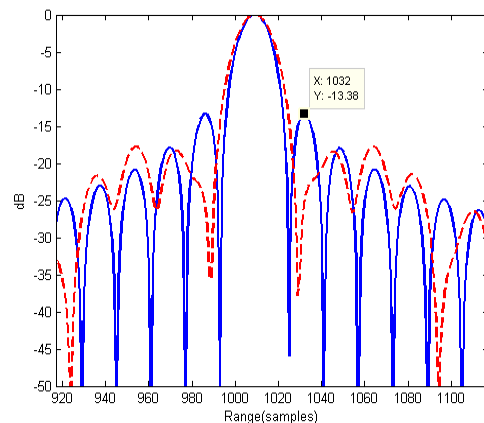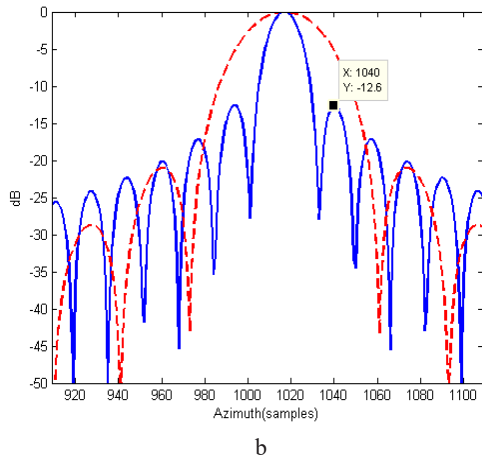

a

89

b

Figure 9. Comparison of the range and azimuth compression quality focused target. a) Range slices;b) Azimuth slices**.**

Figure 9 shows the comparison for the compression quality of the focused target when using the traditional RMA and the proposed RMA separately. The solid lines are the range and azimuth slices from **Figure 8a**, while the dashed lines are from Figure 8b. For the solid line in **Figure 9a** and **Figure 9b**, the 3 dB width of the main lobes is all 15 samples, meaning the range and azimuth resolution are the same. The main lobe of the dashed line in Figure 9b is significantly wider than that of the solid line because the azimuth bandwidth is greatly decreased due to the truncate of the result after traditional Stolt mapping when using the same size of the spectrum.

5.2 Real data processing

The real data was collected by an FMCW SAR. The radar is composed of several customized printed circuit boards and some off-the-shelf microwave components. The radar works at C band has a maximum bandwidth of 150 MHz. The data used in this section was collected during a ground moving vehicle test. The antenna configuration in the test shows in **Figure 10**.

Figure 10. The antenna configuration in the ground test**.**

Table 2. Real data parameters

Parameter	Value	Units
SAR speed	60	km/h
Bandwidth	150	MHz
Centre frequency	5590	MHz
PRF	250	Hz
Squint angle	0	degree
Antenna azimuth beamwidth	8	degree

Two 2 x 8 patch array antennas for transmitting and receiving are enclosed in the white box in **Figure 1**. The antennas were mounted on the top of the van by a wood frame; the radar was mounted inside the van and connected to the antennas via coaxial cables.

The parameters used in the ground test are shown in **Table 2**. The images obtained by the traditional RMA and the modified RMA are shown in **Figure 11**. The vertical direction is a range and the horizontal direction in azimuth.

The images obtained by the traditional RMA and the modified RMA show in **Figure 11**. Four orders of interpolation are used to perform the Stolt mapping. No window is applied in either the range direction or the azimuth direction FFT for better comparison of the focusing quality because noise does not eliminate by windowing at all and will be more obvious in the final images. The same size spectrum after Stolt mapping is used to generate **Figure 11a** and **Figure 11b** as shown in the simulation in **Figure 7**.

As shown by **Figure 11**, the image generated by the modified RMA has a lower level of noise than the one generated by the traditional RMA. This is more clearly shown by the area marked by the red rectangular in **Figure 11a.** By comparing the area

90

in the red box of **Figure 11a** with the same area of **Figure 11b**, higher background noise is observed in **Figure 11a**.

In **Figure 12**, the range compression quality is compared between the traditional and the proposed RMA. The solid line is the range slice of the marked point in **Figure 11a** while the dashed line is range slice of the same point in **Figure 11b**. An improvement in the range focusing quality (the dashed line has a narrower main lobe) of the proposed RMA than the traditional RMA can be observed. The improvements using the modified RMA are not as significant as in **Figure 8** because the SAR parameters used in the field test are very normal (narrow beamwidth, no squint). The parameters used in the simulation are very extreme to reveal the improvement of the proposed RMA.

Figure 12. Comparison of the range profiles of an isolated strong point target marked by the red circle in **Figure 11a.**

6. Conclusion

A modified RMA is proposed and used to process the FMCW SAR signal. The modified RMA takes the advantage of the special characteristics of the IF signal in dechirp-on-receive FMCW radar systems to decreases the computational load and the memory required during image generation. The modified RMA now has almost the same computational speed as compared to the RDA if the same orders of interpolation are used. A better focusing quality is also obtained in the proposed RMA than in the traditional RMA when using the same size of the spectrum after Stolt mapping. The effectiveness of the proposed algorithm is verified by both simulation and real data at the end.

Author contributions

Yake Li designed and built the FMCW radar used in the result section of this paper, conducted the SAR experiment, and proposed the signal processing method introduced in this paper.

Siu O'Young supervised the research work and provided helpful suggestions.

Conflict of interest

The authors declare that they have no conflict of interest.

Figure 11. Images processed by different RMAs. a) Traditional RMA; b) Proposed RMA**.**

References

1. Edrich M. Design overview and flight test results of the miniaturised SAR sensor MISAR. First European Radar Conference 2004: 205–208.

2. Edrich M. Ultra-lightweight synthetic aperture radar based on a 35 GHz FMCW sensor concept and on-line raw data transmission. IEE Proceedings - Radar, and Sonar and Navigation 2006; 153(2): 129–134.

3. Berizzi F, Martorella M, Cacciamano A, *et al*. A contrast-based algorithm for synthetic range-profile motion compensation. IEEE Transactions on Geoscience and Remote Sensing 2008; 46(10): 3053–3062.

4. Essen H, Stanko S, Sommer R, *et al.* Millimetre wave SAR for UAV operation. Asia-Pacific Microwave Conference 2011:963–966.

5. Max F, Wahlen A, Peter W, *et al.* Processing of MIRANDA 35 FMCW-SAR data using a time-domain algorithm. EUSAR, Berlin, Germany 2014.

6. Rossum WV, Otten M, Dorp PV. Multichannel FMCW SAR, EUSAR, Nuremberg, Germany 2012: 279–282.

7. Edwards M, Madsen D, Stringham C, *et al*. microASAR: A small, robust LFM-CW SAR for operation on UAVs and small aircraft. IGASS 2008: 514–517.

8. Wit JJM. de, Meta A, Hoogeboom P. Modified range-doppler processing for FM-CW synthetic aperture radar., IEEE Geoscience and Remote Sensing Letters, 2006; 3(1): 83–87.

9. Meta A, Hoogeboom P, Ligthart LP. Signal processing for FMCW SAR. IEEE Transctions on Geoscience and Remote Sensing 2007; 45(11): 3519–3532.

10. Zaugg EC, Long D. Generalized frequency scaling and backprojection for LFM-CW SAR processing. IEEE Transaction. on Geoscience and Remote Sensing 2015; 53(7): 3600–3614.

11. Wang R, Loffeld O, Nies H, *et al*. Focus FMCW SAR data using the wavenumber domain algorithm. IEEE Transaction Geoscience Remote Sensing 2010; 48(4): 2109–2118.

12. Cafforio C, Prati C, Rocca F. SAR data focusing using seismic migration techniques. IEEE Transaction on Aerospace and Electronic Systems 1991; 27,(2): 194–207.

13. Cafforio C, Prati C, Rocca F. Full resolution focusing of Seasat SAR images in the frequency-wave number domain. International Journal of Remote Sensing 1991; 12(3): 491–510.

14. Reigber A, Alivizatos E, Potsis A, *et al.* Extended wavenumber-domain synthetic aperture radar focusing with integrated motion compensation. IEE Proceedigns-Radar, Sonar and Navigation 2006; 153(3): 301–310.

15. Zhang L, Sheng J, Xing M, *et al*. Wavenumber-domain autofocusing for highly squinted UAV SAR imagery. IEEE Sensors Journal 2012; 12(5): 1574–1588.

16. Xu G, Xing M, Zhang L, *et al.* Robust Autofocusing Approach for Highly Squinted SAR Imagery Using the Extended Wavenumber Algorithm, IEEE Transaction on Geoscience and Remote Sensing 2013; 51(10): 5031–5046.

17. Carrara WG, Goodman RS, Majewski RM. Spotlight synthetic aperture radar: signal processing algorithms. Artech House Remote Sensing Library, 1995.

18. Cumming IG, Wong FH. Digital processing of synthetic aperture radar. Artech House MA, USA, 2005.

19. Vandewal M, Speck R, Helmut. Efficient and precise processing for squinted spotlight SAR through a modified stolt mapping. EURASIP Journal on Advances in Signal Processing 2007: 1–7.

ORIGINAL RESEARCH ARTICLE

Integrating optical and microwave satellite observations for high resolution soil moisture estimate and applications in CONUS drought analyses

Donglian Sun[1]*, Yu Li[1], Xiwu Zhan[2], Chaowei Yang[1], Ruixin Yang[1]

[1] *Dept. of Geography and Geoinformation Science, George Mason University, Fairfax, VA 22030, USA. E-mail: dsun@gmu.edu*

[2] *NOAA/NESDIS Center for Satellite Applications and Research, College Park, MD 20742, USA.*

Abstract

In this study, optical and microwave satellite observations are integrated to estimate soil moisture at the same spatial resolution as the optical sensors (5km here) and applied for drought analysis in the continental United States. A new refined model is proposed to include auxiliary data like soil texture, topography, surface types, accumulated precipitation, in addition to Normalized Difference Vegetation Index (NDVI) and Land Surface Temperature (LST) used in the traditional universal triangle method. It is found the new proposed soil moisture model using accumulated precipitation demonstrated close agreements with the U.S. Drought Monitor (USDM) spatial patterns. Currently, the USDM is providing a weekly map. Recently, "flash" drought concept appears. To obtain drought map on daily basis, LST is derived from microwave observations and downscaled to the same resolution as the thermal infrared LST product and used to fill the gaps due to clouds in optical LST data. With the integrated daily LST available under nearly all weather conditions, daily soil moisture can be estimated at relatively higher spatial resolution than those traditionally derived from passive microwave sensors, thus drought maps based on soil moisture anomalies can be obtained on daily basis and made the flash drought analysis and monitoring become possible.

Keywords: Soil Moisture; High Spatial Resolution; Regional Drought; Microwave and Optical Satellite Remote Sensing

1. Introduction

Drought is considered to be the most severe natural hazard in terms of impact, duration, and spatial extent[1]. The sparse spatial distribution of weather stations makes it daunting for drought monitoring and predicting. Satellite remote sensing capabilities have been greatly improved for decades and served as the main method for drought monitoring. Drought may occur unnoticeably and varyingly. Lack of information to drought may lead to severe disaster. The damage was extensive and the impact to livestock and farm production is uncountable[2].

Government agencies within National Oceanic and Atmospheric Administration (NOAA) and United States Department of Agriculture (USDA) have teamed up with the National Drought Mitigation Center (NDMC) to produce a weekly drought monitor (DM) map that incorporates climate data and professional input from all levels and is well known as the U.S. Drought Monitor (USDM). The USDM maps are consensus product based on several indicators and key variables, and the final maps are adjusted manually by numerous experts throughout the country to reflect the real-world conditions as reported[3]. The

USDM drought conditions are classified into five classes based on a ranking percentile approach: (1) D0 - abnormally, (2) D1 - moderate, (3) D2 - severe, (4) D3 - extreme, and (5) D4 - exceptional dry conditions. They are utilized as (1) D0-D4 (percentile ≤30%), (2) D1-D4 (percentile ≤20%), (3) D2-D4 (percentile ≤10%), (4) D3-D4 (percentile ≤5%), and (5) D4 (percentile ≤2%)[3–5].

The USDM maps are currently distributed online (http://droughtmonitor.unl.edu/) with relatively coarse resolution. They served as one of the criteria to determine the eligibility for relief of aggravation due to drought condition.

Agricultural interest in drought is important in much of the U.S. In fact, there is considerable interest in indices that can monitor agricultural drought. The hydrological condition of agricultural drought is closely linked to soil moisture[6], which is dependent on precipitation, water infiltration, and soil water holding capacity. Since it's hard to measure soil moisture over large area directly, Leese *et al.* concluded it's better to monitor soil moisture with combination of in-situ model and remote sensed variables respond to soil moisture[7]. Satellite remote sensing data with large area coverage is a promising and economical tool to estimate soil moisture and enables drought monitoring based on surface parameters, such as NDVI, LST, evaportranspiration, and soil moisture. The microwave-optical/IR synergistic approach is an efficient method to improve the current drought-related soil moisture products with several advantages including higher spatial and temporal resolutions. Zhan *et al.* described a synergistic technique using optical/infrared frequency products to overcome the coarse spatial resolution of the MW satellite products[8]. This method was later enhanced by Chauhan *et al.*[9]. They built the statistical relationships between near-surface soil moisture and optical-derived soil moisture indices. Merlin *et al.* applied these relations and transferred this method to a wider range of conditions[10]. However, this method requires many surface parameters and micrometeorological data, which may not be available over large areas. It's desirable to find a simple and reasonable model for drought monitoring comparable to the

USDM drought classifications, and to explore the possibility for linking a real-time index with surface wetness condition in a fine resolution. In this study, a new approach to build a drought indicator at fine resolution are implemented with near real time microwave and optical satellite observations. After introduction of the study area and data used, specifics of these approaches and their results in analyzing drought conditions in the continental United States (CONUS, the latitude and longitude range is about 20 ~ 50 °N, and -125° ~ -75 °W) during the recent years are presented in the following sections.

2. Materials and methods

2.1 Data used

A comprehensive data set is collected and processed for deriving soil moisture at optical sensor resolution (5 km in this study) from satellite observations and evaluating drought conditions in the CONUS. These data include:

- MODIS LST and emissivity daily L3 global climate modeling grid (CMG) product (short name: MYD11C1) with a resolution of 0.05°[11].

- MODIS LST/emissivity 8-Day L3 CMG product (short name: MYD11C2) with a resolution of 0.05°[11].

- NDVI data is extracted from the MODIS 16-day composite NDVI product (short name: MYD13C1) with a resolution of 0.05°[12].

- Precipitation data are obtained from the TRMM (Tropical Rainfall Measuring Mission) Multi-satellite Precipitation Analysis (TMPA) with 0.25° spatial resolution and 3-hourly temporal resolution[13].

- Elevation data are derived from the National Elevation Dataset (NED) data at a resolution of 100 meters[14].

- MODIS land cover Climate Modeling Grid (CMG) product (Short Name: MCD12C1) provides the dominant land cover types at a spatial resolution of 0.05°.

- Soil texture data, including sand and porosity, are obtained from the Food and Agriculture Organization/United Nations Educational, Scientific and

Cultural Organization (FAO/UNESCO) soil map, with a resolution of about 0.0833°[15,16].

- Soil moisture data used for calibration is obtained from the Soil Moisture Operational Product System (SMOPS) at 0.25° resolution developed by NOAA-NESDIS. This SMOPS product merges soil moisture retrievals from microwave satellite sensors such as the Advanced Scatterometers (ASCAT) on MetOp-A and B, Soil Moisture and Ocean Salinity of European Space Agency, WindSat of Naval Research Lab based on the Single Channel Algorithm[17,18].

- Soil moisture outputs at 0.125° resolution from the three land-surface models (LSMs): the community Noah[19], the Mosaic[20], and the Variable Infiltration Capacity (VIC) model[21], are obtained from the North American Land Data Assimilation System (NLDAS)[22].

2.2 Temporal compositing and spatial resampling

The datasets used in this study were obtained at different temporal and spatial resolutions. All the datasets were needed to be resampled to the same resolution.

- For calibration using the SMOPS soil moisture (SM) data, all the datasets were aggregated to 25 km, the same resolution as the SMOPS SM data. The SM models were firstly built at 25 km resolution, then were applied to optical sensor data to estimate SM at the optical sensor resolution (5 km here).

- In order to compare with the USDM drought condition maps, all the datasets have been resampled or interpolated to uniform weekly (7 days) temporal and 0.0833° (about 12 km) spatial resolutions.

- For "flash" drought study, all the datasets were resampled or downscaled to the same 5 km spatial resolution as the MODIS LST product and estimate SM at 5 km spatial resolution on daily basis.

Land cover data has been resampled via the nearest neighbor assignment due to its discrete value. The bicubic interpolation assignment[23] was used to re-scale the other datasets, assuming that each point value changes consistently during observations.

2.3 Methods

2.3.1 A new model for high resolution soil moisture estimate

A close relationship exists between vegetation vigor and soil moisture availability, especially in arid and semiarid areas, thus in many cases satellite derived NDVI and LST products have been used to evaluate drought condition. Carlson *et al.* found the relationship between measured surface temperature, vegetation fraction, and soil moisture, known as the "Universal Triangle Model"[24]. Chauhan *et al.* argued that the second or third order polynomial gives a better representation of the data since a single polynomial represents a wide range of surface climate conditions and land surface types[9]. Thus a Universal Triangle Model was developed and can be described as:

$$
\begin{aligned}
SM = {} & a_{00} + a_{10} NDVI^{*} + a_{20} NDVI^{*2} \\
& + a_{01} LST^{*} + a_{02} LST^{*2} \\
& + a_{11} NDVI^{*} LST^{*} + a_{22} NDVI^{*2} LST^{*2} \\
& + a_{12} NDVI^{*} LST^{*2} + a_{21} NDVI^{*2} LST^{*}
\end{aligned}
\tag{1}
$$

where $NDVI^{*} = \dfrac{NDVI - NDVI_{\min}}{NDVI_{\max} - NDVI_{\min}}$, $LST^{*} = \dfrac{LST - LST_{\min}}{LST_{\max} - LST_{\min}}$, sub-scripts max and min refer to the maximum and minimum values. Parameters a_{00}, a_{10}, …, a_{22} are the regression coefficients.

Sun and Kafatos[25] indicated the negative or reverse relation between NDVI and LST can only hold during warm or growing seasons, therefore, NDVI and LST related drought indices may only be used during warm seasons, but not winter. Chauhan *et al.* added surface albedo into the Universal Triangle Model to strengthen the relationship between soil moisture and measurable land surface parameters[9]. Nevertheless, surface types vary significantly, and therefore, even a combination of NDVI, LST or albedo is not enough to fully describe the surface conditions. Soil moisture is also highly related to precipitation (the land water balance equation indicates the change of soil moisture is highly related to precipitation), soil texture (physical properties such as dielectric constant can affect water content in soil), topography (runoff is highly related to the topographic position, slope aspect, and steepness), and

land cover (different land cover will influence the hydrological processes differently). LC data are numerical values. According to the product user guide (https://lpdaac.usgs.gov/sites/default/files/public/product_documentation/mcd12_user_guide_v6.pdf), the LC value range is from 1–17 and is assigned as: Evergreen Need leaf Forest as 1, Evergreen Broadleaf Forests as 2, Deciduous Needleleaf Forests as 3, Deciduous Broadleaf Forests as 4, Mixed Forests as 5, Closed Shrublands as 6, Open Shrublands as 7, Woody Savannas as 8, Savannas as 9, Grasslands as 10, Permanent Wetlands as 11, Croplands as 12, Urban and Built-up Lands, Cropland/Natural Vegetation Mosaics as 14, Permanent Snow and Ice as 15, and Barren as 16, and Water Bodies as 17. Thus it is desirable to combine and integrate all these datasets to build a soil moisture model as:

$$SM = b_0 + b_1 NDVI^* + b_2 NDVI^{*2} + b_3 LST^* + b_4 Pr + b_5 DEM + b_6 Sand + b_7 Poro + b_8 LC \qquad (2)$$

where "Pr" represents precipitation, "DEM" is for Digital Elevation Model (DEM) data, "$Sand$" is the individual grains or particles which can be seen with the naked eyes, "$Poro$" refers to porosity about how many pores/holes a soil has, and "LC" is for land cover data. b_0, b_1, …, b_8 are regression coefficients.

As shown in **Figure 1**, the black line in Figure 1b is the corresponding normalized monthly accumulated precipitation, and the LOWESS (Locally Weighted Scatterplot Smoothing)[26] is applied to describe the nonlinear trends of precipitation (the blue line in **Figure 1b**). The drought condition may not be directly reflected by temporal variation in precipitation because drought is caused by precipitation deficit during some period of time, usually more than a season. It is found that precipitation has an accumulating and lagging effect on drought condition. For example, the trend of precipitation is reduced in 2006 and 2011 (**Figure 1b**), yet the USDM drought maps marked these years as normal conditions (**Figure 1a**) due to sufficient accumulated rainfall in previous period. While in 2014, the precipitation had increasing trend, but short of accumulated rainfall from the previous period in 2013 and early 2014, thus the USDM classified year 2014 as drought con-

dition. This result demonstrated that the accumulated precipitation from the last year's warm season to the current time can describe the drought conditions better than the daily precipitation. Therefore, a refined soil moisture model is proposed by using the accumulated precipitation starting from the last year's warm season. The refined soil moisture model can be described as:

$$SM = c_0 + c_1 NDVI^* + c_2 NDVI^{*2} + c_3 LST^* + c_4 Ac\_Pr + c_5 DEM + c_6 Sand + c_7 Poro + c_8 LC \qquad (3)$$

where Ac_Pr is for the accumulated precipitation starting from April of the previous year until the requested day, all other variables are the same as Equation (2). c_0, …. c_8 are the regression coefficients.
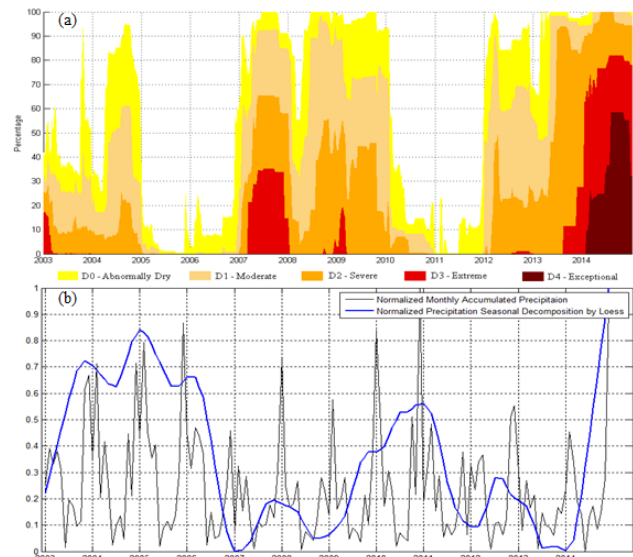
Figure 1. (a) The USDM weekly drought condition map; (b) normalized monthly accumulated precipitation over California (32 - 42 °N, 114 - 125 °W) retrieved from the TRMM, and normalized monthly accumulated precipitation seasonal decomposition by the LOWESS (blue line), from Jan. 2003 to Dec. 2014.

The SMOPS soil moisture products were used for calibration to derive the regression coefficients in Equations (1), (2), and (3). The least square regression was applied to estimate the regression coefficients and 50% data were used for training.

2.3.2 Anomaly calculation

Soil moisture changes slowly, therefore cannot catch the fast change of drought conditions. Soil moisture anomaly is more appropriate to describe

drought conditions than the absolute soil moisture[27]. In this study, we averaged daily soil moisture into weekly to match with the UM drought maps temporally. Soil moisture anomaly maps are obtained by the difference between weekly soil moisture and the long-term average soil moisture based on the equation:

$$SM\_Anomaly = SM - \overline{SM} \quad (4)$$

where the average soil moisture $\overline{SM}$ for each pixel is calculated for the same weeks over the 11 years from January 1 2003 to December 31 2014. Negative soil moisture anomalies stand for the observed data are lower than the averaged data, and indicate dry conditions.

2.3.3 Comparison with some other drought indices

- Evaporative Stress Index (ESI)

The ESI is defined as the anomalies in the ratio of actual-to-potential ET (AET/PET), derived from the thermal remote sensing based on the Atmosphere-Land Exchange Inverse (ALEXI) surface energy balance model[28–31]. The ALEXI uses measurements of morning land-surface temperature retrieved from geostationary satellite thermal band imagery to solve the Two-Source Energy Balance (TSEB) algorithm[32] in time-differential model. Actual ET (AET) output from the ALEXI is estimated as the potential ET (PET) expected under non-moisture limiting conditions, yielding a non-dimensional ET variable, ESI, ranging from 0 (dry) to approximately 1 (wet).

- Vegetation Health Index (VHI)

Kogan *et al.* proposed to combine the Vegetation Condition Index (VCI) and the Temperature Condition Index (TCI) to Vegetation Health Index (VHI)[33]:

$$VHI = a * VCI + b * TCI \quad (5)$$

where the coefficient a and b are usually taken as 0.5. The VCI is defined as:

$$VCI = \frac{NDVI - NDVI_{min}}{NDVI_{max} - NDVI_{min}} \quad (6)$$

where $NDVI_{max}$ and $NDVI_{min}$ are the multi years maximum and minimum $NDVI$ in a given area for growing season. The TCI is defined by Kogan[34] as:

$$TCI = 100 \times (BT_{max} - BT_i)/(BT_{max} - BT_{min}) \quad (7)$$

where BT, BT_{max}, and BT_{min} are smoothed brightness

temperature, its maximum and minimum, respectively calculated for each pixel and week from multiyear data, and i is the year.

The Center for Satellite Applications and Research (STAR) of NOAA Satellite and Information Service (NESDIS) is providing global VCI, TCI, and VHI map every week at: http://www.star.nesdis. noaa.gov/smcd/emb/vci/VH/vh_browse.php.

- Vegetation Temperature Condition Index (VTCI)

Wang *et al.* developed Vegetation Temperature Condition Index (VTCI) based on the triangular space of LST and NDVI for monitoring drought stress[35]. It's defined as following:

$$VTCI = \frac{LST_{NDVIi.max} - LST_{NDVIi}}{LST_{NDVIi.max} - LST_{NDVIi.min}} \quad (8)$$

where $LSTNDVI_{i.max}$ and $LSTNDVI_{i.min}$ are the maximum and minimum land surface temperature of pixels which have the same $NDVI_i$ value, respectively, $LSTNDVI_i$ denotes land surface temperature of one pixel whose $NDVI$ value is $NDVI_i$. If $VTCI(i) < 0.4$, then the area (i) is under severe drought condition.

2.3.4 Correlation analyses

The temporal correlation coefficients are computed between the outputs from the refined soil moisture model and the USDM drought classifications at weekly scales during the growing season from April to October of each year.

3. Results

Figure 2 demonstrates drought conditions over the contiguous U.S. based on soil moisture anomalies (the first 8 rows) and percentiles (bottom) derived from the refined model and compared with the USDM drought maps (the first row), the VTCI (the second row), the VHI (the third row), the ESI (the fourth row), and soil moisture anomalies from the Mosaic LSM (the five row), the community Noah LSM (the six row), and the VIC LSM (the seven row) for drought conditions from 2005 to 2010 (6 years).
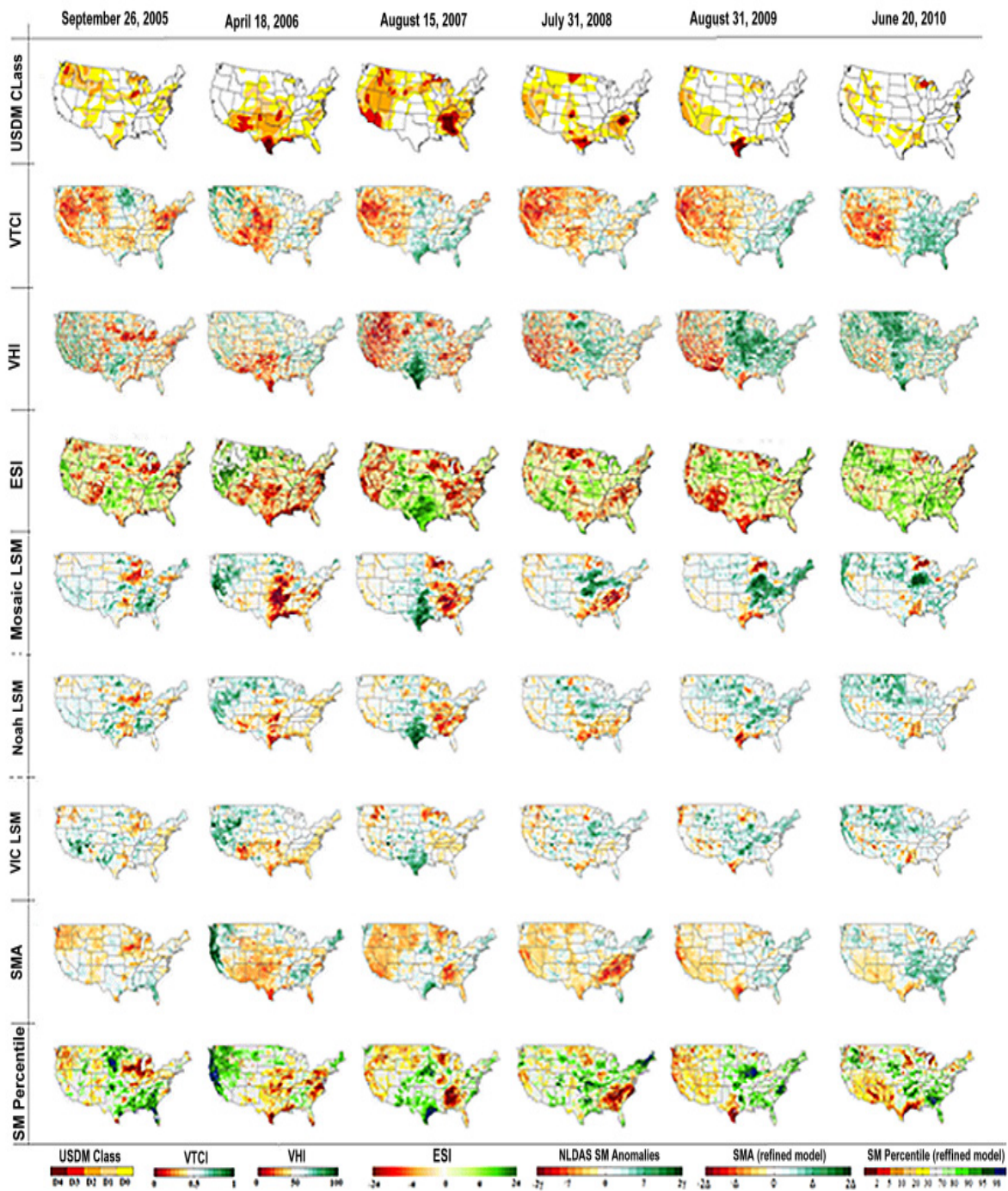
Figure 2. Drought conditions in the contiguous U.S. from different indicators. From top to bottom: the USDM classification (top), VTCI (the 2nd), VHI (the third), ESI (the fourth), the Mosaic LSM (the five), the Noah LSM (the sixth), the VIC LSM (the seventh), soil moisture anomalies based on the refined model (the eighth), and the soil moisture percentile (the bottom) based on the refined model. The three LSMs (Mosaic, Noah, and VIC) share the same color palette**.**

It is found the percentile of soil moisture cannot easily catch the fast changes, so percentile of soil moisture anomalies is used instead. The VHI and ESI show good agreements with the USDM classifica-tions, while the NLDAS three LSM outputs demon-strate similar patterns. The soil moisture derived from the proposed soil moisture model provides an easy way for monitoring surface drought conditions,

98

and the surface dry/wetness patterns agree with the USDM classifications.

Figure 3 shows the temporal correlation coefficients between the soil moisture anomalies derived from the refined model and the USDM drought classes during different years from 2005 to 2010, where greener color indicates a better agreement between the two classifications. In general, the refined soil moisture model outputs have high correlations with the USDM drought classifications. The statistical metrics of Averaged Temporal Correlation Coefficients are also listed in **Table 1**. In general, the basic model with the introduction of soil texture data

show improvement to the triangle model, while the refined model outputs have higher correlation with the USDM drought classifications and show further improvement to the basic model.

Recently, "flash" drought concept appears. Flash drought frequently occurred in the central and eastern United States[36]. The 2012 drought over the Northern American demonstrated the worst surface condition since the 1930s Dust Bowl[37]. The drought started in 2011, extended rapidly in 2012 (especially in June and July according to the USDM classifications), and continued in 2013. This event was pervasive in the central regions of the United
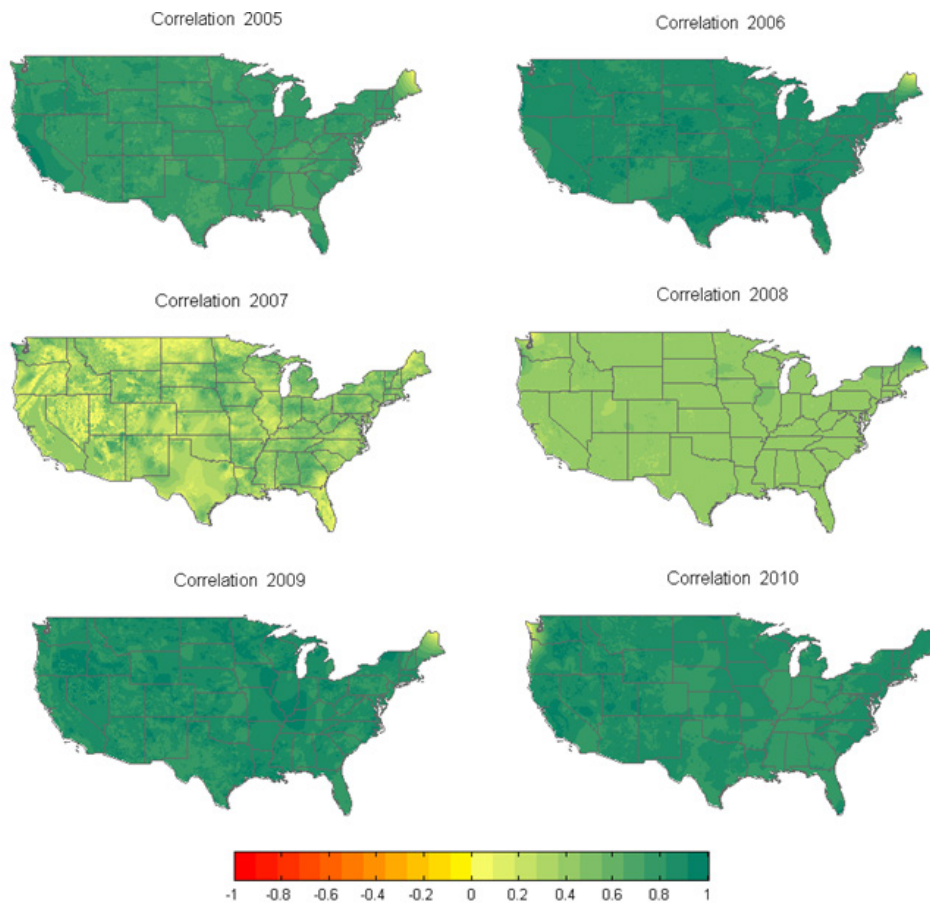
Figure 3. The temporal correlation coefficient maps between the refined soil moisture model outputs and the USDM drought classifications during different years**.**

Table 1. The statistical metrics of Averaged Temporal Correlation Coefficients between the soil moisture outputs from the three different models and USDM classifications

SM models\years	2005	2006	2007	2008	2009	2010
Triangle model	0.245	0.548	0.105	0.219	0.460	0.298
Basic model	0.672	0.720	0.382	0.557	0.486	0.423
Refined model	0.748	0.773	0.599	0.618	0.766	0.759

States due to the absence of rainfall in the growing season. The rapid soil moisture loss led this event as "flash drought"[38]. Unlike the common drought that is caused by external forcing like SST anomalies, the flash drought event was a result of natural weather variations, with little warnings found from the traditional drought metrics or climate model simulations[39]. The flash drought event suggests that the current drought monitoring should enhance its temporal resolution.

In the above drought analyses as shown in **Figure 2** and **Figure 3**, the LST input to the soil moisture model is the weekly composite data. Because thermal infrared (TIR) LST can only be obtained under clear conditions, as shown in **Figure 4a**, there are a lot of gaps or missing values due to clouds in the daily MODIS LST. Only weekly composite can get a clear LST map. Since microwave sensor can penetrate most non-rainy clouds and observe the Earth surface, so we think about using microwave observations to fill the gaps due to clouds in the thermal IR LST. The microwave observations will be firstly calibrated to thermal IR (MODIS here) LST, and then

downscaled to the same spatial resolution as the TIR LST, and then merged with the TIR observations to fill the gaps due to clouds in the TIR LST. The detailed information and processes are described in another paper[40]. Here we show an example in **Figure 4**. As demonstrated in **Figure 4**, the original daily MODIS LST exist a lot of gaps due to clouds (**Figure 4a**), while the LST derived from the AMSR-E with a new proposed five-channel algorithm[40] can get a clear and spatial continuous distribution (**Figure 4b**). **Figure 4c** is the merged MODIS and AMSR-E LST by using the AMSR-E to fill the gaps in the MODIS LST, and **Figure 4d** shows the integrated MODIS and AMSR-E LST by applying the geographically weighted regression (GWR) method to downscale the AMSR-E LST to the same MODIS resolution and further fill the pass gaps in the AMSR-E observations. With the integrated MODIS and AMSR-E LST, spatial continuous LST on a daily basis can be input into the proposed refined SM model to obtain soil moisture anomaly every day. The flow chart of the process is shown in **Figure 5**.

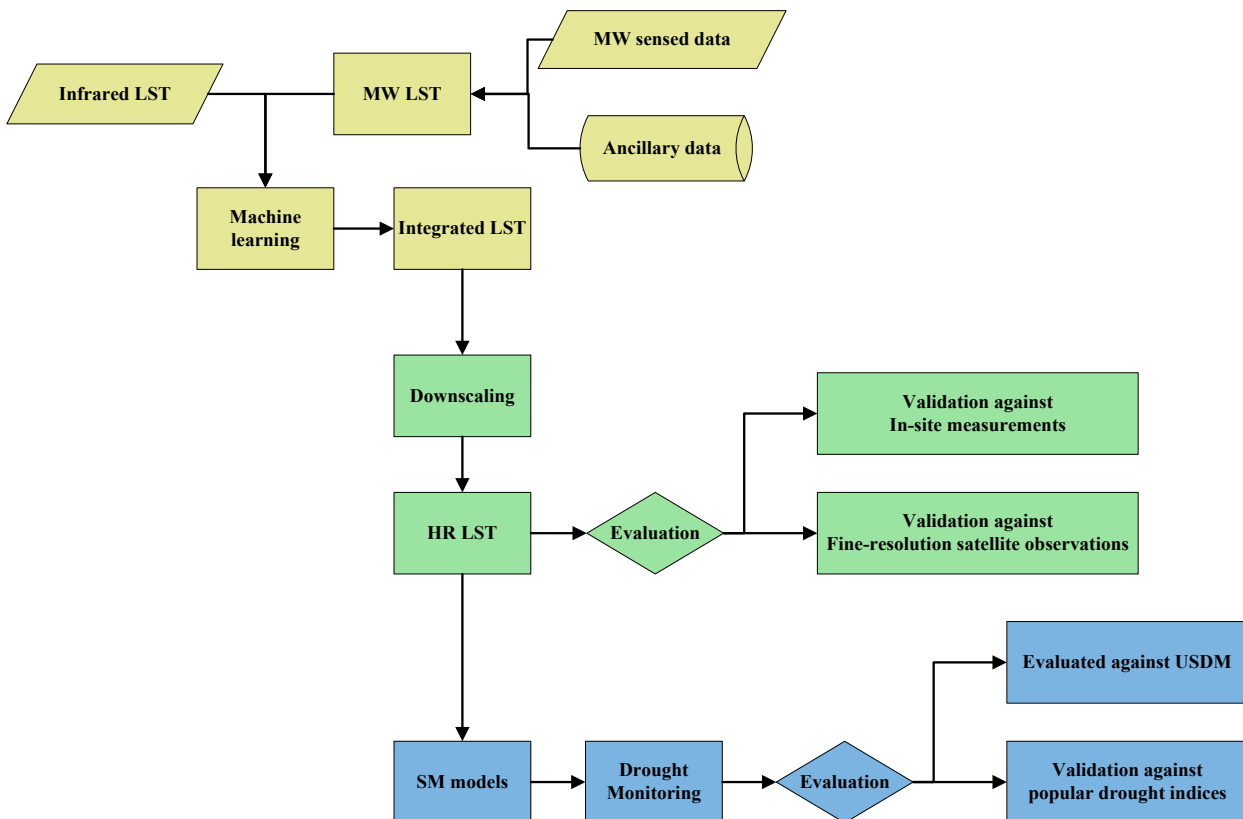The USDM as well as other drought indicators

Figure 5. The flow-chart for soil moisture estimate and application in drought analysis.
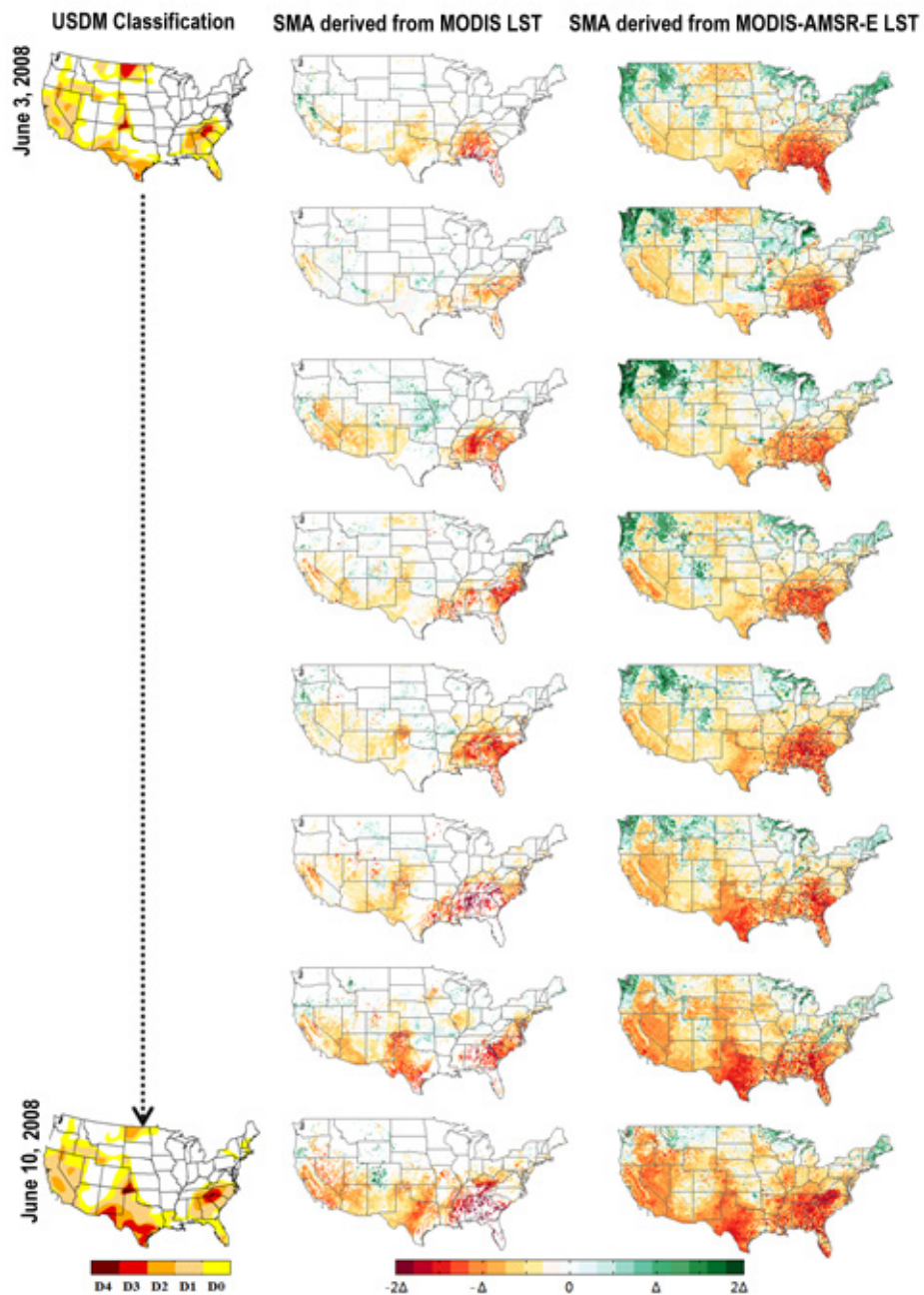
Figure 6. An example of daily SM anomalies compared with the weekly USDM drought map**. First column: weekly USDM observations. Soil moisture anomalies observations in the continuous 8 days (from June 3 to June 10); second column: based on previous LST and third column: based on the new derived Example-based LST. Δ equals to 0.02 (unit: m3m-3).

can provide a weekly drought monitoring, while the new algorithm can provide soil moisture anomaly observations on a daily basis. The previous LST product that input into the soil moisture model is lack of observations due to clouds, and made the observation of soil moisture anomalies with gaps (**Figure 6**, the second column, white area is lack of observation, thus is considered as in the normal surface condition). With the TIR and microwave integrated LST, daily soil moisture anomalies can be obtained continuously without gaps (**Figure 6**, the third column). It matches with the USDM drought maps, and meanwhile catches the flash changes of dought conditions.

101

Figure 4. (a) Cloud free MODIS LST at 5 km resolution; (b) the derived AMSR-E LST at 25 km resolution; (c) the merged MODIS and AMSR-E LST at 25 km resolution; (d) the integrate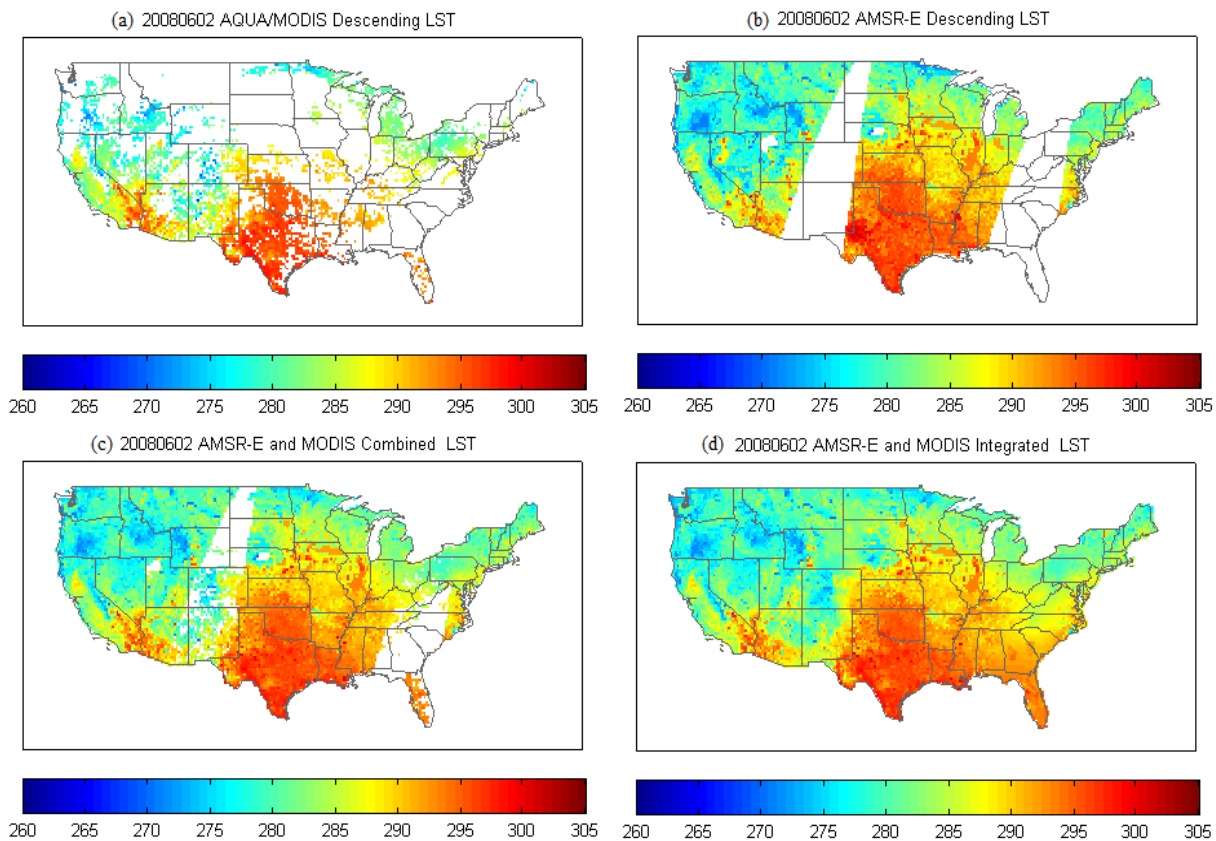d LST from MODIS and AMSR-E with the GWR-based method applied to fill the gaps and also downscale to the same 5 km resolution as the MODIS LST, during daytime on June 2, 2008.

4. Discussion and conclusion

In this study, we integrated microwave and optical sensors to estimate soil moisture at high spatial resolution and used them to evaluate drought conditions in the continental United States. A new model is proposed to estimate soil moisture with the auxiliary data such as precipitation, topography, soil texture, and surface types, in addition to LST and NDVI used in traditional universal triangle model. We further applied the LOWESS model based on time series analysis, and found precipitation had some kind of accumulated and lagging effects on soil moisture, therefore we proposed to use accumulated precipitation starting from last year's warm season, instead of daily precipitation. The drought conditions identified by the soil moisture anomalies derived from the proposed model show close agreement with the USDM classifications.

There are still some limitations in this study: (1) this application was limited to the warm season, while cold season needs further investigation to fulfill the requirement of surface monitoring; (2) to further improve the applications, more agricultural related data should be examined. Since our model output can also provide the information of wetness level, agricultural related data such as irrigation, should be used as an important evaluation for the outputs.

Conflict of interest

The authors declare that they have no conflict of interest.

Acknowledgments

References

1. Kousky C. Informing climate adaptation: A review of the economic costs of natural disasters. Energy Economics 2014; 46: 576–592.

2. Wilhite DA, Glantz MH. Understanding: The drought phenomenon: the role of definitions. Water International 1985; 10(3): 111–120.

3. Svoboda M, LeComte D, Hayes M, *et al*. The drought monitor. Bulletin American Meteorological Society 2002; 83(8): 1181–1190.

4. Mote PW. Climate-driven variability and trends in mountain snowpack in Western North America. Journal of Climate 2006; 19(23): 6209–6220.

5. Xia YL, Ek MB, Peters-Lidard CD, *et al*. Application of USDM statistics in NLDAS-2: Optimal blended NLDAS drought index over the continental United States. Journal of Geophysical Research-Atmosphere 2014; 119(6): 2947–2965.

6. Bolten JD, Crow WT, Zhan XW, *et al*. Evaluating the utility of remotely sensed soil moisture retrievals for operational agricultural drought monitoring. IEEE Journal of Selected Topics in Applied Earth Observation and Remote Sensing 2010; 3(1): 57–66.

7. Leese J, Jackson T, Pitman A, *et al*. Meeting summary: GEWEX/BAHC international workshop on soil moisture monitoring, analysis, and prediction for hydrometeorological and hydroclimatological applications. Bulletin of American Meteorological Society 2001; 82(7): 1423–1430.

8. Zhan X, Miller S, Chauhan N, *et al*. Soil moisture visible/infrared radiometer suite algorithm theoretical basis document. Lanham, MD: Raytheon Syst. Company; 2002.

9. Chauhan NS, Miller S, Ardanuy P. Spaceborne soil moisture estimation at high resolution: a microwave-optical/IR synergistic approach. International Journal of Remote Sensing 2003; 24(22): 4599–4622.

10. Merlin O, Walker JP, Chehbouni A, *et al*. Towards deterministic downscaling of SMOS soil moisture using MODIS derived soil evaporative efficiency. Remote Sensing Environment 2008; 112(10): 3935–3946.

11. Wan ZM, Dozier J. A generalized split-window algorithm for retrieving land-surface temperature from space. IEEE Transactions on Geoscience and Remote Sensing 1996; 34(4): 892–905.

12. Huete A, Justice C, Van Leeuwen W. MODIS vegetation index (MOD13): Algorithm theoretical basis document. 1999.

13. Huffman GJ, Bolvin DT, Nelkin EJ, *et al*. The TRMM multisatellite precipitation analysis (TMPA): Quasi-global, multiyear, combined-sensor precipitation estimates at fine scales. Journal of Hydrometeorology 2007; 8 (1): 38–55.

14. Gesch D, Oimoen M, Greenlee S, *et al*. The national elevation dataset. Photogrammetric Engineering and Remote Sensing 2002; 68(1): 5–32.

15. Henkel M. 21st century homestead: Sustainable agriculture I. Lulu. com.; 2015. p. 98–103.

16. Batjes NH. A world dataset of derived soil properties by FAO–UNESCO soil unit for global modelling. Soil Use and Management 1997; 13(1): 9–16.

17. Jackson TJ. III. Measuring surface soil moisture using passive microwave remote sensing. Hydrological Processes 1993; 7(2): 139–152.

18. Zhan X, Liu J, Zhao L, *et al*. Soil moisture operational product system (SMOPS): Algorithm theoretical basis document. 2011.

19. Ek MB, Mitchell KE, Lin Y, *et al*. Implementation of Noah land surface model advances in the National Centers for Environmental Prediction operational mesoscale Eta model. Journal of Geophysical Research: Atmospheres 2003; 108(D22): 8851.

20. Koster RD, Suarez MJ. The influence of land surface moisture retention on precipitation statistics. Journal of Climate 1996; 9(10): 2551–2567.

21. Liang X, Wood EF, Lettenmaier DP. Surface soil moisture parameterization of the VIC-2L model: Evaluation and modification. Global and Planetary Change 1996; 13(1-4): 195–206.

22. Xia Y, Mocko D, Huang M, *et al*. Comparison and assessment of three advanced LSMs in simulating terrestrial water storage components over the U.S. Journal of Hydrometeorology 2017; 18: 625–649.

23. Keys RG. Cubic convolution interpolation for digital image processing. IEEE Transactions on Acoustics, Speech, and Signal Processing1981; 29(6): 1153–1160.

24. Carlson TN, Gillies RR, Perry EM. A method to

make use of thermal infrared temperature and NDVI measurements to infer surface soil water content and fractional vegetation cover. Remote Sensing Reviews 1994; 9(1-2): 161–173.

25. Sun DL, Kafatos M. Note on the NDVI-LST relationship and the use of temperature-related drought indices over North America. Geophysical Research Letters 2007; 34(24).

26. Cleveland WS. Robust locally weighted regression and smoothing scatterplots. Journal of the American Statistical Association 1979; 74(368): 829–836.

27. Reichle RH, Koster RD. Global assimilation of satellite surface soil moisture retrievals into the NASA Catchment land surface model. Geophysical Research Letters 2005; 32(2): L02404.

28. Anderson MC, Hain C, Otkin J, *et al*. An intercomparison of drought indicators based on thermal remote sensing and NLDAS-2 simulations with US Drought Monitor classifications. Journal of Hydrometeorology 2013; 14(4): 1035–1056.

29. Anderson MC, Hain C, Wardlow B, *et al.* Evaluation of drought indices based on thermal remote sensing of evapotranspiration over the continental United States. Journal of Climate 2011; 24(8): 2025–2044.

30. Anderson MC, Norman JM, Mecikalski JR, *et al.* A climatological study of evapotranspiration and moisture stress across the continental United States based on thermal remote sensing: 1. Model formulation. Journal of Geophysical Research: Atmospheres 2007; 112(D10).

31. Anderson MC, Norman JM, Mecikalski JR, *et al.* A climatological study of evapotranspiration and moisture stress across the continental United States based on thermal remote sensing: 2. Surface moisture climatology. Journal of Geophysical Research: Atmospheres 2007; 112(D11).

32. Norman JM, Kustas WP, Humes KS. Source approach for estimating soil and vegetation energy fluxes in observations of directional radiometric surface temperature. Agricultural and Forest Meteorology 1995; 77(3): 263–293.

33. Kogan FN. Global drought watch from space. Bulletin American Meteorological Society 1997; 78(4): 621–636.

34. Kogan FN. Application of vegetation index and brightness temperature for drought detection. Advanced Space Research 1995; 11: 91–100.

35. Wang P, Li X, Gong J, Song C. Vegetation temperature condition index and its application for drought monitoring. In Geoscience and Remote Sensing Symposium 2001; 1: 141–143.

36. Lorenz DJ, Otkin JA, Svoboda M, *et al*. Predicting the US Drought Monitor (USDM) using precipitation, soil moisture, and evapotranspiration anomalies. Part II: Intraseasonal drought intensification forecasts. Journal of Hydrometeorology 2017; 18: 1963–1982.

37. Grigg NS. The 2011–2012 drought in the United States: new lessons from a record event. International Journal of Water Resources Development 2014; 30(2): 183–199.

38. Otkin JA, Anderson MC, Hain C, *et al*. Assessing the evolution of soil moisture and vegetation conditions during the 2012 United States flash drought. Agricultural and Forest Meteorology 2016; 218: 230–242.

39. Hoerling M, Eischeid J, Kumar A, *et al*. Causes and predictability of the 2012 Great Plains drought. Bulletin of the American Meteorological Society 2014; 95(2): 269–282.

40. Sun D, Li Y, Zhan X, *et al*. Land surface temperature derivation under all sky conditions through integrating AMSR-E/AMSR-2 and MODIS/GOES observations. Remote Sensing 2019; 11(14): 1704.

REVIEW ARTICLE

A review of the research on externality of urban network

Yuhong Cheng, Xiaomin Su*

School of Economics, Jinan University, Guangzhou 510632, China. E-mail: sgcyh@163.com/suxiaomin@stu2018.jnu. edu.cn

ABSTRACT

Urban network research has become the frontier academic field of international urban research and has gradually become a hot spot. At present, the related literature on "urban network" mostly focuses on conceptual discussion, dimension analysis, and network structure analysis. Research on the influence of network on regional economic development is relatively weak. Externality, as an essential attribute of urban network, is of great significance to the evolution of urban network and the development of cities and regions. This article starts from a comparison of agglomeration externalities with urban network externalities, focusing on the review and evaluation of the formation mechanism, utility, and measurement methods of urban network externalities.

The synergy effect, integration effect, and borrowing size are considered important reasons for the formation of urban network externalities. The research on the effectiveness of urban network externalities focuses on two aspects. The first is the role of factor mobility in promoting knowledge diffusion and innovation, and the second is the impact of urban network on competitiveness and economic growth. Based on the existing literatures, the research on the measurement of urban network externalities mainly involves identification and estimation, including three common methods as correlation analysis, regression analysis, and spatial econometric analysis. The existing empirical researches on externalities are still mostly based on static analysis and lack dynamic consideration. The issues that need further attention in the future include theoretical understanding of urban network externalities, externality measurement methods, and empirical research.

Keywords: Urban Network; Externalities; Regional Development; Review

1. Introduction

Since the middle and late 20th century, with the rapid development of transportation, information and communication technology, the profound change of enterprise spatial organization mode and the rapid expansion of modern producer services provide more and more opportunities for various formal and informal exchanges between cities. The cross-border resource flow between cities has shown an increasingly important role for urban regional development in the era of globalization. In this context, the central theory emphasizing the vertical rank relationship between cities is increasingly limited in the interpretation of urban interactions. With the proposal of Castells's "The space of flows" [1], people's understanding to the nature of urbans began to expand from place space to flow space, and the urban research paradigm began to shift from rank to network. For more than a decade, more and more scientific literatures began to focus on the research of "urban networks"[2]. Statistical analysis of the literatures shows that from 2000 to 2008, literatures on the urban network research rose steadily and the keywords

such as "world urban network", "urban external connection" and "interlocking network model" appeared more frequently, indicating the relevant research entered the exploration stage; The number of literatures boomed significantly from 2009 to 2020. During this period, research methods on exploring the structures, hierarchy and relevancy of urban network were more diversified[3]. In general, the current literature on "urban network" mainly focuses on concept discussion, scale analysis and network structure analysis, and the impact of the network on regional economic development is rarely explored. In fact, externality, as an essential attribute of urban network, is of great significance to the evolution of urban network and the development of a city or a region. Therefore, it is necessary to discuss the externalities produced in the evolution of the urban network. After comparing and analyzing the agglomeration externality and urban network externality, this paper combs and evaluates the research on urban network externality from the formation mechanism, utility and measurement methods, in order to provide some reference for relevant studies in future.

2. From agglomeration externality to urban network externality

Agglomeration externality evolved and developed along with the development of the agglomeration economy. The agglomeration economy appeared in some countries and regions as early as the 18th century. In the middle and late 20th century, scholars began to carry out more extensive and in-depth studies on the agglomeration economy. Agglomeration economy usually refers to the clustering phenomenon of economic activity in geographical space, which mainly manifested as the industrial groups or interdependent economic network[4] formed by the same (similar) industries or complementary industries concentrated in a specific or adjacent geographical location. The very important reason for the agglomeration economic phenomenon is the existence of agglomeration externality. Rosenthal et al.[5] gives a concise definition of agglomeration externality, known as the additional benefits of economic behavioral agents from being in the same region. How-

ever, this acquisition of additional benefits is often constrained by the spatial size of agglomeration, and Duranton et al.[6] found that most local agglomeration occurs within 50 km, implying that agglomeration externality is likely a nonlinear function of distance. In fact, in the classical theoretical interpretation, distance cost is always the most important centrifugal force for agglomeration equilibrium. With the rise of urban network theory, the distance cost relatively declined[7].

Network externalities can firstly be traced back to the articles written by Katz et al.[8], published in *American Economic Review*, who believe that network externality is shown as that the utility that a user gets from consumer goods increases with the number of other users, namely, the utility that users get from goods depends on the number of other users in the same network. Unlike Katz et al.'s research on network externalities from the perspective of consumer economics, Capello[9] introduces network externalities into the field of urban network research. Capello regards the urban network as a real "club", and only a participant in the network economy cooperation can obtain the network advantage, which is the externality of the network. According to Lin Bingxi et al.[10], agglomeration externality limits agglomeration economy within cities or administrative boundaries, while ignoring the fact of cross-regional connection. The cross-regional connection between enterprises and cities promotes the agglomeration externality towards the network externality across geographical boundaries. Clearly, urban network externality emphasizes the benefits resulted from connections between cities, while agglomeration externality emphasizes the proximity of geographical location, which significantly differ in effector generation mechanisms. In addition, there are also great differences in the understanding of the degree of agglomeration externality and network externality on urban development. One view emphasizes the role of agglomeration in urban development. For example, Boix et al.[11] incorporate the agglomeration externality and network externality into the urban economic development model, and find that the contribution rate of agglomeration externality is greater to the

economic development than the network externality, so they believes that agglomeration is more important than the network to some extent. The other view is just the opposite, arguing that network externality can replace agglomeration externality. For example, Johansson *et al*.[12] points out its alternative possibility from three perspectives: First, the improvement of transaction conditions enables the network to replace the distance advantage of agglomeration; Second, the standardization of complex goods and services enables the decentralized distribution of production activities; Third, the network can more effectively promote knowledge diffusion and overflow. In general, Johansson *et al*. emphasized the substitutability of network behavior for agglomeration activity under the premise of technological progress. However, more scholars do not directly compare the degree of influence, but believe that the network externality can make up for the disadvantages of agglomeration externality. For example, through the research on the knowledge service industry in urban agglomeration, Gluckler[13] believes that the agglomeration externality is applicable to explain the industry growth phenomenon in the product value chain, while the knowledge service industry does not rely on the product value chain, and the network externality is an important reason for the growth of the knowledge service industry in urban agglomeration. Cabus *et al*.[14] further analyzed the relationship between the two, believing that the proximity of geographical location first promotes the agglomeration externality, and the network externality, as the embodiment of the external economy related to the network itself, is promoted by regional competition. The combination of the two carries out complex geographical transformation in a series of network fields. Therefore, when discussing the externality of the urban network, it should not be opposed to the agglomeration externality. In fact, agglomeration externality is an important reason for cities, and also an important theoretical tool to explain the urban formation and development of urban economics in the early stage. From this perspective, agglomeration externality is usually aimed at single cities, suitable for small urban spatial scale, which has significant distance sensitivity. Whereas,

network externality is based on the network paradigm of urban research, with a single city as the basic analysis unit, focusing on a large regional spatial scale, urban relationship and the theoretical interpretation tool produced by the relationship's impact on urban development. Obviously, in most cases, there is no practical significance of directly comparing the impact size of agglomeration externality and network externality on urban development, and they always complement each other.

3. Formation mechanism of urban network externality

The essence of urban network externality is the benefits the cities get from joining the urban network, and tends to focus on the overflow degree of urban benefits connected to the network. When studying the formation mechanism of urban network externality, special attention should be paid to the interaction between cities and its impact. In conclusion, the theoretical discussion and analysis of the formation mechanism of urban network externality are mainly conducted from the following three perspectives.

3.1 Urban synergy effects

Urban synergy effects are considered to be the most important reason for the formation of urban network externalities, mainly involving two relationships between cities, namely, cooperation and complementarity. Camagni *et al*.[15] believe that urban network externalities may come from the transmission of expertise flows in the same industry (collaborative) or in different industries (complementary). Batten[16] believes that network cities will develop when two or more cities achieve a scope economy under cooperation. Obviously, in earlier discussions, the three concepts of cooperation, complementarity, and collaboration, are often used indiscriminately as the cause of the formation of network externalities. Meijers[17] distinguishes them, thinking that synergy effects refer to the state where two or more cooperative or combined individuals have greater utility than the sum of single individual utility, often expressed by the formula as "1 + 1 > 2". That is to say, when

these close cities are interconnected in a synergistic way, the entire city network exceeds the sum of the parts. Such cities with similar characteristics often have the characteristics of "club" when they unite to achieve some common goals or common interests. Usually, club members cannot afford large facilities individually, but it can be achieved through the club, and more members have positive external effects such as lower membership fees or longer opening time (negative externalities happen when all members want to use club equipment at the same time). When heterogeneous cities play different economic roles and have complementary urban facilities and environment, the urban network is similar to the spider-like web network. Specifically, when two cities become complementary, residents and businesses in one city can take advantage of the various functions offered by another city, whose function are always more specialized because the demand markets they build will become larger when the hinterland overlaps. At the same time, in this way, companies, urban residents and visitors can choose a larger and more professional as well as diverse urban functions, business and residential environment. Therefore, the cooperation, complementarity, externality mechanisms and synergy effects resulted from cooperation and complementarity are achieved. As Meijers[17] concludes homogeneous cities form horizontal synergies through cooperation while heterogeneous cities form longitudinal synergies through complementation, both containing externalities and representing the most important economic advantage in network behavior.

3.2 Urban integration effect

Different from the perspective of the urban relationship, the urban integration effect mainly discusses the formation mechanism of the network externality from the systemic perspective. Integration effects generally refer to the process of connecting scattered things together to form resource sharing and collaborative work, so as to achieve a valuable and efficient overall process. Van Oort et al.[18] first analyzed from the perspective of spatial integration, arguing that spatial integration between cities facilitates acceler-

ating information flow and enhancing connections between cities due to improved transportation and communication. Meijers et al.[19] further proposed the concept of functional integration, institutional integration, and cultural integration, arguing that cities enhance the systematic cohesion of urban networks through functional integration, thus promoting economic complementarity between cities. Institutional integration, on the one hand, promotes the functional integration, and on the other hand also improves the organizational capacity of the region to further share existing resources; Cultural integration can enhance the sense of identity of residents in the network, making it easier for cities to achieve common goals and interests. Obviously, after the formation of urban network, with the multi-dimensional integration of space, system, function and culture, it will be conducive to the further enhancement and improvement of urban network externality due to collaboration between cities.

3.3 Borrowing of urban scale

The concept of borrowing scale was first proposed by Alonso[20], which stems from Alonso's observation and thinking about the relationship between small towns and large cities, namely whether people can produce and live to have both the advantages located in small towns (lower costs and less crowding) and the advantages of large cities (greater markets and more specialized services). The concept of borrowing scale reflects the interaction between small cities and big cities. Meijers et al.[21] redefines this concept from the perspective of urban network, describing the positive impact of network connectivity on urban economy as borrowing scale, namely small cities can borrow the scale effect of big cities by embedding regional urban network. Big cities can borrow the superior resources of international cities by embedding national or world urban networks, and also utilize the consumer market of small and medium-sized cities. According to the view of Meijers, Yao Changcheng et al. further pointed out that the occurrence of the borrowing scale in the urban agglomeration is affected by the spatial structure of the urban agglomeration, and the multi-center urban ag-

glomeration tends to appear in the borrowing scale. In short, borrowing the perspective of scale tends to explore the formation mechanism of urban network externality from the perspective of different city scale.

4. Externality of urban network

The formation mechanism of urban network externality implies that the city will actively join or integrate only if the network has obvious benefits or promotion to the development of the city. At present, the utility research of such "benefits" or network externality focuses on two aspects: first, it focuses on the role of factor mobility on the promotion of knowledge diffusion and innovation, and the other is to focus on the impact of urban network on the improvement of urban competitiveness and economic growth.

4.1 Diffusion and innovation of knowledge

Different from the advantages of agglomeration economy as lower transportation costs and transaction costs, the externality utility of urban network is largely reflected in lower information cost of production and living activities due to the formation of urban network. Batten[16] proposed the idea of cultivating "creative urban agglomeration" in regional spatial policy research, observing that some of the places in the world are developing a similar creative urban agglomeration that provides unique combinations characterized by attractive and cultural diverse environments, advanced research and development and educational facilities, and a flexible and creative workforce. While urban partners can benefit from the dynamic synergies of interactive growth through reciprocity, knowledge exchange, and unexpected creativity. Glückler[13] explores the impact of urban network on knowledge service enterprises from the perspective of "reputation overflow". Different from the traditional analysis methods, his research on knowledge service enterprises focuses on three transformations as transformation from production relations to market relations, from technological knowledge to relationship knowledge, and from cost to opportunity. He believes that urban networks convey

the advantages of overflowing reputation. The closer a city connect to other cities in the city network, the more business opportunities the local companies tend to get. If a city is highly connected within a city system, it will convey accessibility advantages to companies outside. As for the transmission of knowledge information, Boix et al.[11] believe that, different from the traditional urban level paradigm, in the urban network paradigm, knowledge diffusion can not only be transmitted vertically from high-level cities to low-level cities, but also between cities of the same level and even from low-level cities to high-level cities. Lüthi et al.[23] regard knowledge-intensive enterprises as agents who establish a spatial concentrated knowledge portal between regional and global economies, believing that the connection between cities is largely manifested as the connection of knowledge-intensive enterprises, and thus the utility of urban network externalities is largely manifested in promoting knowledge diffusion and promoting innovation.

4.2 Enhancement of urban competitiveness and economic growth

Although urban networks are often spontaneously formed by the multi-dimensional connection of political, economic, social and cultural factors, in the past 10 years, more and more urban governments have begun to consciously and actively integrate into urban networks at different levels and scales, in order to share the benefits of network externalities. The reason is largely that with the rapid development of economic globalization and regional integration, the competition among cities is becoming increasingly fierce. In this context, as a relatively independent competition subject, development strategic ideas began to shift from hierarchical competition perspective to urban regional or network competition and cooperation perspective[24]. Thus, it has aroused the research and attention of urban network on the improvement of urban competitiveness and its economic growth. For example, Wang Yunlin et al.[25] put forward the concept of network competitiveness. They believe that the network structure position that city occupies in the multi-dimensional contact net-

work reflects the city's ability to disperse resources and exert radiative influence in the urban network. Cheng Yuhong et al.[26] deconstructed the source of urban competitiveness acquisition from the perspective of urban network, believing that due to the existence of urban network externality, the relationship between cities is usually in a state of competition and cooperation, and these two relations have an important impact on the competitiveness of urban acquisition. Among them, the urban network cooperation ability and the urban network node advantages in the network since the network cooperation relationship give birth to the exogenous competitiveness of cities. Hu Guojian et al.[27] believe that the developed urban network system makes the urban agglomerations break through the administrative division restrictions, thus promoting the free flow of elements, realizing a reasonable urban division of labor and fully exerting the overall advantages of the region. In addition, some scholars have examined the impact of urban networks on industries such as retail[28] and manufacturing[29]. It is worth noting that some scholars have paid attention to the negative externality of the urban network, for example, Wang Sha[29] and Zhan Yibo[30] believe that the competition network in the same industry may restrict the growth of the urban manufacturing industry. Glaeser et al.[31] have found that urban networks will benefit Europe in the short term, but in the long term, this will lead to a lack of large newly-built corporates in European megacities.

5. Measure for externality of urban network

With the discussion of the formation mechanism of urban network externality and its utility, relevant empirical studies are also been carried out. The primary question of empirical research is how to measure the externality of urban networks. According to the existing studies, the urban network externality measures studies mainly involve two types of identification and estimation, including three commonly used methods.

5.1 Identification measure of urban network externality

Identification measure refers to such empirical research discussing on whether the urban network externality exists, while the size of the network externality value is not the main research goal. The purpose of such measure studies is largely an empirical test of the formation mechanism of urban network externality and its utility, including two methods: association analysis and regression analysis.

The first method to identify the externalities of urban network is mainly based on the association analysis of industry competition and cooperation relationship. Meijers[32] used the method to explore the Ranstard region of the Netherlands based on building the net model. Meijers believes that, since the universities and hospitals always extend their services in multiple cities, they can be used to investigate whether there is complementarity between cities, and then association analysis can be used to study whether universities and hospitals are differentiated in different cities. It is found that competition between universities results in repetition rather than complementary courses, which do not match the network model; while hospitals in different places choose to provide different specialized services to achieve urban complementarity, indicating some degree of network externality in the Ranstard region of Dutch. In 2010, van Oort et al. [18] identified whether network externalities exist in this region from the perspective of enterprise relations. By analyzing the contact data of 1,676 enterprises in Ranstard, they found that the economic interdependence in cities was stronger than the interdependence between cities in the network. There was no spatial integration between cities, and no clear evidence of functional integration was found, so they believed that there was no network externality in Ranstard region. It is found that with this method, the identification measure result of the network externality is largely determined by the research perspective and purpose of the researchers. Meanwhile, whether the sample enterprises selected is typical and representative will have a huge effect on the scientificity and accuracy of the research results.

Capello[9] uses regression analysis to study the measure of urban network externality recognition. Capello argued that the higher its connectivity in the network is, the better its performance will be, meaning that there is a positive network externality. To verify the relationship between the urban network connection and urban performance, he analyzed the "Network of Healthy Cities" built by the World Health Organization and the European Regional Office (The network, composed of European cities, organizes cities from different countries to create common policies in health and related areas), quantifying connection intensity into a weighted sum of the number of urban participating regional meetings and the number of cooperative cities, and quantifying urban performance as the ratio between the number of policies successfully implemented by cities through network cooperation to the total number of local successful policies. Then, a regression model with urban performance as interpreted variable and urban network connection strength as explanatory variable was constructed. The empirical analysis found a significant positive correlation between urban network connection strength and urban performance. Cheng Yuhong et al.[33] further pointed out that the externality size of the urban network is not only related to urban connectivity, but also to the scale (number of nodes) and density (density of connections between nodes). Qin Chenglin et al.[34] took 168 prefecture-level cities in central and eastern China as empirical objects. By constructing urban production functions, he took output as interpreted variables, urban connectivity and other control variables as explanatory variables. The empirical analysis found that every 1% increase in urban connectivity would lead to increase in output by 0.164%. Meijers et al.[21] took the infrastructure network as an indicator of urban connectivity, and further defined the positive impact of network connectivity on the urban economy as "borrowing scale" and the negative impact as "agglomeration shadow", so as to demonstrate the existence of network externality. As Capello[9] noted measures of network externalities need to identify stronger methods in terms of metrics and statistical analyses.

5.2 Estimation measure of urban network externality

Estimation measures mostly measure the urban network externality by using the estimation of spatial spillover effect from the perspective of the theory and methods of spatial econometrics. Compared with the identification measure, such methods provide further possibility for the numerical estimation of the network externality based on the identification of the urban network externality. Boix et al.[11] believes that growth is not only the internal process of a city, but also between cities, and as a result, the economic growth of a city must take into account the growth of the city associated with it. Accordingly, they conclude a simplified the conceptual model of urban growthas shown in the following formula：

$$y_j=f(l_j, c_j, ..., y_{j*}, l_{j*}, c_{j*},....), \ \forall \ j''\neq j \qquad (1)$$

where y represents output, l represents labor, c represents capital, j represents monomer cities, and j' means other cities. The model shows that the economic growth of a city is affected by both the economic factors within the single city and the other cities within the network, namely the network economic factors. The model is actually stripping the externalities of urban networks from the properties of monomeric cities. In the concrete empirical analysis, Boix et al.[11] represented the network relationship between cities by constructing spatial measurement models in the form of a spatial weight matrix, setting the model to:

$$Y = X\beta + WX_\gamma + \mu \qquad (2)$$

where X represents the element matrix such as labor and capital, W represents the urban network connection matrix, β and γ are the parameter vectors to be estimated, and μ is the random vector. By estimating the spatial measurement model, the value of the parameter vector γ can be obtained, which can analyze the spatial spillover effect of the factors affecting the urban economic growth, and then estimate the externality of the urban network. By virtue of above methods, based on measuring the population flow network, enterprise organization network and e-commerce network, Chong Zhaohui[35] examined the spatial spillover effect in the background of urban

network, and found that urban network of different perspectives has significant differences on the network overflow effect of the economic growth's main factors. Based on the train running data of 273 cities in China, Huang *et al.*[36] have verified that the externality of the urban network has a significant impact on promoting urban economic development. Gong *et al.*[37] provide important evidence for network spillover in the housing market by applying spatial lag and spatial Dubin models. Compared with identification measures, the approach treats urban networks as an interconnected integrity, analyzing the factor spillover effects of urban networks by constructing a spatial weight matrix. The advantage of this method lies in that it can estimate the spatial spillover effect influencing the urban network development in the urban network as a whole, whereas there are almost no systematic research on how to integrate the spatial spillover effects of different directions and weightiness so as to scientifically reflect the externality of urban network. In this sense, the measure method based on the spatial measurement model is closer to a measure of urban network externality, but still not a measure of urban network externality.

In general, the measurement study related to urban network externality remains relatively weak. At early stage, it may be primarily subject to the difficulties in obtaining urban relational data, hence leading to a lack of empirical data for accurate characterization and measurement of urban networks[38]. Later, with the development of urban relational data mining method, especially after the proposition of the "interlocking network model", the empirical research on urban network largely focuses on the structural analysis of urban network and network status ranking as a network node city, paying attention to network externality and its influence on urban development experience research is obviously less. The existing empirical research focusing on externalities still mostly based on dynamic analysis and lack of dynamic considerations. There are many problems such as the imperfect theoretical framework and insufficient explanatory power in the present studies, causing that some results can only be interpreted as conditional association instead of causal associa-

tions[21].

6. Conclusion and outlook

At present, urban network research has been a frontier in the international academic field and has gradually become a hot topic. With the continuous progress of diversified data mining of urban relationship and multi-dimensional measurement as well as characterization research of urban networks, as the essential attribute of urban networks, externality related theoretical and empirical research on cities are being carried out and attracting increasing attention in the academic field. From the research of scholars at home and abroad, western studies on the externality of urban network were earlier and mainly focus on global and regional scale, while domestic scholars focused on national and regional scale[39]. In terms of empirical methods and objects, domestic scholars have also made some innovations by learning from the world urban network research, which mainly reflected in emphasizing the national and regional background, and avoiding the globalization view of Europe and the United States. In addition, the construction of urban networks with novel perspectives and data also promotes the progress of urban network externality research[40]. Overall, domestic research on the externalities of urban networks is still relatively weak. Combined with the aforementioned combing and evaluation on the related research of urban network externalities, the following three aspects are worth noting.

First, it is necessary to have a good theoretical understanding of the externality of the urban network. There are some researches on the externality of urban network related to its formation mechanism and influence effects. And some preliminary consensus has been reached. However, most of these studies and consensus are carried out and obtained under the assumption of staticity, ignoring the network scale, which is not fully consistent with the inherent characteristics of the dynamic evolution and properties of the spatial scale in the urban network itself, and will inevitably bring deviate their theoretical understanding. In future studies, scale differences and network mosaic should be further explored from the compar-

ative perspective of dynamic evolution to deepen the theoretical understanding of the externality of urban networks.

Second, it shall further explore measurement method for the externality of urban networks. Existing measures for externalities of urban networks are single and simple to some extent. In most of the urban, connectivity is used as an alternative measure to identify externality, but they often ignore the impact of various factors such as network development level, structural characteristics, scale and spatial scale on urban network externality, thus reducing the scientific nature of the research results. The externality estimation method based on the spatial measurement model is still imperfect. The reason is largely due to the lack of understanding of the theory of urban network externality. The theoretical framework of measurement research in the future should be further explored, so as to build a scientific measurement evaluation index system, and adopt various quantitative methods.

Third, it shall further deepen the empirical research on the externality of the urban network. In general, the current empirical researches on the externality of the urban network are relatively weak both in its quantities and qualities, needing to be further explored. For China, urban agglomeration has become the main form of urbanization and an essential drive force to promote the new urbanization. The development and evolution of urban agglomeration is in essence a process of the continuous evolution of a regional urban network. In this sense, all levels of urban agglomerations finished or under rapid development and construction in China undoubtedly provide a rich practical sample for the empirical research on the regional scale urban network externality. Thus it is of great importance to strengthen the empirical comparative research at this scale, which is not only conducive to the theoretical verification and improvement of urban network externality research, but also conducive to providing scientific theoretical guidance for the development and construction of relevant urban agglomerations.

Conflict of interest

The authors declare that they have no conflict of interest.

Acknowledgments

References

1. Castells M. The space of flows. The rise of the network society: The information age: Economy, society, and culture volume I. Cambridge, USA and Oxford, UK: Blackwell Publishers; 1996. p. 407–459.

2. Neal Z. Does world city network research need eigenvectors? Urban Studies 2013; 50(8): 1648–1659.

3. Zhang J, Su T, Sun C, *et al*. The skeleton and evolution of urban network research: The visualization analysis based on CiteSpace. Inquiry into Economic Issues 2019; 5: 97–106.

4. Chen J, Xiao G. The new development of the study about overseas congregating economy. Jianghan Tribune 2005; 4: 5–12.

5. Rosenthal SS, Strange WC. Evidence on the nature and sources of agglomeration economies. In: Henderson JV, Thisse JF (editors). Handbook of regional and urban economics (volume 4). Amsterdam, Netherlands: Elsevier; 2004. p. 2119–2171.

6. Duranton G, Overman HG. Testing for localization using micro-geographic data. The Review of Economic Studies 2005; 72(4): 1077–1106.

7. Yan L, Wang D, Zhang S. Theoretical foundation and framework for understanding urban centers. Progress in Geography 2020; 39(9): 1576–1586.

8. Katz ML, Shapiro C. Network externalities, competition, and compatibility. American Economic Review 1985; 75(3): 424–440.

9. Capello R. The city network paradigm: Measuring urban network externalities. Urban Studies 2000; 37(11): 1925–1945.

10. Lin B, Gu R, Wang J, *et al*. From agglomeration

externalities to network externalities of crossing borders: Frontier progress of agglomeration economics. Urban Development Studies 2018; 25(12): 82–89.

11. Boix R, Trullén J. Knowledge, networks of cities and growth in regional urban systems. Papers in Regional Science 2007; 86(4): 551–574.

12. Johansson B, Quigley JM. Agglomeration and networks in spatial economies. In: Florax RJGM, Plane DA(editors). Fifty years of regional science: Advances in spatial science. Berlin, Germany: Springer; 2004.

13. Glückler J. Geography of reputation: The city as the locus of business opportunity. Regional Studies 2007; 41(7): 949–961.

14. Cabus P, Vanhaverbeke W. The territoriality of the network economy and urban networks: Evidence from Flanders. Entrepreneurship & Regional Development 2006; 18(1): 25–53.

15. Camagni RP, Salone C. Network urban structures in northern Italy: Elements for a theoretical framework. Urban Studies 1993; 30(6): 1053–1064.

16. Batten DF. Network cities: Creative urban agglomerations for the 21st century. Urban Studies 1995; 32(2): 313–327.

17. Meijers E. Polycentric urban regions and the quest for synergy: Is a network of cities more than the sum of the parts? Urban Studies 2005; 42(4): 765–781.

18. van Oort F, Burger M, Raspe O. On the economic foundation of the urban network paradigm: Spatial integration, functional integration and economic complementarities within the Dutch Randstad. Urban Studies 2010; 47(4): 725–748.

19. Meijers E, Hoogerbrugge M, Cardoso R. Beyond polycentricity: Does stronger integration between cities in polycentric urban regions improve performance? Tijdschrift voor Economische en Sociale Geografie (Journal of Economic and Human Geography) 2018; 109(1): 1–21.

21. Alonso W. Urban zero population growth. Dædalus: Journal of the American Academy of Arts & Sciences 1973; 102(4): 191–206.

22. Meijers EJ, Burger MJ, Hoogerbrugge MM. Borrowing size in networks of cities: City size, network connectivity and metropolitan functions in Europe. Papers in Regional Science2016; 95(1): 181–198.

23. Yao C, Song D. Borrowed-size, network externalities and agglomeration economies in the urban agglomerations. Industrial Economics Research, 2019(2): 76–87.

23. Lüthi S, Thierstein A, Goebel V, et al. Intra−firm and extra−firm linkages in the knowledge economy: The case of the emerging mega−city region of Munich. Global Networks 2010; 10(1): 114–137.

24. Cheng Y, Zhu Y. The turn of the world city study and Chinese world cities. Urban Planning Forum 2015(5): 39–44.

25. Wang Y, Niu W. Study on the city-scale network competitiveness. Urban Studies 2008; 15(2): 99–103.

26. Cheng Y, Chen L. Deconstruction of urban competitiveness from the perspective of urban network. Economist 2012; 8: 72–79.

27. Hu G, Lu Y. Progress, thoughts, and prospect of urban network research based on enterprise perspective. Progress in Geography 2020; 39(9): 1587–1596.

28. Burger MJ, Meijers EJ, van Oort FG. Regional spatial structure and retail amenities in the Netherlands. Regional Studies 2014; 48(12): 1972–1992.

29. Wang S. The study of network effects in Chinese urban system. Changsha, China: Hunan University; 2011.

30. Zhan Y. The effect of city network effects on urban economic growth. Changsha, China: Hunan University; 2015.

31. Glaeser EL, Ponzetto GAM, ZouYM. Urban networks: Connecting markets, people, and ideas. Papers in Regional Science 2016; 95(1): 17–59.

32. Meijers E. From central place to network model: Theory and evidence of a paradigm change. Tijdschrift voor Economische en Sociale Geografie (Journal of Economic and Human Geography) 2007; 98(2): 245–259.

33. Cheng Y, Chen L. Development characteristics of city network and its influence on urban competitiveness: Based on location data of 148 major financial firms on Pearl River Delta. Industrial Economic Review 2014; 5(4): 117–127.

34. Qin C, Sang M. Urban network and urban economic growth. Study and Practice 2015; 4: 5–11.

35. Chong Z, Qin C, Ye X. Economic networks and economic growth of urban agglomeration: An integrated

approach of big data and network analysis. Statistical Research 2018; 35(1): 13–21.

36. Huang Y, Hong T, Ma T. Urban network externalities, agglomeration economies and urban economic growth. Cities 2020; 107: 102882. doi: 10.1016/j.cities.2020.102882.

37. Gong Y, De Haan J, Boelhouwer P. Cross-city spillovers in Chinese housing markets: From a city network perspective. Papers in Regional Science 2020; 99(4): 1065–1085.

38. Ma X, Li G. Research methods for world city network and relevant inspirations. Progress in Geography 2012; 31(2): 255–263.

39. Li Y. Difference between Chinese and western studies on urban networks and its reflection. Urban Planning International 2018; 33(2): 61–67.

40. Pan F, Fang C, Li X. The progress and prospect of research on Chinese city network. Scientia Geographica Sinica 2019; 39(7): 1093–1101.

Journal of Geography and Cartography

Focus and Scope

Journal of Geography and Cartography (JGC) is an international open-access academic journal with rigorous peer-reviewed process. We are interested in the scientific topics from all fields of geography and cartography. Our ultimate goal is to make the journal a platform of global academic sources for high-quality geo-papers.

JGC publishes original research articles, review articles, editorials, case reports, letters, brief commentaries, perspectives, methods, etc.

Examples of relevant topics include but are not limited to:

1. Human geography and urban-rural planning
2. Geography science
3. Geochemistry
4. Natural geography
5. Plant geography
6. Hydrology
7. Soil geography
8. Geophysics
9. Environment science
10. Geographic information system
11. Cartography
12. Remote sensing technique
13. Geography teaching theory
14. Man-land relationship by analyzing and mapping geographic phenomena

EnPress Publisher, LLC

EnPress Publisher, LLC, is a scholastic conduit for an assembly of professionals in the domains of science, technology, medicine, engineering, education, social sciences and many more, as a roundtable for their intellectual discourse and presentation, and as an instrument to galvanize research designs, policy implementation and commercial interests, to facilitate the prevailing over their challenges and to encourage to the full advantage of their resources and true potential.

We are the intellectual and academic home for academic, educators, scholars, clinicians, corporate researchers, who all play important roles in a wide range of national and international research organisations, and whose interests, expertise, research approaches and industry objectives from around the world coalesce together to advance significant contributions in their research and professional fields.

As an instrument of information purveyor, we seek to combine academic rigor and originality with the nuanced development of policy and practice. Via our journals, client database, online campaigns and social media presence, we offer a platform for industry professionals to interconnect, as well as opening doors towards cost-effective solutions for them to succeed, and we confidently hope to inspire a new generation of multidisciplinary researchers, think-tank experts, policymakers and business entities to innovate and advance their knowledge across fields.